5-2018

Optical Properties of Thin-Film High-Temperature Magnetic Ferrites

Brian Scott Holinsworth
University of Tennessee, bholinsw@vols.utk.edu

To the Graduate Council:

I am submitting herewith a dissertation written by Brian Scott Holinsworth entitled "Optical Properties of Thin-Film High-Temperature Magnetic Ferrites." I have examined the final electronic copy of this dissertation for form and content and recommend that it be accepted in partial fulfillment of the requirements for the degree of Doctor of Philosophy, with a major in Chemistry.

Janice Musfeldt, Major Professor

We have read this dissertation and recommend its acceptance:

Charles S. Feigerle, Veerle Keppens, Ziling Xue

Accepted for the Council:
Dixie L. Thompson

Vice Provost and Dean of the Graduate School

(Original signatures are on file with official student records.)

Optical Properties of Thin-Film High-Temperature Magnetic Ferrites

A Dissertation Presented for the

Doctor of Philosophy

Degree

The University of Tennessee, Knoxville

Brian Scott Holinsworth

May 2018

Acknowledgments

First and foremost I wish to thank my advisor, Professor Janice L. Musfeldt, for her support, insight, guidance, and encouragement at all times. Thank you for introducing me to the wonderful world of spectroscopy. Your enthusiasm and drive is always an inspiration to me.

I am grateful to Professors Jon P. Camden, Robert Compton, Verlee Keppens, Charles Feigerle, and Ziling Xue for serving on my committee, as well as for all of their interest and help. Of course the first two are no longer employed at the University of Tennessee, but I am grateful for their assistance in the early stages of this endeavor.

I wish to acknowledge all the members of our research group: Tatiana Brinzari, Qi Sun, Peng Chen, Ken O'Neal, Dipanjan Mazumdar, Michael Yokosuk, Amanda Clune, Laura Casto, Judy Cherian, Amal al'Wahish, Nathan Harms, Kendall Hughey, Kevin Smith, Henok Mikre, Lakenzie Crawford, Brandon Chapman, and Joshua Bleu Wright for their help, encouragement, and collaboration. I am grateful to all the faculty and staff of the Chemistry Department who shared their knowledge with me and helped in variety of ways during my graduate program.

I would also like to thank Stephen A. McGill, Darrell G. Schlom, Hunter Sims, Arun Gupta, William H. Butler, Sanjoy Sarker, Mehmet K. Yurtisigi, Julia Mundy, Dipanjan Mazumdar, Charles Brooks, Hena Das, and Craig J. Fennie for their collaboration and inspiring conversations during these years. Without these brilliant scientists giving their input the work would not have been half of what it became. I am also grateful for those near and far that inspired me through their many conversations that taught me so many valuable things. One such example of an inspiring conversation came from a neighboring lab; Matthew Bailey and I would start talking in the hall from time to time. We could talk for hours and the topics could cover the wide spectrum of existence. We would even discuss the scientific issues we were running into and make suggestions or give each other support as the conversation necessitated.

I thank my parents for always supporting and believing in me, they made me a special kind of crazy. Last but not least, I thank my wife Lakenzie and our children for their support and encouragement throughout my study. My wife has helped me to expand my understanding of life outside of the physical sciences greatly and thus has enriched my passion for life itself. She has also helped me to see the value of what I am doing more deeply. Our children, Elian and Sebastian, have brought a new form of inspiration. They have helped me to realize what is truly important in life, working hard but also enjoying the here and now.

Abstract

Strongly-correlated electron materials reveal rich physics and exotic cross-coupled electronic and magnetic properties, with important fields results e.g. superconductivity and multiferroics. This is because of the competing interaction between charge, structure, and magnetism in the materials. In this dissertation I present a spectroscopic investigation of several model complex iron oxides under external stimuli of magnetic field, electric field, and temperature. The compounds of interest include $NiFe_2O_4$ [nickel ferrite], $CoFe_2O_4$ [cobalt ferrite], h-$LuFeO_3$ [hexagonal lutethium ferrite], and $LuFe_2O_4$ [lutethium ferrite]. These materials are attractive systems in the fields of multiferroics and high-temperature magnets for investigating optical band gap tunability, lattice and charge dynamics, spin-charge coupling, and optically-enhanced magnetoresistive effect. In these works, we have combined optical spectroscopy, magnetic circular dichroism (MCD), and (magneto-)photoconductivity, with high-quality thin-film growth, and first-principles calculations to reveal the nature of the optical excitations within these strongly correlated iron oxides. $NiFe_2O_4$ we found that optical excitations offer the opportunity for producing spin-polarized current. In $CoFe_2O_4$ we showed that the band gap is robust with temperatures up

to 800 K. We found that the direct-gap excitation of $LuFe_2O_4$ is highly sensitive the strain induced by epitaxial growth.

Table of Contents

List of Tables

List of Figures

Chapter 1

Introduction to Ferrites

> Science is built up of facts, as a house is built of stones; but an accumulation of facts is no more a science than a heap of stones is a house. Most important of all, the man of science must exhibit foresight.
>
> Henri Poincaré
>
> Science and hypothesis

In general, complex materials display rich and applicable properties involving electronic and magnetic attributes including a plethora of novel magnetic phenomena and valuable optical properties. The complexity results from interactions over considerably large scales in length, energy, and time. This is exemplified by complexity expanding the system from binary to ternary and beyond. Surveying the binary systems, such as CuO or EuO,[1, 2] one discovers that the materials can posses

properties ranging from insulating to superconducting. Additionally, phenomena such as ferroelectricity and various forms of magnetism emerge. In the higher order systems (ternary, quaternary, and beyond chemical complexes), properties become more exotic and in turn the complexity increases as well. A few noteworthy exotic phenomena include multiferroism, colossal magnetoresistance, and high-temperature superconductivity. Multiferroism arises either in single phase (single material) or multiple phase (composites of 2 or more materials) systems.[3] By a combination of properties, a multiphase system directly represents a form of multifunctionality. Competition between charge, spin, orbital, and lattice degrees of freedom plays a key role in the hosting of rich physics, chemistry, and ultimately phase diagrams.[4, 5, 6]

All of the materials involved in this dissertation belong to the broad family of transition metal oxides and more specifically to the group of ferrites, some also include rare-earth elements. Ferrites are iron and oxygen containing materials, with other elements potentially included. They are well known for resulting in strong electronic correlations. This occurs because the transition metal valence s electrons transfer to the oxygen ions in the local lattice, and then the strongly correlated d electrons ultimately determine the physical properties of the material. In the transference of electrons to the oxygen ions a strong electrical field at the interatomic length scale is setup, strong Coulomb repulsion.[7, 6] The internal electrical field can bring about a strong correlation of the electrons, thus behavior on one atom is dependent on those surround it. This correlation has the potential to turn on cooperative effects, e.g. ferromagnetism, electric transport, magnetism, optical response, and thermal conductivity. The electronic correlations involved in these systems place constraints on

the number of electrons available in a given lattice space, producing a localized entanglement of the charge, spin, and orbital degrees of freedom.[8, 9, 10, 11, 12, 13, 14, 15] When considering the impact of both the constraint and entanglement a laundry list of phenomena arise including: multiferroic, charge, spin, and orbital ordering, Mott insulators, and metal-insulator transitions. [4] The competition and interplay between spin, charge, orbital, and lattice degrees of freedom have been shown to predicate the functionality of this family of materials.[8, 4, 6, 16] The signatures for these competitions are spin-charge coupling, spin-spin interaction, spin-lattice interaction, and spin-orbit coupling. A primary concern for designing functional materials, and devices, stems from being able to control the various interactions. Spectroscopy is a probe used in the investigation of many forms of these interactions, the corresponding excitations, and many other excitations, including: spin-charge, spin-orbit, and spin-lattice coupling effects as seen in Fig. 1.1, as well as those shown in Fig. 1.2.

If an oxide simultaneously contains magnetic ordering and insulating properties, then the door to spintronics opens. Spintronics are strongly rising in importance for device physics, such materials optimize the performance for the device applications within the current framework of knowledge and understanding.[17] An example is accomplishing spin-polarized current of electrons through having a highly effective spin-filtering effect due to spin-dependent tunneling processes.[5] Clearly transition metal oxides are complex materials with a large variety of applicable emerging phenomena.

Through understanding and manipulating these interactions, more purposed fabrication of (multi-)functional complex materials becomes viable via the acquired

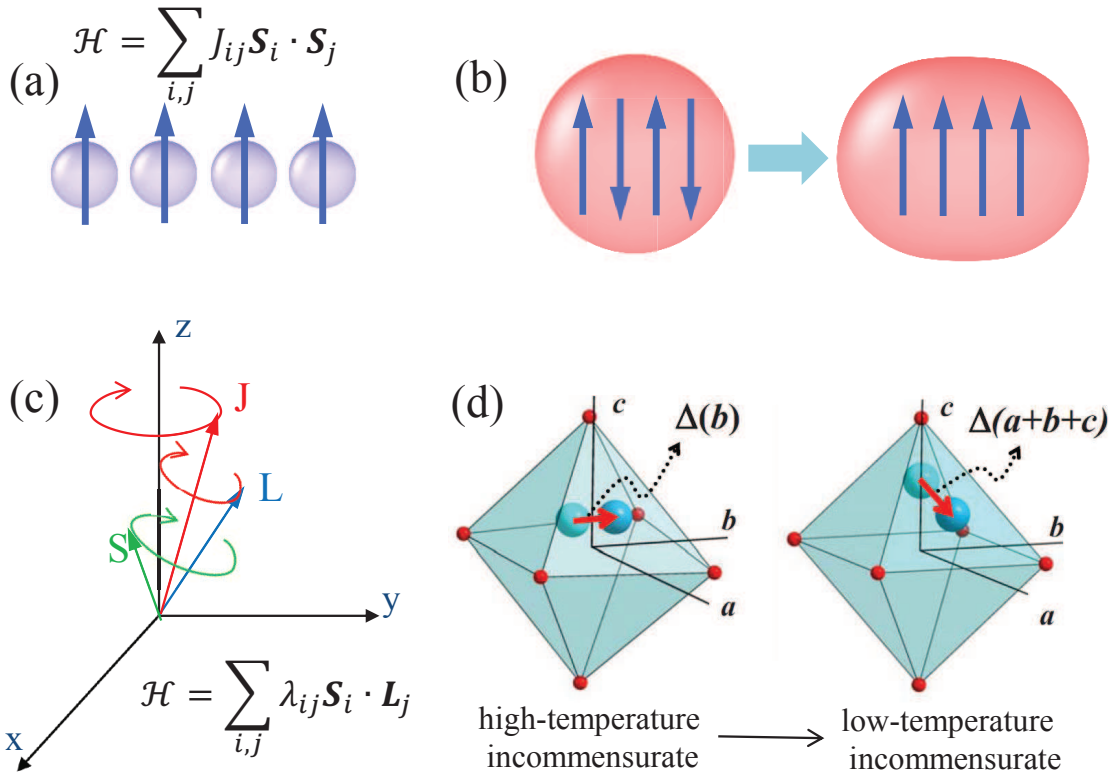

Figure 1.1: Schematic diagrams of (a) Spin-spin interaction, (b) spin-charge coupling-spin order change induced charge density change, (c) spin-orbit coupling, and (d) spin-lattice coupling and the change in local structure with spin orders (after [18]).

knowledge. To establish a clear understanding of these interactions one must measure and investigate from a wide set of tools to produce a variety of responses. These varied tests help to reveal the underlying mechanism(s) that induce a phenomena into existence. To truly understand the physical properties in complex materials one must also conceptually grasp the symmetry of the order parameter. The primary symmetries one should concern themselves with are spatial inversion $\vec{r} \rightarrow -\vec{r}$, time-reversal $t \rightarrow -t$, and gauge. The relationships and some corresponding physical

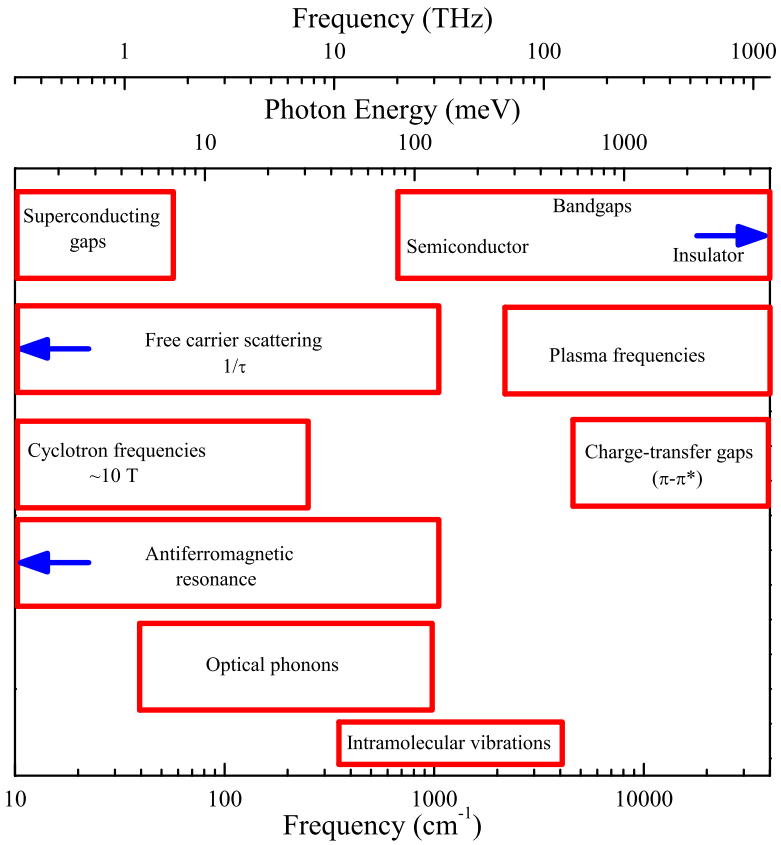

Figure 1.2: Display of a select variety of optically viable excitations seen in complex oxides.

properties are shown in Table 1.1. According to the Neumann principle, the total symmetry is lowered when proceeding through a phase transition. Strictly when one of these properties arises, the corresponding symmetry is required to have been broken [Fig. 1.3].

For example, rotational symmetry breaks in *spin space* upon ferromagnetic ordering, thus the ordered phase has a lower symmetry than the Hamiltonian of the system. To get a sense of how this plays out, evolving the wavefunction ψ in time

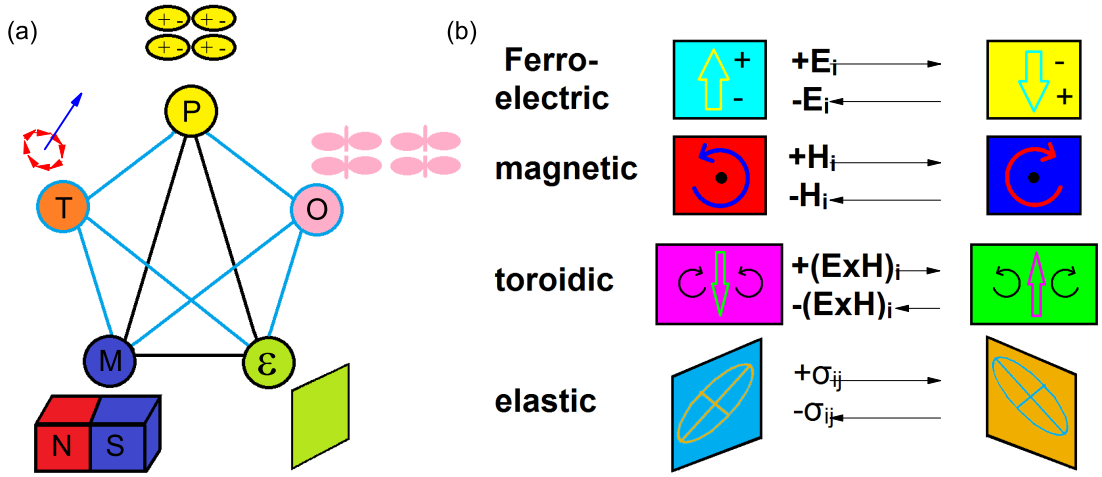

Figure 1.3: Display of a select variety of optically viable excitations seen in complex oxides. After Ref. [19]

is given by $e^{-iEt/\hbar}$. The ferromagnetic ordering transition can also be described by time-reversal symmetry, this is equivalent to taking the complex conjugate of the wavefunction and the rotation of the spinning particle reverse directions under the reversal of time. As another example, breaking spatial inversion symmetry can lead to spontaneous electric polarization in insulators, resulting in ferroelectricity, or pyroelectricity in the case of polar point group symmetry.[4]

Electromagnetic radiation, the backbone of spectroscopy, occurs as a continuous

Table 1.1: Symmetry breaking → physical property

Symmetry	Representation	Physical property
Spatial inversion	$\vec{r} \rightarrow -\vec{r}$	ferroelectricity
Time-reversal	$t \rightarrow -t$	ferromagnetism
Gauge	$\psi \rightarrow e^{i\Theta}\psi$	superconductivity or superfluidity

function. The wavelengths are longer than radio waves through waves that are shorter than x-ray. This results in photon energies ranging from a 10's μeV up to 100's keV just in the range shown in Fig. 1.2.[20, 21, 22, 23, 24] This dissertation focuses primarily on optical properties from far-infrared to ultraviolet. The research emphasizes the near-infared, visible, and ultraviolet portion of the spectrum. Figure 1.2 displays a few energy scales and the common ranges for their resonances. In this regime one is able to probe the nature of chemical bonding, hybridization, and many other properties, with the important note that excitations are to be dipole-allowed. If one uses lower frequency spectroscopy, such as infrared or scattering, the opportunity to directly investigate magnetic and vibrational excitations presents itself. These excitations are important in the thermal and electrical conductance properties. When a crystal vibrational excitation (phonon) interacts with charge and/or magnetic excitations a defect like state such a polaron is created. On the higher frequency side, charge transfer and metal $d \rightarrow d$ on-site excitations are evident throughout the absorption spectrum, because of hybridization of chemical bonds. Delving deeper into these one finds that the charge transfer excitations are responsible for the band gap of ferrites. These excitations are fundamentally described as an electron transferring from the valence band maximum to the conduction band minimum; charge transfer excitations exist in the full range of sizes, molecular to macroscopic crystalline, and can occur from any number of bands (states). Within the field of ferrites, commonly these excitations occur as oxygen $2p$ to a metal center $3d$, hybridization also allows for the possibility of excitation from one metal center to another metal center. To further understand these properties usage of first-principles electronic structure cal-

culations provides a notion into the electronic structure like density of states, band gap of functional materials and can be used to compare with the optical results. [25, 26]

Using external stimuli to control material properties

Controlling a materials physical properties arises from many applied stimulus directions including temperature, magnetic and/or electric field, pressure, finite size, and chemical substitution. These are broadly employed; moreover, these techniques used in the tuning of properties arise because the fundamental constituents, namely chemical bonding/hybridization, charge distribution, electronic structure, and magnetism are highly sensitive to the environmental conditions to which the material is exposed. [27, 28, 29] Strain engineering is by definition a superset of pressure physics, strain ϵ is represented by a 3×3 symmetric tensor with six (dimensional) independent components,[30, 31] and presents viable technique to manipulate material properties e.g. electronic structure, conductivity, ionic diffusion, magnetism, ferroelectricity, and crystallographic symmetry. The latter of these grants access to unexposed phases and functionality, nonexistent in the bulk phase. Strain is introduced in this work through epitaxial growth; therefore, the substrate lattice has a direct impact on the film lattice, of course this typically occurs over a narrow thickness and mismatch range.[32] Epitaxial growth, or biaxial strain, changes the in-plane lattice vectors directly by clamping the grown material to the substrate; additionally this will alter the out-of-plane lattice vector. Addtionally, epitaxial growth gives access to induced strain at the interface, this offers an axis of property tuning. Additionally, this should be amplified in a superlattice architecture.[33, 34] Specifically,

strain is known to be an efficient tuning parameter for complex oxides and in particular ferrites.[35, 36, 32, 37, 38, 39] For instances strain has been used to induce the magnetoelectric effect in $BaTiO_3$–$CoFe_2O_4$ and $BiFeO_3$–$CoFe_2O_4$ composites along with $La_{0.67}Sr_{0.33}MnO_3$–$BaTiO_3$ as a heterostructure.[39, 40, 41, 42] Strain has been used to enhance electron mobility in transistors, catalytic activity, alter band structure, and transition temperatures for various ordering parameters.[36, 43] We also explore the outcome of using temperature, electric-, and magnetic-field to alter the electronic structure of the thin-film ferrites. The temperature variations tend to have the effect of sharpening the excitations with decreasing temperature.

Another highly tunable parameter is the band gap. Briefly, the band gap offers great importance as an electronic energy scale, because it determines a variety of physical properties such as the *dc* resistivity; the gap is essential to a myriad of applications such as spin filtering and energy acquisition via light harvesting.[44, 45, 46] The fundamental electronic gap of Mott and charge-transfer type insulators are determined by their *d*–*d* and charge-transfer excitations, respectively.[47, 48, 49] Being able to tune this energy scale allows one an unprecedented pathway to develop complex ferrites with emergent electronic, optical, and magnetic properties.[50] Here, a spin-charge coupling effect appears as a rigid shifting of the band gap, offering incredible sensitivity.[51, 52, 53]

In this work, I focus on epitaxial ferrite thin films, these films fill an important gap between fully bulk single crystals/thick films and ultra-thin films that introduce confinement effects.[54, 55, 56, 57, 58] They not only prove technological promise as a way to incorporate customizable magnetic properties but also give an opportunity to

better understand the structure-property relationships of this material family. To exemplify this consider the short wavelength magnetostatic wave devices. Single-crystal films provide the necessary reduction in wave attenuation because they effectively eliminate scattering due to fewer grain boundaries. Also, fundamentally they are valuable because they provide a great model systems to investigate super-exchange interactions. Finally, epitaxy gives an incredible opportunity to directly see how the strain and relaxation effects the electronic and magnetic properties.[59]

When looking more specifically at spinel ferrites $A\mathrm{Fe_2O_4}$ an important and interesting technologically useful property (resistivity) is tunable by four orders of magnitude (10^4), without significantly effecting the magnetic transition temperature (T_C), in $\mathrm{Co_{1-x}Fe_{2+x}O_4}$ and $\mathrm{Zn_xFe_{3-x}O_4}$.[60, 61, 62] Depending upon the metal ion chosen to take residence in the A position and the level of doping, the magnetic moment can be broadly tuned up to $8\mu_B$. This tunability is achieved by cation substitution, replacing a portion of the A in $A\mathrm{Fe_2O_4}$ increases the overall scattering of the bound state excitation. However, this unfortunately results in a loose coupling of the spin and charge.

Another set of technologically valuable materials are the rare-earth ferrites, these materials occur in a large variety of compositions and crystal structures. In this work, we probe this extension by the incorporation of Lu cations into the lattice, we investigated $\mathrm{LuFe_2O_4}$ and h-$\mathrm{LuFeO_3}$. The value of these materials lies in their ferroelectric and magnetic ordering. This brings into vision the world of strongly-correlated electrons and the physics that results from these interactions (including spin-orbit coupling), encompassing such phenomena as superconductivity, superflu-

idity, and various forms of magnetism.[63]

Using circularly polarized light gives rise to increased sensitivity to chiral centers within a material, by applying an external magnetic field (or additionally by having remnant magnetization or exchange driven spin-split band structure)[64] along with the circularly polarized light one can access deeper understanding of the electronic structure and excitations.[65, 66, 67, 68, 69] This methodology allows for sensitivity to the ordering in the orbital environment, along with the response/ordering of the spin environment through spin-orbit interaction/coupling.[70, 71, 72, 69]

1.1 Overview of Dissertation

In this dissertation, I combine optical and magneto-optical spectroscopies to investigate several model and directly applicable materials, high-temperature magnetic spinel ferrites along with multiferroic ferrites, in a variety of extreme environmental conditions including high magnetic field, high electric field, and high (low) temperature. The systems of interest are all epitaxial thin films, the compounds include: $NiFe_2O_4$, $CoFe_2O_4$, h-$LuFeO_3$, and $LuFe_2O_4$. Scientifically the concern amongst these materials largely focused towards lattice-charge coupling, charge-transfer gap tunability, and spin-charging coupling. The important electronic energy scales, such as the band gap, can be tuned with surprising sensitivity to external stimuli. We also find that spin-charge coupling is strongly correlated to magnetic transitions and that charge-transfer excitations can display considerable information with regards to being spin-polarized in magnetic circular dichroism. Our findings are summarized in

Tables tables 1.2 to 1.5.

Table 1.2: Scientific problems and important findings in $NiFe_2O_4$

Model Compound	**Scientific Problem**	**Our Findings**
$NiFe_2O_4$	• Fundamental gap identity and energy • Spin-dependent nature of electronic structure • Spin-polarized optical excitations • Generation of spin-polarized current • Metamagnetic transition influence	• Fundamental gap is indirect at 1.55 eV • Two distinct magnetic sublattices create spin-dependent electronic structure • Spin-polarized fundamental gap evidenced by dominate absorbance of a single angular momentum of light • Higher energy optical excitations show preferential absorbance of specific angular momentum in narrow energy windows • Minority channel excitation window promotes spin-polarized current production • Flipping the Ni spin induces a metamagnetic state that promotes $\alpha(H)$ tunability

Table 1.3: Scientific problems and important findings in $CoFe_2O_4$

Model Compound	**Scientific Problem**	**Our Findings**
$CoFe_2O_4$	• Energy and position of charge-transfer optical band gap(s) • Spin-charge coupling on approach to T_{FM} • Assignment of excitations • Magneto-optical response and spin-polarized excitations	• 1.2 eV fundamental indirect gap at $X \to \Gamma$ • Gap remains robust up to ferrimagnetic–paramagnetic transition, spin-charge coupling is weak • Hybridized Co + O valence edge gives O $p \to$ metal d and intersite metal $d \to$ metal d charge-transfer like transitions, with minority channel dominated by Co + O $\to$ Fe(O_h) • MCD displays asymmetry in response • Spin-polarized excitations induce enhanced magnetoresistance via spin-polarized current production

Table 1.4: Scientific problems and important findings in h-$LuFeO_3$

Model Compound	**Scientific Problem**	**Our Findings**
h-$LuFeO_3$	• Energy and position of fundamental gap • Assignment of excitations • Magneto-optical response • Spin-charge coupling	• Fundamental gap assigned to the 1.1 eV direct gap involving • Hybridized Fe $3d_{z^2}$ + O $2p_z \to$ Fe d excitations at the Γ and A points • Magnetic circular dichroism confirms electronic band structure supports lower energy excitations • Significant spin-charge coupling, allows for deduction of paramagnetic $\to$ antiferromagnetic transition

Table 1.5: Scientific problems and important findings in $LuFe_2O_4$

Model Compound	**Scientific Problem**	**Our Findings**
$LuFe_2O_4$	• Energy and position of charge-transfer gap in thin film • Strain dependence of gap • Spin-charge coupling • Single crystal vs thin film response	• Oscillator strength of excitation edges shift to significantly higher energy • Energy of gap shifts at a rate of 16:1 compared to the lattice parameter change • Spin-charge coupling appears in

$NiFe_2O_4$ attracted our attention because it is a model and technologically viable ferrimagnetic insulator at room temperature. By growing films on a similarly structured substrate one can reduce concerns with antiphase boundaries and thus increase sensitivity to the magnetic and optical properties by reducing overall scattering. It is important to note that the potential usefulness of these domain walls have come under investigation. Primarily it is important to know the implications of all parts of a material, from interface attributes to tendency for defects to surface(bulk) properties. Through combining magnetic circular dichroism, photoconductivity, and magneto-photoconductivity we reveal that fully inverse spinel structure $NiFe_2O_4$ has a spin-polarized fundamental indirect gap and can support spin-polarized charge carrier transport. The corresponding electronic structure calculations display the former of these results clearly, indicated by the spin-splitting of the valence and conduction bands. Photoconductivity shows that the films are high-quality, not leaky due to oxygen vacancies. The applied magnetic field shifts the magnitude of current flow through the sample when the light is turned on by 6.5%, vs. a nominal 1% without light.[73] This provides a direct opportunity for application in the arena of spintronics, where materials are viewed from the perspective of being able to manipulate spin

not just charge. Spintronics is an extremely promising field for new technologies, the premise is to manipulate the spin degrees of freedom of electrons in semiconductors and insulators for the purpose of applications in the realms of memory, operation, and communication for starters.[74]

With the application of epitaxial strain already being considered within the spinel ferrites ($NiFe_2O_4$), the next parameter we exploited is chemical substitution. When done within a given structure the emergence of phenomena can result, simply by changing the distribution of ions. This is a highly effective method to fine tune the physical properties of functional materials. $CoFe_2O_4$ is unique amongst spinel ferrites because it has a large magnetic anisotropy, that is accompanied by a large anisotropic magnetostriction.[75, 76, 77] Some consider this material to not be technologically viable because of its very short spin-lattice relaxation rate; however, this is only an opinion because technology exists for the full expanse of the frequency spectrum. When comparing $NiFe_2O_4$ and $CoFe_2O_4$ reports show that the former is completely inverse, where as the latter has an inversion fraction (λ) of $\approx$70–80%. This has been attributed to the differences in atomic radius for Ni vs. Co ions. These magnetic insulators stem from the metallic parent compound of magnetite (Fe_3O_4), ultimately coming from the parent compound of complex oxides α-Fe_2O_3.[78] To investigate this system and probe the usefulness of the magnetic phase, we employed temperature-dependent optical spectroscopy and complementary electronic structure calculations in one portion of our investigation. We also employed temperature dependent growth on $MgAl_2O_4$, ultimately focusing on the 690 °C grown film. We revealed that $CoFe_2O_4$ is fundamentally an indirect gap material with the gap going

from $X \rightarrow \Gamma$ at an energy of 1.2 eV. The valence band edge is hybridized Co + O states, whereas the conduction band states are comprised of Fe (T_d, A-) and Fe (O_h, B-sites), respectively. From theory it is seen that the fundamental gap is expected to occur near 0.9 eV.

The tunable nature of optical band gaps and excitations through epitaxial strain, via stabilization of phases otherwise not accessible, drew our attention to $LuFeO_3$. Additionally, this material had recently been classified as a multiferroic and so we wanted to get our hands on it to investigate this from an optical perspective. The symmetry of the bulk phase is orthorhombic ($Pbnm$), whereas if grown on Yttria-stabilized zirconia (or Al_2O_3) one has access to the multiferroic hexagonal phase ($P6_3cm$, h-$LuFeO_3$.)[79] Evidence had been presented for a fundamental gap of 2.0 eV, with the lower energy excitation being considered as tail of multiple internal reflections and impurities.[80] We investigated h-$LuFeO_3$ by combining high-quality single-crystal thin film growth, temperature-dependent optical spectroscopy, magnetic circular dichroism, photoconductivity, and complementary electronic structure calculations. This comprehensive approach allows for a thorough understanding to be reached of the electronic properties of h-$LuFeO_3$. We revealed that h-$LuFeO_3$ is fundamentally a direct-gap material at an energy of 1.1 eV. This gap occurs at the Γ and A points being comprised of the hybridized Fe $3d_{z^2}$ + O $2p_z \rightarrow$ Fe d excitation and does show some minor characteristics of being indirect. The minor indirect contribution makes logical sense. Indirect excitations prove to be much smaller in their absorption cross-section because of the multistep process compared to one step process for a direct excitation; therefore, since the fundamental gap does not have

the sharpness of a traditional direct excitation then it must correspond to having partial indirect character. Along side this, we also revealed the sensitivity of the charge transfer gap to the paramagnetic → weakly ferromagnetic transition (147 K) but at the reported paramagnetic to antiferromagnetic (440 K) transition nothing is seen. We used the well documented higher-energy gap to track the temperature-dependence and get a cross-sectional view of the spin-charge coupling. With the application of magnetic circular dichroism we clarified that the electronic excitations do indeed exist down to ≈1.0 eV, corresponding with the lower energy charge-transfer gap put forward by our work. Ultimately the epitaxial strain stabilizes the hexagonal phase and results in a material with a marketable overlap with the solar spectrum, along with spin-charge coupling that we were able to use to track across the the paramagnetic → weakly ferromagnetic transition (147 K.)

The approach of epitaxial strain was also employed for the investigation of $LuFe_2O_4$. This material had been reported to be a charge ordered multiferroic near room temperature.[81] The bulk phase has a fundamental indirect gap estimated to be ≈0.35 eV with a higher energy direct gap at 3.1 eV. These excitations correspond to $Fe^{2+} \rightarrow Fe^{3+}$ charge transfer and O $p \rightarrow$ Fe d along with the O $p \rightarrow$ Lu s charge transfer excitations, for the bands centered at ≈1 and 4 eV, respectively.[82] The films we probed were on the order of 75 nm thick, and they were grown on $MgAl_2O_4$, along with silicon carbide, with the ab-plane exposed. The films were not fully commensurate but the average in-plane lattice parameter on $MgAl_2O_4$ is 3.42±0.02 a 0.6% reduction from bulk. The resulting epitaxial strain of $MgAl_2O_4$ blue shifted the direct gap to 3.4 eV, this correspond to a ratio of 16.6:1 band gap to lattice pa-

rameter change, suggested that further reduction of the lattice parameter will further shift the excitation energies. However, the fundamental indirect gap is un-discernible in these thin films due to their leakier tendency i.e. the uncertainty is significantly increased due to limited optical density.[83, 84]

To delve deeper into the physics of these materials, we employed the magneto-optical spectroscopic technique magnetic circular dichroism to investigate spin-charge and spin-lattice coupling in these materials. Fundamentally this investigative technique measures the difference in absorption of the two poles of helicity ($\sigma_{\pm}$) in a DC magnetic field that is parallel to the $\vec{k}$, Faraday geometry.[85] Ultimately any change in this value signifies a change in projected orbital angular momentum along the magnetic field direction, with the prerequisite of spin-orbit interaction to get a vision of the spin angular momentum. The magnitude of this value corresponds to the quantity of electrons that absorb circularly polarized photons in heeding to the conservation of angular momentum.[86] This probe shows a significant change in the vicinity of spin-polarized excitations, based upon field direction, of $NiFe_2O_4$. When investigating the multiferroic h-$LuFeO_3$ we elucidated that the electronic excitations are allowed at much lower energy than previously supposed. Through this we also learn that because the transition is spin disallowed the optical absorption is fundamentally lower than expected. In the cases of multiferroic h–$LuFeO_3$ and $LuFe_2O_4$, the findings improved the realm of applicability by validating the lower bound of the electronic excitations and showing the epitaxial strain mediated tunability of the charge transfer gap.

During the course of this work I was also given the opportunity to design, build,

and implement an instrument to measure photoconductivity. A significant motivation for building this instrument was the complimentary nature of the technique. Of course, it adds a degree of freedom to light-matter interactions. More specifically, photoconductivity provides information about the electronic structure and mechanism(s) of transport in accordance with the energy spectrum of the mechanism(s). A virtue of photoconductivity is that it only corresponds to *active* absorption, such that incidental lossy responses i.e. free carrier absorption or scattering via imperfections are not embedded in the information recovered. The approach for building the instrument was strongly heuristic because the method is inherently a complex one, because the process invokes thermal and hot carrier relaxation processes, charge carrier statistics, electrode effects, and a variety of recombination process mechanisms.[87] This instrument was key in revealing the change in magnetoresistance caused by a static external electric field, over-layed with an oscillating electric field (incident electromagnetic radiation), along with an applied magnetic field ($\approx$1.5 T). The experiment was done in a current-in-the-plane (CIP) device architecture.[88]

Ultimately, the research involved in this dissertation was an investigation of the electronic structure, optical and magneto-optical properties, along with frequency-dependence (optical frequencies) of transport and magneto-transport properties. The remainder of this dissertation is organized as follows: Chapter 2 presents a literature survey of strongly-correlated ferrites with individual foci on the systems of interest here. Chapter 3 discusses our experimental methodology, namely infrared and optical techniques, interaction of light with solids, magneto-optical and electro-optical experiments, and sample preparation and characterization. Chapter 4 is devoted

to $NiFe_2O_4$, with a primary focus on the electronic structure and optical properties involved in the magnetic interaction. Chapter 5 details the optical investigation and outcomes of $CoFe_2O_4$, this is extended into the magneto- and electro-optical experiments. Chapter 6 presents our optical investigation and results on h-$LuFeO_3$ and $LuFe_2O_4$, focusing on optical band gap, temperature-dependence of optical response, and magneto-optical response in regards to long-range ordering. Chapter 7 is devoted to the building and development of the photoconductivity instrument. Chapter 8 summarizes my work.

Chapter 2

Literature Survey of Magnetic Oxides

> Without fiction, there is no imagination; without imagination, there is no dream; without dreams, facts hardly matter. ... There would be no progress, not even scientific progress, without the imaginative fashionings after the real.
>
> Charles Lemert,
>
> Dark Thoughts: Race and the Eclipse of Society

2.1 High T magnetic oxides, towards spintronics and multiferroicity

The question that inspired the work presented in this dissertation is: do complex ternary oxide materials have potential application in the energy harvesting, sensing,

data storage, and spintronics industries? What makes this a good question? It points to a specific group (complex ternary oxide materials) for investigation and gives purpose for doing the research (application in energy harvesting, sensing, data storage, and spintronics industries).

Ternary oxides are chemical compounds containing oxygen and two other (typically transition metal) elements. Or it could contain oxygen and one element in two oxidation states, e.g. Fe^{2+} and Fe^{3+}. This leads to the more specific form that we chose to explore, complex ferrites such as the two oxidation states presented just prior. Complex ferrites exist over a wide variety of crystalline structures and display a large range of physical phenomena, arising because of interactions over extended length, energy, and time scales, such as the ternary level of complexity [Fig. 2.1].[89, 90, 20]

This family of materials offers an ideal platform to investigate electron correlations due to interaction between the metal d and/or f electrons with oxygen p electrons. These correlations result in highly intertwined degrees of freedom of the charge, spin, lattice, and orbitals.[4, 91, 92, 93, 94, 95, 96, 97] Ultimately by combining the intrinsic degrees of freedom materials rich in physical phenomena are presented, such as multiferroics, superconductivity, quantum criticality, charge transfer, and symmetry breaking, the latter of these contains both time and spatial breakage, as shown in Fig. 2.2. As of late, much emphasis has been placed on the manipulation of these phenomena, with the hope of creating new phenomena or properties.[22, 98, 99, 100, 101]

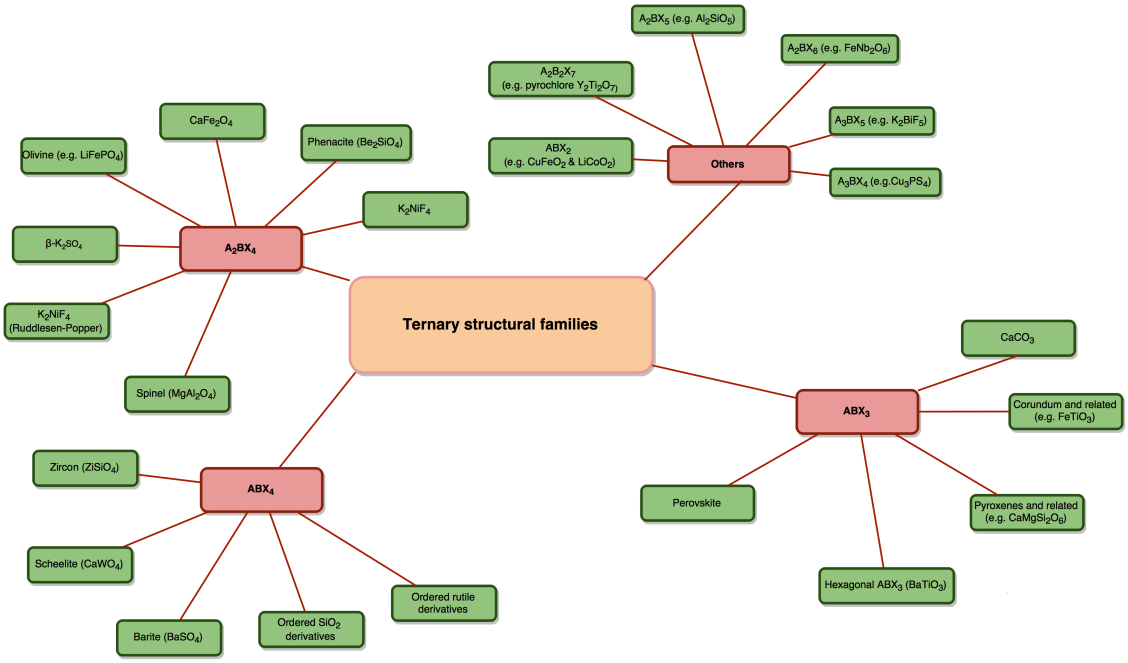

Figure 2.1: A diagram depicting the variety of ternary structures.

2.1.1 High T magnetic and spintronic materials

When deciding on the realm of application for a material the thermodynamic transition temperature and robustness of the phase of functionality prove to be important factors to consider, e.g. paramagnetic to ferromagnetic and/or paraelectric to ferroelectric. If the desire is to have the application at room temperature, it would be best to ensure that the phase is well established. Thus having the transition temperature above this regime, say 50 K, of application allows for the desired phase to be established and still have energetic room for temperature fluctuations. In this dissertation, we focus potential application mainly towards room temperature but any advancement is highly appreciated. The high-T_C materials selected to be investigated in this dissertation have transition temperatures near 800 K and tend to display robust if not virtually static trends with regards to changes in optical properties versus temperature. This outcome provides a way to characterize the stability of a particular thermodynamic phase and potentially gain insight into several forms of coupling, such as spin-charge and spin-lattice. In the investigations discussed here within this dissertation we also show interest and concern with how the motion of the electrons can be correlated, in particular this arises most strongly in the case of $NiFe_2O_4$.

It is important that we establish what it means for a material to have strongly-correlated electrons; however, if we are to consider correlated electrons it is rational to take a step back and describe uncorrelated electrons. In an uncorrelated system the Hartree product [Eq. 2.1] displays the probability of simultaneously finding electron 1 at site $\mathbf{x}_1$, electron 2 at site $\mathbf{x}_2$, etc. This is given by

$|\Psi^{HP}(\mathbf{x}_1, \cdots, \mathbf{x}_n)|^2 d\mathbf{x}_1 \cdots \mathbf{x}_n$, in turn this just becomes $|\chi_i(\mathbf{x}_1|^2 d\mathbf{x}_1 |\chi_j(\mathbf{x}_2|^2 d\mathbf{x}_2 \cdots |\chi_k(\mathbf{n}_1|^2 \mathbf{x}_n$. Which is the probability of finding electron 1 at $\mathbf{x}_1$ times electron 2 at $\mathbf{x}_2$, etc., thus the product of the probabilities. In the end the Hartree product is an independent particle model, so the electrons are uncorrelated. The electrons move independently, or can be described as not "seeing" the others in their environment.

$$\Psi^{HP}(\mathbf{x}_1, \mathbf{x}_2, \cdots, \mathbf{x}_n) = \chi_i(\mathbf{x}_1)\chi_j(\mathbf{x}_2) \cdots \chi_k(\mathbf{x}_n) \tag{2.1}$$

A first step towards strongly correlated electrons is to look at the Hartree-Fock model. This is classically described as an "uncorrelated" electron system, however upon closer survey of the outcome the electron motions are not completely independent. When considering the spins of the electrons in the system two outcomes arise, either the spins are parallel or they are anti-parallel.

When considering two electrons residing on a specific lattice site having anti-parallel spins. The probability of finding electron 1 at $\mathbf{r}_1$ and electron 2 at $\mathbf{r}_2$ is as follows

$$\begin{aligned} P(\mathbf{r}_1\mathbf{r}_2)d\mathbf{r}_1 d\mathbf{r}_2 = d\mathbf{r}_1 d\mathbf{r}_2 \int d\omega_1 d\omega_2 |\Psi^2| \\ = \frac{1}{2}[|\Psi_1(\mathbf{r}_1)|^2 |\Psi_2(\mathbf{r}_2)|^2 + |\Psi_1(\mathbf{r}_2)|^2 |\Psi_2(\mathbf{r}_1)|^2] d\mathbf{r}_1 d\mathbf{r}_2. \end{aligned} \tag{2.2}$$

These electrons are allowed to coexist at the same lattice site, therefore they are uncorrelated. Now taking a looking at the scenario where the two electrons have parallel spins. The probability of finding them residing at the same lattice site is

$$P(\mathbf{r}_1\mathbf{r}_2)d\mathbf{r}_1 d\mathbf{r}_2 = \frac{1}{2}(|\Psi_1(\mathbf{r}_1)|^2|\Psi_2(\mathbf{r}_2)|^2 + |\Psi_1(\mathbf{r}_2)|^2|\Psi_2(\mathbf{r}_1)|^2 d\mathbf{r}_1 d\mathbf{r}_2$$
$$- [\Psi_1^*(\mathbf{r}_1)\Psi_1(\mathbf{r}_1)\Psi_2^*(\mathbf{r}_2)\Psi_2(\mathbf{r}_2) + \Psi_1(\mathbf{r}_2)\Psi_2^*(\mathbf{r}_1)\Psi_2(\mathbf{r}_1)\Psi_1^*(\mathbf{r}_2)])d\mathbf{r}_1 d\mathbf{r}_2. \quad (2.3)$$

Here $P(\mathbf{r}_1\mathbf{r}_2) = 0$, therefore when the two electrons being considered have parallel spins they can not coexist on the same lattice site. This can also be stated quite succinctly by the Pauli exclusion principle, two identical fermions (particles with 1/2 integer spin) can not simultaneously occupy the same quantum state.

Finally, for a big picture view of what it means for a material to have strongly correlated electrons, the motion and residence of the "local" electrons is controlled by the remainder of the "local" electron population and their quantum mechanical angular momentum known as spin.[103, 104] From a simple model, it is clear that the Coulomb interaction of the quantum numbers of charge and spins produces an environment of the nature previously described.[8, 63, 105, 106, 107, 108, 109, 110, 111]

Connecting this basic picture to the generally more complicated nature of the investigations presently at hand, we will consider $NiFe_2O_4$ for our example. By examining the chemical formula of this system it is evident that strong correlations should be expected due to the *d*-orbital electrons presented by the transition metal ions Fe and Ni.[112] These electrons invoke an on-site Coulomb repulsion U. This repulsion is relatively large with U values of 4.5 eV and 4 eV, for Fe and Ni respectively.[113, 114, 115, 116] However, the U effect is not well understood in this

material yet so it can take on a value of 2, 4, or 6 eV.[117, 118] The localization that is induced by this on-site repulsion causes the material to be an insulator rather than a metal, this is also seen in the binary material NiO.[119, 120, 121, 122] Additionally, the magnetic nature of $NiFe_2O_4$ require inclusion of exchange-correlation J values into most models to get an accurate picture of expected outcomes. The J, which represents the screened exchange energy, for Fe and Ni take on values of 0.89 and 1.0 eV, respectively.[113, 114, 123, 118] Ultimately, these values of J result in a spin-split density of states, as shown in Fig. 2.4.[124]

2.1.2 Mott-Hubbard transport model for insulators

Starting from a tight-binding model, it is viable to describe the atoms in the lattice by a single atom. Whereas the overlap of the electronic wave functions appears as a perturbation of this single atom. This results in available electrons hopping from one lattice site to the next. The hopping of the electron lowers the kinetic energy and thus the electron(s) are no longer localized to a specific lattice site. The result of this is the creation of bands, not just states anymore. These bands have a width W, this value is proportional to the hopping matrix element ($W \approx t$) In the case of elements such as Ni or Fe the $3d$ band is partially occupied and thus should have metallic characteristics. However, the tight-binding model has not taken into consideration electron-electron interactions. To incorporate these interactions into the Hamiltonian a new term U must be introduced. The Hamiltonian describing the hopping process is as follows

$$\hat{H} = -t \sum_{(i,j),\sigma} (c^{\dagger}_{i,\sigma} c_{j,\sigma} + c^{\dagger}_{j,\sigma} c_{i,\sigma}). \tag{2.4}$$

The U term introduces the neglected Coulombic interactions of two electrons residing at the same site.[48, 125] This expands the existing Hamiltonian to

$$\hat{H} = -t \sum_{(i,j),\sigma} (c^{\dagger}_{i,\sigma} c_{j,\sigma} + c^{\dagger}_{j,\sigma} c_{i,\sigma}) + U \sum_{(i=1),\sigma}^{N} n_{i,\uparrow} n_{i,\downarrow}. \tag{2.5}$$

In Eqs. 2.4 and 2.5, $\hat{H}$ represents the Hamiltonian, t is the hopping matrix element, $\langle i, j \rangle$ are the adjacent lattice sites, σ produces the spin, while $c^{\dagger}_{i,\sigma}$ and $c_{i,\sigma}$ are the creation and annihilation operators with spin σ on site i. In Eq. 2.5, $n_{i,\sigma} = c^{\dagger}_{i,\sigma} c_{i,\sigma}$ produces the value of one if the site is occupied with the specified electron, other the value is zero. This perceivable notion of the U term imparts its contribution when two electrons in the band remain on the same site, reducing the mobility and increases localization.

Now we consider the environment more accurately. If the on-site repulsion U is large than the width of the band W, then the band splits into a filled lower "Hubbard"-band and an empty upper "Hubbard"-band. The separation (complete or not) of the bands depends upon the actual ratio of U/W. Therefore, as U/W increases the system shifts from metallic to insulating characteristics. As per the previously stated environment, partially occupied orbitals (bands) such as the $3d$ in $NiFe_2O_4$ have the propensity to create an insulating environment.

As the orbital overlap increases for the d-wavefunctions of the transition-metal ion and the p-wavefunctions of adjacent oxygen ions, so does hybridization. How-

ever, the strength of the hybridization has dependency upon the atomic number of the transition-metal ion, when nuclear charge increase the chemical potential of d electrons decrease. Therefore, the relative difference in energy of the d and p bands decreases, $\Delta = |\epsilon_d - \epsilon_p|$. Here Δ is the charge-transfer energy. In the transition metal oxide family of materials, the $2p$-bands presented by the resident oxygen ions dwell closely to the Fermi energy. When the charge gap is determined by U ($U < \Delta$) the O p band lies below the lower Hubbard band and the low-energy excitations will display d characteristics. This is referred to as a *Mott-Hubbard insulator* and schematically shown by Fig. 2.5 (b). However, if the U value is large ($U > \Delta$), then the lower Hubbard band of the metal ion can be pushed below the O $2p$. In this scenario the O $2p$ levels become the highest occupied band. Therefore, the band gap is defined by the energy (distance) between the O $2p$ and the upper Hubbard band. This type of system is defined as a *charge-transfer insulator* and schematically shown by Fig. 2.5 (c). In charge-transfer insulators the hybridization is strong resulting in low-energy excitations having mixed d and p characteristics.[126]

2.1.3 Spintronics

Introduction to Spintronics

To overcome the limit of decreasing transistor size down to single atomic center sizes, one can invoke new degrees of freedom.[105, 127] The history of which is shown in App. A.1. One such degree of freedom includes the quantum mechanical angular momentum known as spin, rather than the traditional utilization of charge drift in existing electronic devices.[128] This technological innovation direction is known

as *spintronics*, an amalgamation of spin and electronics.[129, 130] Broadly, investigations into spintronics characterize the electrical, optical, and magnetic properties embodied by specimen as a result of the equilibrium and non-equilibrium of spin populations, along with the spin dynamics.[86, 131, 132, 133, 134, 135, 136, 137] The fundamental direction is an umbrella for electron spin derived phenomena in solids. Moreover, the fundamental investigations give insight into the nature of spin interactions e.g. spin-orbit, hyperfine, and spin exchange coupling.[138] When considering device motivated researchers, investigations typically are split into two approaches: (i) perfecting the GMR-based technology and (ii) developing more novel and radical ways to generate and utilize spin-polarized currents (actively controlling spin dynamics).[139, 140, 141] Potentially vital roles that spintronics would play is that of amplifier and general multi-functional devices. This is certainly a limitation of existing transistor technology.

As a generalization, the spin is a dynamic species in the material/device system. Investigations in the field of spintronics are both fundamentally and technologically focused. There are three basic requirements in spintronic systems to investigate (for either direction): (i) Spin relaxation, the method of creation and anhilation of the spin, along with spin transport (how the spin moves in metallic, semiconductive, and insulating materials) are vitally important for basic physically understanding but also in electronic technology.[141, 142] (ii) Efficient spin injection, the method to transfer spins from one material to another, transporting spin from a metal to a semiconductor is inherently challenging due to intrinsic impedance mismatches of the materials.[143, 144, 130] and (iii) The reliability to detect spin within investigated

materials; therefore, the ability to know the magnitude of spin polarization that is present in the system is granted.[145, 146] One such device presently in use is the *giant magnetoresistive* (GMR) sandwich structure. The overarching goals of spintronics are: (i) spin control of electrical properties and (ii) electrical control of spin, or I-V characteristic and magnetization, respectively.[138]

Now we will explore a few examples to understand spintronic systems requirements. The processes required for spintronic applications and investigative verification are summarized in Fig. 2.6. Importantly, each process is of equal weight, even though the hierarchy begins with the spin injection. The logic behind this, spin injection gives a direct way of introducing non-equilibrium processes of spins into a conductor. As an example, take a piece of iron bar and a piece copper bar. If you connect the two in series and apply a voltage, thereby making a current flow. Then the outcome is highly likely to be electrical spin injection into the copper, as exemplified by Fig. 2.6 (a). This occurs because most of the electrons in the iron are spin polarized and causes spin accumulation in the copper bar. Of course, spin injection is just the beginning. Once it is injected further manipulation/ control is necessary; therefore, by applying an external magnetic field the desired manipulation and control can be achieved through rotation of the spin. Additionally, spin-orbit coupling allows for control to be exerted over the spin electronically.[138]

After the spin is injected it must remain coherent long enough to be detected. Once the spin is transferred out of the ferromagnet, the inhibiting irreversible processes of spin relaxation and spin dephasing start to decay the magnetization, as seen in Fig. 2.6 (b).[147] Therefore, the thickness of the receiving material (non-magnetic

conductor) depends upon the lifetime and/or coherence length. The irreversible processes causing magnetization decay occur at a rate of $M = M_0 \exp -(x/L_s)$ and emerge from a combination of spin-orbit interaction and momentum relaxation. When considering interaction with the solid-state environment, the processes are highly complex and can be descriptively derived from effective perturbation approximations.[138]

Finally, we have come to spin detection, as shown in Fig. 2.6 (c). Continuing with our example of the iron and copper bars, even though the probability is high that the current flowing out of the iron is spin polarized, it is critical to validate (or refuting) that the claim of spin accumulation is true. This method of spin detection is derived from Silsbee-Johnson spin-charge coupling.[148, 149, 150, 151]

$$j_n \sim n_0(\zeta)[\exp(qV/k_BT)(1 + \delta P_n P_{n0}) - 1]. \tag{2.6}$$

Here, j_n is the current density, V is the bias voltage (positive for forward bias), $n_0(\zeta) = (n_i^2/N_a)\cosh(q\zeta/k_BT)$ represents the equilibrium number of electrons in the p region, with n_i being the intrinsic carrier density, and N_a is the acceptor doping. Technically speaking, this is a generalization of Silsbee-Johnson spin-charge coupling for magnetic $p-n$ junctions.[130]

With spin-charge coupling being invoked, we effectively reverse spin injection; therefore, the method of spin-charge coupling allow for direct investigation of spin accumulation. In further detail, spin-injection electrical current drives spin-polarized electrons from a ferromagnetic source to a non-magnetic drain, whereas in spin-charge coupling the electrical contact ferromagnetic drain and a nonmagnetic source

(containing a non-equilibrium of spin population) generates an electrical current in an open circuit. Hence, in this method detection of the electron spin is presented electrically. A viable optical detection option for detecting the existence of electron spin accumulation is when spin-polarized electrons recombine with unpolarized holes will emit circularly polarized light.[138]

As an overarching perspective, spintronics is purposed toward understanding the interaction between a particles quantum mechanical spin angular momentum and the solid-state environment in which it exists. Thereby, one premise is increasing efficiency for the derived devices via the understanding that is gained.[152, 153, 154, 155] Additionally, a common perspective of many of the conceived spintronic devices is that of maximizing spin detection sensitivity, with the ambition to detecting more than just the presence of spin but also detecting changes to the spin states.[130, 156, 157, 158, 159] The emerging spintronic devices foretell faster switching, lower consumption of electrical power, and a higher density of circuit elements. These improvements are direct derivatives of the lowered heat production per switching element because the spin is the signal transporter and frees the system from "ohmic" energy dissipation.[153, 160, 161, 162, 154, 163]

2.1.4 Subset of strongly-correlated electron materials: multiferroics

Spontaneity and uniformity are not two words that are commonly used together to describe atomic or molecular attributes. However, when it comes to magnetic moments they spontaneously and uniformly generate a magnet, specifically a ferromagnet.

These materials have intrigued humans for approximately 2,500 years. Fast-forward through that time to almost 100 years ago, the scientific community was astonished by the discovery of the spontaneous ordering of electric dipole moments.[164] Due to having ferromagnetic analogous properties e.g. hysteresis between two stable states in an external electric field, the new phenomenon was named ferroelectricity. The scientific endeavor to combine the two phenomena in one phase of a material, establishing the field of multiferroics. Of course, the premise of multiferroic materials is to possess two or more simultaneous ferroic functionalities, with the hope being primary ferroic functionalities.[165, 166] The primary ferroic functionalities are listed in Table 2.1, with their order parameter and the symmetry that is broken in order for that functionality to arise, along with an example material for each. As an aside, conceptualization of symmetry breaking started with Pierre Curie.[167] Although the complete validity of his theory in spontaneous symmetry breakage (as can be applied to ferroic orderings) is disputed, it still gives profound realization towards understanding symmetry breakage.[168, 169, 170, 171, 172, 173] Curie's theorem can be condensed into two points. 1) A phenomenon derives its existence from the lowering of symmetry. 2) Symmetry elements of the causes must be found in their effects. Interestingly enough, the converse is not true. This principle holds true for causal or deterministic physical laws. The early investigations into this field were initiated by Smolenskii and Ioffe, who suggested to introduce magnetic ions into ferroelectric perovskites, thereby creating solid solutions that host magnetic long-range order but do not sacrifice their ferroelectric order.[174] The most aggressively investigate materials were boracite compounds, e.g. $Ni_3B_7O_13I$, in which a significant linear magnetoelec-

tric effect was discovered.[175, 176] Following this, Cr_2BeO_4 was investigated and led to the discovery that a spin-spiral like arrangement of magnetic moments led breaks spatial inversion symmetry.[3] Ultimately this led up to the conference on magnetoelectric phenomena.[177]

In a more contemporary view, multiferroic materials have been under intense investigation from the perspective of both fundamental and applied science.[99, 178, 179, 180, 12] These materials are mostly encompassed in two rationales: (1) the possibility to exploit the functionalities of both orders, for example a four-state memory element is a potential outcome, (2) novel functionalities are plausible to emerge from the coupling of the ferromagnetic and ferroelectric states. The re-invigoration into investigating multiferroics was initiated in 2000, when Hill (Spaldin) returned to the early thoughts of Smolenskii. She ultimately explained why magnetic and ferroelectric ordering are antithesis of each other, specifically in perovskites.[181] Additionally, they revealed as a consequence of the inverse proportionality an external electronic or structural driving force must be present in order for the two primary ferroic orderings to be simultaneously present.

Hans Schmid considered the symmetry,[182] culminating in the suggestion that there exists an ensemble of 31 point groups that allow for existence of Ferro-elasticity, electricity, or magnetism individually. If they are to coexist in a single phase this brings the number of point groups down to 13 for any given pair and for coupling of these three primary ferroic orderings the overlapping of point groups reduces to 9. For completeness, the term ferroic was coined by Aizu[183] and defined as:

when it has two or more orientation states in the absence of a magnetic

field, electric field, and mechanical stress and can shift from one to another of these states by means of a magnetic field, an electric field, a mechanical stress, or a combination of these. ([183, 184, 165])

Additionally ferroic materials must display long-range ordering regarding at least one macroscopic property, along with developing domains that can be switched by a conjugate field.[185, 179, 184] The primary functionalities, ferroelasticity, ferroelectricity, ferromagnetism, and ferrotoroidicity, arise through ferroic phase transitions via an ordering parameter as shown in Table 2.1.

Table 2.1: Results of Broken Symmetry

Broken Symmetry	Functionality	Order Parameter	Example
Translation	Unit cell enlargement	Phonon mode amplitude	
Rotation	Ferroelasticity[186]	Strain	$Pb_3(PO_4)_2$[187]
Spatial Inversion	Ferroelectricity[188]	Polarization	$BaTiO_3$
Time Reversal	Ferromagnetism[189]	Magnetization	Fe_3O_4
Spacial Inversion &Time Reversal	Ferrotoroidicity[190]	Toroidization	$LiCo(PO_4)_3$[191]

Where as ferroic transition is defined as the following: "(a) it can be viewed as a nondisruptive modification of a certain 'prototypic phase', and (b) it involves a loss of one or more point-symmetry operators present in the prototype." This offers a great segue to have a brief introduction to the concept of Neumann Theorem. This theorem rests on the fact that all properties of a crystal extend from its atomic structure all the way out to the macroscopic world. It is expressed as follows: "The symmetry elements of any physical property of a crystal must include the symmetry

elements of the point group of the crystal." ([192]) This leads us to the necessity of understanding variant and invariant tensors. Symbolically, the tensors can (or not) possess time-reversal symmetry. Magnetic field $\vec{H}$, for example, which is viewed as emerging from the motion of charged particles in an electric current, changes sign upon time reversal:

$$\vec{H}(-t) = -\vec{H}(t). \tag{2.7}$$

However, an electric field $\vec{E}$ is time symmetric:

$$\vec{E}(-t) = \vec{E}(t). \tag{2.8}$$

Additionally, the dielectric permittivity ϵ is also time symmetric:

$$\epsilon(-t) = \epsilon(t). \tag{2.9}$$

Based upon the notation established by Birss in 1963, $\vec{H}$ is a c-tensor and $\vec{E}$ (ϵ) is a i-tensor.[193]

Ultimately, it is desirous to obtain a series of singular materials that contain two (or more) primary ferroic functionalities, e.g. ferromagnetism and ferroelectric. However, this has proven to be rather challenging. The difficulty in realizing a single phase multiferroic arises from the nature of the mechanisms that promote the two desired cross-coupled properties.[194] The mechanism for traditional ferroelectricity, such as in the cubic perovskites, requires the d orbitals to be empty, d^0. On the contrary, ferromagnetism exists when the d orbitals are partially filled

d^{1-9}. [99, 181] Following this realization, a few multiferroics have been revealed, h-$YMnO_3$, o-$TbMnO_3$, $TbMn_2O_5$, $BiFeO_3$, $LuFe_2O_4$, $Ni_3V_2O_8$, and $R MnO_3$ (R = rare earth);[22, 99, 100, 101, 195, 196, 197] but, the definition was expanded to include ferri- and antiferro-magnetism along with corresponding antiferroelectricity.[42] The hope with having these functionalities coexisting is that they will be cross-coupled. This cross-coupling of the order parameters can give rise to magnetoelectric effects –these include induction of magnetization by an external electric field or polarization by an external magnetic field. The result is quantifiable from an expansion of the free energy for a specific material,

$$F(E,H) = F_0 - P_i^S E_i - M_i^S H_i - \frac{1}{2}\epsilon_0\epsilon_{ij}E_iE_j - \frac{1}{2}\mu_0\mu_{ij}H_iH_j - \alpha_{ij}E_iH_j \\ -\frac{1}{2}\beta_{ijk}E_iH_jH_k - \frac{1}{2}\gamma_{ijk}H_iE_jE_k - ... \tag{2.10}$$

Polarization and magnetization can be obtained by differentiating equation 2.10 to E and H, respectively.

$$P_i(E,H) = P_i^S + \epsilon_0\epsilon_{ij}E_j + \alpha_{ij}H_j - \frac{1}{2}\beta_{ijk}H_jH_k + \gamma_{ijk}H_iE_j - ..., \tag{2.11}$$

$$M_i(E,H) = M_i^S + \mu_0\mu_{ij}H_j + \alpha_{ij}E_i + \beta_{ijk}E_iH_j + \frac{1}{2}\gamma_{ijk}E_jE_k - ..., \tag{2.12}$$

Here, E and H are the electric field and magnetic field vector, respectively. P^S and M^S denote the spontaneous polarization and magnetization, whereas ϵ and μ are the electric and magnetic susceptibilities. The tensor α_{ij} corresponds to induction of polarization by a magnetic field or magnetization by an electric field, as shown in

the following relationship:[198, 199, 200]

$$\alpha_{ij}^{\vec{E}\vec{H}} = \left(\frac{\partial \vec{P}_i}{\partial \vec{H}_j}\right)_{\vec{E}} = \mu_0 \left(\frac{\partial \vec{M}_j}{\partial \vec{E}_i}\right)_{\vec{H}} . \tag{2.13}$$

This tensorial response coefficient is exactly what has captured the attention of such a large audience of the scientific community. It is designated as the linear magnetoelectric effect and is considered a *special magnetic property*.[201] *Special magnetic properties* are elaborated on in App. B. In Eqn. 2.11 β and γ are the high order magnetoelectric effect tensors. [201, 202] The magnetoelectric tensor, e.g. $B_i = \alpha_{ij}E_j$, is a *special magnetic property* because it arises from a cross-coupling of a c- and i-tensor. Large magnetoelectric coefficients have been observed for $LiCoPO_4$ (α_{yx} = 30.6 ps m^{-1}), yttrium iron garnet films (30 ps m^{-1}) and $TbPO_4$ (α_{xx} = 36.7 ps m^{-1}). [203, 204, 205] Because of the potential of the cross-correlation between the magnetic and electric properties for technical applications, magnetoelectric coupling attract intense experimental and theoretical work. [202, 206, 207] Now to bring the conversation back to α_{ij}, since this coefficient indicates the magnitude of the induced polarization or magnetization the electronic structure response must be present due to the changing symmetry in the local environment.[208, 198, 209, 210, 211]

Daniel Khomskii presented a form to classify multiferroics dichotomously. Type I tend to have transition temperatures for both ferroelectricity (FE) and magnetism significantly above room temperature (300 K), with the caveat that the FE occurs at a higher temperature, but the coupling is incredibly weak. Type II the magnetism transition occurs in a higher temperature regime than the FE but the coupling be-

tween the orderings is strong.[212] For a summary of the types of multiferroism look at Table 2.2. The mechanisms that are known to support the emergence of multifer-

Table 2.2: Types of Multiferroism

Type I	Type II
Weak coupling of FE and magnetism	Strong FE and magnetism coupling
FE transition $T <$ than magnetism	FE occurs in a low T regime
Strong $\vec{P}$	Weak $\vec{P}$

roism are broken up into four distinct classes: lone pair, geometric, charge ordering, and spin-driven. Of course, the independent phenomena have their own mechanistic foundations, for example, ferroelectricity appears in environments that contain: electronic lone pairs, charge ordering, geometric driven effects, or magnetism.[212, 213] Upon deeper investigation one finds that the first three have the ferroelectric and magnetic orders transpiring independently.[179, 214, 215] Now for a brief introduction of the mechanisms and model materials displaying these underlying driving forces.

Lone-pair mechanism

The name in and of itself suggests that a lone pair of electrons must be present. The resulting mechanism arises from the spatial asymmetry (anisotropy) derived from the distribution of the unbonded valence electrons, as shown in Fig. 2.7 (a). A good example of this mechanism occurs in $BiFeO_3$, where a pair of $6s$ Bi^{3+} valence electrons create a local dipole moment. This creates the spontaneous polarization of $\sim 100\,\mu C\,m^{-2}$. When considering the lone-pair materials, $BiFeO_3$ is truly the only room-temperature single-phase multiferroic material.[179, 98, 216, 217]

Geometric driven ferroelectricity

Steric effects, such as space-filling and geometric constraints, have the potential to cause structural instabilities. This can lead to ionic shifts resulting in polar symmetries (non-centrosymmetric *etc*) allowing access to geometric ferroelectricity, as shown in Fig. 2.7 (b). One highly endorsed example is h-RMnO$_3$ (R = Sc, Y, In, or Dy-Lu). The ferroelectric ordering polarization arises from a unit-cell tripling.[218, 219, 220] The magnetic ordering emerges at $T_N \leq$120 K.[221] In line with this dissertation, h-LuFeO$_3$ displays a similar response. However, the magnetoelectric coupling has yet to be presented.[53, 179, 222, 223]

Charge ordering

When the valance electrons around host ions in a crystal lattice are distributed with non-uniformity, they can form a period superstructure, as shown in Fig. 2.7 (c). A highly regarded example from the work included in this dissertation is LuFe$_2$O$_4$. The Fe^{2+} and Fe^{3+} ions form a superlattice when they have an alternating pattern.[224] This can lead to an electric polarization i.e. ferroelectricity. When opting to step away from the rigorous environmental requirements of single-phase multiferroic materials, charge-ordering multiferroism becomes a viable options. For example, it is well known that perovskite titanates can be ferroelectric (BaTiO$_3$ d^0) or even (anti-)ferromagnetic (YTiO$_3$ d^1.) So, in the formation of the superlattice of SrTiO$_3$/PbTiO$_3$[225] or more generally ABO$_3$/$A'B'$O$_3$.[226] Ultimately this environment produces an entanglement between the charge ordering (Ti^{3+} $\leftrightarrow$$Ti^{4+}$) and the orbital ordering, controlling the nature of the ferromagnetism and insulating attributes. Therefore, ferromagnetism and ferroelectricity both reside in this system and the former is in-

duced due to the charge-ordering mechanism.[179, 14]

Spin-driven mechanism

So far we have considered cases where ferroelectricity emerges in systems that have magnetic ions; but, depending upon the entanglement of the degrees of freedom the ferroelectricity and magnetism may (or may not) be coupled. Interestingly, magnetic ordering can break the inversion symmetry. Therefore, entanglement of spins and charges has the potential to transfer the non-centrosymmetric state from the magnetic to electric lattice; moreover, this would result in the create of a polar state from the magnetism, as shown in Fig. 2.7 (d-f). Independently these mechanisms arise from detailed differences. Figure 2.7 (d) emerges from spin-orbital coupling and an optimization of the local spin configuration.[227, 228] Figure 2.7 (e) again exists due to an optimization of the spin symmetry through exchange striction.[229] Finally, in Fig. 2.7 (f) a screw-like spin configuration induces a spontaneous polarization, this occurs because the metal-ligand hybridization is not constant with respect to spin-orbit coupling.[179, 230]

Composite multiferroics

To overcome the limitation of single-phased materials, interfacing materials such as $BaTiO_3$ (ferroelectric) and $CoFe_2O_4$ (ferrimagnetic)[40, 231, 232, 233] has shown to be a way forward to obtain the desired magnetoelectric cross-coupling effect.[194] Getting back to the root of this concern, if the two order parameters are coupled then a large set of new devices are made possible. These applications include: multi-state memory elements, magnetotransport, information storage, sensing and actuation, magnetic random access memory, and spintronics.[181, 222, 234] Only a few of the

known materials have been cited as being multiferroic, at room temperature or above, these include: $BiFeO_3$, $BiCoO_3$, corundum $ScFeO_3$, and h–$LuFeO_3$, via the expanded definition.[98, 223, 235, 236, 237] However, the latter of these has been removed in part by the work done in this dissertation.

The ultimate goal of multiferroics is to strap two (or more)[177] primary ferroic functionalities into one phase with strong coupling between the ferroic ordering parameters.[238, 239] With the primary push being towards the simultaneous possession of ferromagnetism and ferroelectricity. This from a device perspective is for the overarching purpose that the coupling (typically referring to the lineaer magnetoelectric effect). Magnetoelectric coupling of this nature refers to induction of magnetization via an electric field or polarization via a magnetic field.[202] This hopeful and idealistic goal has ignited and captured the imagination of researchers all over the globe.[238] The critical concern is to have the cross-coupling be strong and present at room-temperature. Therefore, the push towards understanding the magnetoelectric coupling α more inherently has being taking place and since Daniel Khominskii introduced the definitions for Type I and Type II multiferroics the push for increasing the temperature regime of materials with strong magnetoelectric coupling has drawn a specific interest. Additionally, the idea of have composite multiferroics (interfacial driven multiferroism) has also become more realistic as to producing a strong magnetoelectric coupling at room temperature.

2.2 High Temperature magnetic spinel oxides: $NiFe_2O_4$ and $CoFe_2O_4$

In this section, the fundamental details necessary to describe the physical properties of the magnetic insulators $NiFe_2O_4$ and $CoFe_2O_4$ will be presented. The representative crystal structure is inverse spinel, consisting of a face-centered cubic oxygen lattice with the Ni and Fe cations distributed amongst the octahedral and tetrahedral interstitial sites. However, $CoFe_2O_4$ is not fully inverse. The $3d$ transition metal ions transfer their $4s$ electrons to the oxygen lattice, while leaving the $3d$ band partially filled, resistivity ρ covering m$\Omega\rightarrow$GΩ dependent upon growth conditions. Yet both $NiFe_2O_4$ and $CoFe_2O_4$ still display an insulating nature. This can be understood via a localization of the electrons residing in the $3d$ band, being well described by the Mott-Hubbard model, see Sec. 2.1.2. As well, we explore the exchange interaction that results in the ferrimagnetic ordering (T_C 850 K with a range of moments 2 $\rightarrow$8 μ_B).[240]

2.2.1 Polder Susceptibility

The magnetic susceptibility of ferrite materials can readily be modeled by the Polder susceptibility tensor. The tensor notation is critical because ferrimagnetic materials, i.e. $NiFe_2O_4$ and $CoFe_2O_4$, become anisotropic under the application of a magnetizing field. Fundamentally this model derives from the Landau-Lifshitz equation of motion for torque that defines the phenomenological precession about the applied magnetic field of the magnetization.[241, 242, 243, 244, 245, 246, 247, 248, 249, 250,

251, 252, 253, 254, 255, 256, 257, 258, 259, 260, 261, 262]

2.2.1.1 Magnetization Dynamics

Below the transition (Curie) temperature T_C for ferro- and ferri-magnetic materials, the magnetic moments respond to an external magnetic excitation field, such as the weak alternating field found by exposure to electromagnetic radiation. This can be modeled by the aforementioned Landau-Lifshitz equation, first to explore the nondissipative solution. Then finally walk through the effect of anisotropy, e.g. shape and surface, on a symmetric resonance.[263]

2.2.1.2 Equation of Magnetization Motion

In a more general sense, ferromagnetic materials have a net magnetic moment and the microscopic exchange interaction requires that the spin orbital angular momentums of the electrons be aligned parallel in a very well defined direction. On an important note, if a weak alternating (dynamic) field such as the electromagnetic radiation described previously impinges upon the ferromagnetic material then the resonant excitation will drive the magnetic moments away from their equilibrium position. However, the spin moments will remain aligned over a distinct region. The spin moments being discussed are under a continuum approximation and are well described by a magnetization vector $\vec{M}$. The response of $\vec{M}$ to an external static magnetic field $\vec{H}$ is shown in Fig. 2.8. The Landau-Lifshitz equation describing of

the magnetization precession motion appears as the following:

$$\frac{d\vec{M}}{dt} = -\gamma\mu_0\vec{M} \times \vec{H}_{eff}. \tag{2.14}$$

Here, γ is the gyromagnetic ratio and μ_0 is the permeability of free space. The relationship express the rate of change of the magnetization vector $\vec{M}$ to the torque exerted on said vector by the effective field $\vec{H}_{eff}$. For materials with an exchange driven net magnetic moment (ferro- and ferri-magnetic) $\vec{H}_{int}$, $\vec{H}_{eff}$ is strictly

$$\vec{H}_{eff} = \vec{H}_0 + \vec{H}_{int}, \tag{2.15}$$

$$\vec{H}_{int} = -\frac{\partial E}{\partial \vec{M}}. \tag{2.16}$$

To further define, $\vec{H}_{int}$ is a sum of all of the fields acting on the magnetization such as anisotropy fields, exchange fields, and dipolar fields.[264] The magnitude of $\vec{M}$ is conserved:

$$\frac{\partial}{\partial t}\vec{M}^2 = 0, \tag{2.17}$$

this is indicative of $\vec{M}$ precessing on the surface of a sphere.

Solution for magnetization motion equation

The example for the solution will be a ferromagnetic sample in a static magnetic $\vec{H}_0$ field pointing along the $z-$axis with $\vec{M}_{eq}||\vec{H}$, such that

$$\vec{H}_0 = H_0\vec{e}_z \tag{2.18}$$

$$\vec{M}_0 = M_s\vec{e}_z. \tag{2.19}$$

The excitation source will oscillate in the xy-plane. The dynamical components of the field $\vec{h}(t)$and the magnetization$\vec{m}(t)$. The time-dependent perturbations are appended to the $\vec{H}$ and $\vec{M}$ to become

$$\vec{H} = \vec{H}_0 + \vec{h}(t) \tag{2.20}$$

$$\vec{M} = \vec{M}_0 + \vec{m}(t). \tag{2.21}$$

Importantly, the dynamic components are assumed to be much smaller than the static components:

$$\vec{m}(t) = \vec{m}\exp(-i\omega t), \quad \left|\vec{M}\right| \gg |\vec{m}(t)|, \tag{2.22}$$

$$\vec{h}(t) = \vec{h}\exp(-i\omega t), \quad \left|\vec{H}\right| \gg \left|\vec{h}(t)\right|. \tag{2.23}$$

To understand what is happening inside of the sample while being exposed to the large static magnetic field and perturbing alternating magnetic field one can define the dynamic susceptibility $\bar{\chi}$, as a response of the dynamic magnetization $\vec{m}(t)$, as per the following:

$$\vec{m}(t) = \bar{\chi}\vec{h}(t). \tag{2.24}$$

This dynamic susceptibility $\bar{\chi}$ is the 2×2 Polder tensor. We must first derive this tensor before solving for the magnetization motion and to derive the Polder tensor we need to solve Eqn. 2.14. It first appears as the following:

$$\frac{\partial \vec{m}}{\partial t} = -\gamma\mu_0 \left[\left(\vec{M}_0 \times \vec{H}_0\right) + \left(\vec{m} \times \vec{H}_0\right) + \left(\vec{M}_0 \times \vec{h}\right) + \left(\vec{m} \times \vec{h}\right)\right]. \tag{2.25}$$

Due to the orthogonality principle of cross-products the first term $\vec{M}_0 \times \vec{H}_0$ will be 0 because we defined $\vec{M}_{eq} || \vec{H}$. Additionally, the last term, concerned with the dynamic components, $\vec{m} \times \vec{h}$ can also be neglected due to the first order approximation and the contribution being inherently small. Therefore, the linearized version of Eqn. 2.25 becomes:

$$\frac{\partial \vec{m}}{\partial t} = -\gamma \mu_0 \left[\left(\vec{m} \times \vec{H}_0 \right) + \left(\vec{M}_0 \times \vec{h} \right) \right]. \tag{2.26}$$

If we project Eqn. 2.26 onto coordinate axes shown in Fig. 2.8 (b) and additionally assuming that the time-dependent oscillations are of the form $\exp(-i\omega t)$, then the linearized equation becomes:

$$-i\omega \vec{m} = \vec{z} \times \left[\omega_M \vec{h} - \omega_0 \vec{m} \right]. \tag{2.27}$$

Here, $\omega_M = \gamma \mu_0 M_s$ and $\omega_0 = \gamma \mu_0 H_0$.

By solving the system of equations above and expressing h_x and h_y in terms of m_x and m_y, one acquires:

$$\begin{pmatrix} \vec{h}_x \\ \vec{h}_y \end{pmatrix} = \frac{1}{\omega_M} \begin{pmatrix} \omega_0 & i\omega \\ -i\omega & \omega_0 \end{pmatrix} \begin{pmatrix} \vec{m}_x \\ \vec{m}_y \end{pmatrix}. \tag{2.28}$$

Equation 2.28 follows the form of $h = \bar{\chi}^{-1} m$. In order to obtain the Polder susceptibility tensor the inverse of Eqn. 2.28 should be calculated, producing:

$$\bar{\chi} = \begin{pmatrix} \chi & i\kappa \\ -i\kappa & \chi \end{pmatrix}, \tag{2.29}$$

where,

$$\chi = \frac{\omega_0 \omega_M}{\omega_0^2 - \omega^2}, \kappa = \frac{\omega \omega_M}{\omega_0^2 - \omega^2}. \tag{2.30}$$

The Polder tensor is a non-diagonal and antisymmetric tensor, it strictly corresponds to resonance conditions in an unbounded sample. In a finite (real) sample, the resonance frequency also depends upon the total geometry and topology of the sample. The preceding derivations are derived from Refs. [265, 252, 266, 267, 268, 269, 270, 271, 272, 273]

2.2.1.3 Damping of the Landau-Lifshitz Equation

The solution for Eqn. 2.14 strictly holds true for scenarios where spin moment is isolated and can thereby precess indefinitely. In real material systems the treatment must incorporate a mechanism for relaxation, or deceleration, of the macroscopic precessional motion because a magnetic moment in a solid interacts with its environment. This interaction results in dispersion of energy; in the end, the transferred energy produces microscopic thermal motions such as spin waves (magnons), lattice vibrations (phonons), and thermal excitation of conduction electrons.[274, 275, 271] The actual mechanisms taking place in this transfer process are far too complicated to be described in full detail. Yet, one route to implementing and understanding this is by introduction of a phenomenological damping term into the field equations. This approach brings forward an amenable parameter to balance the rate of energy transfer.

Before introducing the phenomenological damping term, it is best to express what

is happening in the system qualitatively. Damping represents a force in opposition to the macroscopic driving force in the physical system. Therefore, when they are in balance a steady-state of the system is established; moreover, this suggests that the energy gained from the driving force is equal to the energy lost by the damping force. This is represented by the following:

$$\frac{\partial \vec{M}}{\partial t} = -\gamma \mu_0 \vec{M} \times \vec{H}_{eff} - \frac{\lambda}{m} \vec{M} \left(\vec{M} \times \vec{H}_{eff} \right). \tag{2.31}$$

Here, $\lambda > 0$ is a characteristic of a material that is a phenomenological constant, in this case it presents the relaxation frequency which characterizes the dipole-dipole interaction between magnetic moments. Suggesting that a torque being applied to the magnetization acts to push it towards $\vec{H}_{eff}$. In 1955 this was altered by Gilbert [274] to what is currently known as the Landau-Lifshitz-Gilbert equation:

$$\frac{\partial \vec{M}}{\partial t} = -\gamma \mu_0 \vec{M} \times \vec{H}_{eff} + \frac{\alpha}{M_s} \vec{M} \times \frac{\partial \vec{M}}{\partial t} \tag{2.32}$$

Here, $\alpha = \frac{\lambda}{\gamma m}$ and is a non-dimensional damping parameter, the time-dependent derivative of the magnetization $\partial \vec{M}/\partial t$ suggests that the damping increases with an increasing derivative. The latter portion of the Gilbert damping represents a viscous force, as can be seen in Fig. 2.9.

On an interesting note, if the damping is small, as in Yttrium-Iron Garnet and several spin ferrites, then the Landau-Lifshitz and the Landau-Lifshitz-Gilbert equations (2.14 and 2.32) are equivalent.[267, 276]

The purpose of this discussion covering the precession of $\vec{M}$ about $\vec{H}_{eff}$ is to

introduce the narrative of investigation of dynamical response of the magnetization vector and methods/opportunities to expand the understanding of this elusive energy reservoir.

2.2.2 Magnetic Properties for Transition Metal Oxides (Goodenough-Kanamori-Anderson Rules)

Simple models of exchange interaction ignore transitions to and from orbitals of differing angular momentum. This fashion of transition to typically weakly allowed. A critical empirical finding by Goodenough, Kanamori, and Anderson[277, 278, 279] proved to predict exchange interactions in transition metal oxides:

- Antiferromagnetic ordering occurs in the superexchange interaction between two magnetic cations having partially filled d orbitals, under a cation–ligand–cation 180° configuration.
- Weak ferromagnetic ordering occurs in the double-exchange interaction between two magnetic cations having partially filled d orbitals, under a cation–ligand–cation 90° configuration.
- Weak ferromagnetic ordering also occurs in superexchange interaction between a magnetic cation having partially filled d orbital and a magnetic cation having a full or empty d orbital, under cation–ligand–cation 180° configuration.

Importantly, these rules apply to the cation/ligand environment found in the inverse spinel structure of $NiFe_2O_4$. This can be used to establish a foundation for the creation of the observed ferro(ferri)-magnetic moment. The following subsection will discuss the crystal structure.

2.2.3 Spinel crystal structure

$NiFe_2O_4$ and $CoFe_2O_4$ crystallize into an inverse spinel structure, this structure falls into the subset of cubic space groups and has a space group $Fd\bar{3}m$. The latter does not fully invert, such that a fraction of the Co^{2+} cations do not displace the Fe^{3+} cations, resulting in the necessity to define the inversion parameter λ. In $CoFe_2O_4$ λ takes on a value in the range 70–80. The general formula of spinels is AB_2O_4. A few of the general features of this structural family include:

- face-centered cubic lattice of oxygen anions
- 1/8 tetrehedral sites filled
- 1/2 octrahedral sites filled

The unit cell of the spinel structure includes 56 atoms: 32 oxygen (O^{2-}), 16 trivalent (B^{3+}) metal cations, and 8 divalent (A^{2+}) metal cations. The extremes for this crystal structure are normal and inverse spinel. The normal spinel structure has all of the divalent A^{2+} (trivalent B^{3+}) cations in the tetradedral (octahedral) lattice sites. In $NiFe_2O_4$ structure is the inverse form where the divalent cations replace 1/2 of the trivalent cations in the octahedral interstitial sites. The trivalent are distributed equally between the sites. Of course, a mixture of the two can arise, quantitatively described by λ the inversion parameter. $0 \leq \lambda \leq 1$ represents the possible values for the inversion parameter, with zero being normal spinel and one being fully inverse. In its bulk form $NiFe_2O_4$ presents the fully-inverse (one) spinel crystal structure with a cubic lattice parameter of 8.388 Å as shown in Fig. 2.10.

2.2.4 Magnetism of $NiFe_2O_4$ and $CoFe_2O_4$

Magnetic semiconductors are at the heart of modern device physics; however, magnetic insulators are emerging with distinct value because they naturally provide a non-zero magnetic moment below the ordering temperature, spin-dependent band gap, and spin polarization that originates from exchange-coupled magnetization or an applied field creating a spin-split band structure.[280, 281, 4, 282, 283, 284] Strongly correlated spinel ferrites are amongst the most noteworthy contenders for semiconductor spintronics.[285, 284] $NiFe_2O_4$, in particular, displays spin-filtering, linear magnetoresistance, and wide application in the microwave regime.[285, 73, 250, 249, 245, 267, 247, 265] The namesake materials of this section ($NiFe_2O_4$ and $CoFe_2O_4$) along with $MnFe_2O_4$ and Fe_3O_4 readily form ferrimagnetic spinels with magnetic transition temperatures (Curie temperature T_C) remarkably greater than room temperature, e.g. bulk $NiFe_2O_4$ and $CoFe_2O_4$ $T_C = 865$ and 795 K, respectively.[286, 116] This occurs as a result of exchange interaction between the cations housed in the inverse spinel structure. Namely, the antiferromagnetic ordering due to $Fe^{3+} \leftrightarrow Fe^{2+}$ superexchange between the octahedral (B) and tetrahedral (A) sites respectively [Fig. 2.11 (a)]. The magnetic B-site sublattice also house ferromagnetic ordering due to intrasublattice superexchange interaction and a double-exchange interaction between the Ni and Fe cations [Fig. 2.11 (b & c)]. Ultimately the sublattices are ferromagnetic ordered independently and antiferromagnetically ordered with respect to each other; this results in a theoretical magnetic moment of 2 μ_B.

2.2.5 Electronic Structure from First Principles

The investigation of $NiFe_2O_4$ and $CoFe_2O_4$ from a theoretical perspective has invoked the application of density functional theory (DFT), with specific methodologies such as local (spin) density approximation (L(S)DA+U), self-interaction local spin density (SIC-LDS), and hybrid functionals.[287, 288, 289, 290, 291, 292, 293, 294, 295] Calculations were done on normal and inverse spinel structural configurations; it has repeatedly been shown that the resulting magnetic moment along with the exchanging splitting largely increase, upon changing from bulk inverse to normal spinel structure. When doing an analysis of the energetic nature of the environment, it is found that the inverse spinel structure represents the ground state configuration of $NiFe_2O_4$. Looking at the density of states (DOS), such as that depicted in Fig. 2.12, the fundamental band gap has been stated to range ≈1.6 eV; higher energy gaps appear at 2.4 and 2.8 eV. The total conduction band exchange splitting is $2\Delta E_{Ex} = Value$. The reported value of the fundamental gap from experimental results has been extremely varied covering 0.33–3.7 eV.[296, 297, 298, 299, 300]

2.2.6 Spin filtering

Insulating magnetic materials show promise for the desired production of spin-polarized currents.[127, 302, 47] This is simply because of the intrinsic nature to pass an unpolarized current through the material and obtain a finite level of polarization in the current in the output, as exemplified by Fig. 2.13. Eu chalcogenides such as EuS,[303] EuSe,[304] and EuO, [305] have showed some promising experimental results by application of the Tedrow-Meservey technique.[306] The fundamental

understanding gained in these investigations have limited applications to them directly because from a practical perspective their Curie temperatures are too low.[307] The architecture that directly allows for implementation of the spin-filtering effect integrates a (ultra-)thin insulating barrier between non-magnetic electrodes. This contrasts to the more conventional approach of magnetic tunnel junctions (MTJs), two ferromagnetic electrodes are separated by a nonmagnetic electrically insulating barrier.[307] Back to spin filtering, the magnetic properties of the barrier spin split the lowest energy, above the Fermi energy, conduction band. Whereas in the MTJs the flow of tunneling current depends upon the relative orientation of magnetization of the electrodes. The former occurs naturally in $CoFe_2O_4$. The spin-splitting of the conduction band produces a spin-dependent tunneling barrier height $\Phi_{\uparrow\downarrow}$. This shows up on the probability of transmission for an electron current passing through the barrier. The tunneling transmission has an exponential dependence on the barrier height; therefore, the current induced by the tunneling conductance clearly has a spin dependency for spin-split electronic structure. Importantly, the architecture defined derives its spin selectivity from the magnetic properties of just one layer. Whereas in the traditional ferromagnet/insulator/ferromagnet tunnel junctions the spin selectivity depends upon the available states of the second electrode. A mathematical description of the transmission probability for a non-magnetic tunnel barrier is as follows

$$T = \exp\left[2d\sqrt{\frac{2m}{\hbar^2}(\Phi - E_{kin})}\right]. \tag{2.33}$$

Here, d is the thickness, m is the mass of the tunneling particle (electron), E_{kin} is

its kinetic energy, and Φ represents the barrier height. The barrier height is also the offset from the lowest conduction band and the Fermi energy. If a magnetic insulator is used, then the conduction band spin splits by the value of the exchange energy $2\Delta E_{exch}$. That spin splitting produces the spin-dependent barrier height $\Phi_{\uparrow\downarrow}$:

$$\Phi_{\uparrow\downarrow} = \Phi_0 \pm \Delta E_{exch}. \tag{2.34}$$

This range result from growth conditions that can give oxygen vacancies, this also effects the net magnetic moment. When stoichiometry is pure the theoretical moment is supposed to be 2 μ_B but due to the oxygen vacancies this value can increase by 4 fold to 8 μ_B, the variation does not necessarily represent deleterious issues. The band structure and density of states have been thoroughly explored from the theoretical standpoint.[287, 288, 289, 290, 291, 292, 293, 294, 295] The resulting band structure shows that the valence and conduction bands are offset by 1.6 eV with spin splitting that lends itself to the possibility of spintronics. These applications include spin-filtering, spin-torque, and spin-calortronics. To exemplify the possibility for spin-filtering, it is paramount that the valence and conduction band splitting be a large energy, resulting in a preferential spin direction being allowed.

In its bulk form $CoFe_2O_4$ is a ferrimagnet (T_C = 795 K) with a high electrical resistivity, corresponding to its moderate fundamental band gap width of 1.2 eV. From a structural perspective this material is a partially cubic inverse spinel with an inversion fraction of ≈70–80%, this corresponds to a space group of *Imma*, whereas the fully inverse space group is $Fd\bar{3}m$.[289] The unit cell size changes from the cubic cell with 56 atoms to a tetragonal unit cell with 28 atoms, this corresponds to 8 and

4 formula units, respectively. The organization within the unit cell is based upon an face-centered-cubic (*Fcc*) lattice of oxygen, trivalent iron (Fe^{3+}) occupies $1/8^{th}$ of the 64 tetrahedral interstitial sites, whereas divalent nickel (Co^{2+}) and trivalent iron occupy 1/2 of the 32 octahedral sites.[308] The magnetic moment from a theoretical standpoint is 2 μ_B with the experimental range covering 1.8–8 μ_B.[59, 80, 286, 309] This variation in experimentally realized magnetic moment arises from growth conditions, resulting in changes in oxygen vacancy or valency of the transition metal ions.

2.2.7 Contemporary discoveries

In most cases, single crystal growth does not start with thin films but for $NiFe_2O_4$ and $CoFe_2O_4$ the situation is reverse of typical. This might be assigned to the recent push for increasing the quality of engineering complex oxide materials to atomic resolution.[310, 311, 312] High-quality single crystal epitaxial thin films have been achieved on a variety of substrates (such as MgO, $MgAl_2O_4$, $SrTiO_3$, $MgGa_2O_4$, $CoGa_2O_4$, and Co_2TiO_4.) Another route of recent interest for potential application resides in the nanosized particle regime. Nanotechnology, in general, has been one of the scientific fields with the most growth over the past couple of decades. This is because of the emerging properties that are exhibited by materials in this regime.[313] When altering the size and shape of $CoFe_2O_4$ a multitude of emergent properties present themselves, such as superparamagnetism[314] and supercapacitance.[315] The former is present below a critical particle size and over a particular temperature range; superparamagnetism exists in these scenarios because formation of

magnetic domains walls is not energetically favorable.[316, 317] It has been shown that $CoFe_2O_4$ becomes superparamgnetic in the range of 7–10 nm;[314] however, the upper-bound size has been extended to include 14.4 nm particles.[318] The variation in this size can easily be attributed to growth methods and other environmental factors. When size confinement reaches the nanoparticulate regime, the lattice tends to soften, resulting in increased lattice parameters and further mixing of the cation distribution ($[Fe_{1-x}Co_x][\ Co_{1-x}Fe_{1+x}]O_4$).[319, 320, 321] By varying the value of x a different magnetic moment results because of the changing compensation of the magnetic sublattices. Another physical property that can be tied to x is the ordering temperatures in ferrites, this connection arises through the strength of the super-exchange interactions through the O^{2-} lattice. Therefore, it is critical to quantitatively determine this value in order to build a more comprehensive model of the magnetic phenomenon.

To qualitative understand a plot of saturation magnetization it is imperative to recall that saturation is reached when the potential magnetic energy $H \cdot \mu$ and thermal energy $\kappa_B T$ are of the same order of magnitude.

When constraining size along only one axis, thereby obtaining thin films ca. t <5 nm, t is the thickness, spin-filtering in $CoFe_2O_4$ has been in specific . Spin-filtering becomes available when a difference in tunneling effective masses ($m^*_\uparrow \lesssim m^*_\downarrow$) presents itself, this requires that the tunnel barrier heights (energy) are not equal. Ultimately leading to a higher probability for one spin: $\mathbf{J}_{\uparrow(\downarrow)} \propto exp(-\Phi^{1/2}_{\uparrow(\downarrow)} t)$, again t denotes thickness. So, as the thickness increases, probability of separating the two spin directions falls off exponentially.

2.3 Multiferroic *h*-$LuFeO_3$

h-$LuFeO_3$ is isostructural to $YMnO_3$ with ferroelectricity setting in above room temperature in both (T_C ≈1000 and 900 K, respectively) of the materials stated here. This results from a structural transition from nonpolar $P6_3/mmc$ to polar $P6_3cm$ space group. Some complications have occurred when the magnetic phase comes into the discussion, it was suggested that this phase of $LuFeO_3$ gives room temperature multiferroicity with an onset of antiferromagnetic ordering (440 K) and a second transition resulting in a net magnetic moment due to canting along the *c* axis (147 K.) However, upon further investigation into this materials multiferroic material it was realized that antiferromagnetic ordering sets in at a much more modest temperature (155 K), and the canting along the *c* axis is reported to occur at this transition as well. The coupling of the order parameters (ferroelectricity and antiferromagnetism) is known to be weak in the isostructural Mn based material; suggestions have been made that the ordering parameter coupling should increase by substituting the Mn for Fe. The theoretical magnetic symmetry has been reduced to 6 possibilities as shown in Fig. 2.15. Thus far the only reported successful growth of *h*-$LuFeO_3$ is in epitaxial films with substrates of yttria-stabilized zirconia [$ZrO_2(Y_2O_3(111))$], and $Pt(111)/Al_2O_3(0001)$.[322, 323] In the structural form factor discussed here, i.e. epitaxial films, the film-substrate interfacial interaction energetically favors the *h*-$LuFeO_3$ structure, if the substrates symmetry falls into the triangular or hexagonal space group families. However, this energetic favorability only dominates up to some critical thickness.[223, 324, 325, 323, 326, 327] Once this thickness is reached the orthorhombic form *o*-$LuFeO_3$ is the main growth method,

due to a lower free energy. As a final point about growth mechanisms, when the thickness surpasses this critical thickness h-$LuFeO_3$ may be present as a metastable state due to an energy barrier for nucleation of the orthorhombic phases upon the hexagonal phase.[322]

Ultimately, it is important to note that the magnetic symmetry of this material in its ferroelectric state is such that it is a strong candidate for linear magnetoelectric coupling. This suggests that the ferromagnetic moment can be directly controlled by an electric field.

2.4 $LuFe_2O_4$

Rare-earth ferrites have the general formula of RFe_2O_4. $LuFe_2O_4$ is structurally a layered material, with Fe-containing double layers of triangular connectivity stacked along the c axis. The unit cell is made up of three Fe_2O_4 bilayers (W layers) and single Lu_2O_3 between each bilayer. So, the Fe ions have mixed valency in this system with an average of $Fe^{2.5+}$. Ferroelectricity is initiated by a charge ordering transition above room temperature (320 K) and ferrimagnetism sets in just below room temperature (240 K.) The crystal structure at room temperature is rhombohedral ($R\bar{3}m$,) with interaxis angles $\alpha = \beta = 90$ deg and $\gamma = 120$ deg.[330, 331, 332] Delving further into the phase diagram one finds that the charge-ordering phase extends up to 500 K but above the aforementioned transition, at 320 K, the system is quasi-two-dimensional (2D) and becomes three-dimensional (3D) below. This 3D charge ordering culminates with Fe^{2+} and Fe^{3+} rich W layers.[333, 224, 334, 335, 336] Growth of this material

has been achieved through several methods such as pulsed laser deposition, molecular beam epitaxy, and floating zone.[337, 338, 82, 339, 224, 334] Epitaxial films have been grown on sapphire, (111) MgO, (111) $MgAl_2O_4$, and (0001) 6H-SiC.

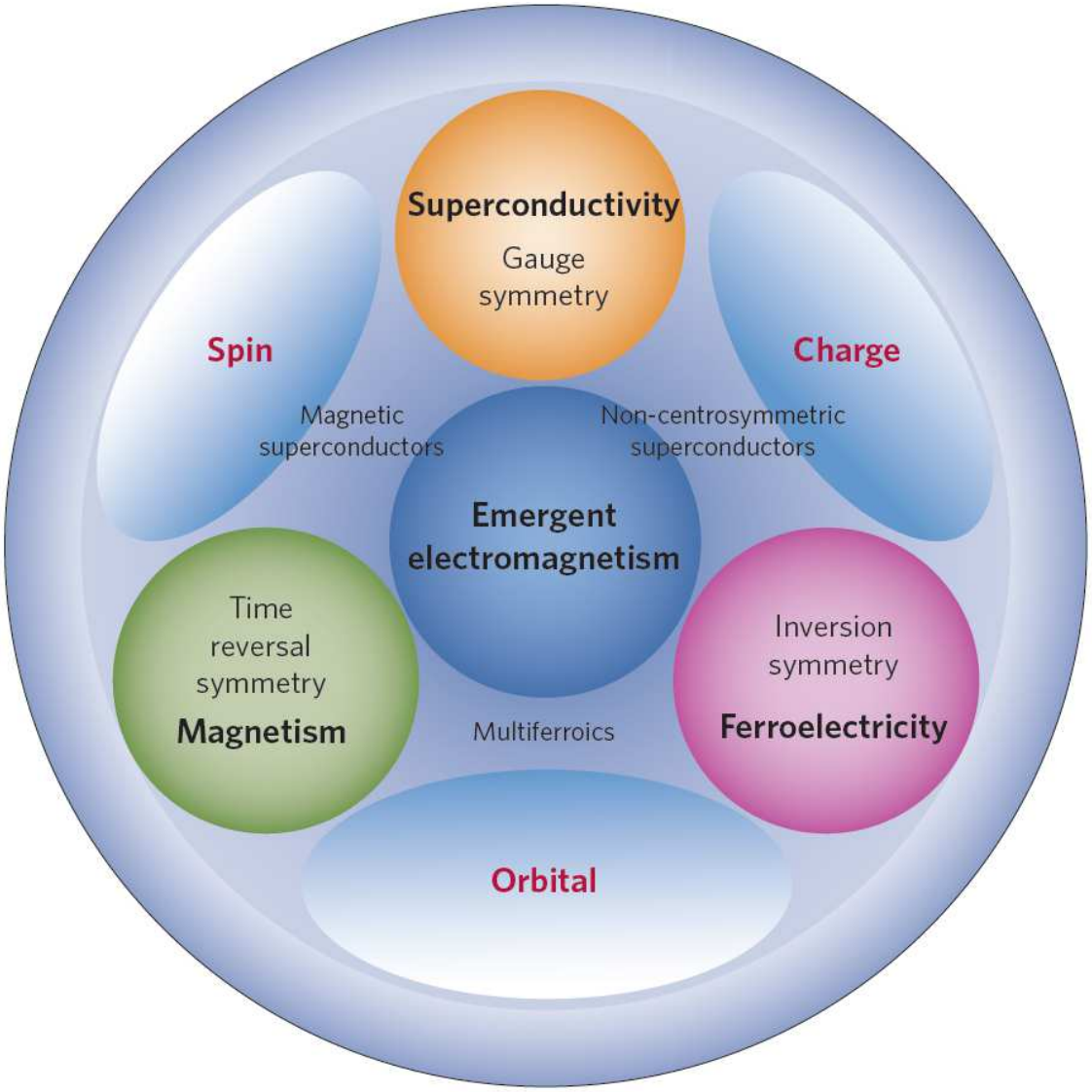

Figure 2.2: The rich physics of complex oxides including multiferroicity, frustration, superconductivity, quantum critical transition, and symmetry breaking arise from the interactions between their charge, orbital, spin, and lattice degrees of freedom. (after [4])

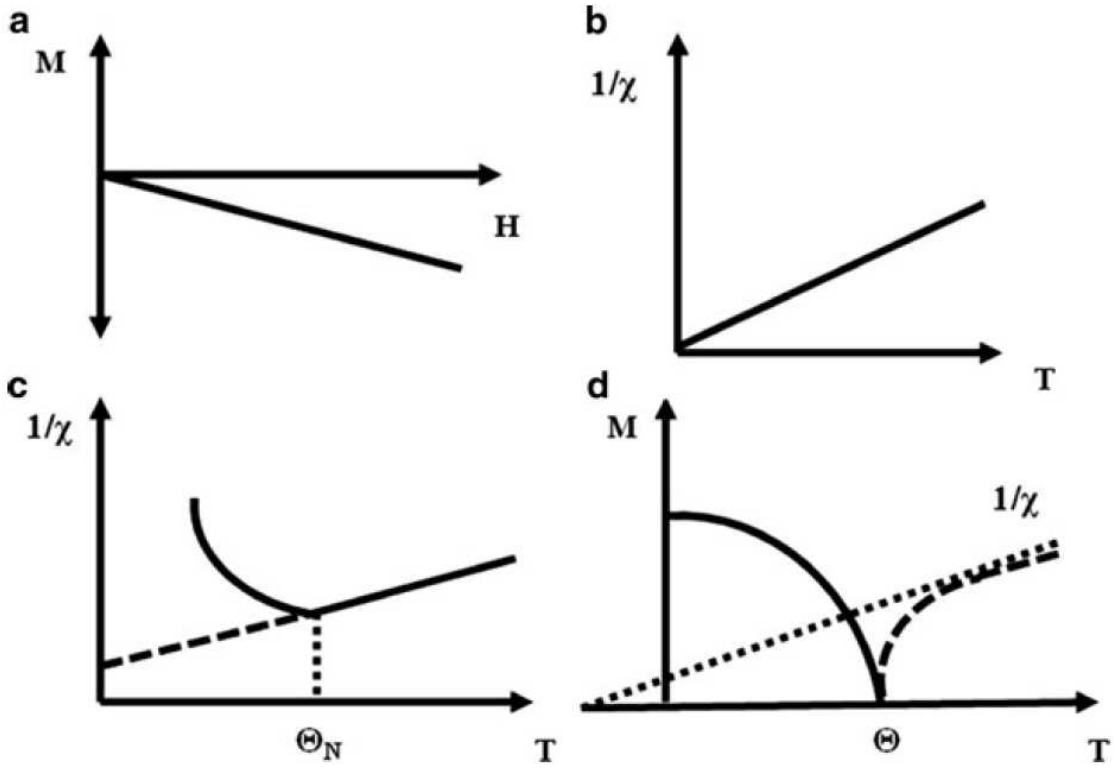

Figure 2.3: (a) Displays the traditional (linear) magnetization vs. magnetic field plot for a diamagnetic material. (b) Shows the Curie-Weiss law of paramagnetism, the inverse susceptibility is proportional to the absolute temperature. (c) Shows how susceptibility varies with temperature when measuring an antiferromagnetic materials. (d) Indicates the spontaneous magnetization of a ferro-(ferri-)magnetic material. Also shown here is how as the temperature increases and approaches the transition temperature the spins become disturbed by thermal perturbations, after [102].

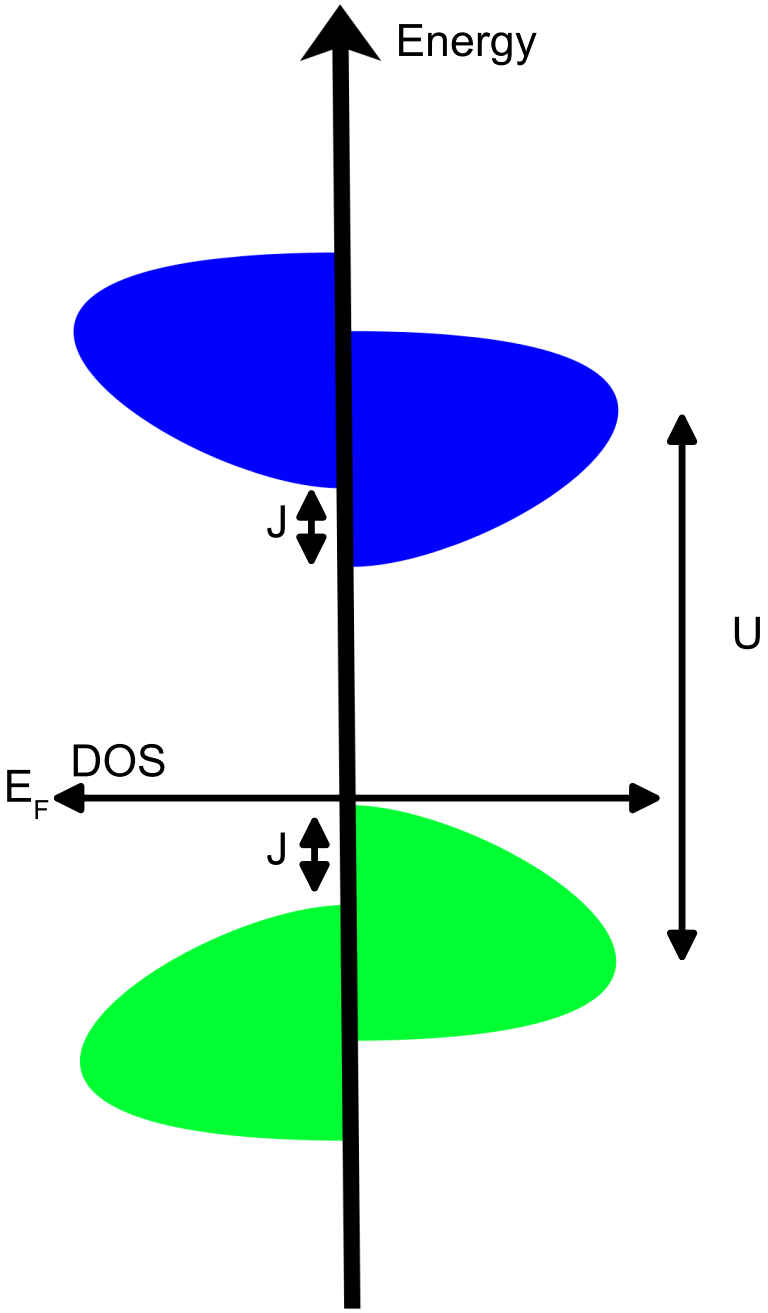

Figure 2.4: Schematic presenting a simple Hubbard band structure for a magnetic material.

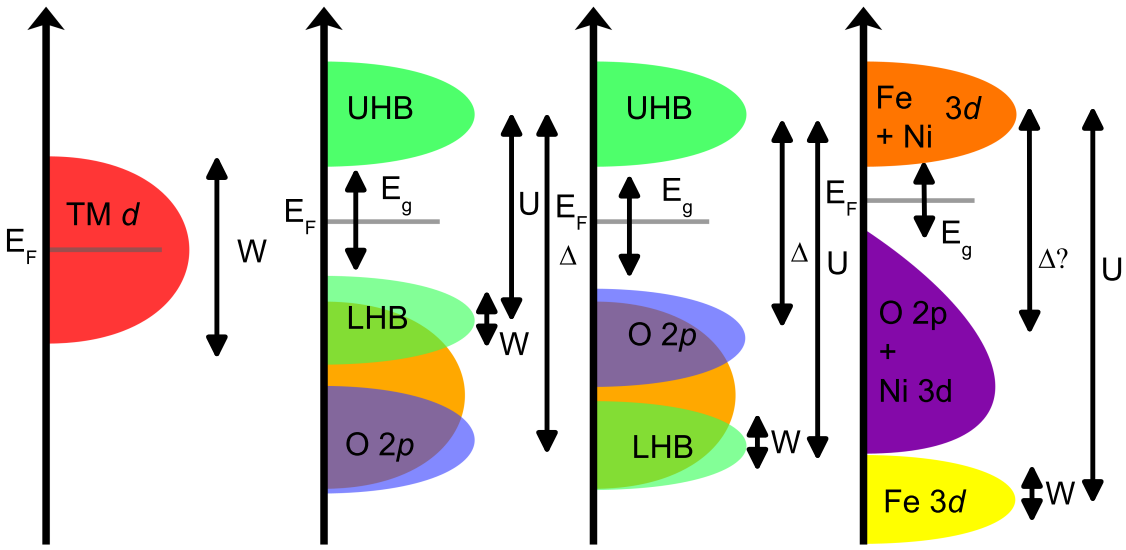

Figure 2.5: Schematic presenting the band structure for a variety of scenarios concerning correlation of electrons. (a) Shows the band structure for an uncorrelated metal, the band has states at the Fermi energy with width W. (b) Displays a Mott-Hubbard insulator with the bands split apart due to on-site Coulomb interaction U, the band gap Δ is between the deeper oxygen band and the upper-Hubbard band. (c) Depicts the scene when the onsite Coulomb interaction is great enough to push the lower-Hubbard band below the oxygen states, at this point the band gap Δ decreases in width and becomes a charge-transfer type insulator. (d) Schematic of real strongly correlated transition metal oxide material $NiFe_2O_4$, here the band of nickel states is hybridized with the oxygen band.

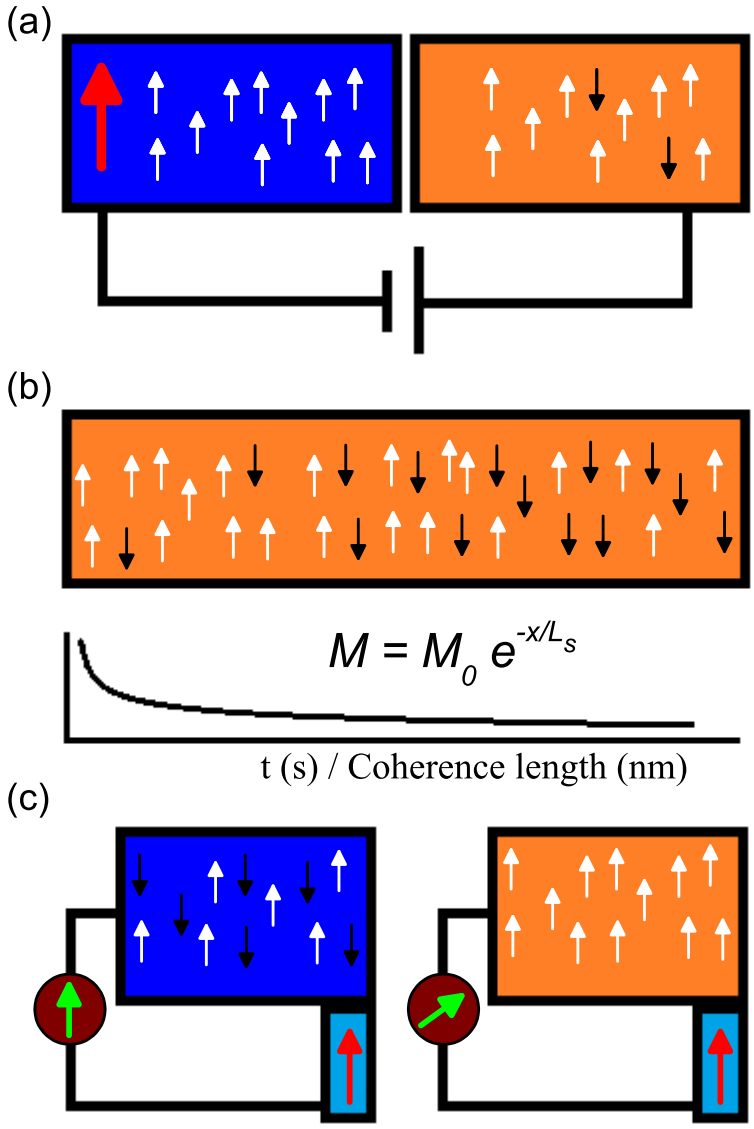

Figure 2.6: Panel (a) displays spin injection from a ferromagnetic material into a non-magnetic conductor (left to right), spin accumulation is occurring in the non-magnetic conductor. Panel (b) shows the spin relaxation with respect to time or distance. Panel (c) shows how reliable spin detection comes into play. This is based upon Silsbee-Johnson spin-charge coupling. (after Ref. [138])

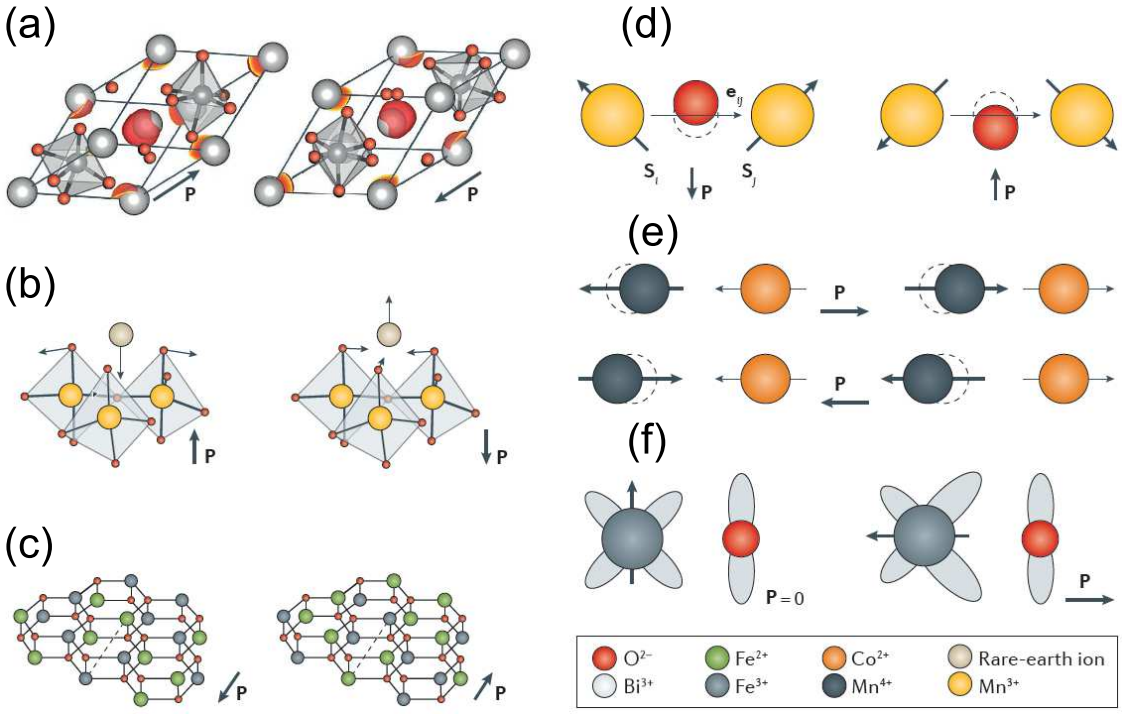

Figure 2.7: In (a) the lone-pair mechanism is displayed by the example of $BiFeO_3$. The two Bi $^{3+}$ electrons move towards the FeO_6 octahedra and away from the Bi^{3+} ion. (after Ref. [179])

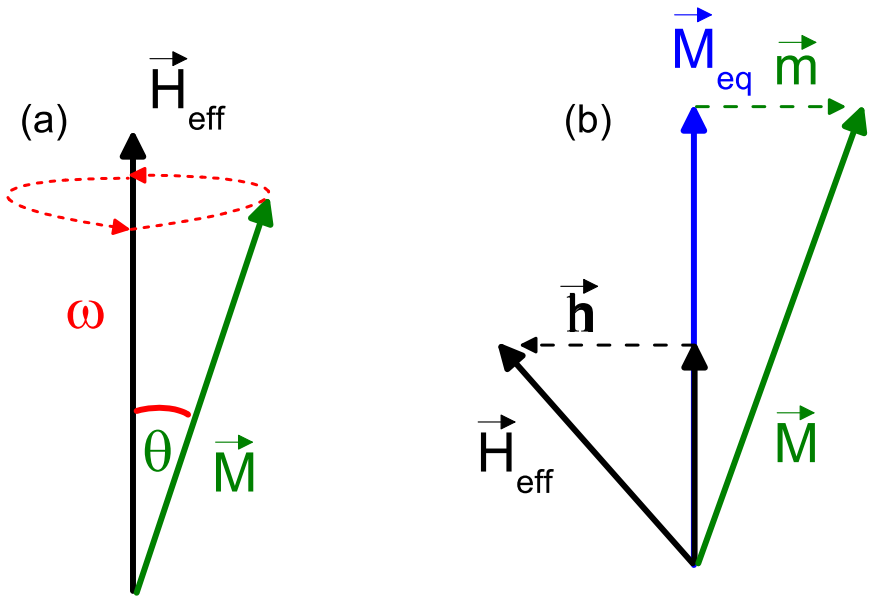

Figure 2.8: (a) Shows a schematic diagram of the precession of the magnetization vector $\vec{M}$ about the effect magnetic field $\vec{H}_{eff}$

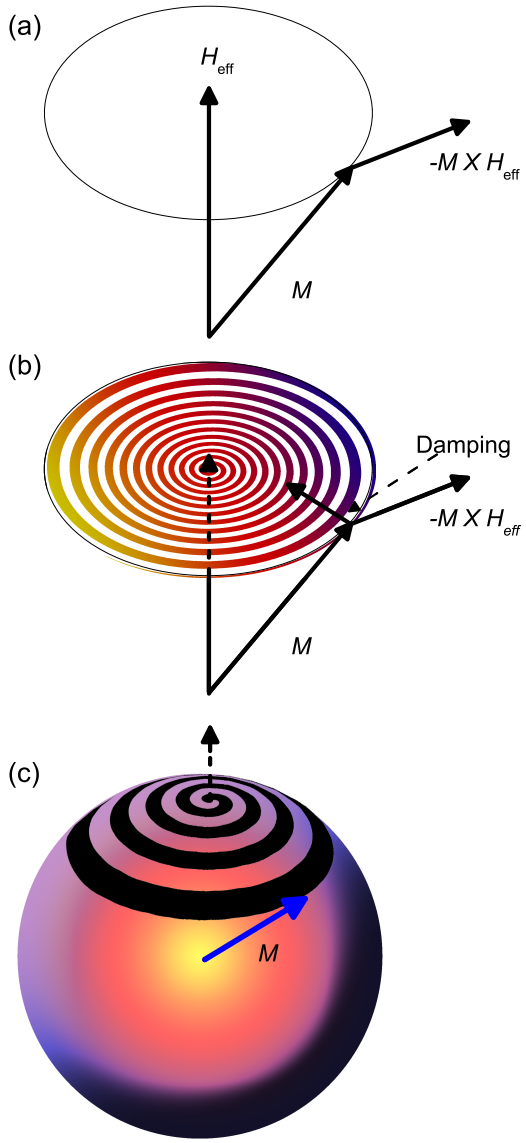

Figure 2.9: (a) Shown here is a schematic representation of the Landau-Lifshitz equation. The magnetization vector $\vec{M}$ continuous to precession indefinitely about the effective magnetic field $\vec{H}_{eff}$. In (b) one can see that the realistic damping of the precession of $\vec{M}$ due to some characteristic damping process. (c) shows the conservation of angular momentum as the damping of the precession creates an alignment between $\vec{M}$ and $\vec{H}_{eff}$.

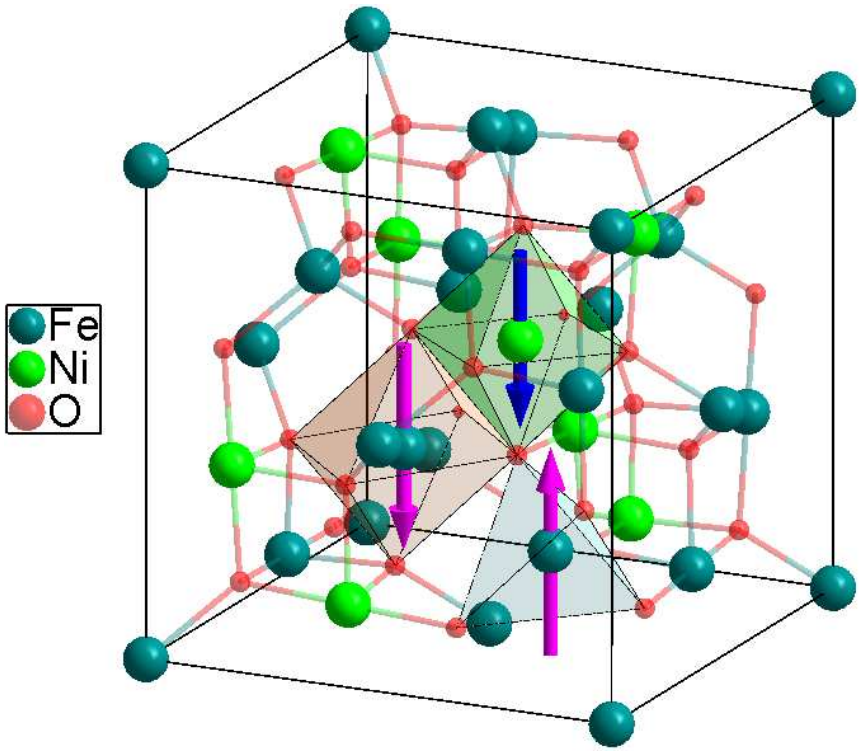

Figure 2.10: Schematic representation of the inverse spinel lattice for $NiFe_2O_4$ and $CoFe_2O_4$: Fe^{3+}-cations (teal) are distributed equally across tetra- (T_d) and octahedral (O_h) lattice sites, while $Ni(Co)^{2+}$-cations (bright green) occupy O_h sites. An antiferromagnetic coupling between the T_d and O_h sites compensates the magnetic moments of the Fe^{3+}-cations, why only the Ni^{2+}-cations account for the net macroscopic magnetization of 2 μ_B f.u.

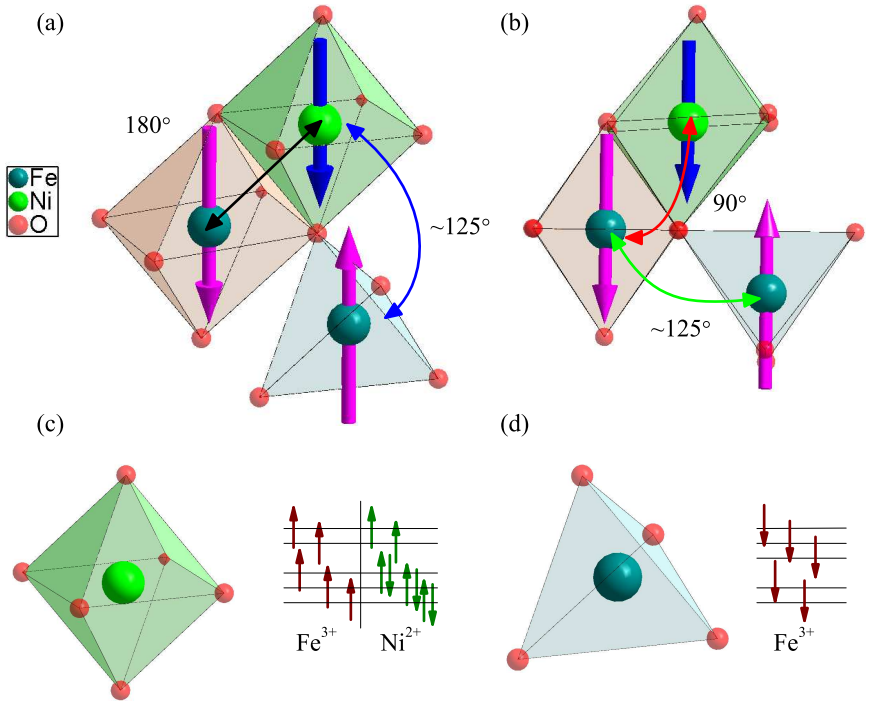

Figure 2.11: (a-b) Exchange interactions in inverse spinel ferrites namely: $NiFe_2O_4$ and $CoFe_2O_4$. Panel (a) shows ferromagnetic double-exchange interaction (black double-headed arrow) 180° between cations on octahedral O_h lattice sites and antiferromagnetic superexchange interaction (blue curved double-headed arrow) 125° between the differing (Ni (Co)/Fe) cations on octahedral O_h and tetraedral T_d lattice sites, (b) displays ferromagnetic superexchange intercation (curved red double-headed arrow) between the differing (Ni/Fe) cations on octahedral O_h lattice sites and antiferromagnetic superexchange interaction (curved green double-headed arrow) between like (Fe/Fe) cations on tetrahedral T_d and octahedral O_h lattice sites. (c) Occupation of the magnetic sublattices in the inverse spinel structure of $NiFe_2O_4$. Additionally, the splitting of the d levels due the crystal field is depicted. (d) The angles between the respective cations are (a) 180° (b) 90° (c) 125° and (d) 121°

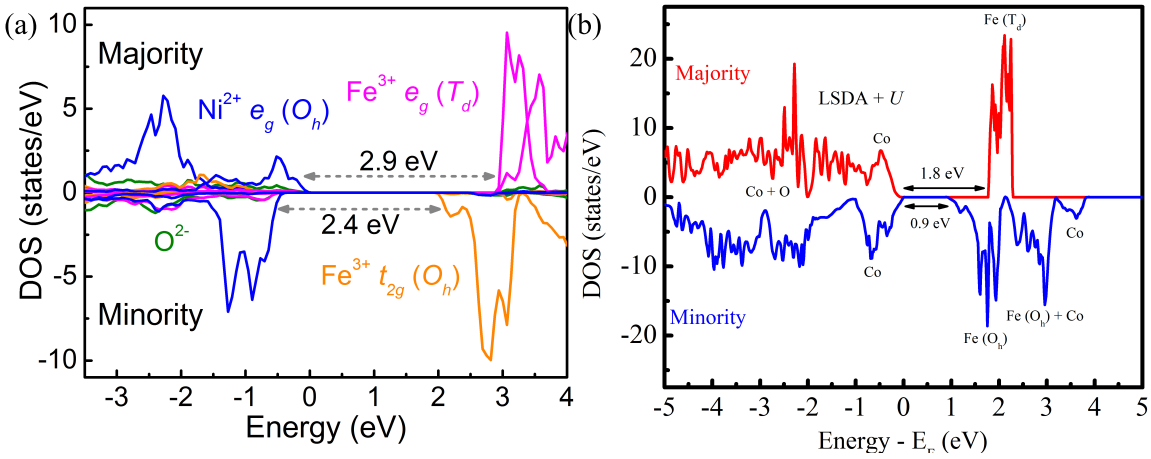

Figure 2.12: (a-b) Display of spin dependent projected density of states (DOS) of $NiFe_2O_4$ and $CoFe_2O_4$ for the inverse spinel structure, with the upper half consisting of the majority DOS, and the lower half (negative side of the y-axis) showing the minority DOS, the constituents of the primary bands are indicated. Adapted from [116, 301]

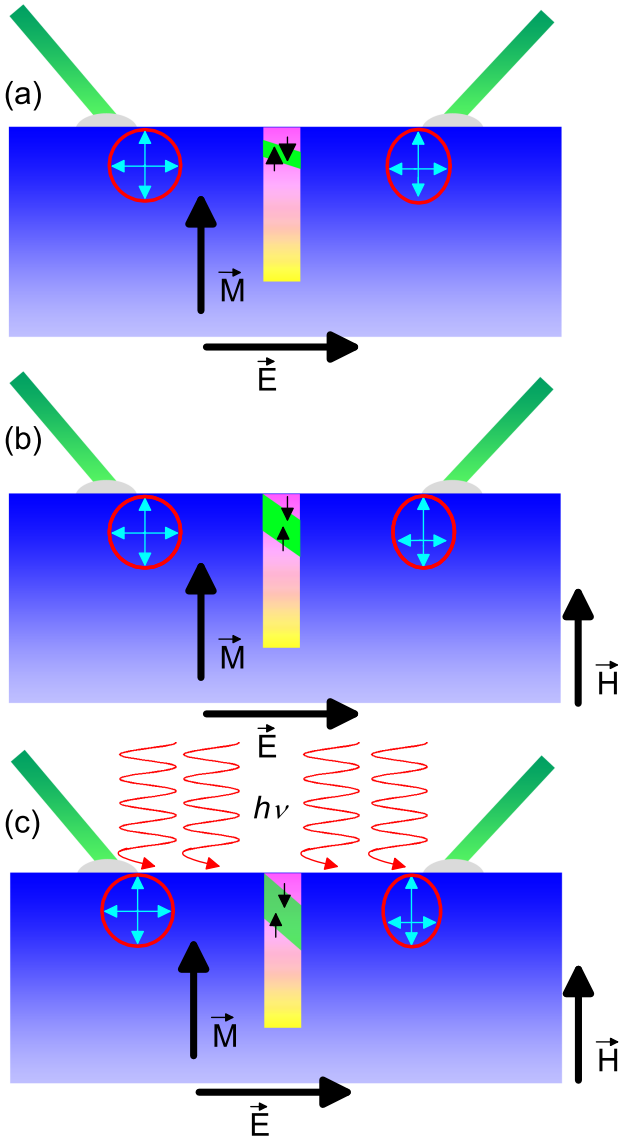

Figure 2.13: Shown in panel (a) is the MR (spin filtering) effect as produced via tunneling through a thin film of a magnetic insulator in ambient conditions. (b) Display of how applying a magnetic field alters the spin-polarized current. Panel (c) shows the method by which we are producing an enhanced spin-polarized current. The resulting magnetoresistance can be projected along the frequency plane and thereby obtain information about high-frequency components of MR.

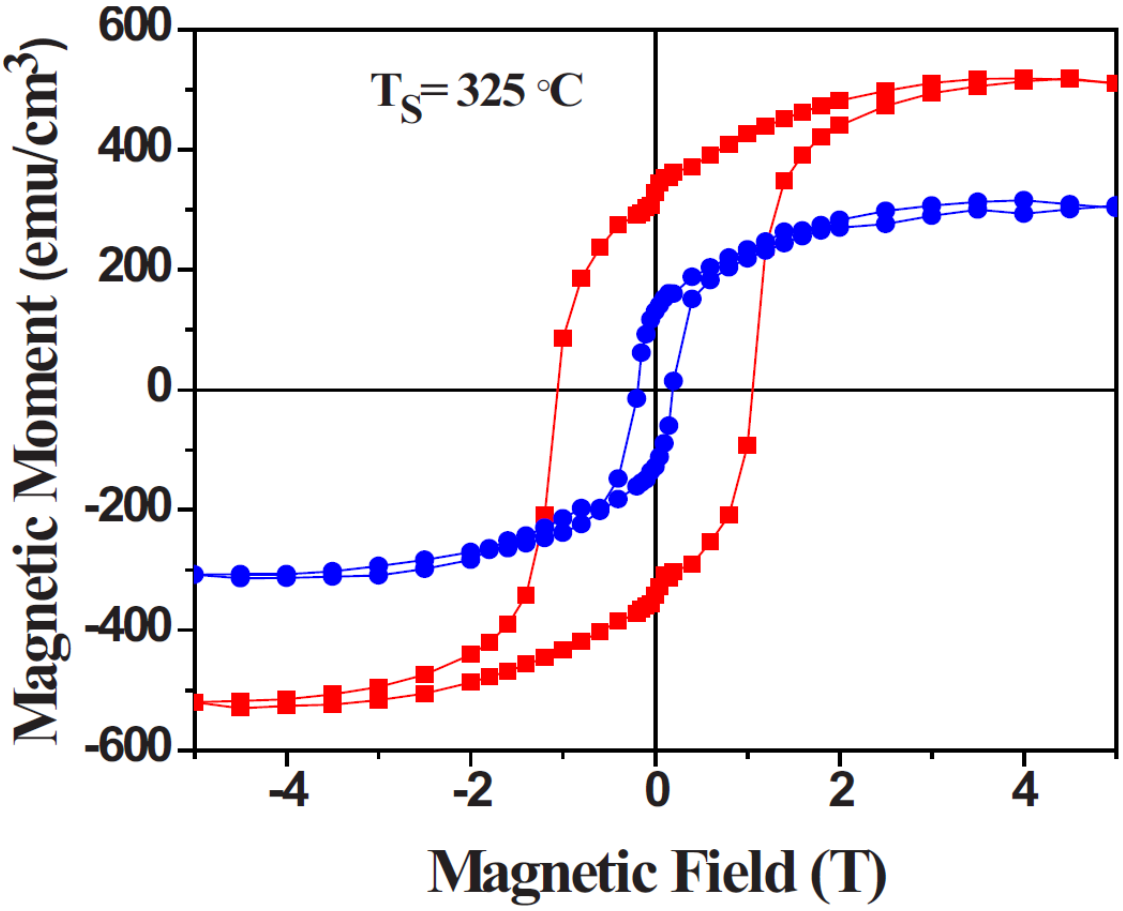

Figure 2.14: Shown here is a typical magnetic hysteresis loop for $NiFe_2O_4$ (filled circles) and $CoFe_2O_4$ (filled squares), films were grown at 325 °C and measured at 5 K. The magnetic field is applied along the [001] in-plane direction, after [286].

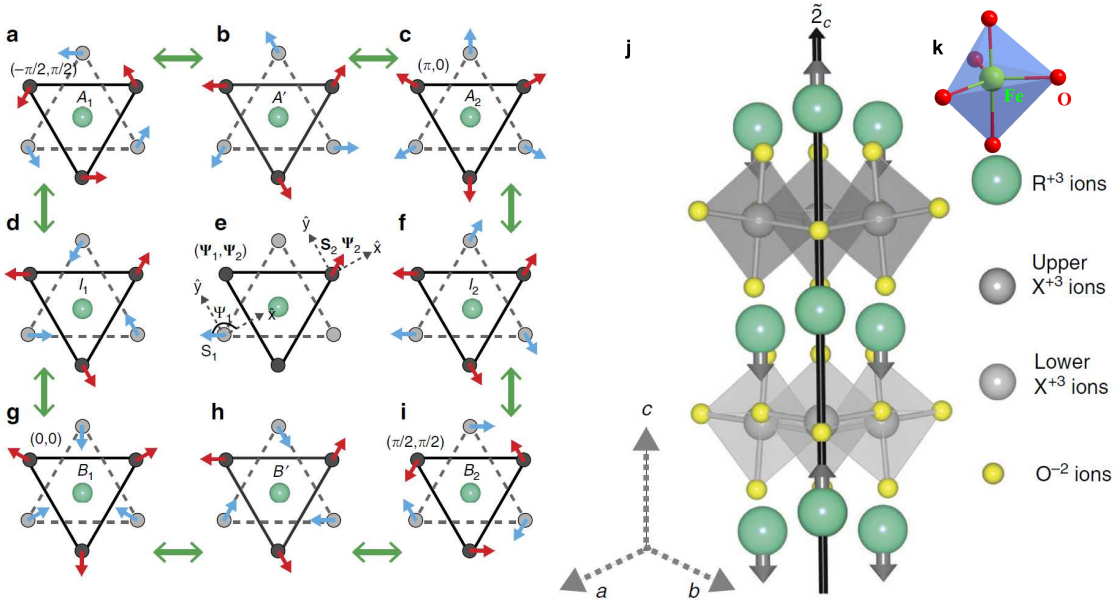

Figure 2.15: (a-i) Shows the non-collinear spin configurations, displaying the possible spin ordering patterns within the 120° in the $\Phi = 0$ structural domain, after [328]. The angles are defined by $\Psi_| = \Psi_1$ and $\Psi_{||} = \Psi_2$. The magnetic ion spin directions are indicated by the blue and red arrows. The magnetic ions in layer | are light grey, small balls and the magnetic ions in layer || are dark grey, small balls, respectively. (j) Shows the ferroelectric crystal structure and polarization that occurs in the α^+ domain, after [328]. (k) Shows the local trigonal pyramidal symmetry about the Fe ions, after [329]

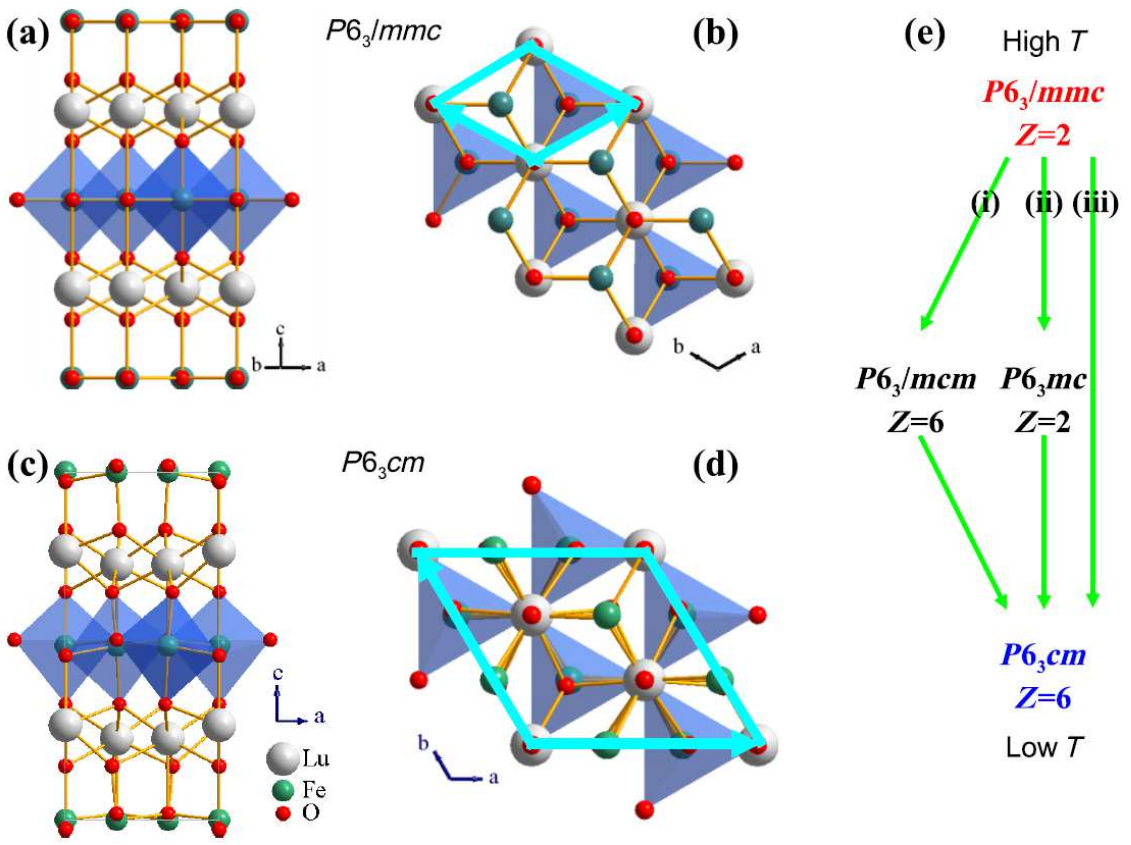

Figure 2.16: (a) and (c) show the paraelectric *P63/mmc* and ferroelectric *P63cm* crystal structures viewed along the [120] and [100] directions, respectively. (b) Shows the *P63/mmc* structure viewed from the [001] direction with the unit cell in the a-b plane depicted by the bold line. (d) Shows the *P63cm* structure viewed from the [001] directions, again the unit cell in the a-b plane is depicted by the bold line. (e) Schematic of the potential structural transformation routes from *P63/mmc* to *P63cm* structures, after [223]

Chapter 3

Experimental and Theoretical Techniques

> Experiment is the sole source of truth. It alone can teach us something new; it alone can give us certainty. These are two points that cannot be questioned. But then, if experiment is everything, what place is left for mathematical physics?
>
> Henri Poincaré
>
> Science and hypothesis

3.1 Optical Theory

The interaction of light and matter is closely connected to the microscopic properties of the material being investigated. Importantly, at the microscopic level the material

behavior can be described via quantum mechanics where the information about the system is stored in the proverbial wavefunction $|\Psi(t)\rangle$. Access to the wavefunction is gained through Schrödinger's non-relativistic time-dependent equation,

$$\hat{H}(t)\,|\Psi(t)\rangle = i\hbar\frac{\partial\,|\Psi(t)\rangle}{\partial t}, \tag{3.1}$$

via perturbing the Hamiltonian with external fields,

$$\hat{H}(t) = \hat{H}_0 + \hat{V}(t). \tag{3.2}$$

Here, $\hat{H}_0$ is the unperturbed Hamiltonian seen in Eq. 3.4 and $\hat{V}(t)$ defines the time-dependence of the interaction of the system with external (perturbing) field(s). The interaction operator $\hat{V}(t)$ introduces time-dependence into the Hamiltonian, and is defined, to first order, by the following:[340]

$$\hat{V}(t) = \sum_i \frac{q_i}{m_i}\vec{A}(r_i, t)\cdot\hat{p}_i. \tag{3.3}$$

Here, the sum runs over all particles in the system, q_i is the charge of a given particle, m_i is the particles mass, and $\hat{p}_i$ is the linear momentum operator such that $\hat{p}_i = -i\hbar\nabla_i$.

For an unperturbed system the Hamiltonian is given by

$$\hat{H}_0 = \hat{T}_{el} + \hat{T}_{nuc} + \hat{U}. \tag{3.4}$$

Here, $\hat{T}_{el}$ is the kinetic energy operator for the electron(s), $\hat{T}_{nuc}$ is the kinetic energy

operator for the nuclear envelope, and $\hat{U}$ is the potential energy operator for the interaction between particles.[341]

The resulting optical interaction can communicate information concerning the properties of the electronic and magnetic structures of the material. Therefore, interpretation of the optical properties is essential to understand the spin and charge dynamics from a microscopic view. Experimentally, we determine optical properties from the frequency-dependent reflectance $R(\omega)$ and transmittance $T(\omega)$ measurements. Our first goals are the extraction of optical constants including absorption $\alpha(\omega)$, dielectric function $\varepsilon(\omega)$, optical conductivity $(\sigma_1(\omega))$, plasma frequency (ω_p), effective mass $(m^*(\omega))$, oscillator strength (f), and relaxation time $(\tau(\omega))$. The absorption $\alpha(\omega)$ and dielectric function $\varepsilon(\omega)$ are responsible for the lossy and dispersive nature of a material. Taking $\alpha(\omega)$ for example, from a fundamental perspective when the frequency of impinging light matches the energy difference of the two quantum states or bands, the light may be absorbed or emitted, as shown in Fig. 3.1. For instance, the transition rate created by one-photon from initial state $|i\rangle$ to final state $|j\rangle$ is, in accordance with Fermi's golden rule, proportional to the transition moment squared of the invoking operator,[340, 342, 343, 344] as shown by the following:

$$P_{ij}(\omega) = \frac{\pi}{2\hbar^2}|V_{ij}|^2\delta(\omega - \omega_j). \tag{3.5}$$

Here, ω is the frequency of the optical field, $\hbar\omega_{ij} = E_j - E_i$, and $V_{ij} = \langle i|\hat{V}(t)|j\rangle$. Since all light is either reflected, transmitted, or absorbed, $R + A + T = 1$. Rearranging, $A = 1 - R - T$ and thereby determine the absorption coefficient by $R+T = \exp(-\alpha(\omega)h)$.[345] Here, h is the thickness of the optical element. The afore-

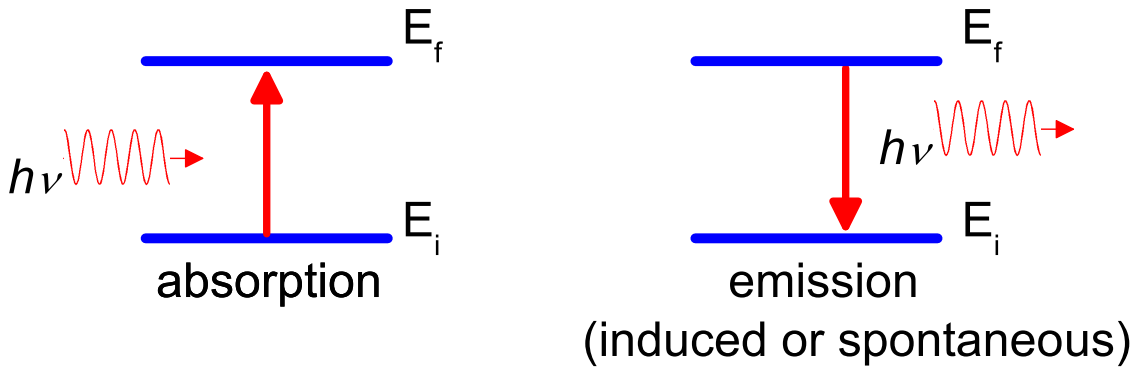

Figure 3.1: The quantum mechanical process of one-photon absorption and emission.

mentioned optical constants are usually derived from Beer's law, Kramers-Kronig analysis, or Glover-Tinkham analysis. [346, 347]

3.1.1 Maxwell's Equations

The relationship and interaction between light and matter is well described by the macroscopic form of Maxwell equations (SI units), shown here are the differential and integral forms [346, 348, 264, 349, 350, 85, 351, 352, 353, 354]: where $\vec{E}$ and $\vec{H}$

Table 3.1: Differential and integral forms of Maxwell's equations

Differential	Integral
$\nabla \cdot \vec{D} = \rho^{ext}$	$\oint_s \vec{D} \cdot \hat{n}\, da = q_{free,enc}$
$\nabla \cdot \vec{B} = 0$	$\oint_s \vec{B} \cdot \hat{n}\, da = 0$
$\nabla \times \vec{E} = -\frac{\partial \vec{B}}{\partial t}$	$\oint_c \vec{E} \cdot d\vec{l} = -\frac{d}{dt}\int_s \vec{B} \cdot \hat{n}\, da$
$\nabla \times \vec{H} = \frac{\partial \vec{D}}{\partial t} + \mathbf{J}^{cond} + \mathbf{J}^{ext}$	$\oint_c \vec{H} \cdot d\vec{l} = I_{free,enc} + \frac{d}{dt}\int_s \vec{D} \cdot \hat{n}\, da$

are the electric and magnetic fields, $\vec{D}$ and $\vec{B}$ are the displacement field and magnetic

induction, $\vec{J}^{cond}$ is current density arising from the motion of conduction electrons, and $\vec{J}^{ext}$ and ρ^{ext} are current and charge density induced by external force.

For isotropic media and weak electromagnetic field, only the linear response will be retained, and thereby obtain the following relations:

$$\vec{D} = \epsilon \vec{E} \tag{3.6}$$

$$\vec{B} = \mu \vec{H} \tag{3.7}$$

$$\vec{J}^{cond} = \sigma \vec{E}, \tag{3.8}$$

where ϵ is the dielectric function, and σ is the optical conductivity, and μ is the magnetic permeability. Here both ϵ and σ are scalar quantities rather than tensors for the isotropic and homogeneous media.

It is important to note that since a significant portion of the work involved in this dissertation involves circularly polarized light, so we will also show how some corresponding relationship/extension in parallel to the classically defined methodology. The complex refractive index shown here with non-polarized and circularly polarized $\pm$ notation [346, 355, 356]

$$\begin{aligned} N(\omega) &= n(\omega) + i\kappa(\omega), \\ N_{\pm}(\omega) &= n_{\pm}(\omega) + i\kappa_{\pm}(\omega), \end{aligned} \tag{3.9}$$

and the complex dielectric function

$$\epsilon(\omega) = \epsilon_1(\omega) + i\epsilon_2(\omega),$$
$$\epsilon_\pm(\omega) = \epsilon_{1\pm}(\omega) + i\epsilon_{2\pm}(\omega), \tag{3.10}$$

where n and κ are the refractive index and the extinction coefficient, $\epsilon_1(\omega)$ and $\epsilon_2(\omega)$ are the real and imaginary part of complex dielectric function, and the $\pm$ symbolize the right- and left-circularly polarized (RCP/+ and LCP/-) light components. $N(\omega)$ and $\epsilon(\omega)$ are related by the following equation

$$N(\omega) = \sqrt{\epsilon(\omega)}$$
$$N_\pm(\omega) = \sqrt{\epsilon_\pm(\omega)}. \tag{3.11}$$

Finally, solving Maxwell's equations 3.1-3.1 for a plane wave environment (to be defined further for this dissertation in Sec. 3.1.3)

$$\vec{E} = \vec{E}_0 exp[i(\vec{q}\cdot\vec{x} - \omega t)],$$
$$\vec{E}_\pm = \vec{E}_{0\pm} exp[i(\vec{q}\cdot\vec{x} - \omega t)], \tag{3.12}$$

gives the following relation,

$$\epsilon(\omega) = 1 + \frac{i\sigma(\omega)}{\omega\epsilon_0},$$
$$\epsilon_{\pm}(\omega) = 1 + \frac{i\sigma_{\pm}(\omega)}{\omega\epsilon_{0\pm}}. \tag{3.13}$$

or

$$\epsilon(\omega) = \epsilon_1(\omega) + i\epsilon_2(\omega) = \epsilon_1(\omega) + \frac{4\pi i\sigma_1(\omega)}{\omega},$$
$$\epsilon_{\pm}(\omega) = \epsilon_{1\pm}(\omega) + i\epsilon_{2\pm}(\omega) = \epsilon_{1\pm}(\omega) + \frac{4\pi i\sigma_{1\pm}(\omega)}{\omega}. \tag{3.14}$$

Here $\sigma_1(\omega)$ is the frequency dependent (optical) conductivity. In the case of weak absorption, $\epsilon_1 = n^2 - k^2 \approx n^2$, and $v \approx c/n$, the absorption coefficient α can be written as

$$\alpha = \frac{4\pi\sigma}{\epsilon_1 v} = \frac{4\pi\sigma}{nc},$$
$$\alpha_{\pm} = \frac{4\pi\sigma_{\pm}}{\epsilon_{1\pm} v} = \frac{4\pi\sigma_{\pm}}{n_{\pm} c}. \tag{3.15}$$

Until further attention is needed, the symmetry of the contribution from RCP and LCP can be assumed to remain equivalent. So, they will not be denoted.

Table 3.2 lists the relationships between the various response functions.

Table 3.2: Relationships between the various response function $\epsilon(\omega)$, $\sigma(\omega)$, and $N(\omega)$

Dielectric constant $\epsilon(\omega)$	Conductivity $\sigma(\omega)$	Refractive index $N(\omega)$
$\epsilon = \epsilon_1 + i\epsilon_2$ $\sigma_1 = \frac{\omega\epsilon_2}{4\pi}$ $\sigma_2 = (1-\epsilon_1)\frac{\omega}{4\pi}$ $n = \left[\frac{1}{2}((\epsilon_1^2+\epsilon_2^2)^{1/2}+\epsilon_1)\right]^{1/2}$ $k = \left[\frac{1}{2}(\epsilon_1^2+\epsilon_2^2)^{1/2}-\epsilon_1)\right]^{1/2}$	$\epsilon_1 = 1 - \frac{4\pi\sigma_2}{\omega}$ $\epsilon_2 = \frac{4\pi\sigma_1}{\omega}$ $\sigma = \sigma_1 + i\sigma_2$ $n = (\frac{1}{2}(((1-\frac{4\pi\sigma_2}{\omega})^2 + (\frac{4\pi\sigma_1}{\omega})^2)^{1/2} + (1-\frac{4\pi\sigma_2}{\omega})))^{1/2}$ $n = (\frac{1}{2}(((1-\frac{4\pi\sigma_2}{\omega})^2 + (\frac{4\pi\sigma_1}{\omega})^2)^{1/2} - (1-\frac{4\pi\sigma_2}{\omega})))^{1/2}$	$\epsilon_1 = n^2 - k^2$ $\epsilon_2 = 2nk$ $\sigma_1 = \frac{nk\omega}{2\pi}$ $\sigma_2 = (1-n^2+k^2)\frac{\omega}{4\pi}$ $N = n + ik$

3.1.2 Polarized light

A considerable portion of the work done for this dissertation imparts circular polarized light. The electric field vector of a monochromatic linearly polarized light wave is given by [357]

$$\vec{E}(\vec{r},t) = \vec{E}_0\cos(\omega t - \varphi), \tag{3.16}$$

or

$$\vec{E}(\vec{r},t) = \mathrm{Re}\Big\{\vec{E}_0\exp(-i\omega t)\Big\}. \tag{3.17}$$

Here, ω is the waves monochromatic frequency, $\vec{r}$ is the position vector, and $\vec{k}$ is the wave vector as defined by:

$$\vec{k} = \frac{n\omega}{c}\vec{i}_z. \tag{3.18}$$

Here, n defines the refractive index, c is the speed of light, and i_z is unit vector in the direction of the propagation. The tip of the electric field vector oscillates along a fixed direction. Now to redefine the electric field as the real part of the following complex phasor ($\tilde{\vec{E}}$ represents a complex vector) expression:

$$\tilde{\vec{E}}(\vec{r},t) = \tilde{\vec{E}}_0 \mathrm{e}^{i\varphi}\mathrm{e}^{-i\omega t}. \tag{3.19}$$

We are going to assume that the wave has a sinusoidal spatial dependence; therefore, we can rewrite the spatial phase φ as:

$$\varphi = \vec{k}\cdot\vec{r} + \delta. \tag{3.20}$$

To clarify, δ is the reference phase at the waves origin, typically this value is set to zero.[264] Equation 3.19 can be expanded and present the electric field by the following:

$$\begin{aligned}\vec{E}(\vec{r},t) =& \frac{1}{2}\left[\tilde{\vec{E}}_0 \mathrm{e}^{i(\vec{k}\cdot\vec{r}-\omega t)} + \tilde{\vec{E}}_0^{*}\mathrm{e}^{-i(\vec{k}\cdot\vec{r}-\omega t)}\right] \\ =& \frac{E_0}{2}\left[\vec{i}_E \mathrm{e}^{i(\vec{k}\cdot\vec{r}-\omega t)} + \vec{i}_E^{*}\mathrm{e}^{-i(\vec{k}\cdot\vec{r}-\omega t)}\right].\end{aligned} \tag{3.21}$$

Here, $\vec{i}_E$ is the unit vector of the electric vector in the polarized field.

When considering plane waves, linearly polarized waves are a special case. Plane waves are defined as having the same value over any plane normal to the direction of propagation, thereby they have no field components in the direction of propagation (Cartesian coordinate system), as shown in Fig. 3.2.[358] Therefore, if the wave is

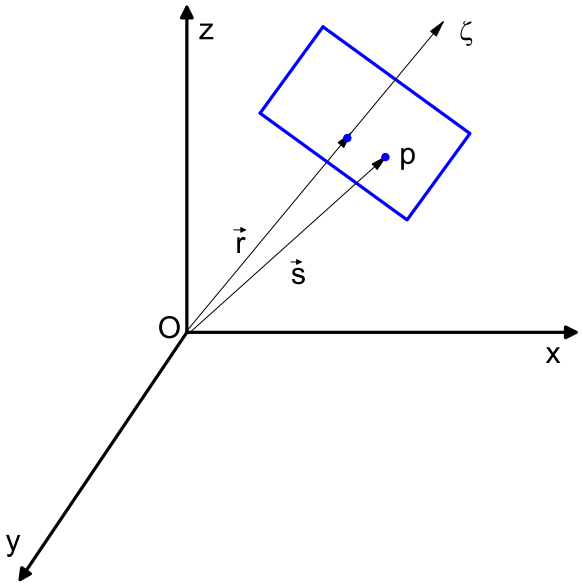

Figure 3.2: $\vec{r}$ is the position vector of the point P in space and $\vec{s}(s_x, s_y, s_z)$ is a unit vector in a fixed direction. Any solution of $\nabla^2 V - 1/v^2(\partial^2 V/\partial t^2)$ that takes the form of $V = V(\vec{r}\cdot\vec{s}, t)$ produces a *plane wave*. This arises because at each instant in time V is constant over each of the planes, such that $\vec{r}\cdot\vec{s} =$ constant.[358]

propagating in the z direction, then any plane can be written as the sum of two coherent waves linearly polarized in the x and y directions,

$$\tilde{\vec{F}} = \tilde{E}_x \vec{i}_x + \tilde{E}_y \vec{i}_y. \tag{3.22}$$

Now that we have the plane, if the phase components for the waves $\tilde{E}_x$ and $\tilde{E}_y$ are the same, then $\tilde{\vec{E}}$ will be a linearly polarized wave. Another valuable special case (of elliptically polarized waves) is that of circularly polarized light, this occurs when $\tilde{E}_x$ and $\tilde{E}_y$ have equal magnitude but are $\pi/2$ (or $\lambda/4$) out of phase. This is case implemented in the work presented in this dissertation.

The tip of the electric field vector $\vec{E}$ will rotate and inscribe a circle as time progresses, at a fixed point in space, as described by the following:

Right-hand polarization:

$$\hat{k} \cdot \left(\vec{E} \times \frac{d\vec{E}}{dt} \right) > 0, \tag{3.23}$$

Left-hand polarization:

$$\hat{k} \cdot \left(\vec{E} \times \frac{d\vec{E}}{dt} \right) < 0. \tag{3.24}$$

These definitions are displayed in Fig. 3.3. The rotation of $\vec{E}$ generates the spin angular momentum $\vec{S}$ of electromagnetic radiation when the Poynting vector $\vec{P}$ is parallel to the the wavevector $\vec{k}$.[359, 360, 361, 362, 363, 364] However, when the electric field distribution spins through space instead of time the phase wavefront will generate either a right or left rotating helix. This helicity carries the orbital angular momentum.[365, 366, 367, 368, 369, 370, 371, 372, 362] The orbital angular momentum beam has an azimuthal phase dependence of $\exp(im\varphi)$, where φ is the azimuthal angle and m is the angular momentum index. The orbital angular momentum is quantized for each helically phased beam as $m\hbar$ per photon.[373] The assignment of left- or right-circularly polarized light depends upon the orientation of the viewer, such that if the light is right-circularly polarized when viewed along the propagation direction, then it will be left-circularly polarized when viewed against the propagation direction. This can be seen in Fig. 3.4. Mathematically the two

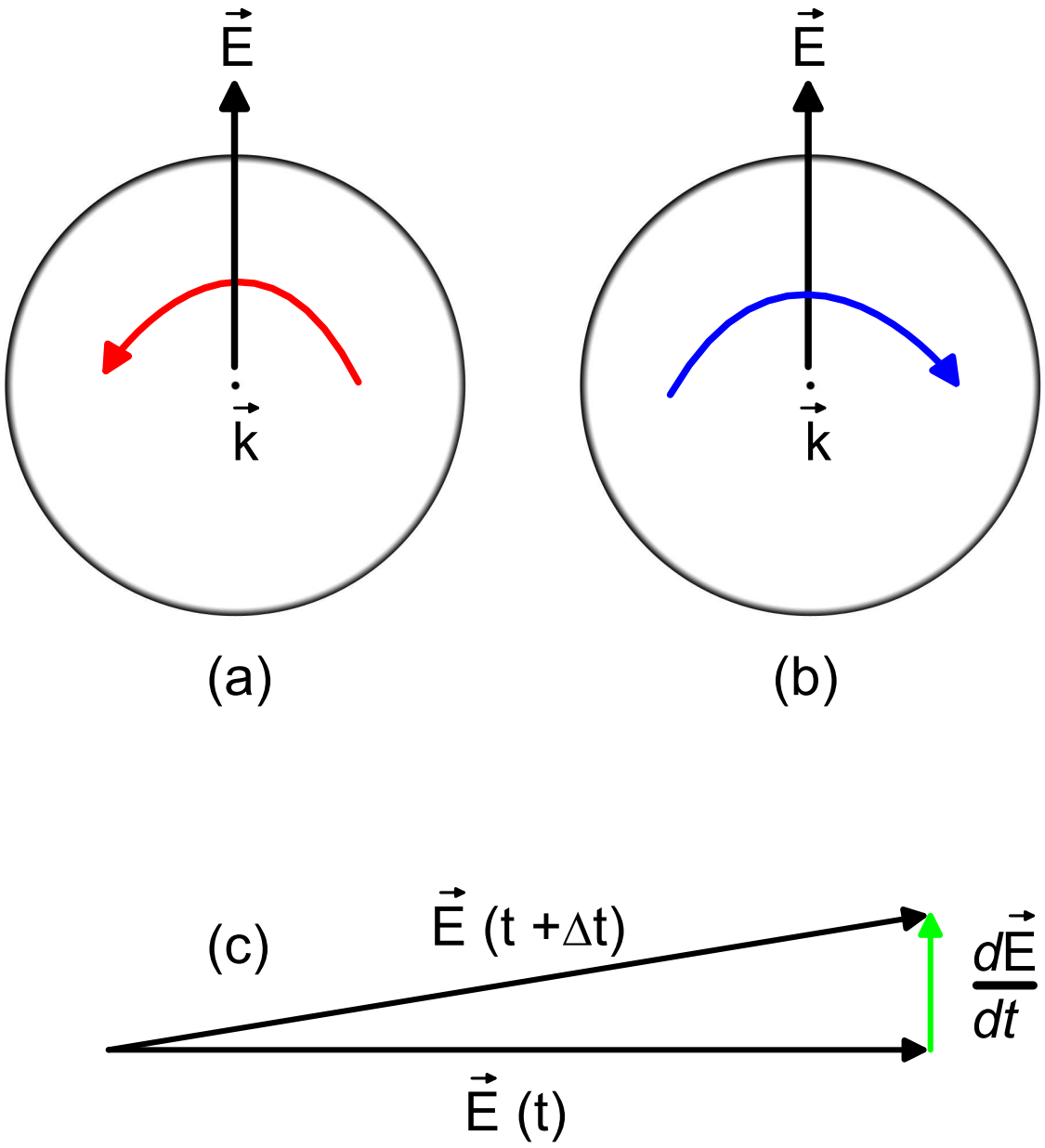

Figure 3.3: (a-b) Show the circular polarization states: right-circular polarization (a) and left-circular polarization (b). (c) Displays the definition of the vector $d\vec{E}/dt$.

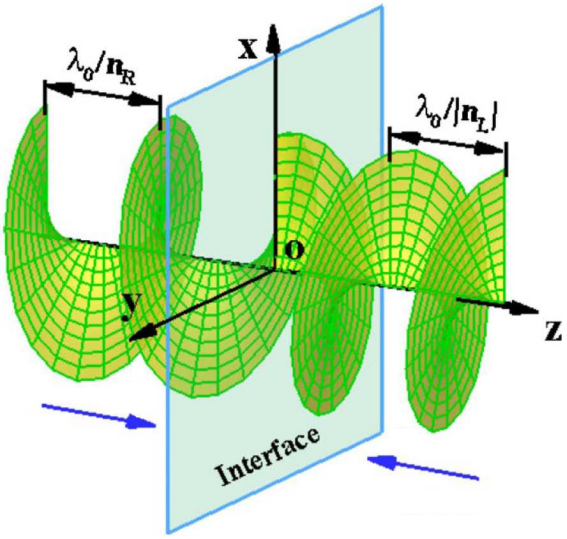

Figure 3.4: Shown here is the helical wave traveling in two directions, after [374]. These are Laguerre-Gaussian beams with orbital angular momentum $l = 1$ that results from an azimuthal phase structure of $\exp\{-i\varphi\}$.

forms of circularly polarized light will be presented by

$$\tilde{\vec{E}}_+(\vec{r},t) = \frac{E_0}{2}\left[\vec{i}_+ e^{i(\vec{k}\cdot\vec{r}-\omega t)} + \vec{i}_+^{*} e^{-i(\vec{k}\cdot\vec{r}-\omega t)}\right], \tag{3.25}$$

$$\tilde{\vec{E}}_-(\vec{r},t) = \frac{E_0}{2}\left[\vec{i}_- e^{i(\vec{k}\cdot\vec{r}-\omega t)} - \vec{i}_-^{*} e^{-i(\vec{k}\cdot\vec{r}-\omega t)}\right]. \tag{3.26}$$

The unit vectors for the electric field component of the two circularly polarized light

forms take on the following complex structure:[71, 341, 375, 376, 267]

$$\vec{i}_+ = \frac{1}{\sqrt{2}}(\vec{i}_x + i\vec{i}_y)\mathrm{e}^{-i\omega t}, \tag{3.27}$$

and

$$\vec{i}_- = \frac{1}{\sqrt{2}}(\vec{i}_x - i\vec{i}_y)\mathrm{e}^{-i\omega t}. \tag{3.28}$$

From this Eqn. 3.19 evolves into:

$$\vec{E}_+(z) = \frac{1}{2}\vec{E}_0\,(\hat{x} + i\hat{y}) \tag{3.29}$$

$$\vec{E}_-(z) = \frac{1}{2}\vec{E}_0\,(\hat{x} - i\hat{y}) \tag{3.30}$$

3.1.3 Plane waves in a poorly conducting (rightly insulating) and lossy dielectric medium

The following text is derived from [194, 264, 358, 377, 378, 379, 380, 381, 382, 383, 384, 385].

With the solutions to Maxwell's equations for plane waves being expressed in Eqn. 3.12, we can now look at how this applies to the work done for this dissertation. The materials investigated here are poor conducting and lossy dielectrics; therefore, the materials fall under the conditions that $\sigma/\omega\epsilon_0 \ll \epsilon''$. Within this framework the wave (propagation) vector becomes:

$$k \to \frac{2\pi}{\lambda_0}(\epsilon' + i\epsilon'')^{1/2}. \tag{3.31}$$

The amplitude of the electric field along the x-axis for the propagating plane waves through these medium forms is attenuated by the dissipative losses due to ϵ'', such as:

$$\vec{E}_x = \vec{E}_0 \exp\left(i \left[\frac{2\pi}{\lambda_0} (\epsilon' + i\epsilon'')^{1/2} z - \omega t \right] \right). \tag{3.32}$$

The expectation value $\langle |\epsilon''/\epsilon'| \rangle$ should be $\ll 1$ for most cases, this leads to the wave vector taking the form:

$$k \approxeq \frac{2\pi}{\lambda_0} \sqrt{\epsilon'} \left(1 + i \frac{\epsilon''}{2\epsilon'} \right), \tag{3.33}$$

this leads to a restating of Eqn. 3.32 as:

$$\vec{E}_x = \vec{E}_0 \exp\left(\left[\frac{2\pi}{\lambda_0} \left(\frac{\epsilon''}{2\sqrt{\epsilon'}} \right) z \right] \right) \exp\left(i \left[\left(\frac{2\pi}{\lambda_0} \right) \sqrt{\epsilon'} z - \omega t \right] \right), = \qquad \frac{2\pi}{\lambda_0} (\eta + i\kappa) \tag{3.34}$$

Here, the former exponential factor dampens $\vec{E}_0$'s amplitudes with continued propagation along z; whereas, the latter factor portrays a harmonic wave oscillation traversing through a medium as characterized by $\sqrt{\epsilon'}$. Therefore, it is most logical to consider the two components a depicting a harmonic traveling plane wave that is damped.

The wave impedance in lossy mediums derives from Faraday's law, such as the

following:

$$\vec{E}_x = \sqrt{\frac{\mu_0}{\epsilon_0 \left(\epsilon' + i\epsilon''\right)}} \vec{H}_y \tag{3.35}$$

and (3.36)

$$Z = \sqrt{\frac{\mu_0}{\epsilon_0 \left(\epsilon' + i\epsilon''\right)}} = \frac{Z_0}{\eta + i\kappa}. \tag{3.37}$$

Here is the free space (vacuum) impedance $Z_0 = 376.7\,\Omega$. An important caveat to this is that the materials under consideration are magnetic and as of thus far in the derivation $\mu_r = \mu/\mu_0 = 1$. Therefore, if one was to follow through and use the preceding to model the interactions, then it would most likely produce grievous errors.[386, 387, 388, 389, 390, 391]

3.1.4 Beer-Lambert law

For a sample of thickness $d < \delta = \frac{c}{\omega k}$, the penetration depth, the absorption coefficient can be directly determined from transmittance. This is one of the simplest and well known relations.

If a light beam with intensity I_0 is incident to a small element of thickness dx with cross section of absorption σ, the change in intensity is

$$dI = -\sigma I(N_0 - N_1)dx, \tag{3.38}$$

or

$$dI/I = -\kappa dl, \tag{3.39}$$

where N_0 and N_1 are the number of atoms in the ground and excited state, respectively. In the latter form, κ is the Lambert's law absorption coefficient, therefore $\kappa = -dI/Idl = (4\pi\nu\alpha)/c$ where is the k is the imaginary portion of the refractive index. This correlates to the absorption coefficient, expressed in Sec. 3.1.1, by $\alpha = 4\pi k\omega$. For a transition from state a to state j, the probability

$$-dI/dl = h\nu(N_a P_{a\to j} - N_j P_{j\to a}). \tag{3.40}$$

Following an assumption that $P_a = P_j$ (absorption and emission have the same probability), we see that $\kappa(\nu)$ evolves to become

$$\kappa(\nu) = \frac{h\nu}{I(\nu)}(N_a - N_j)P_{a\to j}. \tag{3.41}$$

Upon integrating Eq. 3.38 over the absorption path, we obtain

$$\int_{I_0}^{I} \frac{dI}{I} = -\sigma(N_0 - N_1)\int_0^l dx. \tag{3.42}$$

Usually, the cross section and quantity of atoms, or concentration c, are combined to an absorption coefficient and we know transmittance $T = \frac{I}{I_0}$, thus $\alpha = -\frac{1}{lc}ln(T)$.

One limitation of the Beer-Lambert law is the requirement of a small contribution of the reflectance, which is not always negligible. If reflectance is important, say $R > 10\%$, then the optical constants should be determined from combined reflectance and transmittance measurements. Strictly speaking, the Beer-Lambert law only

considers transmittance as per the following:

$$A = -\log(T) = \log\left(\frac{P_0}{P}\right). \tag{3.43}$$

Here A is the absorbance, T is the transmittance, P_0 is the incident power, and P is the detected power. This suggests that in the colloquial equality of $R + A + T = 1$ R is ignored when considering P and for this to remain linear the contribution from the reflectance must be tiny. An algorithm has been developed to more accurately determine A because $A_{meas} > A_{actual}$. This analysis technique includes the contribution from R and is called the Glover-Tinkham analysis. We present the derivation of the algorithm below.

3.1.5 Glover-Tinkham Analysis

A single crystal surrounded by air can be approximated using a three-layer model, as shown by Fig. 3.5 (a). The complex refractive indices are N_1 (ether around crystal), N_2, and N_1, respectively, where $N_1 \approx 1$ and $N_2 = n + i\kappa$. For this three-layer model the transmission and reflection coefficients take the forms, in terms of the refractive indices:

$$\begin{aligned} t_0 &= \frac{2n_0}{n_0 + n_1} & t_1 &= \frac{2n_1}{n_0 + n_1} \\ r_0 &= \frac{n_0 - n_1}{n_0 + n_1} & r_1 &= \frac{n_0 - n_1}{n_0 + n_1} \end{aligned} \tag{3.44}$$

$$T = \frac{4n_0 n_1}{(n_0 + n1)^2} \tag{3.45}$$

$$R = \left(\frac{n_0 - n1}{n_0 + n1}\right)^2 \tag{3.46}$$

When multiple internal reflections are included, the transmission (t_c) and reflection coefficients (r_c) in normal incidence are:[358, 355, 392, 393, 394, 395, 396, 397, 398]

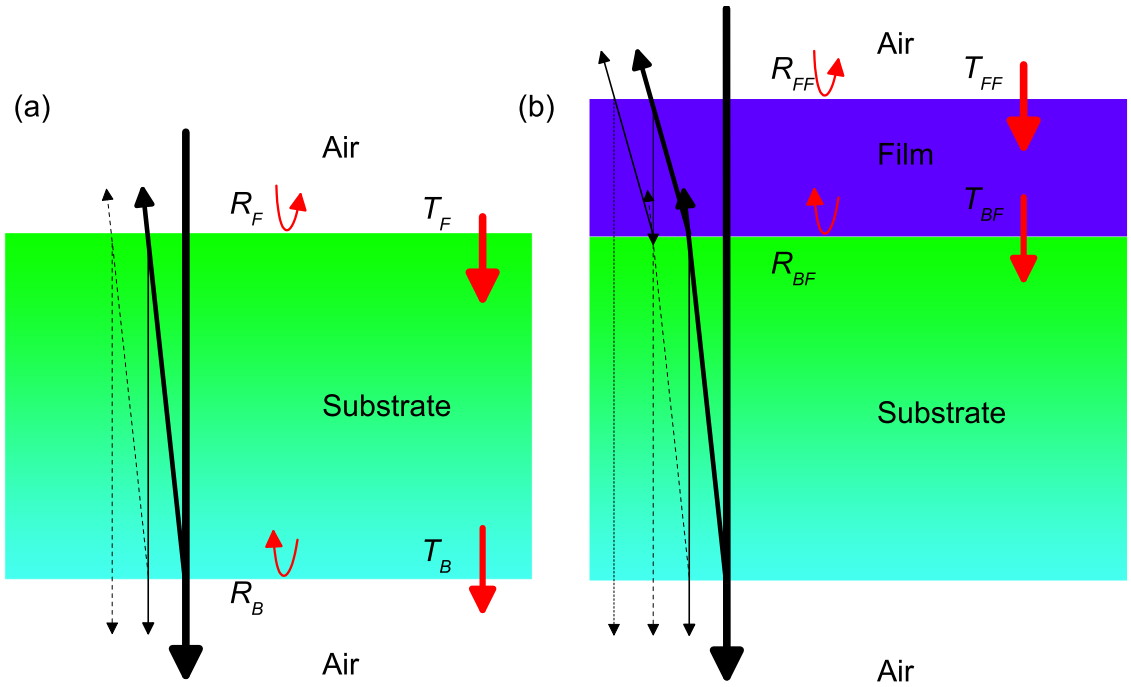

Figure 3.5: (a) Diagram of the a three-layer model consisting of only the substrate, of course air can also be replaced by vacuum. (b) Schematic diagram of four-layer model used in Glover-Tinkham analysis. The light beams reflected from a surface or interface are tilted from the normal for clarity, with different angles representing different refractive indices.

$$t_c = t_{12}t_{21}e^{i\theta}[1 + r_{21}^2 e^{i2\theta} + (r_{21}^2 e^{i2\theta})^2 + ...] \tag{3.47}$$

$$= \frac{t_{12}t_{21}e^{i\theta}}{1 - r_{21}^2 e^{i2\theta}}, \tag{3.48}$$

$$r_c = r_{12} + t_{12}r_{21}t_{21}e^{i2\theta}[1 + r_{21}^2 e^{i2\theta} + (r_{21}^2 e^{i2\theta})^2 + ...] \tag{3.49}$$

$$= \frac{r_{12} + r_{21}e^{i2\theta}}{1 - r_{21}^2 e^{i2\theta}}, \tag{3.50}$$

where $r_{ij} = \frac{N_i - N_j}{N_i + N_j}$, $t_{ij} = \frac{2N_i}{N_i + N_j}$, and the complex phase depth for a crystal with thickness d is $\theta = N_2\frac{\omega d}{c}$. The power transmittance (T_c) and reflectance (R_c) are defined as:

$$T_c = |t_c|^2 \text{ and } R_c = |r_c|^2. \tag{3.51}$$

Thus, we obtain the formula for the measured transmittance and reflectance of a crystal

$$T_c = \frac{[(1 - R_s)^2 + 4R_s sin^2\phi]e^{-\alpha d}}{(1 - R_s e^{-\alpha d})^2 + 4R_s e^{-\alpha d} sin^2(\phi + \beta)}, \tag{3.52}$$

$$R_c = \frac{(1 - e^{-\alpha d})^2 + 4e^{-\alpha d} sin^2\beta}{(1 - R_s e^{-\alpha d})^2 + 4R_s e^{-\alpha d} sin^2(\phi + \beta)} R_s. \tag{3.53}$$

Here, single bounce reflection of the crystal $R_s = |r_{12}|^2 = \frac{(1-n)^2+\kappa^2}{(1+n)^2+\kappa^2}$, phase ϕ is defined as $r_{12} = \sqrt{R_s}e^{i\phi}$ and $\tan\phi = -\frac{2\kappa}{1-n^2-\kappa^2}$, phase depth $\beta = n\frac{\omega}{c}d$, α is the absorption coefficient of the crystal, ω is the photon frequency, and c is the light speed. Integrating Eqs. 3.52 and 3.53 over $d\beta$, we get

$$T_c = \frac{(1 - R_s)^2 e^{-\alpha d}}{1 - R_s^2 e^{-2\alpha d}} \tag{3.54}$$

$$R_c = \frac{1 + (1 - 2R_s)e^{-2\alpha d}}{1 - R_s^2 e^{-2\alpha d}} R_s. \tag{3.55}$$

Therefore, optical constants n and α of the crystal can be extracted from Eqs. 3.54 and 3.55 using frequency dependent T_c and R_c as inputs.

If the system of interest is a thin film or crystal on a substrate with index n, it becomes a four-layer problem (Fig. 3.5 (b)). The film can be treated as a sheet of conductor with complex admittance $y_1 + iy_2$. The transmission through the film (T_f) and the reflectance (R_f) from the film is approximated as [347, 399, 400, 401, 402, 403]

$$T_f = \frac{4n}{(y_1 + n + 1)^2 + y_2^2}, \tag{3.56}$$

$$R_f = \frac{(y_1 + n - 1)^2 + y_2^2}{(y_1 + n + 1)^2 + y_2^2}. \tag{3.57}$$

The complex admittance is related to the conductivity σ by

$$y_1 + iy_2 = Z_0(\sigma_1 + i\sigma_2)d, \tag{3.58}$$

where d is the thickness of the film and Z_0 is the impedance of free space,

$$Z_0 = \sqrt{\frac{\mu_0}{\epsilon_0}} = 376.7\Omega. \tag{3.59}$$

When the absorption coefficient is large in the film, the overall reflectance and transmittance in this four-layer system are

$$R \approx R'_f, \tag{3.60}$$

$$T = \frac{(1 - R_s)e^{-\alpha d}}{1 - R_s R'_f e^{-2\alpha d}} T_f. \tag{3.61}$$

Here,

$$R'_f = \frac{(y_1 - n + 1)^2 + y_2^2}{(y_1 + n + 1)^2 + y_2^2}, \tag{3.62}$$

and d is the film thickness. The refractive index n and absorption coefficient (α) of the substrate can be obtained by independently measuring the transmittance and reflectance of the substrate using the three-layer model mentioned above with Eqns. 3.54 and 3.55. Combined with measurements of T and R for the film+substrate, we can determine the optical constants $\sigma_1(\omega)$ and $\sigma_2(\omega)$.

For Glover-Tinkham analysis, the assumption is that the T and R are of approximately equal; however, if this is not the case, and the R is of dominant importance, say $T < 10\%$ (strictly $T = 0\%$), then the appropriate method of analysis is through Kramers-Kronig transformation.

3.1.6 Kramers-Kronig Analysis and Sum Rules

The dielectric function can be derived by Kramers-Kronig transformation of the reflectance spectrum measured over a wide (strictly ∞) frequency range. The reflectivity is defined as:

$$r = \frac{E_r}{E_i} = \frac{N_a - N_b}{N_a + N_b}, \tag{3.63}$$

where N_a and N_b are refraction indices of mediums a and b. When the light is incident from vacuum onto a sample surface at normal incident, N_a=1, and N_b=N=n+$i\kappa$, the power reflectance is given by

$$R(\omega) = rr^* = \frac{(1 - n)^2 + \kappa^2}{(1 + n)^2 + \kappa^2}. \tag{3.64}$$

The reflectance $R(\omega)$ and phase-dispersion shift $\phi(\omega)$ are related by Kramers-Kronig transformation [346, 404, 405, 406, 407, 408]:

$$\phi(\omega) = \frac{\omega}{\pi}\int_0^\infty \frac{lnR(\omega) - lnR(\omega^{'})}{\omega^{'2} - \omega^2} d\omega^{'}. \tag{3.65}$$

Since reflectivity

$$r = \sqrt{R}e^{i\phi}, \tag{3.66}$$

and combining Eqs. 3.64, 3.65, and 3.66, n and k can be determined by $R(\omega)$ and $\phi(\omega)$ as[409, 378, 410]

$$n(\omega) = \frac{1 - R(\omega)}{1 + R(\omega) - 2\sqrt{R(\omega)}cos\phi(\omega)} \tag{3.67}$$

$$\kappa(\omega) = \frac{2\sqrt{R(\omega)}sin\phi(\omega)}{1 + R(\omega) - 2\sqrt{R(\omega)}cos\phi(\omega)}. \tag{3.68}$$

Then from Eqs. 3.9 and 3.14, the real part of dielectric function and the optical conductivity can be determined:[355, 356]

$$\epsilon_1 = n^2 - k^2 \tag{3.69}$$

$$\begin{aligned}\sigma_1 &= \frac{\omega\epsilon_2}{4\pi} \\ &= \frac{\omega nk}{2\pi}.\end{aligned} \tag{3.70}$$

All of these optical constants are frequency (ω) dependent. In Eq. 3.65, the integration is from zero to ∞. Since our optical measurements usually cover the frequency

range from far-infrared to ultraviolet, proper extrapolations should be used. In this dissertation, a constant conductivity is chosen for semiconductor in the low frequency range. Otherwise a Hagen-Rubens relation $R(\omega) = 1 - (2\omega/\pi\sigma_0)^{1/2}$ would be chosen for metals,[411] and a Lorentzian would be used to fit for an insulator.[412, 413] In the high frequency regime, the optical response is modeled as $R \approx \omega^{-\alpha}$, where α varies from 0-4 and can be determined by comparing the absorption and calculated optical conductivity.[414, 415]

Together with physical arguments about the behavior of the response in certain limits, the Kramers-Kronig relation can also be used to derive sum rules.[416, 417] That is

$$\int_0^\infty \omega' Im(-1/\epsilon(\omega'))d\omega' = 1/2\pi\omega_p^2, \tag{3.71}$$

where ω_p is the plasma frequency. A partial sum rule [346] is also useful in quantifying the change of absorption spectra

$$f \equiv \frac{2c}{N_e \pi \omega_p^2} \int_{\omega_1}^{\omega_2} n\alpha(\omega, B)\, \mathrm{d}\omega. \tag{3.72}$$

Here, f is the oscillator strength, N_e is the number of electrons per magnetic ion site, n is the refractive index, ω_p is the plasma frequency$\equiv\sqrt{\frac{e^2\rho}{m\epsilon_0}}$, e and m are the charge and mass of an electron, ϵ_0 is the vacuum dielectric constant, ρ is the density of magnetic ion sites, c is the speed of light, and ω_1 and ω_2 are the frequency limits of integration.

Importantly, optical methodologies are typically non-intrusive, and can be performed with other experimental variables such as magnetic field, electric field, tem-

perature, and pressure. With these stimuli, optical spectroscopy provides foundational microscopic insight into the electronic and magnetic structures of complex oxides.

3.2 Transport

Fundamentally transport measurements give an extension to the optical conductivity at the zero frequency limit (dc). To get a deeper understanding of this probing technique one needs to have a working knowledge of Fourier transforms, basic quantum mechanics, equilibrium (quantum) statistical mechanics, band theory of solids, and material phenomenology such as transport in metals. These will be included in the chapter for photoconductivity (Ch. 7.) Transport can be useful in establishing understanding between dc and the high-frequency regime one investigates for a given material. This can be achieved by sweeping across the frequency axis, but of course when one steps away from dc the equation becomes inherently complex (i) due to frequency dependence. We will start by briefly deriving the conductivity at dc (static),

$$-\nabla V = \vec{E}, \tag{3.73}$$

$$\vec{j} = \sigma \vec{E}. \tag{3.74}$$

Where the electric field $\vec{E}$ is the Coulomb force per unit charge,

$$\vec{E} = \frac{1}{4\pi\epsilon_0}\frac{q}{r^3}\vec{r}. \tag{3.75}$$

In Eq. 3.73 one considers that the voltage Φ is a gradient across a circuit element, creating an electric field $\vec{E}$. The $\vec{E}$ drives an electron current seen in Eq. 3.74 as $\vec{j}$ and produces the material dependent quantity of conductivity σ. Now that we have established the fundamental result of applying a voltage gradient. We will consider an electric field varying slowly in space and sinusoidally in time, $\vec{E}(t) = \vec{E}\cos(\omega t)$. When applying this to a bulk solid, the current density $\vec{j}$ expressed in Eq. 3.74 evolves, to first order, into the following:

$$\vec{j}_\alpha(t) = \sigma^1_{\alpha\beta}\vec{E}\beta\cos(\omega t) + \sigma^2_{\alpha\beta}\vec{E}\beta\sin(\omega t). \tag{3.76}$$

First to simplify let us remove the anisotropic dependency, tensor notation, of the conductivity $\sigma_{\alpha\beta}$ so it looks like σ. An equivalent form of Eq. 3.76 is shown by $\vec{j}(t) = \mathrm{Re}[\sigma(\omega)\vec{E}\exp -i\omega t]$ with a complex conductivity $\sigma = \sigma_1 + i\sigma_2$. To clarify, the real part of the the complex conductivity denotes the in-phase (dissipative) and the imaginary part denotes the out-of-phase (reactive) response to the $\vec{E}$ field.[418] The frequency and time domains are related by conventional Fourier transforms, such as:

$$\vec{E}(t) = \int_{-\infty}^{\infty} \frac{d\omega}{2\pi}\vec{E}(\omega)\exp -i\omega t \tag{3.77}$$

$$\vec{E}(\omega) = \int_{-\infty}^{\infty} dt\vec{E}(t)\exp\{i\omega t\}. \tag{3.78}$$

The total conductivity σ which is comprised of the dc and ac (frequency depen-

dent) components can independently be represented by the following:[419, 420]

$$\begin{aligned}\sigma &= \sigma_{dc} + \sigma_{ac} \\ &= \sigma_{dc} + \epsilon_0 \omega \epsilon^2(\omega).\end{aligned} \tag{3.79}$$

The deeper intricacies of the latter form can be explored through Table 3.2. From a functional standpoint transport measurements reach a limit governed by the intrinsic noise level of the method Fig. 3.6, voltage noise is represented by the following equation:

$$N_V = \sqrt{(}r \times \Gamma \times T) \tag{3.80}$$

To approach this limit, instrumentation with far more sensitivity than a standard digital multimeter must be used.

The method of transport in this dissertation primarily focuses on photoconductivity. We can build a gedanken experiment that shows the displacement of the excitonic components (electrons and holes) and allows one to understand the increase in measured current. This thought experiment goes as the following: starting with the unperturbed system with the electrons in their equilibrium positions we excite an electron into the conduction band and thus create an exciton, of course with out the presence of an external field the exciton recombines, effectively, immediately. Now we apply an external field and measure the conductivity. After some time we excite the electron, again creating the electron-hole pair, and the displacement, before recombination, is added to the measured conductivity. This displacement is

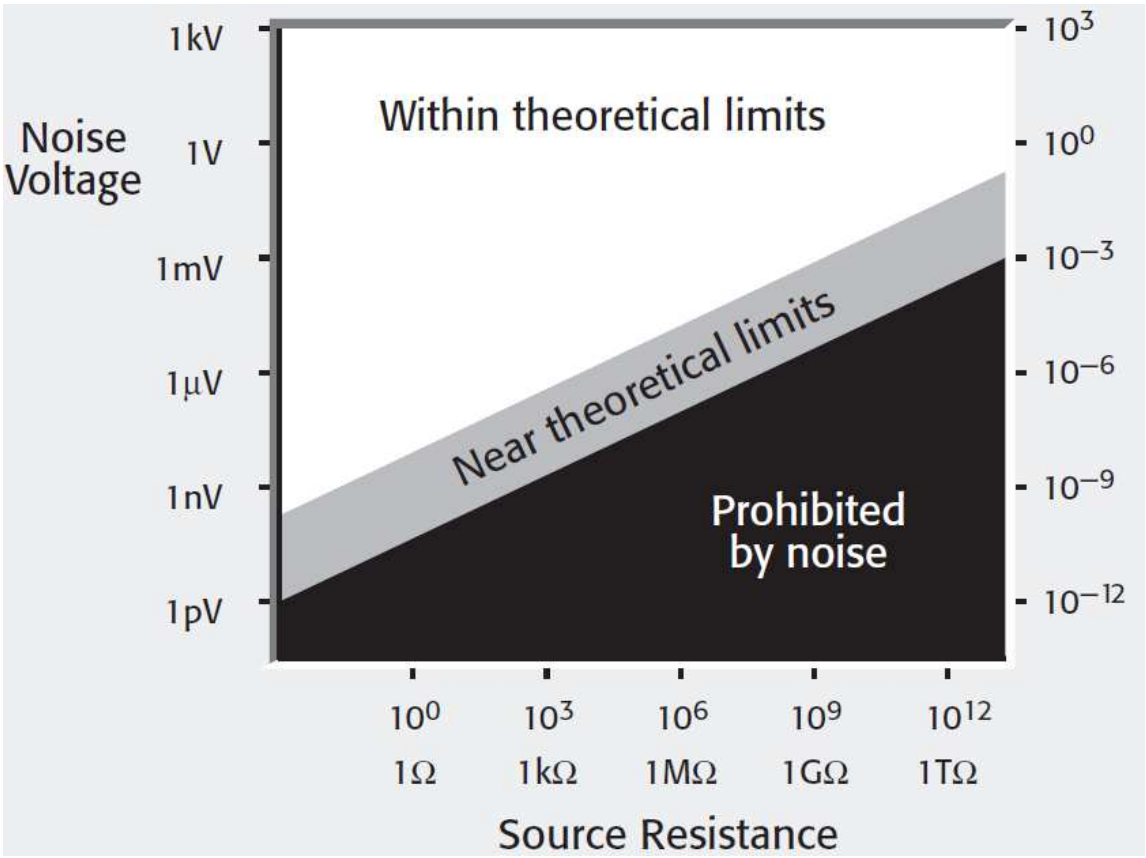

Figure 3.6: Theoretical limit for transport measurements, after [421].

a physical separation of the excitonic components and thus increases the effective exciton radius. The difference in current can be expressed as

$$I_{total} = I_{off} + I_{ph}. \tag{3.81}$$

Where I_{total} represents the total current, I_{off} represents the current with the lights off, and I_{ph} represents the current with the circuit element (sample) having light shown on it. This leads to rearranging the equation, expressing the difference between

total (on) and off as

$$I_{ph} = I_{total} - I_{off}. \tag{3.82}$$

We repeat this process, measuring the I–V curves for on and off scenarios for the necessary energy slices chosen by using bandpass filters.

Conductance is yet another valuable subset of information that can be garnered from this measurement. The value of this is such that the

$$G = \frac{dI}{dV}. \tag{3.83}$$

In the materials considered within this dissertation this should appear as an approximately straight line, but a discontinuity appears at 0 V as expected, and anomalies at the gap voltage. This can be understood by relating the gap to a tunneling barrier, where the height is the E_g and its thickness is equivalent to $E_g/e|\vec{E}|$, where $|\vec{E}|$ is the magnitude of the electric field. Overall this looks like

We also implemented a magnetic field to manipulate the response and acquire further evidence in regards to the correlation and nature of spin related excitations. This grants access to several valuable and probing relationships of the optical and physical properties, such as the magnetoresistance. Even though magnetoresistance has been theoretically predicted and experimentally measured in photoconductive measurement previous to our setup,[422, 423, 131, 424] no one has established a coupling beyond the following traditional definition:

$$MR\% = 100 \times \frac{\rho_H - \rho_0}{\rho_0}. \tag{3.84}$$

Here, ρ_H represents, where $\rho = 1/\sigma$, the sample resistance in a magnetic field , whereas ρ_0 represents the sample resistance in the absence of a magnetic field. We show in Sec. 3.2.1 that the opportunity to take the analysis one step deeper presents coupling of the photons and magnetic field.

3.2.1 Transport analysis

Since we are doing photoconductivity we need to determine the amount of current generated by shining light on the sample I_{ph} but first we need to measure the dark current I_{dark}. To obtain this information we do two separate measurements, in close time so as to limit the amount of drift within the system due to uncontrolled parameters, resulting in the following relationship

$$I_{total} = I_{off} + I_{ph}. \tag{3.85}$$

Here, I_{total} represents the total current produced by the dark current and the photon induced current. By rearranging 3.85 equation, we are able to isolate the photocurrent level:

$$I_{ph} = I_{total} - I_{off}. \tag{3.86}$$

Now we have the photocurrent, this value corresponds to $\sigma_{pc}AE$. In the aforementioned relationship A is the cross-sectional area of the sample and $\vec{E}$ is the electric

field $\vec{E} = V/L$ (actually a vector), with V being the voltage and L being the distance between electrodes. The next step is to convert the value of I_{pc} to photoconductance (Eqn. 3.88 or photoconductivity (Eqn. 3.87), depending upon if the pathlength l of the particular circuit element is known but in our case we can assume that it is the distance between the electrodes. We also need to know the power density,

$$\sigma_{pc} = \frac{I_{pc}}{(P/A)} \tag{3.87}$$

$$\sigma_{pc} = \frac{\frac{I_{pc}}{(P/A)}}{V}. \tag{3.88}$$

3.2.2 Magnetotransport

Having a basic understanding of electronic structure for ferromagnetic transition metals, and alloys, is a necessary requirement to understanding electron transport in the effort to produce spin-polarized current. One well known mechanism for the production of spin-polarized current emerges from the incorporation of circularly polarized light. This occurs because the spin angular momentum of light corresponds to the helicity induced by the right- and left-circularly polarized light from a paraxial beam, Poynting vector $\vec{P}$ is parallel to the the wavevector $\vec{k}$.[85, 425, 426, 427] To express this correlation, if the mean momentum of the beam can be defined as $\langle\vec{k}\rangle$, then the beam will carry spin angular momentum

$$\langle\vec{S}\rangle = \frac{\sigma\langle\vec{k}\rangle}{k} \tag{3.89}$$

Here, the positive and negative $\sigma = \pm$ correspond to right- and left-handedness (helicites) of the photons polarization and $\langle\vec{k}\rangle$ is the mean momentum or, more precisely, the mean wave vector of the beam.[428, 429] When considering the physics of paraxial-beam optics[430, 431, 373, 432, 433] and quantum mechanical aspects of photons,[434, 435, 436, 437, 438, 439] it is well known that the spin angular momentum of light aligns with the propagation direction of the beam.[440, 441, 442, 443, 444] The spin angular momentum of photons arises from the optical polarization (electric vector rotates with respect to time), e.g. elliptical or circular polarization, where each photon of circularly polarized light carriers a spin angular momentum $= \hbar$. Whereas, the orbital angular momentum emerges from the spatial field distribution namely helically phased wavefronts. The beam making up the orbital angular momentum has an azimuthal phase dependence of $\exp(im\varphi)$, where φ is the azimuthal angle and m is the angular momentum index. The orbital angular momentum is quantized for each helically phased beam as $m\hbar$ per photon.[373, 445, 446] Looking at Fig. 3.7 for an example, one sees the two-current model. In this model electrons with different quantum mechanical spins contribute to the total resistance in two channels connected in parallel.[47, 48, 447, 448, 449, 450, 451] This model assumes that electrons with different spins inherently have a variation in their distribution functions and relaxation times.[452] For instance if we compare the electronic structures for Cu and *fcc* Co, in this case we will discuss the DOS as shown in Fig. 3.8. In the case of copper, the majority and minority channels will be identical; therefore, the net spin moment is zero. Upon switching to cobalt, the majority and minority DOS differ, as is shown in the right panel of Fig. 3.8. The area above the axis

represents the majority channel (spin "up") and the area below the axis represents the minority channel (spin "down"). When considering the valence states, it is clear that the majority density of states (DOS) has a greater area under the curve than the minority DOS, below the Fermi energy E_F. This can be approximated as a shift downward in energy for the majority relative to minority; the shifting is commonly known as the spin-splitting energy. In the case presented here the spin-splitting energy is approximately 1.5 eV. If one integrates the majority (minority) curve below E_F, the total number of valence electrons for each spin is given. Then upon taking the difference of these values, the net spin magnetic moment per Co atom is 1.6 μ_B.[453]

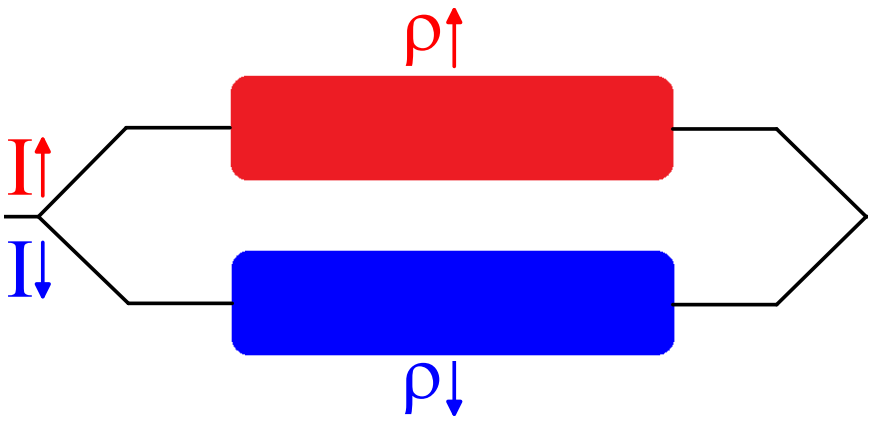

Figure 3.7: Shows the two-current model of a ferromagnetic material, strictly for a ferromagnetic metal.

To convert this information from a qualitative to quantitative approach we will evaluate a few constitutive equations:

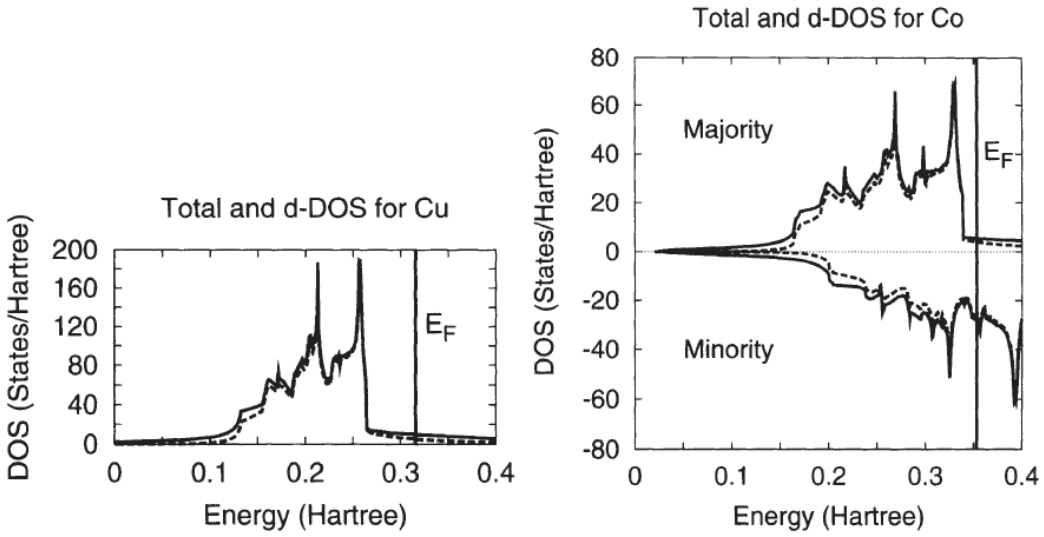

Figure 3.8: Electronic DOS for copper (left) and for *fcc* cobalt (right). The dashed lines present the *d*-component of the density of states. Figure after [453]

$$MR\% = 100 \times \frac{\rho_H - \rho_0}{\rho_0} \tag{3.90}$$

Here, we see how the transport properties of a material responds to an applied magnetic field by a change in the magnetoresistance $MR\%$. A variety of different physical mechanisms give rise to the MR effect.[422] In bulk manganite crystals, MR occurs because of magnetic phase separation;[454, 455] however, in the case of spin valve and tunneling structures MR emanates from phenomena invoked by spin-dependent scattering and tunneling.[456, 283] Additionally, a few MR phenomena are related to manipulating spin-polarized currents influenced by the spin-orbit (SO) interaction, specifically, the spin Hall[457, 458] and Rashba [459] (or Dresselhaus effects).[460, 422, 461] Critically, the above does not incorporate the fact that we use

a light source to manipulate the current beyond traditional MR.

$$MPR\% = 100 \times \frac{(\rho_{H,h\nu} - \rho_{H,0}) - (\rho_{0,h\nu} - \rho_{0,0})}{(\rho_{0,h\nu} - \rho_{0,0})} \tag{3.91}$$

$$MPR\% = 100 \times \frac{(\rho_{H,h\nu} - \rho_{0,0}) - (\rho_{0,h\nu} - \rho_{0,0})}{(\rho_{0,h\nu} - \rho_{0,0})} \tag{3.92}$$

$$MPR\% = 100 \times \frac{(\rho_{H,h\nu} - \rho_{0,h\nu})}{(\rho_{0,h\nu})} \tag{3.93}$$

$$MPR\% = 100 \times \frac{(\rho_{H,h\nu} - \rho_{0,h\nu})}{(\rho_{0,0})} \tag{3.94}$$

$$MPR\% = 100 \times \frac{(\rho_{H,h\nu} - \rho_{0,h\nu} - \rho_{0,0})}{(\rho_{0,0})}. \tag{3.95}$$

In these five equations, $\rho_{H(0),h\nu(0)}$ tells if the measured resistance corresponds to magnetic field being on (H) (off (0)) and if the light is on ($h\nu$) (off (0)). To clarify the correctness (incorrectness) of each equation, we will assign values for the components as shown in Table 3.3.

Table 3.3: Assinging values for equation components

Component	Value
$\rho_{H,h\nu}$	50
$\rho_{0,h\nu}$	100
$\rho_{H,0}$	200
$\rho_{0,0}$	300

Each equation [eqs. (3.91) to (3.95)] has a logical origin, to be explained now. We will start with the simplest versions [eqs. (3.93) and (3.94)] and build our way outwards. In these, we see that the relationship is akin to Eqn. 3.90 but with the switching action of the magnetic field and light, not just magnetic field, the resulting values are $(50-100)/100 = -50\%$ and $(50-100)/200 = -25\%$. Now to consider Eqn. 3.95, this suggests removing the dark resistance with no magnetic field, included in each other resistance. Here, the value is $(50-100-300)/300 = -116\%$. Continuing on to Eqn. 3.92, in principle this should effectively result in a similar value to Eqn. 3.95 because of subtracting off the background, $(50-300)-(100-200)/(100-200) = 150\%$. The difference appears because of the denominator subtraction. Finally we will take a look at Eqn. 3.91, the logic behind this equation is to separate out the contribution from each component of the total measurement. If step back for a moment and look at the total measurement and what it consists of we get the following:

$$\rho_{H,h\nu} = \rho_{H,0} + \rho_{0,h\nu} + \rho_{0,0}. \tag{3.96}$$

So, from the above we can see that is necessary to include each component of the measurement to obtain the MPR that corresponds to the pure magneto-photoresistance. Following through, we obtain $((300-100)-(200-50))/(200-50) = 33.\bar{3}\%$. Again it is important to reiterate that the values used here are in no way representative of measurement values; however, the values are representative of the experimental trends where the resistance reduces with the application of magnetic field and optical field.

3.3 Spectrometers

3.3.1 Perkin-Elmer λ-900 Spectrometer

The near-infrared/visible/ultraviolet spectra in this dissertation were measured on the Perkin-Elmer λ-900 spectrometer. The Perkin-Elmer λ-900 spectrometer features an all-reflecting, double-monochromator, double-beam optical system. The energy range covered by the λ-900 spectrometer is 3300-190 nm ($\sim$ 3000-52000 cm^{-1}). The spectrometer is operated under nitrogen purging. The optical system is depicted schematically in Fig. 3.9.

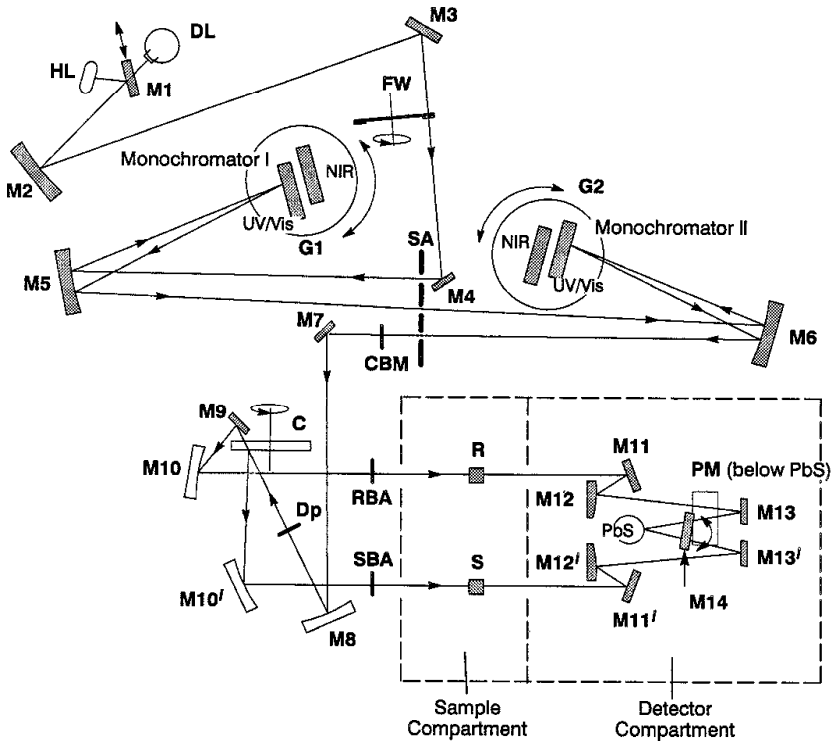

Figure 3.9: Optical layout of Perkin-Elmer λ-900

Table 3.4: λ-900 operating parameters

Range (cm^{-1})	Source	Monochromator	Detector	Polarizer
3100-14250	Halogen Lamp	1200 lines/mm	PbS	Glan-Thompson prism
11240-31330	Halogen Lamp	1200 lines/mm	Photomultiplier	Glan-Thompson prism
31330-52000	Deuterium Lamp	2400 lines/mm	Photomultiplier	Glan-Taylor prism

There are two radiation sources, a deuterium lamp and a halogen lamp. The latter lamp is used for near-infrared and visible range, whereas the former lamp is used for ultraviolet range. Source change is controlled by flipping mirror M1. The radiation of source is reflected by mirror M2, M3, and passes optical filter FW. Then, the beam is brought in monochromator I through M4, slit SA, and M5. Depending on the desired wavelength range, the collimated radiation beam strikes either the 2400 lines/mm grating or the 1200 lines/mm grating. The rotation position of the grating effectively selects a segment of the spectrum, reflecting this segment to mirror M5, to go through the exit slit, and enter Monochromator II. The advantage of the double-monochrometer is to maintain high spectral purity with an extremely low stray radiation content. The automatic grating change during monochromator slewing avoids the time-consuming re-alignment of the optics pathway due to the monochromator change.

The double beam is achieved via the chopper assembly C. As the chopper rotates, a mirror segment, a window segment and two dark segments are brought alternately into the radiation beam. When a window segment enters the beam, radiation passes through to mirror M9 and is then reflected via mirror M10 to create the reference

beam (R). When a mirror segment enters the beam, the radiation is reflected via mirror M10′ to form the sample beam (S). When a dark segment is in the beam path, no radiation reaches the detector, permitting the detector to create the dark signal (D). Then, the measured spectrum is expressed as

$$spectrum = (S - D)/(R - D).$$

Two detectors are used in the Perkin-Elmer λ-900 spectrometer. A lead sulfide (PbS) detector is used in the near-infrared range while a photomulitplier (PM) is used in the Ultraviolet/Visible range. Detector change is automatic by rotating mirror M14 during scans.

3.3.2 Reflectance Stages

To measure the absolute reflectance spectrum, a reflectance stage (as shown in Fig. 3.11) is used to bring the near normal incidence ($< 6°$) light to a solid sample or reference mirror. [409, 410] An aluminum mirror is usually used as a reference material to obtain a baseline scan, then the reflectance spectrum of the sample is measured relative to the baseline. The absolute reflectance spectrum of the sample is obtained by renormalizing the measured spectrum with absolute Al mirror reflectance, as shown in Fig. 3.10.

Anisotropic materials and polarizers

The optical theory outlined in Section 3.1 is based on Maxwell's equations 3.1–3.1 and Eqs. 3.6–3.8. The Eqs. 3.6– 3.8 are the material equations for an isotropic

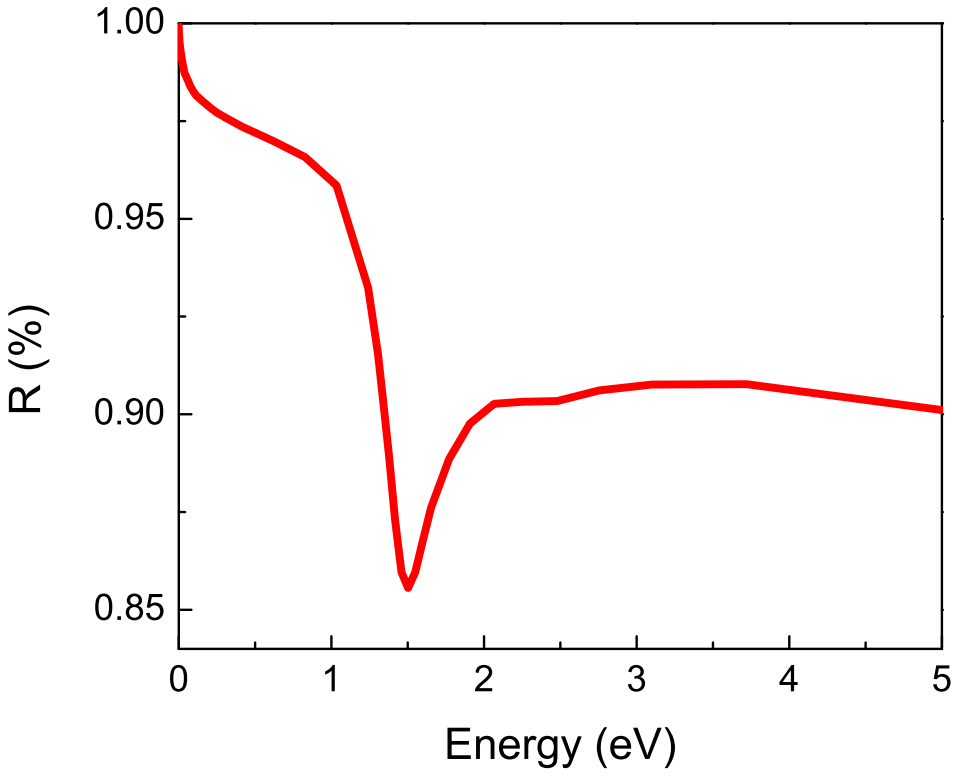

Figure 3.10: Reflectance spectrum from an aluminum mirror.

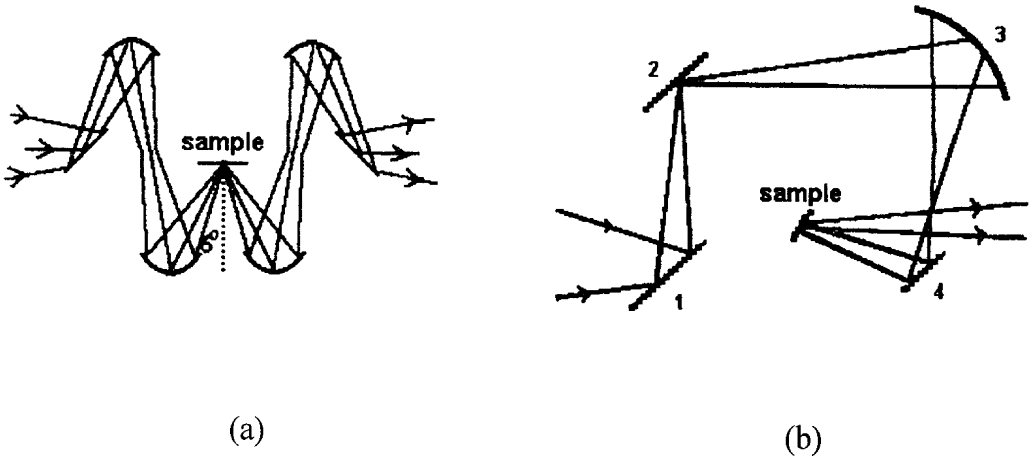

Figure 3.11: Reflectance set-up for (a) Bruker IFS 113v FTIR and (b) Perkin-Elmer λ-900

medium. In an anisotropic crystal, $\vec{D}$ and $\vec{E}$ are related by the following form:

$$D_x = \epsilon_{xx}E_x + \epsilon_{xy}E_y + \epsilon_{xz}E_z, \tag{3.97}$$

$$D_y = \epsilon_{xy}E_x + \epsilon_{yy}E_y + \epsilon_{yz}E_z, \tag{3.98}$$

$$D_z = \epsilon_{zx}E_x + \epsilon_{zy}E_y + \epsilon_{zz}E_z. \tag{3.99}$$

The nine quantities ϵ_{xx} ϵ_{xy}, ... are constants of the medium, and constitute the dielectric tensor. It is always possible to find a set of axes, *the principle dielectric axes*, such that the complex dielectric tensor can be put into diagonal form, i.e.,[462]

$$\overleftrightarrow{\epsilon}(q,\omega) = \begin{vmatrix} \epsilon_{xx} & \epsilon_{xy} & 0 \\ -\epsilon_{xy} & \epsilon_{yy} & 0 \\ 0 & 0 & \epsilon_{zz} \end{vmatrix}. \tag{3.100}$$

Along the principle axes, $\vec{D}$ and $\vec{E}$ have the same directions. Since the dielectric tensor varies with frequency, the directions of the principal axes may also vary with frequency. This dispersion of the axes can arise only in crystals with monoclinic and triclinic symmetry. In the reflectance experiment on single crystals, the principal axes can be determined by considering the crystal shape and measuring the polarization dependence of the reflectance response.

To find the dielectric tensor along the principle axes of the single crystals, a polarized electric field of the light $\vec{E}$ is required. The polarized light is obtained by inserting a polarizer in the path of the beam. Several polarizers are used to cover the spectral range from far-infrared to ultraviolet. In the infrared, the polarizers used are made of a gold wire grid, vapor-deposited on polyethlylene (far-infrared) or silver bromide substrates. Wire grid polarizers implement the response of the material to emit an electric field A set of plastic Polaroid film polarizers are used for the infrared microscope. In the near-infrared/visible/ultraviolet range, dichroic Glan-Thompson and Glan-Taylor polarizers are used for Perkin-Elmer λ-900.

3.3.3 Magneto-optical properties

As we have already seen, the displacement vector is proportional to the electric field vector, $\vec{D} = \epsilon\mu\vec{E}$, where all elements are dependent on ω. In traditional optical circumstances the magnetic permeability is considered to be unitary $\mu = 1$ and the off-diagonal components of the dielectric tensor equal 0 $\epsilon_{ij\neq i=j} = 0$, thus μ was not included previously. However, in the case of magnetic materials or in a magnetic field these components no longer exist as spectators, they participate and/or dominate

the light-matter interactions.[463, 464] If we consider expanding Eq. 3.2 ($\hat{H}(t) = \hat{H}_0 + \hat{V}(t)$) to incorporate the perturbation induced by the magnetic field applied parallel (anti-parallel) to the propagation direction of the light, the perturbating operator $\hat{V}(t)$ becomes:

$$\hat{V}(t) = -E_0(\vec{i}_E\hat{m}) - B_0(\vec{i}_B\hat{\mu}) - \frac{\nabla E_0}{2}(\vec{i}_z \cdot \hat{Q} \cdot \vec{i}_E) - B_{ext}(\vec{i}_z\hat{\mu}). \tag{3.101}$$

Here, $\hat{m}$ is the electric dipole moment operator, $\hat{\mu}$ is magnetic dipole operator, $\hat{Q}$ is electric quadrupole operator, and the values $\vec{i}_E, \vec{i}_B$, and $\vec{i}_z$ are the unit vectors such that the unit vector in the direction of the magnetic component of the field is given by $\vec{i}_B = \vec{i}_E \times \vec{i}_z$.[341] The moment operators are defined respectively by

$$\hat{m} = \sum_i q_i\vec{r}_i \tag{3.102}$$

$$\hat{\mu} = \sum_i \frac{q_i}{2m_i}(\vec{r}_i \times \vec{p}_i) \tag{3.103}$$

$$\hat{Q} = \sum_i q_i\vec{r}_i\vec{r}_i. \tag{3.104}$$

The diagonal terms for this tensor are even in $\vec{M}$, thus independent of the $\vec{M}$. This describes typical optical response of a nonmagnetic solid material. However, the off-diagonal positions are odd with respect to $\vec{M}$, thus to the first order they are proportional to $\vec{M}$. The ratio for the off- and on-diagonal components in the visible and ultra-violet frequency range is of the order $10^3 - 10^{-2}$, and this is the cause of magneto-optical properties such as the Kerr and Faraday effects, depending upon the change in ellipticity of polarized light. This description extends to the soft-x-ray

frequency regime as well. [465, 466] In an absorbing medium the tensorial components of ϵ become complex, $\epsilon_{ij} = \epsilon_{1,ij} + i\epsilon_{2,ij}$. The absorptive part of the diagonal tensor components $\epsilon_{2,xx}$ is proportional to the sum of RCP and LCP photons,

$$\epsilon_{2,xx} = \alpha_R + \alpha_L. \tag{3.105}$$

However, the absorptive portion of the off-diagonal dielectric tensor components $\pm\epsilon_{1,xy}$ is proportional to the difference of RCP and LCP.[467]

$$\epsilon_{1,xx} = \alpha_R - \alpha_L. \tag{3.106}$$

The inversion of role for the real and imaginary portions in describing the absorption results from a dependence of $\epsilon_{2,xy}$ on the spin-orbit coupling and it is an imaginary operator itself. [466, 468] This corresponds to the Onsager relations, these say that the diagonal components are even in time or with respect to the $\vec{M}$, where as the off-diagonal are odd in time or $\vec{M}$.[378, 469, 470, 471] All of these values interchange, with regards to the imaginary and real components, if one shifts concerns to the optical conductivity σ_{ij}. In the magneto-optical work contained in this thesis we have performed magnetic circular dichroism (MCD). The difference from the Faraday effect being, that instead of being concerned with the real part of the off-diagonal components, MCD is proportional to the imaginary part of the off-diagonal components in the dielectric tensor and can be summarized by the following

relationship:[472, 126, 467]

$$MCD = \frac{T^+ - R^-}{T^+ + T^-} = -\frac{\chi''_{xy}}{n(n^2-1)}, \tag{3.107}$$

where

$$\chi''_{xy}(\omega) = -\frac{1}{4V\hbar}\sum_{v,c}(\rho_v - \rho_c) \times (|M_+|^2_v c - |M_-|^2_v c)\frac{(\omega_c - \omega_v - \omega)}{(\omega_c - \omega_v - \omega) + \Gamma^2}. \tag{3.108}$$

Here, ρ_c and ρ_v represent the density functions of the conduction and valence bands, respectively, $|M_+|^2_v c$ and $|M_-|^2_v c$ are the squared dipolar transition matrix elements for the σ^+ and σ^- photon polarizations, respectively.[473] When the probing frequency ω approaches a critical point in the band structure $|M_+|^2_v c$ and $|M_-|^2_v c$ increase in proportion with E_g^+ and E_g^-, respectively, in accordance with the Kane $k \cdot p$ perturbation theory.[474] In this sense, E_g^+ and E_g^- are the band gaps, interband transition gaps, for the two optical helicities, σ^+ and σ^-. Importantly, the Lorentzian form of the third term in Eqn. 3.108 requires that the MCD signal decreases rapidly as ω departs from the excitation. Classically, Faraday rotation was typically measured using a single wavelength, whereas we measure across multiple wavelengths to obtain a spectrum. As a rule of thumb, dichroism can only exist if the symmetry does not contain a component that reverses one measurable observable but leaves the remaining portion of the system unchanged. Taking the Faraday effect as an example [Fig. 3.13], when imposing the time reversal operator inverts the direction of light propagation and the magnetization, by that the entire physical

system is returned invariant. Due to being time non-invariant, non-reciprocal optical effects put forward magnetic moments. To clarify non-reciprocal optical effects in a more succinct manner we must first approach reciprocity, a schematic depicting the nature of optical reciprocity is shown in Fig. 3.12. Reciprocity is governed by a law

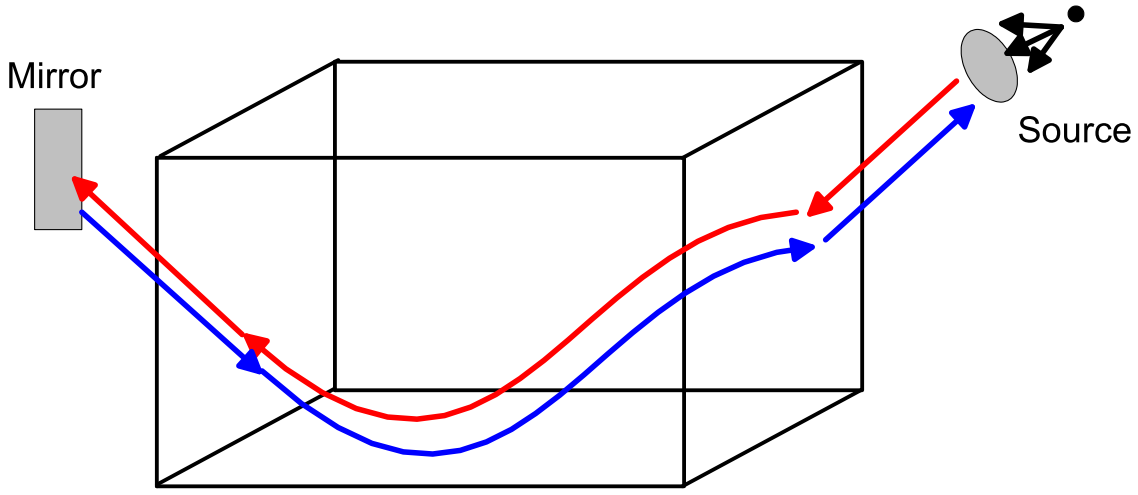

Figure 3.12: Shown here is a schematic depicting optical reciprocity. The path traced by a electromagnetic ray propagating through a "normal" material will be followed in reverse upon reflection of the light. This suggests that the path integral will also be equivalent upon reversing the sign.

stating that the total Hamiltonian of the system illuminated should be time-reversal T invariant.[475, 476, 477, 478, 479] this has been proven to exist in fields such as statistical mechanics, quantum mechanics, and electromagnetism.[194, 480] This suggests that when the time-reversal transformation is applied to a macroscopic state $\{t\}$

produces the equivalent state $\{-t\}$, as shown in the following relationships:[481, 482]

$$-\hat{H}(t) = \hat{H}(-t) \tag{3.109}$$

and

$$\int \vec{j}_1(\vec{r}) \cdot \vec{E}_2(\vec{r}) d\vec{r} = \int \vec{j}_2(\vec{r}) \cdot \vec{E}_1(\vec{r}) d\vec{r}. \tag{3.110}$$

These relationships are also shown schematically in Fig. 3.14. In EM radiation Eqn. 3.110 holds valid even for lossy media.[194, 482] However, when an internal (Weiss) magnetic field is present the states are not equivalent,$\{t\} \neq \{-t\}$, upon reversal of direction or a polarizing magnetic field and out of this arrives non-reciprocal effects because T reversal is spontaneously broken.[481, 483, 484, 485, 486, 487, 371, 488, 489, 490] To finish up an explanation of reciprocal optical effects it is best to consider the idea of degeneracy. Considering the case of circularly polarized modes that are eigenmodes for an optically active medium, such as quartz. If we consider the right-circularly polarized mode to be propagating forward, then upon time-reversal the backward propagating mode will also be right-circularly polarized. In this inversion of symmetry one introduces mode degeneracy. This emerges from a general association between symmetry and degeneracy.[492, 480, 493, 494] Therefore, in an optically active medium the circularly polarized modes propagate forwards and backwards at the same velocity. However, in a magneto-optical medium a similar connectivity between time-reversal and degeneracy emerges. The caveat for this case is that the velocity only remains the same for the counter propagating waves if the magnetization of the medium is simultaneously reversed. Thereby, time-reversed waves with a fixed

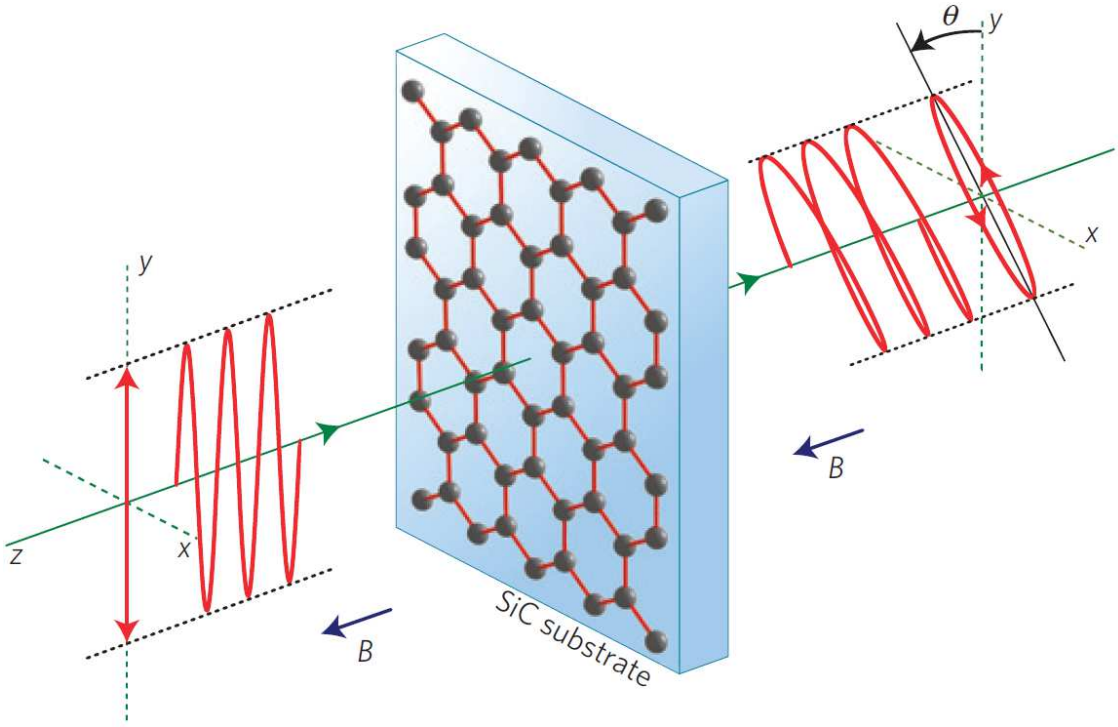

Figure 3.13: Shown here is a schematic depicting the Faraday effect (or Faraday rotation) due to a sheet of graphene on SiC, after [491].

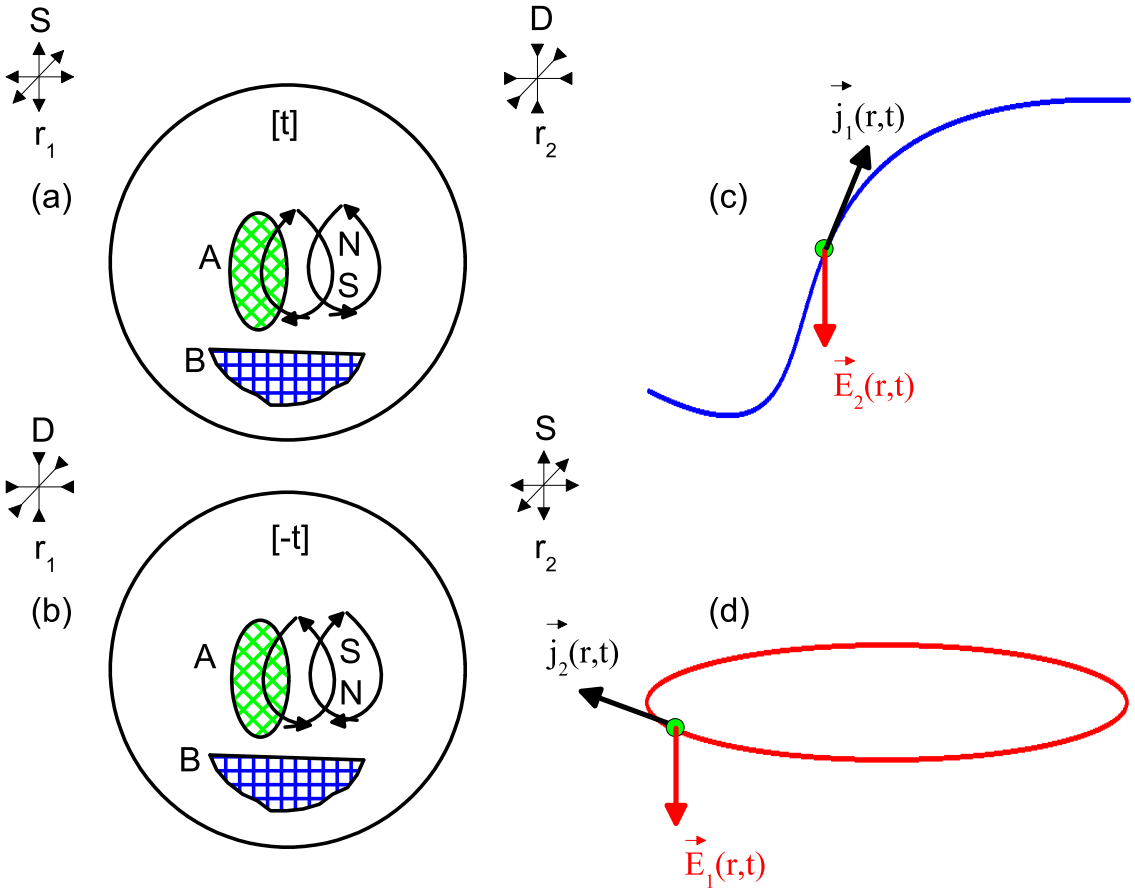

Figure 3.14: The schematic depicted here shows the formulation of the reciprocity law. In (a) the electromagnetic radiation propagates from left to right $\{t\}$, whereas in (b) it propagates from right to left $\{-t\}$. The intensity measured in (a) $I_{21}(\{t\})$ is the same intensity as that measured in $I_{12}(\{-t\})$. (c) and (d) display a schematic of two currents $\vec{j}_i$ and the electric fields $\vec{E}_i$ induced by $\vec{j}_i (i = 1, 2)$. The curves indicate the location where the current exits.

direction magnetization are no longer degenerate and, accordingly, a non-reciprocal propagation is in induced within this portion of the system.[480] Moreover, MCD belongs to this category of effects and because a magnetic moment is a product of the non-reciprocal optical effect it does not have to be measured in materials containing net magnetic moments, ferro- and ferrimagnets.[495, 496, 481, 497, 294, 498] The data acquired through MCD offer keen importance because they aid in the investigation for intricate details of the electronic structure along with the static and dynamic processes in magnetic and non-magnetic materials alike. When considering the roots of MCD response, two routes are available for response emergence: (i) application of an external field (ii) exchange-coupled intrinsic magnetizaiton.[64] These are exemplified by Fig. 3.15.

It is important to note that expressions for material properties can be derived by expansion of the optical activity tensor and through this expansion one can obtain the geometrical relation between different measurable quantities.[489] For additional generalization about related optical effects, such as optically induced magneto-electricity, look at Table 3.5. For a list of geometrically related measurable quantities that can be obtained via expansion of the optical activity tensor see Table **??**. To develop an understanding of the physical meaning behind the dielectric tensor, the power P absorbed by the sample volume fraction V illuminated is expressed as:

$$P(\omega, t) = -\int_V d^3r \frac{d}{dt}\vec{D}(\omega, t)\vec{E}(\omega, t). \tag{3.111}$$

Since MCD requires right- and left-circularly (RCP and LCP) polarized light, we need to express those as well

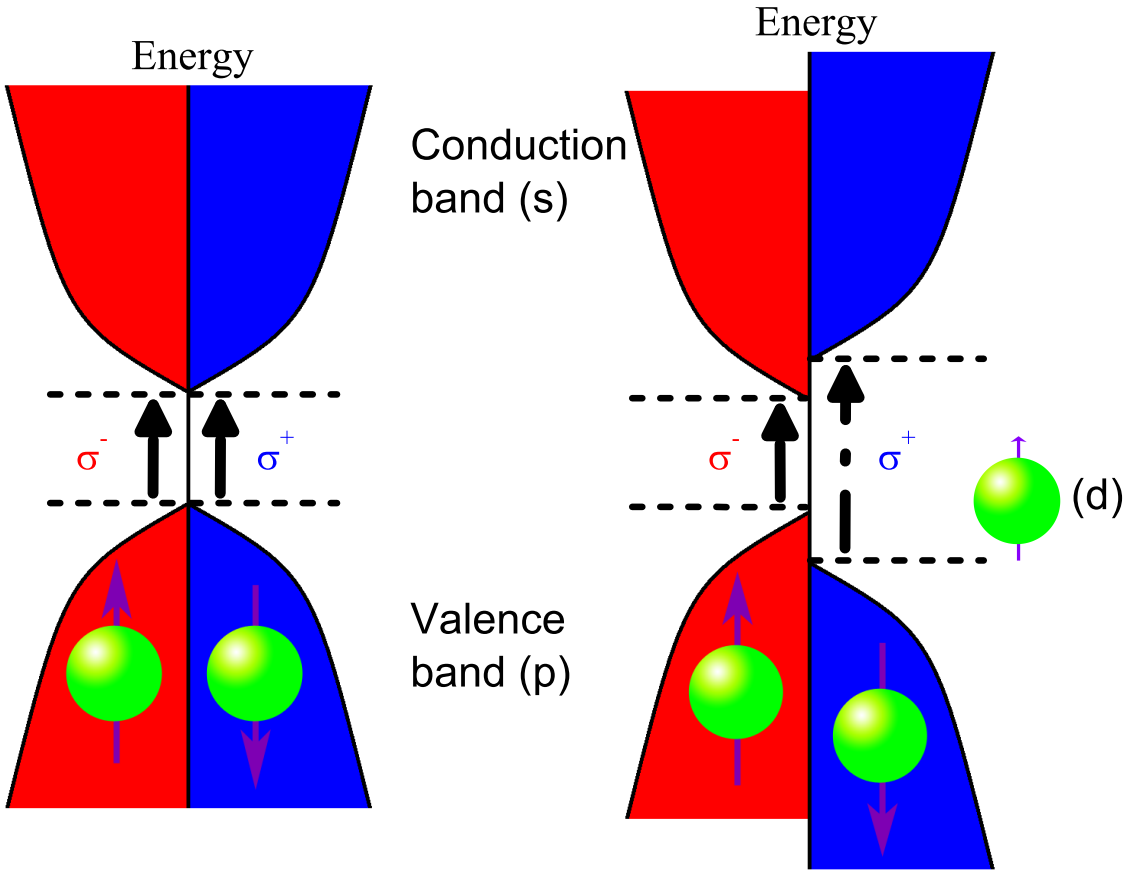

Figure 3.15: (a) Shows a schematic density of states for a nonmagnetic material. By close examination it is evident that an excitation from the valence band to the conduction band has no spin dependence, therefore, spin-up and spin-down electrons have no distinguishing features. (b) Shows a schematic density of states for a magnetic material, in this scenario the d electrons from the magnetic ion interact with the s and p electrons from the material lattice. This interaction induces exchange splitting in the valence and conduction bands that depends upon the spin direction (Zeeman splitting). Therefore, the material has a intrinsic spin-polarized (non-equilibrium) band structure that results in a differential absorption (MCD effect) when comparing RCP and LCP ($\sigma_+ \& \sigma_-$).

Table 3.5: The four distinct classes of optical activity effects are shown in this table. The phase factors for parity (P- inversion) and time reversal (T) symmetry are $(\#)^P$ and $(\#)^T$, respectively. The symbols 0 and 1 denote even and odd, respectively, thereby representing invariance and sign reversal. Importantly, the parity value corresponds to an optical tensor of equivalent rank. The value of time reversality corresponds to the real (0) and imaginary (1) part of the tensor, respectively. For example, the electric field, $\vec{E}$, is a polar (i.e. parity-odd) time-even vector and the magnetic field, $\vec{M}$, is an axial (i.e. parity-even) time-odd vector.[496, 489, 357]

P	T	Optical Effect	Difference Signal
0	0	Birefringence	Magnetic linear dichroism (MLD)
0	1	Faraday rotation	Magnetic circular dichroism (MCD)
1	0	Optical rotation	Natural circular dichroism (NCD)
1	1	Magneto-electricity	Non-reciprocal linear dichroism

$$\vec{E}^{\pm}(\omega, t) = E(\omega)(\mathbf{x} \pm i\mathbf{y})e^{-\omega t}. \tag{3.112}$$

Here, $\mathbf{x}$ and $\mathbf{y}$ indicate the coordinate unit vectors and the superscripts (+) and (-) refer to the RCP and LCP, respectively. For a measurable MCD response, the absorption of RCP and LCP will be different, this corresponds to the following:

$$P^{\pm}(\omega, t) = \omega V E^2(\epsilon^2_{xx} \pm \epsilon^1_{xy}). \tag{3.113}$$

This establishes ϵ^2_{xx} and ϵ^1_{xy} as the absorptive components of the tensor elements. Further transformation results in:

$$\epsilon_{2,xx} = \frac{P^+ + P^-}{2\omega V E^2} \tag{3.114}$$

and

$$\epsilon_{1,xy} = \frac{P^+ - P^-}{2\omega V E^2}. \tag{3.115}$$

Ultimately, the absorptive part $\epsilon_{2,xx}$ of the diagonal tensorial elements comes from the sum of absorption of RCP and LCP light. Additionally, it reveals how the counter argument, $\epsilon_{1,xy}$, corresponds to absorptive off-diagonal tensorial elements being proportional to their difference.[126]

An interesting result of the analytical consideration of causality produces the Kramers-Kronig dispersion relations between the real and imaginary parts of ϵ_{ij}:[404, 405, 499, 414, 417, 500]

$$\epsilon_{1,ij} = \frac{2}{\pi} \mathrm{P} \int_0^\infty \frac{\omega' \epsilon_{ij}^2(\omega')}{\omega'^2 - \omega^2} d\omega', \tag{3.116}$$

$$\epsilon_{2,ij} = -\frac{2\omega}{\pi} \mathrm{P} \int_0^\infty \frac{\omega' \epsilon_{ij}^1(\omega')}{\omega'^2 - \omega^2} d\omega', \tag{3.117}$$

where P represents the principle value of the integral.

Now to develop a sense of the effect induced by an applied magnetic field (or even magnetization). In the absence of an applied magnetic field, the transmitted light intensity is expressed by:

$$I = I_0 exp(-\alpha(E)d). \tag{3.118}$$

Here, $\alpha(E)$ is the absorption coefficient at a given energy E, d is the thickness of the sample, and I_0 is the initial intensity of input before interacting with the sample. After applying a magnetic field the change in transmitted light intensity can be

expressed in a slightly more complicated fashion

$$I = I_0 exp(-\alpha^{\pm}(E \pm \frac{\Delta E}{2})d). \tag{3.119}$$

The next step is to consider the circularly polarized light,

$$I = I_0 exp(-\alpha(E)_{\pm}d). \tag{3.120}$$

In this adaptation we have incorporated the Zeeman splitting energy, that is field dependent and also related to the effective g-value, g_{eff}, by

$$\Delta E = -g_{eff}\mu_B H. \tag{3.121}$$

Of course this value for the ΔE is for a simple $S = \frac{1}{2}$ system; for the systems that we are concerned with in this dissertation $S > \frac{1}{2}$. So, the Zeeman-like splitting takes on a more convoluted perspective.

An important note is that in the presence of a magnetic field, the varying forms of magnetism display different absorption cross sections, probability of absorption, that are dependent upon the polarization of the impinging photons.[501] This formally describes the effect known as dichroism but on a deeper level produces a probe for the change in angular momentum projected on the applied magnetic field direction for electrons that absorb the circularly polarized photons in accordance with conservation of angular momentum.[70] The variations can be remarkable and grant access to insight about exchange mechanisms, along with other physical characteristics of

the material(s) being investigated such as $\vec{M}$ or magneto-elastic coupling. Other potentially valuable knowledge that can be acquired from a MCD spectrum include the following: the degeneracy of ground and excited state orbital and spin angular momentums, spectral band polarization, individual split components arising from the Zeeman splitting, and transition metal ion oxidation, spin states, and coordination environments.[502, 357] Yet, the simplest application is the detection of weak transitions. The revealed transitions may either be obscured by nearby stronger transitions or just too weak to observe in traditional absorption spectroscopy.[357]

To give an example of the physical effects displayed in an MCD experiment. When a magnetic field is applied, all of the electronics states in the material will be split by energies on the order of $g_{eff}\mu_{\mathrm{B}}|B|$, where g_{eff} is the effective Lande g, as expressed in the following relationship:[503, 504, 505, 506, 507, 508, 509, 510]

$$\Delta E_{\mathrm{Z}} = g_{int}\mu_{\mathrm{B}}B + \langle S_z \rangle = g_{eff}\mu_{\mathrm{B}}B. \tag{3.122}$$

So, one possible avenue to acquire information on the Zeeman splitting arives by inflating the g_{eff} value. Of course, this is most obviously applicable towards molecular systems or dilute magnetic semiconductors due to delocalization effects because the Zeeman shift energy, on the order of $1\,\mathrm{cm}^{-1}$, is a rather small perturbation in comparison to the broad band of an electronic excitation, $2000\,\mathrm{cm}^{-1}\cong 0.25\,\mathrm{eV}$.[511, 512, 513, 514, 515, 516] Even though this seems rather bleak when it comes to the broad bands expected in solids and in-particular in electronic excitations. However, MCD does have a way to open a window of understanding into the underlying Zeeman structure , this is exampled in Fig. 3.16. Essentially the magnetic field causes a

Zeeman splitting of the band structure and allows for the adoption of selection rules for circularly polarized electromagnetic radiation, in which $\Delta M_s = \pm 1$ corresponding to $\sigma = \mp 1$. As can be seen in Fig. 3.16 (c) the $\Delta\alpha(\omega)$ is strikingly frequency dependent. Unfortunately, this aforementioned perturbation is extraordinarily small in comparison to an electronic excitation, again on the order of $(g_e + g + g)\mu_{\mathrm{B}}B$. Expressing this mathematically, we first need to show how Fig. 3.16 (c) emerges to have such frequency dependence,

$$\Delta\alpha(\omega) = \alpha_+(\omega) - \alpha_-(\omega). \tag{3.123}$$

From a general perspective the system will have a response with respect to the polarization akin to the following equation:

$$I(\omega, \hat{\epsilon}) = I_0\omega, \hat{\epsilon}) \exp(-\alpha\omega, \hat{\epsilon})l). \tag{3.124}$$

Here, $\hat{\epsilon}$ is the established polarization for the system and l is the sample length along the attenuation axis. Upon consideration the small absorption limit under application of Eqn. 3.124 the following is obtained:

$$\Delta\alpha(\omega) \simeq -\frac{2(I_+(\omega) - I_-(\omega))}{l(I_+(\omega) + I_-(\omega))}. \tag{3.125}$$

Here, $I_+(\omega)$ and $I_-(\omega)$ correspond to the transmitted intensities of the circularly polarized light of σ_+ and σ_-, respectively, at frequency ω. Of course, from an experimental standpoint the transmitted intensities are determined. A convenient form

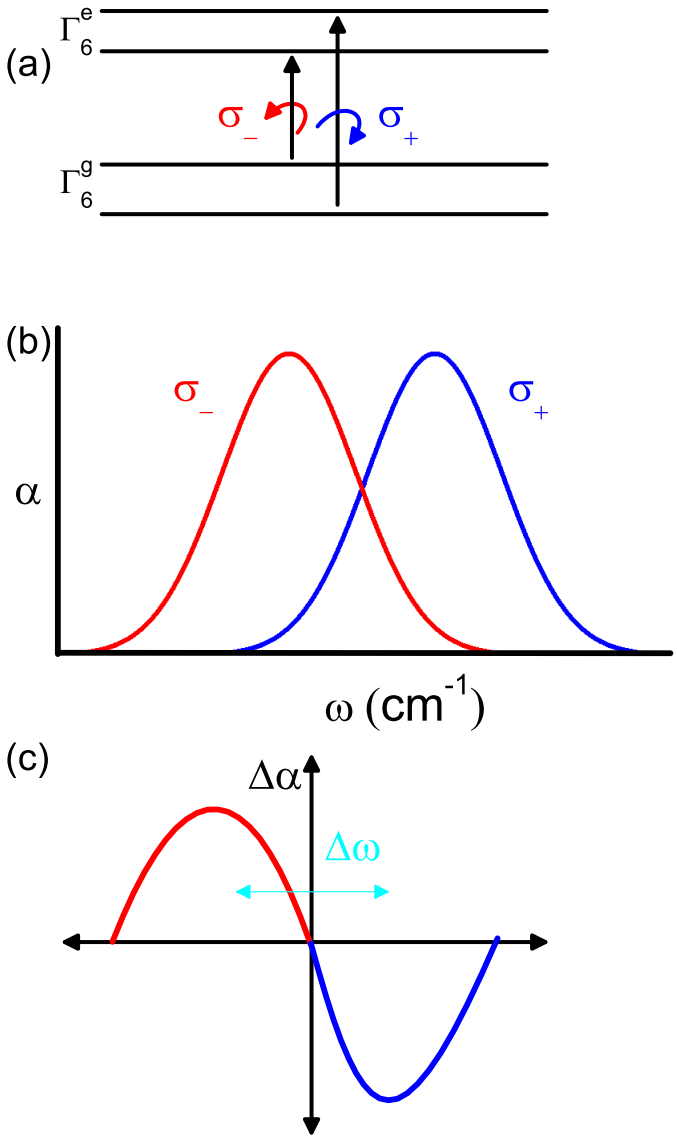

Figure 3.16: (a) Shows the splitting of an arbitrary ground and excited states, Γ_6^g and Γ_6^e, respectively due to magnetic field. Additionally, the selection rules for circularly polarized transition are exemplified here. In (b) the shifting of broad absorption bands due to the two polarizations are shown. Finally, (c) shows an example MCD response from this excitation pattern.

for the MCD response signal is

$$\begin{aligned} I_{MCD}(\omega) &= \Delta\alpha(\omega)l \\ &= -\frac{\Delta I(\omega)}{I_{total}(\omega)}, \end{aligned} \tag{3.126}$$

where $\Delta I(\omega) = I_+(\omega) - I_-(\omega)$ and $I_{total}(\omega) = 1/2(I_+(\omega) + I_-(\omega))$. If $\Delta\alpha(\omega)$ is measured as a function of the magnetic field the Zeeman structure can be resolved. To show I_{MCD} in a second fashion,

$$I_{MCD} = \frac{\alpha_+ - \alpha_-}{\alpha_+ + \alpha_-} = -\frac{\Im[\sigma_{xy}(\omega)]}{\Re[\sigma_{xx}(\omega)]}. \tag{3.127}$$

Here I am expressing an earlier statement in Sec. 3.3.3, this discusses the dependence upon the $\Re$and$\Im$ components of the optical conductivity. Now to express an approximation of $I_{MCD}(\omega)$, from the product of magnetic splitting appearing as $\Delta\omega$, rate of change of absorption coefficient with frequency $d\alpha(\omega)/d\omega$, and the sample thickness l. From these one can obtain,

$$I_{MCD(\omega)} = \Delta\omega \frac{d\alpha(\omega)}{d\omega} l. \tag{3.128}$$

For simplicity, the excitation band will be symmetrical and structureless; therefore, the approximation appears as

$$\frac{d\alpha(\omega)}{d\omega} \simeq \frac{\alpha(\omega_0)}{\Gamma}, \tag{3.129}$$

such that,

$$\Delta\omega = \frac{I_{MCD(\omega)}}{l}\frac{\Gamma}{\alpha(\omega_0)}. \tag{3.130}$$

For typical experimental scenarios $I_{MCD}(\omega) \simeq l\Delta\alpha(\omega) \simeq 10^{-5}$ and $l\alpha(\omega_0) \approx 1$, from this one estimates $\Delta\omega = 10^{-5}\Gamma$. So, this approximation says if $\Gamma \simeq 0.25\,\text{eV} \simeq 2000\,\text{cm}^{-1}$, then $\Delta\omega \simeq 0.02\,\text{cm}^{-1}$. This result is on the same order of magnitude as the Zeeman splitting.[515] In the Fig. 3.17, the band gap is shown to be shifting rigidly with respect to the change in spin direction of the electron. This suggests that one could reach beyond the Zeeman structure and actually obtain information corresponding to the exchange splitting of a particular excitation.

Continuing on, in the scenario that the system contains partially occupied levels, this splitting will result in an induced magnetization because of the unequal population of the states.[517, 518, 519] To explain this more exactly, the absorption corresponding to σ^+ or σ^- in the Faraday geometry, as shown in Fig. 3.18, with absorption measured in the direction parallel to the magnetization or magnetic field. At this point it should be fairly apparent that the intensity will be anti-symmetric but why? This is because of the biased orbital population effecting the total oscillator strength for $\Delta m = \pm 1$ of electric dipole transitions. The spectrum arising from this form of excitations is historically referred to as paramagnetic and tracks the absorption spectrum with variance induced by the strength of the Zeeman splitting and spin-orbit interaction occurring in the electronic states involved in the transition.[502, 518, 520, 521]

In the consideration of a nonmagnetic material ($\mu = 1$) in a magnetic field of 10 T, the induced population variance will be of the order of 10^{-3} eV. However, this

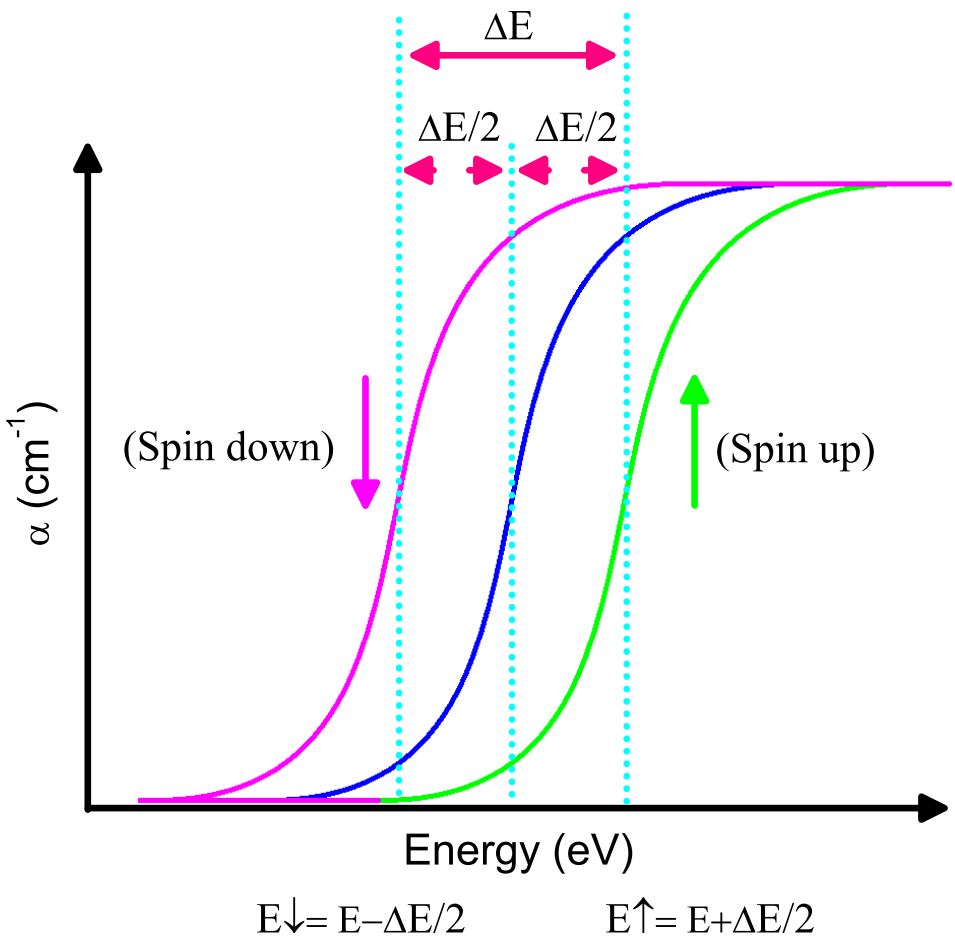

Figure 3.17: This schematic shows the rigid shift model. From this schematic, it is also plausible to get a feel for a subset of information that can be gained by this analysis. Such additional information can correspond to the exchange splitting for a given electronic excitation.

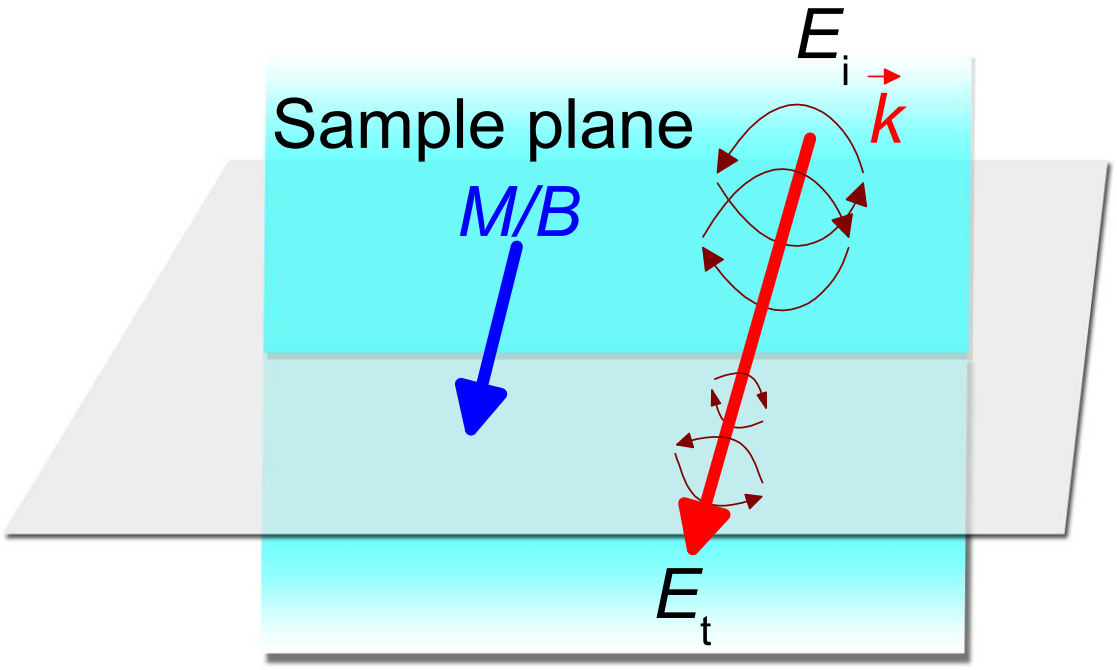

Figure 3.18: Faraday geometry. The transmission of the circularly polarized light propagating with wavevector $\vec{k}$ depends on the direction of the magnetization (or magnetic field B) M or, alternatively, on the helicity $\sigma^{\pm}$ of light indicated by the paired circles before and after the sample plane. E_i denotes the incident and E_t indicates the departing or transmitted electric field of the light. [522]

value will be altered when considering magnetic materials. Classically, the scheme depicting this is based upon the Zeeman energy, where the potential energy E is defined as the following:

$$E = \vec{M} \cdot \vec{H}. \tag{3.131}$$

.

Here $\vec{M}$ is the magnetization of the material and $\vec{H}$ is the external magnetic field

(in Tesla). Ultimately the value of $\vec{M}$ takes into consideration the Landau-Lifshitz energy equation, as shown below:

$$E = E_{ex} + E_D + E_\lambda E_k + E_H. \tag{3.132}$$

Here, E is the free energy, E_{ex} is the exchange energy, E_D is the magnetostatic energy, E_λ is the magnetoelastic anisotropy energy, E_k is the magnetocrystalline anisotropy energy, and E_H is the Zeeman energy.

Continuing on with a description of the MCD response, we come to the historical "diamagnetic" form of the spectrum. This occurs in materials with and without partially filled shells. The signals of this fashion arise schematically due to an effective rigid shift of the bands.[71] Therefore, the signal is the outcome from the energy differences of σ^+ and σ^- transitions.[520] The resulting signal in a nonmagnetic material corresponds to energy on the order of 10^{-4} eV. These types of signal are the only form of MCD response that correspond to completely full and/or empty bands.[518]

To qualitatively understand this behavior we will consider a simple classical oscillator model, or the Lorentz-Drude model. From this model it is feasible to derive expressions for the diagonal and off-diagonal components of the dielectric tensor. These components of the tensor will present a magnitude when they exhibit a resonant behavior corresponding to the oscillation frequency. The best place to start is equation for electron motion in an electric field $\vec{E}$ from light with a static magnetic field $\vec{B}$. If the $\vec{B}$ is oriented in the z-direction, then the Lorentz force $F_L = e \cdot d\mathbf{x}/dt \times \vec{B}$ will act in the xy-plane and the electron will precess about the z-axis.[409, 522, 381, 410] The

electron response to the oscillating electric field of light is presented by the dielectric tensor, resulting in a precession of the electric field vector $\vec{E}$ about the z-axis. For $\omega_L \ll \omega$ and for the linear approximation in ω_L, the Lorentz-Drude model predicts ϵ_{xy}^2 to be highest at the inflection points of the resonance peak, represented as the following:

$$\epsilon_{2,xy}(\omega) = i\omega_L \frac{d\epsilon_{xx}}{d\omega}. \tag{3.133}$$

Here, $\omega_L = e|\vec{B}|/(2m)$ being the Larmor frequency, e is the charge of the particle and m is the mass of the particle (electron). For the general approximation using ferromagnets, this is valid for photon energies in and above the visible spectral range, since $\hbar\omega_L$ is in the range of 10 to 100 meV for magnetic fields inside a ferromagnet. The Lorentz-Drude model offers many qualitative suggestions for basic understanding of magneto-optical spectroscopy and effects; however, the correct description can only be found in the quantum mechanical framework.[468, 523]

From a fundamental standpoint MCD can be used to optically obtain information about the electron spin.[524] However, to gain access to this information the material must have spin-orbit interaction, or relativistic motion of electrons in their orbit. This emerges from a disproportionation of the orbital polarization, resulting from the spin polarization.[518] The physical origin of this level of interaction is expressed as the following:

$$\vec{B} = \left(\frac{1}{c}\right) \vec{E} \times \vec{v}. \tag{3.134}$$

Here, $\vec{v}$ is the velocity of an "observer", in an electric field $\vec{E}$, results in the presence of a magnetic field $\vec{B}$, and c is the speed of light. From the above equation we can see that $\vec{B}$ is perpendicular to both $\vec{v}$ and $\vec{E}$ and in the atomic environment this is ultimately parallel to $\vec{L}$ the orbital angular momentum.

Another important identity to address is conservation. It is well known that energy, mass, and linear momentum must be conserved but angular momentum should be included in this list. Electromagnetic waves have angular momentum, just the same as particles. This arises in the photons from the right- and left-circular polarizations having a projection of their angular momentum along the direction of propagation, producing the helicity, equal to ± 1, respectively, as shown in Fig. 3.20.[525, 526, 527, 429] These raising and lowering values are in units of $\hbar$. Linearly polarized light is in a superposition of these two states. When decomposing information presented by MCD, it is important to consider that the conservation of angular momentum is the primary driving force behind the magnitude of response. Principally this provides information about the changing angular momentum projected along the magnetic field direction, as shown by Fig. 3.19.[528, 529] This results from torque $\vec{T}$ acting on the magnetic dipole moment $\vec{m}$ from the external magnetic field $\vec{B}_0$ through the angular momentum $\vec{P}$, via the gyromagnetic ratio γ

$$\gamma \vec{B}_0 \times \vec{P} = \vec{T}. \tag{3.135}$$

To clarify, the gyromagnetic ratio appears as $\gamma = \vec{m}/\vec{P}$. Additionally, when spin-orbit interaction is considerable the outcome corresponds direct information about the nature of the spin angular momentum component that is parallel to the mag-

netic field. Interestingly, when considering a microscopic model circularly polarized transitions occur specifically between magnetically quantized electronic states such that $\Delta m_j = \pm 1$ represents the RCP and LCP.[530, 531]

Incident circularly polarized photons each impart one quantum of orbital angular momentum ($\Delta M_L = \pm 1$).[72, 525, 526, 375] Thus ΔM_L becomes the primary (or minimum) selection rule used in MCD. Additionally, the The total angular momentum remains conserved in both magnitude and direction when a photon is absorbed, thus if spin-orbit interaction comes into play, the selection rule shifts to $\Delta M_J = \pm 1$, as shown in Fig. 3.21 (b). It is valuable to note that the transition is spin dependent because the helicity, the projection of the angular momentum onto the linear momentum, couples to the parallel spin direction. A more visual explanation of helicity is the resulting vector executes a clockwise or counterclockwise helical precession motion about the propagation direction with respect to time, as shown in Fig. 3.21 (f).

MCD data analysis and interpretation

As previously stated the budding quantum mechanical theory of the early 20^{th} century was a harbingering of MCD theory.[71, 532] So, that to say the roots of this method require a firm understanding of many intricate parts of quantum mechanical theory.[533, 534, 535] It is important to note that the foundations of this field are from atomic/molecular chemistry, only on a ever so slightly more contemporary front ca. late 1970s with the inception of dilute magnetic semiconductors did the method start to move towards crystalline solids.[536, 537, 538, 539, 540, 541] The investigation of single crystal thin-film materials is a forefront of its own in the field

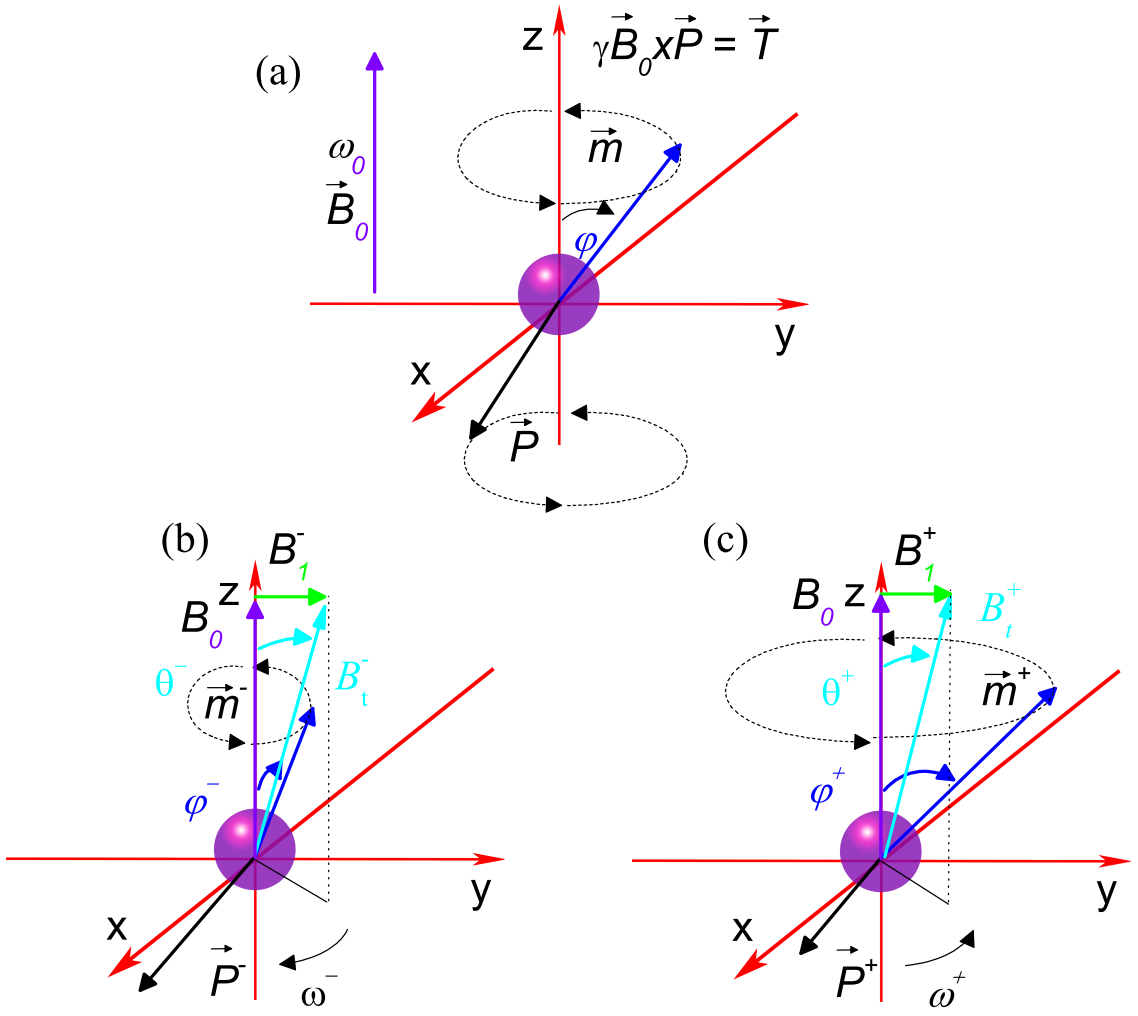

Figure 3.19: (a) Shown here is the resulting precession of a magnetic dipole $\vec{m}$ around the external magnetic field direction B_0 by angle φ with $\vec{P}$ being the angular momentum. (b) Represents the resulting change in momentum when the helicity momentum points antiparallel to the $\vec{m}$ (or the bulk magnetization), the precession angle decreases. (c) Shows the change in momentum when the helicity momentum points parallel to the $\vec{m}$, causing an increase in the precession angle.

of MCD investigations because technologically, thin-film materials are emerging as highly important. So, it is only logical that we take our journey along this path as

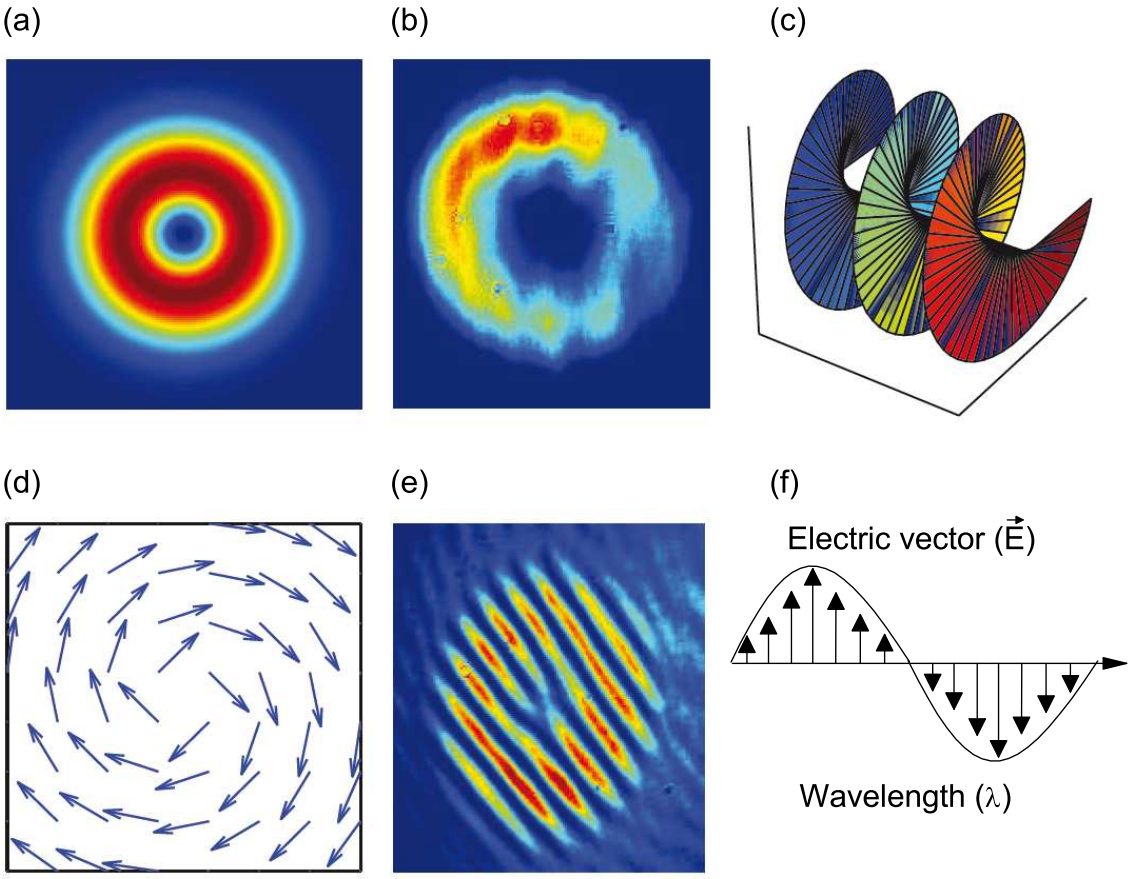

Figure 3.20: (a) Shows the transverse intensity map of a beam of light with orbital angular momentum and (b) displays the experiment results. In panel (c) it can be seen that the beam phase twists helically about the central dark spot shown in (a-b). This produces a spiral staircase style phase wavefront, where the center represents the spin angular momentum. (d) Schematic of the spiraling phase wavefront, showing the local orbital angular momentum appears with a velocity pattern akin to a tornado or fluid vortex, hence the singular spots being named optical vortices. (e) Shows a interference pattern that is expected for $m = 1$, the fork-like structure characterizes this result. (f) The projection of the circular electric field vector, shown in (c), onto the direction of propagation. This shows how circularly polarized photons impart one quantum of orbital angular momentum, $\Delta M_L = \pm 1$. This figure was adapted from Ref. [525].

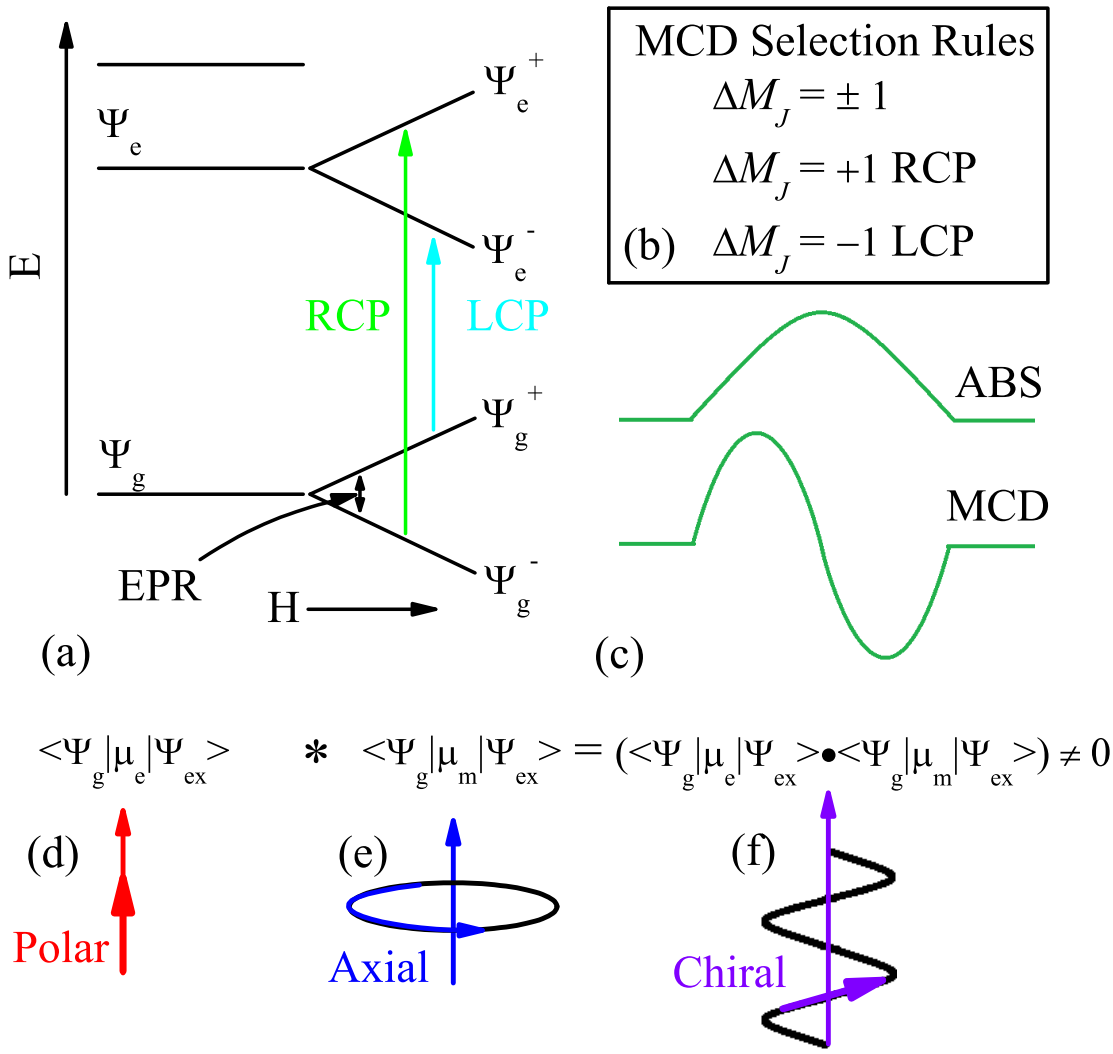

Figure 3.21: (a) Generic model of excitation with selection of RCP and LCP for atomic/molecular transitions as described by (b) the selection rules and splitting shown in (c). On the right side of the figure we see models for (d) an electric dipole (polar), (e) magnetic dipole (axial), and (f) combined (chiral) transition moments. In solids these are changed from atomic/ molecular transitions to interband transitions.

well.

History

This technique derives from magnetic optical rotation. The two are related via a Kramers-Kronig integral transform, strictly a Hilbert Transform,[542] and strictly covering all frequencies.[543, 544, 545, 546] The Faraday effect can be expressed in a concise manner by the following complex equation:

$$\hat{\Phi} = \phi - i\theta = \hat{V} \int_0^l H(l) dl. \tag{3.136}$$

Here, $\hat{\Phi}$ is the complex rotation with ϕ being the real part akin to the rotation of polarization for a linearly polarized beam after traversing the thickness of the material l parallel to the magnetic field H. Where as θ depicts the corresponding ellipticity, being strictly nonzero in regimes of absorption. The Verdet constant $\hat{V}$ is a frequency dependent characteristic of a given material.[546] ϕ and θ are related via the Kramers-Kronig relationship that can be generalized to connect the dispersive and absorptive components of any response function, as shown by the following:[357, 416]

$$\eta(\phi) = \frac{1}{\pi} \mathscr{P} \int_{-\infty}^{\infty} \frac{\eta(\phi)}{\omega' - \omega} \tag{3.137}$$

$$\eta(\theta) = -\frac{1}{\pi} \mathscr{P} \int_{-\infty}^{\infty} \frac{\eta(\theta)}{\omega' - \omega}. \tag{3.138}$$

To explain, in this representation ϕ is the magneto-optical rotation and θ is the MCD

response.

The general model for MCD response across all forms of materials take the form of the following:

$$\Delta\alpha(E) = \gamma\mu_B B[\frac{A_1}{h}\frac{\partial g(E)}{\partial E} + \left(B + \frac{C}{k_b T}\right) g(E)]. \tag{3.139}$$

Here, $\Delta\alpha(E)$ is the difference between the absorption of RCP and LCP at energy E, B is the magnetic field, A_1, B, and C are the Faraday terms, g is the band shape function, γ is a series of optical constants, and μ_B is the Bohr magneton. For a derivation of this equation from the quantum mechanical roots look at Appendix C.1. From an overarching perspective, Eq. 3.139 provides an approximation of the three primary optical activity mechanisms taking place in MCD. The general expectation of shape is shown in Fig. 3.22, in these plots the y-axis represents the central frequency of an excitation. Here, Fig. 3.22 (a) corresponds to derivative response function expressed by $A_1/h\partial g(E)/\partial E$ and (b) shows the response forms expected by B and C, with the magnitude of response being altered by a dependence on temperature for C as shown by $C/k_B T$. This interdependence on temperature for the C-term means that this will mainly show up in the "low"-temperature regime.

Thin-film MCD response

Now, we will explore a general thin-film MCD response and how to analyze it. So, again since we are looking at a Faraday magneto-optical response the spectra gives information in regards to the (complex) dieletric tensor. This provides a logical determination of the necessarily complex refractive index $n_\pm = n'_\pm + in''_\pm$ for the

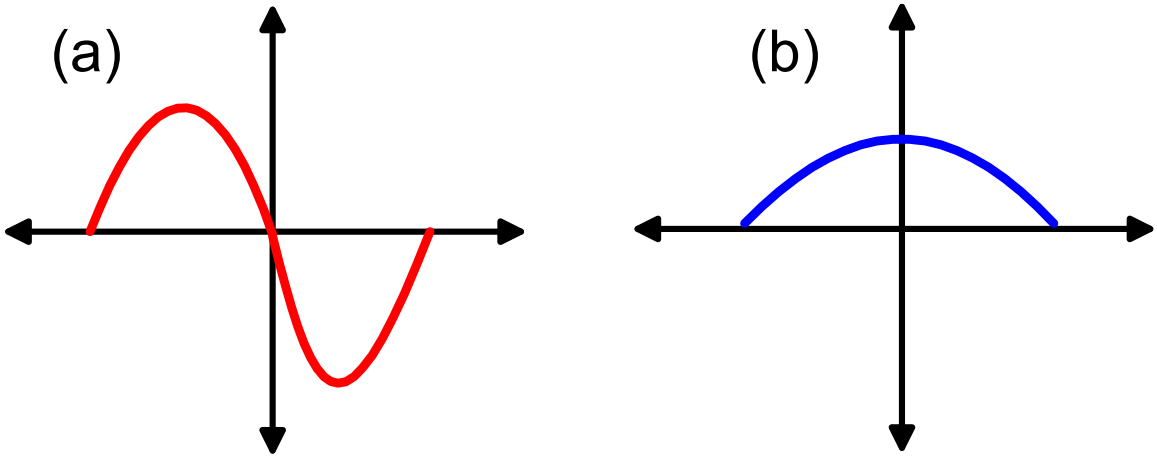

Figure 3.22: Diagram of MCD response (a) shows the derivative-like A-term response function and (b) show the expected shape for B and C term response functions.

circularly polarized light based upon Eq. 3.100

$$\overleftrightarrow{\epsilon} = \begin{vmatrix} \epsilon_{xx} & i\epsilon_{xy} & 0 \\ -i\epsilon_{xy} & \epsilon_{yy} & 0 \\ 0 & 0 & \epsilon_{zz} \end{vmatrix}, \tag{3.140}$$

$$\epsilon_{\pm} = \epsilon_{xx} \pm \epsilon_{xy}, \tag{3.141}$$

$$n_{\pm} = \sqrt{\epsilon_{\pm}} \cong n_0 \pm \frac{\epsilon_{xy}}{2n_0}, \tag{3.142}$$

$$n_0 = \sqrt{\epsilon_{xx}}. \tag{3.143}$$

in which case z is the magnetization direction.

To clarify, a thin film is one where it is necessary to consider contributions of waves making multiple passes coherently through the sample. In contrast, a thick

sample will have sufficient dephasing effects, thereby allowing direct addition of the intensities from each contribution. Therefore, a thin sample will be represented by $\lambda_{n1} \approx d$, whereas a thick sample will be represented by $\lambda_{n2} \ll L$, d and L are the respective thicknesses. λ_{n1} and λ_{n2} are the wavelengths in the film and substrate, presented respectively by $\lambda_{n1} = 2\pi c(\omega n_1)^{-1}$ and $\lambda_{n2} = 2\pi c(\omega n_2)^{-1}$, where n_1 and n_2 are the refractive indices.[347, 547, 401, 402, 548, 399]

As with Glover-Tinkham analysis (Sec. 3.1.5), the composite systems, thin film and substrate, transmission is calculated by first taking consideration of the bare substrate. The energy transmitted through the front and back surfaces are T_F and T_B, respectively, the same symmetry holds true with respect to the reflected light, the coefficients are R_F and R_B.

We will follow the derivation presented in [547]. The transmission coefficient for a slab of material with an attention factor of γ per pass is given by

$$T_{tot} = \frac{T_F T_B e^{\gamma}}{1 - R_F R_B e^{=2\gamma}}. \tag{3.144}$$

In the case that the material slab is completely transparent ($\gamma = 0$)

$$T_F = T_B = \frac{2s}{(1+s)^2}; \quad R_F = R_B = \left(\frac{s-1}{s+1}\right)^2. \tag{3.145}$$

Here s is the refractive index for the substrate. This produces the common result of

$$T_{tot} = \frac{2s}{(s^2+1)}. \tag{3.146}$$

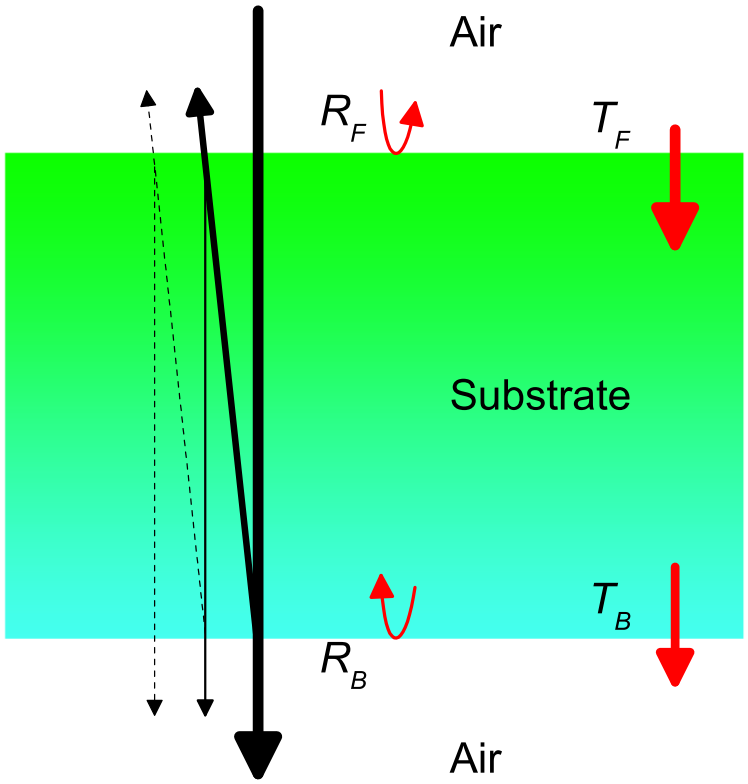

Figure 3.23: Diagram of the a three-layer model consisting of only the substrate, of course air can also be replaced by vacuum. The incident light impinges from above.

Now that we have established the framework for the transmission coefficient of a three-layer model [Fig. 3.23] environment, we can incorporate the four-layer model as shown in Fig. 3.24. If we assume that the thin film has a complex refractive index $N = nj + ik$ on the front surface with transmission and reflection coefficient amplitudes at the film-air (film-substrate) interface of t_1 and r_1 (t_2, r_2). Then the tractable forms of T_F and R_F become

$$T_F = \frac{\chi |t_1 t_2|^2}{s|1 - \chi r_1 r_2 e^{i\varphi}|}; \quad R_F = \left| \frac{r_2 + \chi r_1 e^{i\varphi}}{1 - \chi r_1 r_2 e^{i\varphi}} \right|^2 . \tag{3.147}$$

Here $\chi = \exp(-\alpha d), \alpha = 2\omega k/c$ is the attenuation through the film, and $\varphi = 4\pi\omega nd/c$ is the phase change when the light passes through the film twice.[549, 550] As we have already stated, and shown in Eq. 3.139, MCD is the result of the differential absorption (or transmission) of right- and left-circularly polarized light according to the following:

$$MCD = T_{tot}^{+} - T_{tot}^{-}; \quad T_{tot}^{\pm} = \frac{T_F^{\pm} T_B e^{-\gamma}}{1 - R_F^{\pm} R_B e^{-2\gamma}}. \tag{3.148}$$

Importantly, this method can be used to study a full suite of material including, insulating, semiconducting, dilute magnetic semiconductors, and conducting (metallic) systems on substrates.[551, 552] By using Eq. 3.144 along with the values obtained for T_F and R_F one can obtain the transmission of a conducting sheet, as per the following:

$$T_F = \left| \frac{2}{1 + s + Z_0\sigma} \right|^2; \quad R_F = \left| \frac{1 - s - Z_0\sigma}{1 + s + Z_0\sigma} \right|^2. \tag{3.149}$$

Here Z_0 is the impedance of free space and σ is the conductance of the sheet.[553] One contemporary example is that of graphene, where the approximation that $Z_0\sigma_{\pm} \ll 1$ must be used.[491]

3.3.4 Photoconductivity setup

The photoconductivity data presented in this dissertation was measured on an instrument that was designed and built in house. This instrument covers the optical (2000–280 nm) region of the electromagnetic spectrum. The optical path is shown in

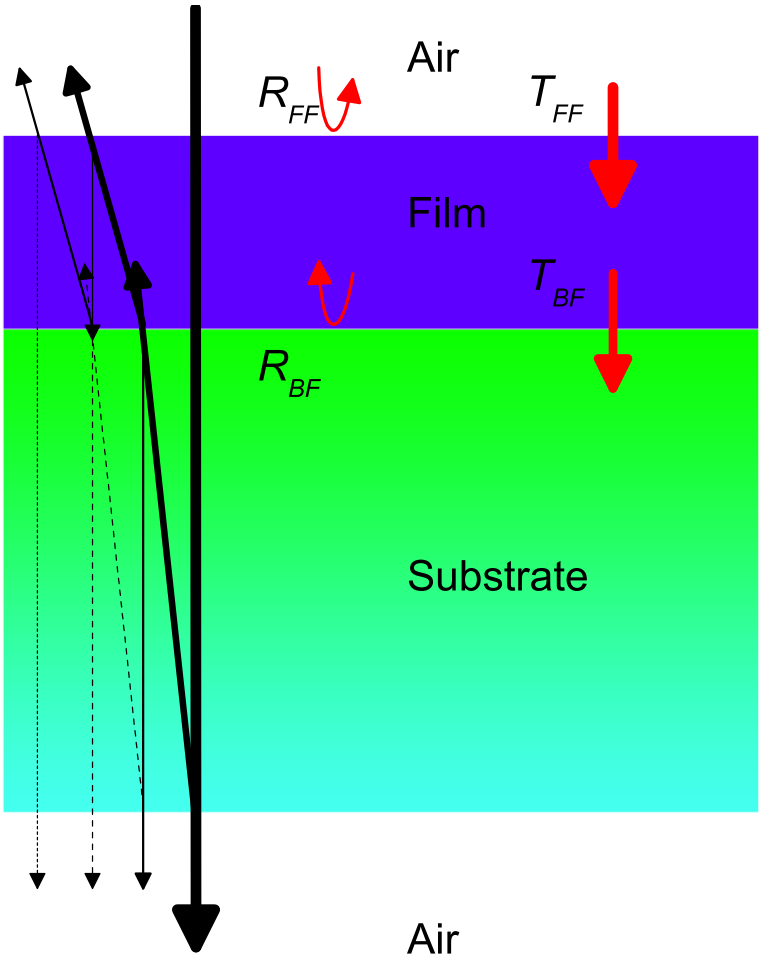

Figure 3.24: Diagram of the a four-layer model consisting of a film on a substrate, of course air can also be replaced by vacuum. The incident light impinges from above.

Fig. 3.25, in a minimized design.

The main components of this instrument are the light source (xenon arc lamp), lenses, and bandpass filters, ls, ln, and bp, respectively. The bandpass filters details are shown in Table 3.6.

This instrument has also been adapted to be able to measure photoconductivity

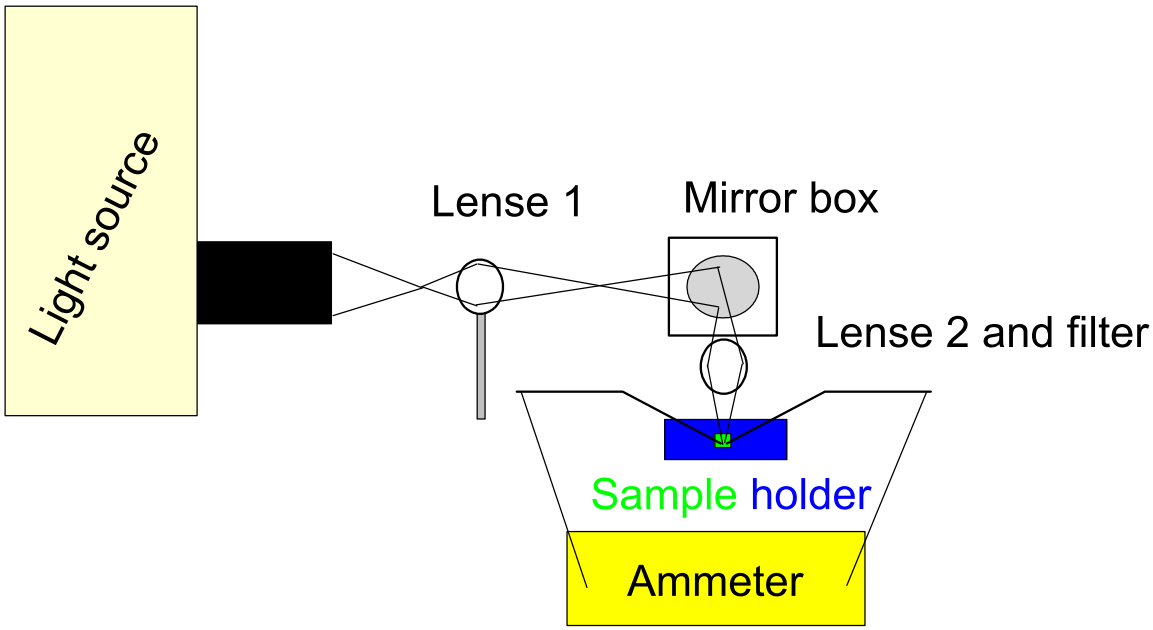

Figure 3.25: Schematic layout of the photoconductivity instrument, currently minimized to include as few components as necessary. These components include a light source, lenses (1 & 2), mirror box (with mirror inside), filter, sample space, and ammeter. This is designed to measure steady-state photoconductivity.

Table 3.6: Photoconductivity bandpass filters

Center λ (nm)	Bandwidth (nm)	Blocked range (nm)	T_{max} (%)
2000	500±100	200–12000	70
1500	12±2.4	200–1850	70
1250	10±2	200–3000	70
1000	10±2	200–3000	70
900	40±8	200–1150	70
800	40±8	200–1150	70
700	40±8	200–1150	70
650	40±8	200–1150	70
600	40±8	200–1150	70
550	40±8	200–1150	70
500	40±8	200–1150	70
400	40±8	200–1150	45
380	10±2	200–3000	25
360	10±2	200–3000	25
340	10±2	200–3000	25
313	10±2	200–10000	15
300	10±2	200–10000	15
280	10±2	200–10000	12

in a magnetic field. For more detail about this instrument and the methodology see the independent chapter about this topic, Ch. 4.

3.4 Spectra under Extreme Conditions: Variable Temperature and High-Field Measurements

3.4.1 Low-Temperature Techniques

The low-temperature measurements were carried out with an open-flow cryostat. The low-temperature experiments with the Perkin-Elmer λ-900 are performed in combination with an APD LT-3-10 Heli-Tran cryostat system with dual temperature sensors and a Lakeshore Model 330 temperature controller.(Fig. 3.26). The variable-temperature experiments done at high temperature, above 300 K, are performed in combination with an APD LT-3-12 Heli-Tran cryostat system with four temperature sensors, this requires combined usage of the Lakeshore Model 330 and the Lakeshore Model 340. The temperature sensors for the high-temperature cryostat allow for one to presumably measure the full range, 4.2–800 K. However, due to helium consumption and time to cool, it is best to not maintain temperature below 30 K for times longer than necessary.

The principles of operation are illustrated in Fig. 3.27. Cooling is accomplished by a controlled liquid He transfer through a high efficient transfer line to a heat exchanger adjacent to the sample interface. A needle valve at the end of the transfer

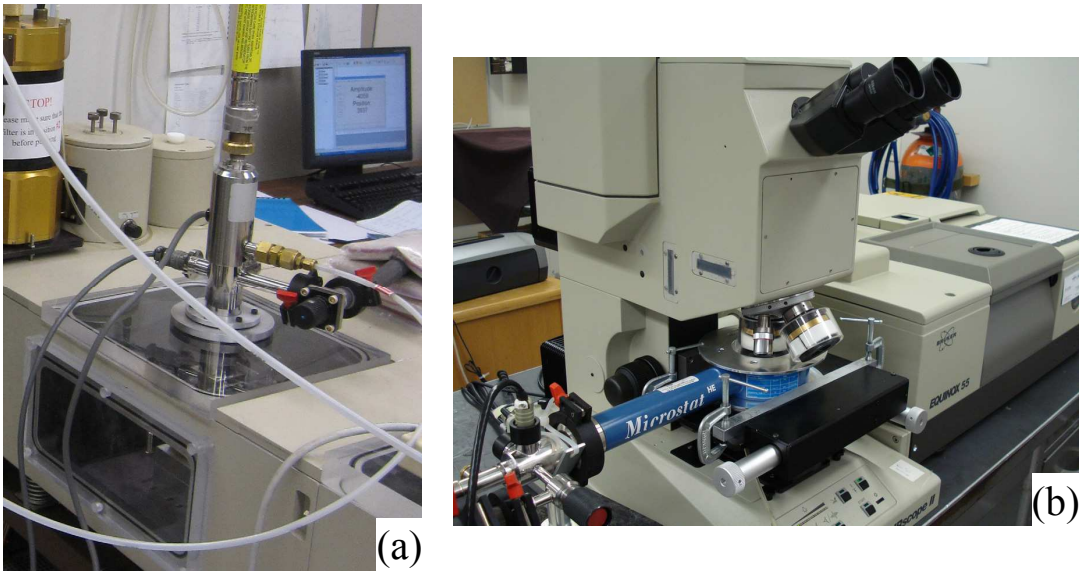

Figure 3.26: (a) and (b) Close-up views of the cryostats mounted for optical measurements in Bruker IFS 113v and Bruker Equinox 55, respectively.

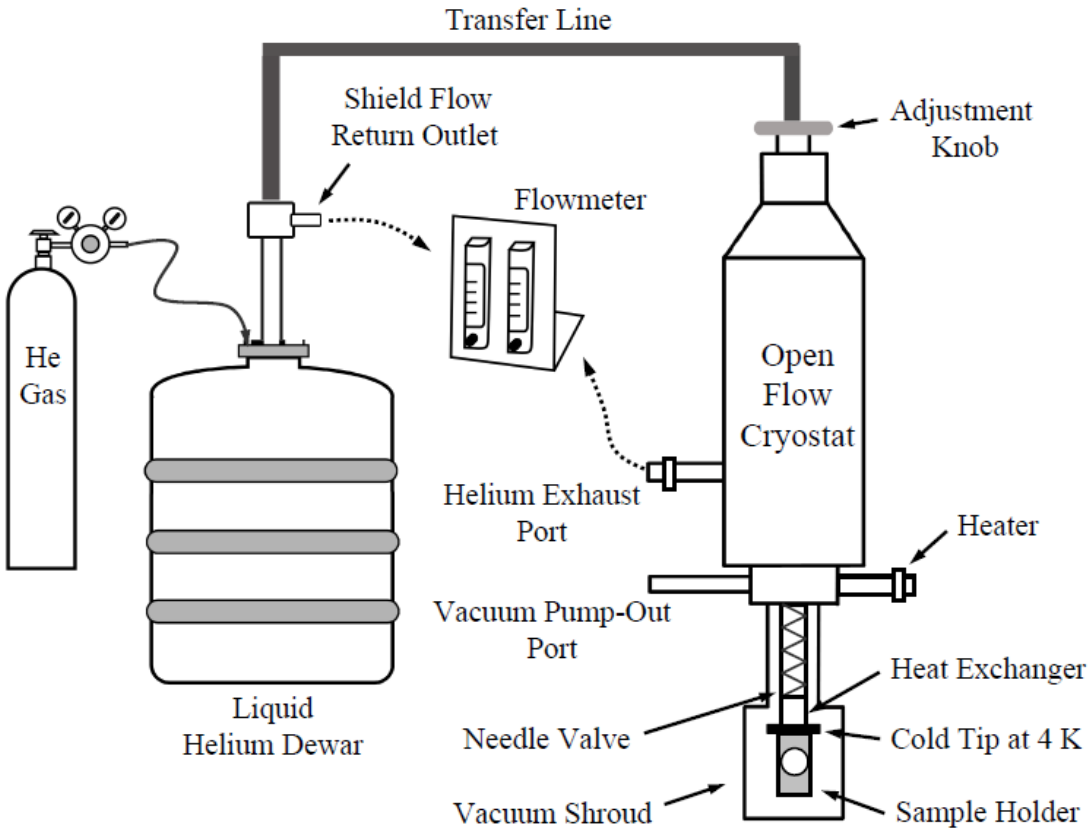

Figure 3.27: Set-up of LT-3-110 Heli-Tran liquid transfer line and cryostat.

line permits precise control of the flow rate. The cooling rate can be regulated by changing the pressure of the supply dewar, adjusting the flow-meter, and optimizing the position of the needle valve. It often takes about 25 min to pre-cool the system, and the lowest stable temperature obtained of ~ 4.2 K takes on the order of 60-90 min.

In the low-temperature experiments, the thermal contact is improved by applying crycon grease or Indium foil between the cold stage of the cryostat and the sample holder. A sample is mounted by applying GE Varnish, silver paste, and/or silver

paint. There are two thermal sensors that are used in conjunction with the cryostat, one is embedded in the cold stage/finger tip, the other hangs free until experimenter attaches it to the sample holder. In this configuration, the temperatures provided by the two sensors allow us to approximate the real sample temperature. As for high-temperature experiments, the thermal contact is improved by applying silver paint between the sample and sample holder, while also securing the sample to the sampler holder. GE Varnish and silver paste have to be avoided because they will melt, potentially covering the sample and thus changing the optical signal.

An issue that arises in the process of high-temperature investigations, paint and other surface containments evaporate from the surface and deposit onto the sample, windows, and cryostat housing. This gives rise to features appearing in the spectra that are not related to the sample itself. Since the cryostat housing is pumped continuously the pressure reaches a static point (steady-state pressure) and thus the net flux of gas is negligible or resulting in an environment that does not have a pressure gradient. So, when the contaminants eject from the surface they are not directly pumped away, thus they continue on a collision course path with the housing, windows, and sample. To overcome this, it is my experience that one should purposely oxidize the surface of the sample holder because the process of cleaning with solvents and scrubbing is not sufficient to remove the contaminants. The surface oxidation should help to remove contaminants that are on the surface by evaporating them. After oxidizing one should polish the areas of contact with the sample, mirror, thermocouple, and cryostat.

3.4.2 Experimental Set-up at the NHMFL

Various magnet forms that are taking shape and being built at NHFML including superconducting, resistive, hybrid, and pulsed magnets (Fig. 3.28). The world record magnets and magneto-optics facilities at NHMFL make it possible to investigate the unusual nature of low-dimensional solids in very high magnetic fields.

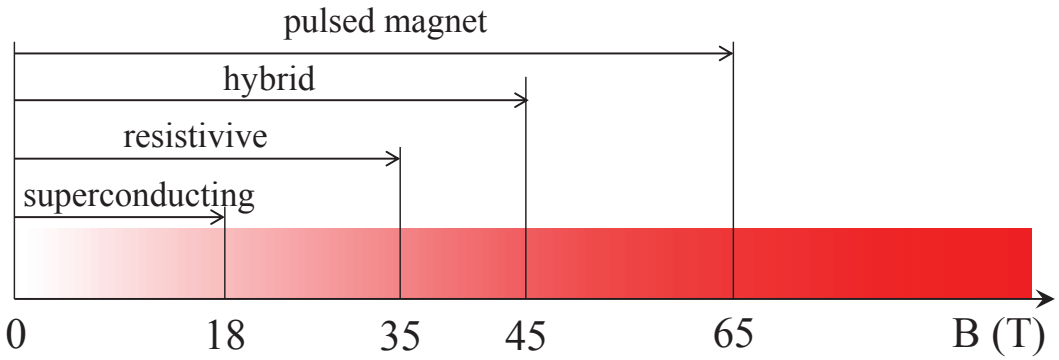

Figure 3.28: A schematic energy scale of various magnets (superconducting, resistive, hybrid, and pulsed magnets) at NHMFL.

Figure 3.29 displays a schematic of the optical set-up for magnetic circular dichroism (MCD) measurements in the 10 T Oxford superconducting magnetic (Spectromag.) The MCD measurements were performed in transmission mode, using a 300 W Xe lamp, a 1/4 m monochromator, and a ^{3}He insert to reach 1.6 K. The signal-to-noise ratio was increased by chopping unmodulated light; dynamic separation of right and left circularly polarized light (RCP & LCP) in time, $\delta(t) = \lambda/4 \sin(\omega t)$, was achieved by passing linearly polarized light through a photoelastic modulator. These signals were separated by standard lock-in amplifier methods. The probe has to be carefully positioned in the magnet so that the sample is at the center of the field. It is also important to keep the magnetic field vector $\vec{B}$ and light propagation

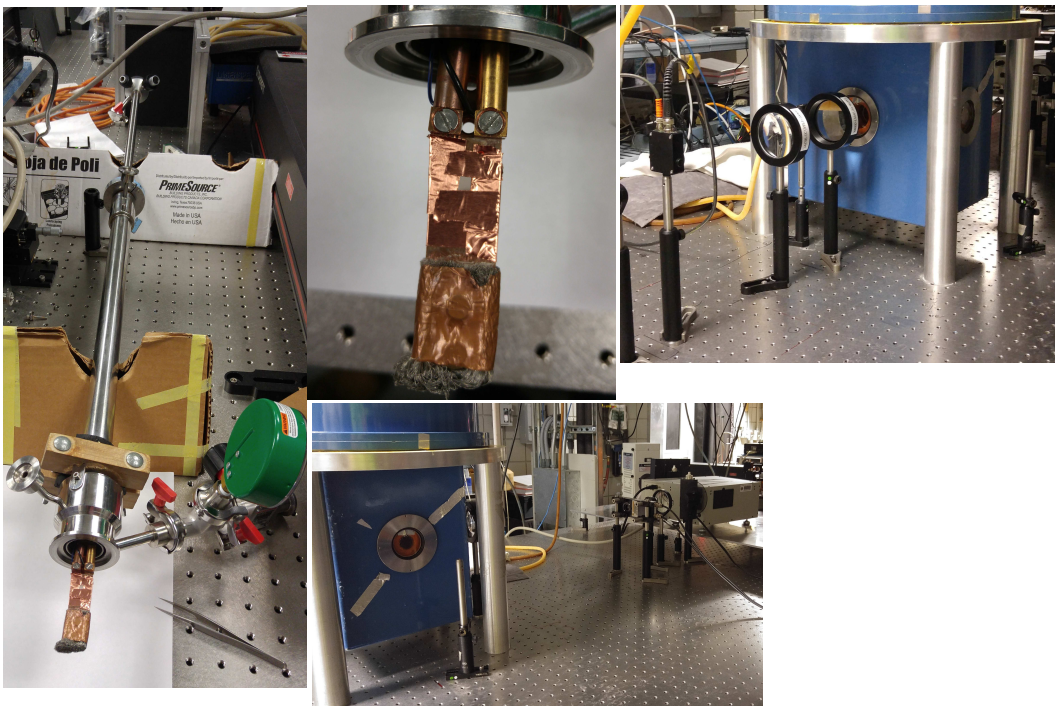

Figure 3.29: A schematic and images of magnetic circular dichroism set-up in a superconducting magnet at NHMFL.

vector $\vec{k}$ perpendicular to the plane of the film, perpendicular to the film surface.

A unique magnet that was designed, developed, and built at NHMFL is the Split-Florida Helix magnet [Fig. 3.30]. Figure shows a cutaway schematic of the magnet design. This magnet consists of two resistive coils with four wide optical ports. These ports are used to shine light on the sample from the horizontal plane, giving access to more intricate and complicated measurements. We used this magnet to do magnetic circular dichroism (MCD). The MCD measurements were performed using a 300 W Xe lamp and a 1/4 meter monochromator. The signal-to-noise ratio was increased by chopping unmodulated light; dynamic separation of right and left circularly polarized light (RCP & LCP) in time, $\delta(t) = \lambda/4 \ \sin(\omega \ t)$, was achieved by passing linearly

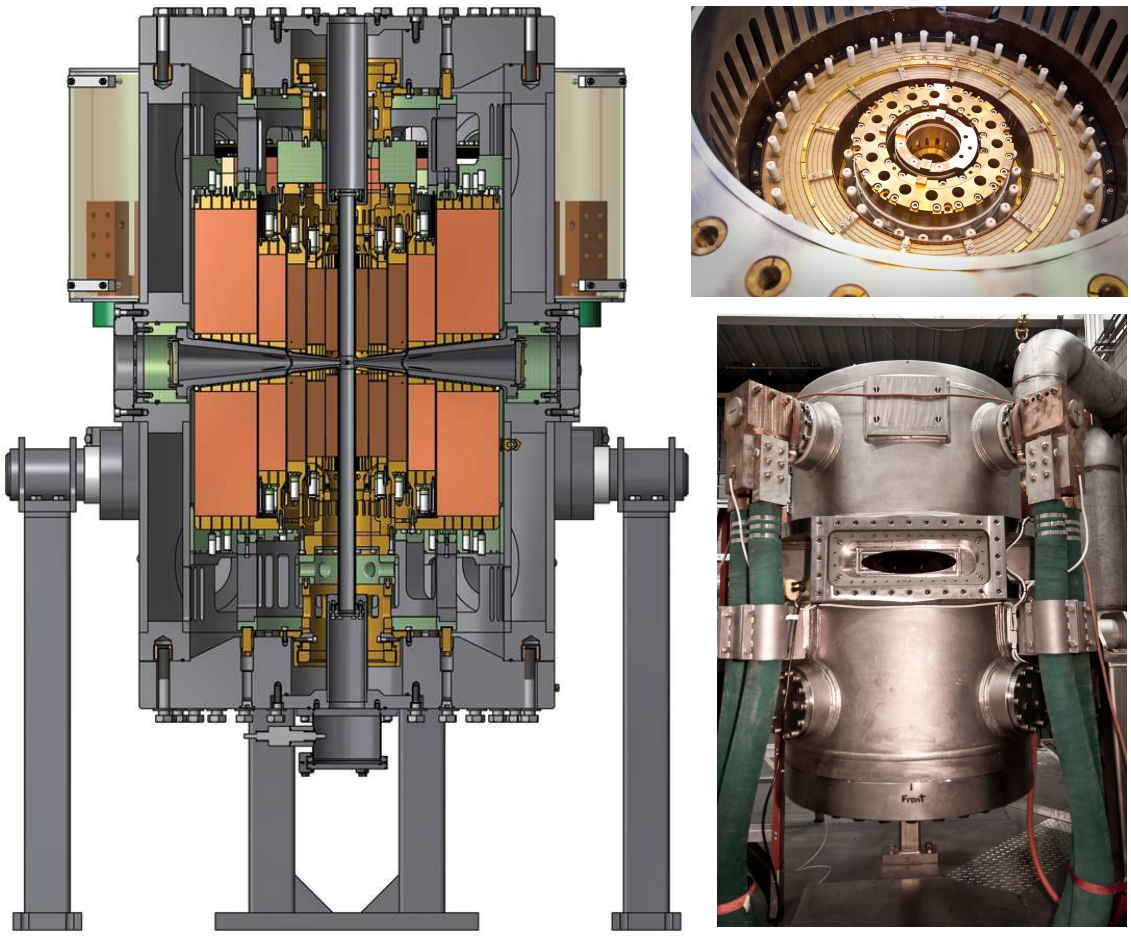

Figure 3.30: A cutaway schematic and images of resistive magnetic used for magnetic circular dichroism set-up at NHMFL. Bottom displays a schematic of the optical path layout, as viewed from above. Images available from http://nationalmaglab.org

polarized light through a photoelastic modulator. These signals were separated by standard lock-in amplifier methods. On this magnet the horizontal plane ports were used to access the vertical axis of the magnet without the use of fiber-optics and allowed light to be shined on the samples. For both investigative environments [Figs. 3.29 and 3.30] a plethora of directly controllable variable arise, i.e. photon energy (E), temperature (T), magnetic field (H), and helicity of the light ($\sigma^{\pm}$); therefore, the general MCD response takes the form of $\Delta\alpha(E, T, H, \sigma^{\pm})$.[554, 555]

3.4.3 Experimental high voltage field

"High field" applies to more than high magnetic field, for this thesis it also applies to high electric fields. The magnitude of the electric field in our setup can reach levels as high as $2e^6 V\,m^{-1}$, where the breakdown voltage of dry air is on the order of $3e^6 kV\,m^{-1}$. We are able to reach this by having a separation of our electrodes of 250 µm. By sweeping across the voltage axis we are able to investigate the response linearity, we check for linearity because this can provide insight into the transport mechanisms. One of the many plans for continued development for this instrument is to deposit the pads at a variety of spacings, primarily with the intent to decrease the separation of electrodes.

3.5 Materials of Interest: Measurements and Calculations

3.5.1 $NiFe_2O_4$

$NiFe_2O_4$ is a superb research platform for exploring the interplay between charge excitations and interpenetrating magnetic sublattices. This system crystallizes in an inverse spinel structure (cubic space group $Fd\bar{3}m$), where the Ni^{2+} cations occupy interstitial octahedral sites and the Fe^{3+} cations are equally distributed between octahedral and tetrahedral locations. [284, 285] Antiferromagnetic coupling of the sublattices cancels the Fe moments, while the Ni^{2+} spins remain uncompensated,[277] resulting in a theoretical net macroscopic magnetic moment of $2\,\mu_B$ and $T_C = 850\,\mathrm{K}$. [286] Magnetic field drives a reorientation of the Ni spins at a critical field $B_{c(Ni)}$ of 0.3 T. [286] The Fe spins presumably saturate at much higher fields ($B_{c(Fe)}$).

The density of state displays the well-known spin-split valence and conduction bands. The latter arises naturally from coupling of the two independent sublattices and suggests that $NiFe_2O_4$ may be able to support spin-polarized optical excitations. [284, 307] Recent electronic structure calculations combined with linear optical spectroscopy revealed $NiFe_2O_4$ as an indirect gap material.[556] In fact, the 1.6 eV indirect gap along with the 2.4 and 2.8 eV direct gaps overlap the solar spectrum.[556] That said, questions have arisen [557] about the indirect nature of the 1.6 eV gap that require deeper investigation. Additionally, experimental evidence verifying (or refuting) key aspects of the predicted electronic structure[556, 284] is highly desirable.

In this work, we bring together magnetic circular dichroism (MCD), photo-

conductivity, and first-principles calculations with prior optical absorption spectroscopy [556] to unravel the electronic structure of $NiFe_2O_4$. Analysis reveals a large number of field-tunable states that can be attributed to minority channel excitations, significant spectral differences across the metamagnetic transition that are traced to coupling between the Ni spin orientation and the minority channel Ni $\rightarrow$ Fe charge transfer excitations, exchange splittings of 0.2 to 0.3 eV depending on the excitation, and enhanced photoconductivity between the two minority channel gaps under applied field. Together these findings establish an energy window or "sweet spot" in the electronic structure that can be used for generating spin-polarized carriers with light and, at the same time, demonstrate how they can be manipulated with magnetic field. These discoveries are important in the continuing race to generate, manipulate, and detect spin polarized currents and highlight new opportunities in the area of oxide electronics.[302, 558, 307, 4]

Thin film growth

Epitaxial $NiFe_2O_4$ thin films were grown by Arun Gupta's team at University of Alabama. A series of films grown at temperatures between 175–700 °C (448–973 K) with a thickness range of ≈50 - 250 nm were deposited on $MgAl_2O_4$ substrates by pulsed laser deposition. The resulting space group was $Fd\bar{3}m$.[286]

Transmittance and reflectance measurements

Near-infrared, visible, and near-ultraviolet transmittance and reflectance spectra were collected using a Perkin-Elmer Lambda-900 spectrometer (3200 – 190 nm; 0.41 – 6.53 eV), spectral resolution was 1 nm in the whole range. Aluminum mirrors

were used as references for reflectance measurements. We calculated the absorption coefficient $\alpha(E)$ using Glover-Tinkham analysis from combined transmittance and reflectance measurements.[347] Kramers-Kronig analysis was also used to calculate $\alpha(E)$ of the pure reflectance in the region where transmittance falls to ≈0%. Variable temperature measurements between 4.2 and 800 K were also carried out, using an open-flow helium cryostat and temperature controller.

Band gap determination

The theory of energy gap determination in solids is well established. The absorption coefficient, $\alpha(E)$, consists of contributions from both the direct and the indirect band gap transitions [559, 560], and is given by

$$\alpha(E) = \frac{A}{E}(E - E_{g,dir})^{\frac{1}{2}} + \frac{B}{E}(E - E_{g,indir} \mp E_{ph})^2, \tag{3.150}$$

where $E_{g,dir}$ and $E_{g,ind}$ are the magnitude of direct and indirect gaps, respectively, E_{ph} is the emitted (absorbed) phonon energy, and A and B are constants. The precise profile assumes a simple band shape and may not be exactly followed in a material with complex band structure. The direct energy gap can be extracted by plotting $(\alpha \cdot E)^2$ as a function of photon energy (E). And the indirect energy gap can be extracted by plotting $(\alpha \cdot E)^{0.5}$ as a function of photon energy (E).

Field dependent measurements - magnetic circular dichroism

The magneto-optical, MCD, properties were measured at the National High Magnetic Field Laboratory (NHMFL) in Tallahassee, FL, using 10 T Oxford supercon-

ducting magnet in transmission mode, a 300 W Xe lamp, a 1/4 meter monochromator, an optical chopper, optical lenses, a linear polarizer, and photoelastic modulator, the magnet produces magnetic fields up to 30 T. The signal-to-noise ratio was increased by chopping unmodulated light; dynamic separation of right and left circularly polarized light (RCP & LCP) in time, $\delta(t) = \lambda/4 \sin(\omega t)$, was achieved by passing linearly polarized light through a photoelastic modulator.[561] These signals were separated by standard lock-in amplifier methods.[69, 517, 562]. The experiments were carried out between 4.2 and 300 K in the spectral range of 0.8–3 eV using InGaAs and Si diode detectors. Data were collected on both increasing and decreasing magnetic field, in a loop-like pattern. The MCD response was calculated as $I_{MCD} = \frac{P_x - P_y}{C_x - C_y}$, here C is the chopper lock-in signal and P is the PEM lock-in signal.

Photoconductivity measurements

Transport measurements were carried out in the presence of a dark background and focused arc lamp beam, along with an external magnetic field. We used a series of bandpass filters, covering the spectrum from 2000-300 nm (0.62-4.13 eV), to obtain information about how the electronic structure connects to the transport properties. The external magnetic field, on the order of 1.5 T, allows one to investigate correlation between the electronic structure and the magnetic properties. To proceed with these measurements we deposited gold "pads" on the surface of a cleaned sample by negative images of the mask. The pads are 250 μm in diameter and their closest edges are 250 μm apart, this allows us to establish an electric field, $\vec{E} = V/d$, up to 2 000 000 V m^{-1} with a high-voltage source. To establish the electric field we used

tungsten needle tips to contact the pads. We were able to investigate the frequency dependent magnetoresistance by measuring the current in a combination of environments. To extract valuable information out of the combined environments in this measurement, we applied the following equation,

$$MR_{ph} = 100\% \frac{(\rho_{H,h\nu} - \rho_{0,h\nu})}{\rho_{0,h\nu}} \tag{3.151}$$

Here, $\rho_{x,y}$ is the resistance with the x, y representing the presence (or lack there of) for a magnetic field (H) and photons ($h\nu$.) In this case we were able to establish a frequency dependence to the magnetoresistance but not isolate the pure component related to the light and field coupling to alter the magnetoresistance.

3.5.2 $CoFe_2O_4$

Multifunctional, high Curie temperature (T_C) magnetic insulators are attracting attention due to their suitability for application. They naturally provide a non-zero magnetic moment along with spin-dependent band gaps that can be utilized in spintronics[282] as well as in emerging areas such as spin-caloritronics.[563] Examples include spin-filters[564, 283] and spin-transfer torque devices.[282] Among the various candidate materials, the most noteworthy are strongly-correlated spinel oxides (general formula AB_2O_4),[565] particularly the spinel ferrites (general formula AFe_2O_4). While high quality single crystals are challenging to grow, thin film spinel ferrites have allowed researchers to investigate structural [566], electronic [567, 290, 289], and transport [568, 569, 570, 571] properties. Recent spectroscopic work on nickel ferrite

($NiFe_2O_4$) also revealed a hierarchy of band gaps,[314, 572] and a favorable overlap with the solar spectrum. $CoFe_2O_4$ is another high T_C material that presents an opportunity to quantify charge gaps and electronic structure trends within the spinel ferrite family. Prior theoretical work focused primarily on magneto-elastic properties and cation-ordering [291, 290, 289, 288] due to challenges both in accounting for electron correlation effects and the absence of reliable experimental gap values.

In this work, we bring together high quality film grown, optical properties work, and first principles calculations to investigate the electronic structure of $CoFe_2O_4$. This system displays an indirect gap at 1.2 eV and a direct gap at 2.7 eV. In addition to resolving the long-standing band gap controversy in $CoFe_2O_4$ (with values between 0.11 and 2.6 eV quoted in the literature)[296, 573] and showing the robustness of the 2.7 eV gap on approach to T_C, we reveal how the charge gaps, electronic structure, and band dispersions change with chemical substitution. For instance, we find that the minority channel $X \rightarrow \Gamma$ indirect gap is almost 0.5 eV lower than that in the Ni analogue. The improved overlap with the solar spectrum, which offers electronic and light harvesting functions, combined with the modest temperature dependence of the 2.7 eV features establishes $CoFe_2O_4$ as a robust magnetic semiconductor and a promising material for applications.

Thin film growth

Epitaxial $CoFe_2O_4$ thin films were grown by Arun Gupta's team at University of Alabama. A series of films grown at temperatures between 175–700 °C with a thickness range of ≈50 - 250 nm were deposited on $MgAl_2O_4$ substrates by pulsed laser deposition. The resulting cubic space group was $Fd\bar{3}m$.[286]

Transmittance and reflectance measurements

Near-infrared, visible, and near-ultraviolet transmittance and reflectance spectra were collected using a Perkin-Elmer Lambda-900 spectrometer (3200 – 190 nm; 0.41 – 6.53 eV), spectral resolution was 1 nm in the whole range. Aluminum mirrors were used as references for reflectance measurements. In the regime where both transmittance and reflectance measurements give valuable information, we used Glover-Tinkham and Kramers-Kronig analysis methods to calculate the absorption coefficient $\alpha(E)$.[347, 346] Kramers-Kronig analysis was also used to calculate $\alpha(E)$ of the pure reflectance in the region where transmittance falls to ≈0%. Variable temperature measurements between 4.2 and 800 K were also carried out, using an open-flow helium cryostat and temperature controller.

Band gap determination

The theory of energy gap determination in solids is well established, the energy required to excite an electron from a valence band maximum to a conduction band minimum. The absorption coefficient, $\alpha(E)$, consists of contributions from both the direct and the indirect band gap transitions [559], and is given by

$$\alpha(E) = \frac{A}{E}(E - E_{g,dir})^{\frac{1}{2}} + \frac{B}{E}(E - E_{g,indir} \mp E_{ph})^2, \tag{3.152}$$

where $E_{g,dir}$ and $E_{g,ind}$ are the magnitude of direct and indirect gaps, respectively, E_{ph} is the emitted (absorbed) phonon energy, and A and B are constants. The precise profile assumes a simple band shape and may not be exactly followed in a material with complex band structure. The direct energy gap can be extracted by

plotting $(\alpha \times E)^2$ as a function of photon energy (E). The indirect energy gap can be extracted by plotting $(\alpha \times E)^{0.5}$ as a function of photon energy (E) and establishing a linear extrapolation to $y = 0$ for both cases.

Magnetic field dependent measurements - magnetic circular dichroism

The magneto-optical properties were measured, via MCD, at the National High Magnetic Field Laboratory (NHMFL) in Tallahassee, FL, using 10 T Oxford superconducting magnet (Spectromag) in transmission mode, a 300 W Xe lamp, a 1/4 meter monochromator, a optical chopper, optical lenses, a linear polarizer, and photoelastic modulator, the magnet produces magnetic fields up to 30 T. The signal-to-noise ratio was increased by chopping unmodulated light; dynamic separation of right and left circularly polarized light (RCP & LCP) in time, $\delta(t) = \lambda/4 \sin(\omega t)$, was achieved by passing linearly polarized light through a photoelastic modulator. These signals were separated by standard lock-in amplifier methods.[69, 517, 562]. The experiments were carried out between 4.2 and 300 K in the spectral range of 0.8 - 3 eV using InGaAs and Si diode detectors. Data were collected on both increasing and decreasing magnetic field, in a loop-like pattern. The MCD response was calculated as $I_{MCD} = \frac{C_x - C_y}{P_x - P_y}$, here C is the chopper lock-in signal and P is the PEM lock-in signal. The sample is placed so as to be in the center of the magnetic field, with the field vector $\vec{B}$ pointing perpendicular to the surface plane of the film. The light propagation direction $\vec{k}$ is either parallel or antiparallel to $\vec{B}$, depending upon the sign of the field.

Photoconductivity measurements

Transport measurements were carried out in the presence of a dark background and focused arc lamp beam, along with an external magnetic field. We used a series of bandpass filters, covering the spectrum from 2000-300 nm (0.62-4.13 eV), to obtain information about how the electronic structure connects to the transport properties. The external magnetic field, on the order of 1.5 T, allows one to investigate correlation between the electronic structure and the magnetic properties. To proceed with these measurements we deposited gold "pads" on the surface of a cleaned sample by negative images of the mask. The pads are 250 μm in diameter and their closest edges are 250 μm apart, this allows us to establish an electric field, $\vec{E} = V/d$, up to 2,000,000 V/m with a high-voltage source. We used two approaches to contact the pads/sample, first we used tungsten needles with a tip diameter of either 5 or 25 μm and then second we used 80 μm copper "magnet" wire along with silver epoxy to establish a more solid/continuous contact.

$$MR_{ph} = 100\% \frac{(\rho_{H,h\nu} - \rho_{H,0}) - (\rho_{0,h\nu} - \rho_{0,0})}{(\rho_{0,h\nu} - \rho_{0,0})}. \tag{3.153}$$

Here, $\rho_{x,y}$ is the resistance with the x, y representing the presence (or lack there of) for a magnetic field (H) and photons ($h\nu$.) In this case we were able to isolate the component of the magnetoresistance that corresponds purely to the light and magnetic field being present, due to some steps taken to increase the sensitivity by at least an order of magnitude. These two components couple together giving a final result that is dependent upon them both being present. From this measurement we are able to establish frequency dependence of the coupled output.

First-principles investigation

Electronic band structure calculations were performed with the Vienna *ab-initio* simulation package (VASP)[292, 293] on a relaxed 14-atom primitive $CoFe_2O_4$ cell using LDA+U and GGA+U techniques (U_{eff} = 4.5 eV for Fe and 4.0 eV for Co)[115] and projector augmented wave pseudopotentials.[295, 292, 293] Additional 28-atom supercell calculations were performed to understand the effect of partial inversion on the electronic properties. We employed a plane wave cutoff of 500 eV and a Γ-centered $7 \times 7 \times 7$ **k** mesh for the 14-atom density of states (DOS) and relaxation calculations.

3.5.3 *h*-$LuFeO_3$

High temperature multiferroics with strong magnetoelectric coupling are immensely desirable for magnetic memory, tunable filtering, energy harvesting, and medical/biotechnology applications [574]. Single phase materials have, however, proven elusive; at least under a classical definition where they must be simultaneously ferroelectric (d^0) and ferromagnetic ($d^{\neq 0}$) [177, 181]. The more logical approach to obtaining multiferroics from the classical definition using current technology and understanding involves multi-phase (composite and heterostructure) materials, such as $BaTiO_3$–$CoFe_2O_4$, $BiFeO_3$–$CoFe_2O_4$, and $La_{0.67}Sr_{0.33}MnO_3$–$BaTiO_3$.[40, 575, 576, 577, 42, 39] These combinations result in a magnetoelectric phase via strain-driven Once the description was broadened to include other forms of magnetism [212], viable candidates including $BiFeO_3$, $LuFe_2O_4$, and $TbMnO_3$ emerged [224, 578, 579, 580, 196]. Another recent approach approach for obtaining multiferroism and an increased

T_C is by locating the contribution of order (ferroelectric or magnetism) on separate ions, a prominent example is that of $BiFeO_3$.[98] Further broadening to include field-induced multiferroics led to the inclusion of CuO and hexaferrites [581, 582]. In type I multiferroics it is possible to have an appreciably increased temperature range of overlap[212] however the cross coupling of the magnetism and ferroelectricity is typically weak[580, 583, 99]. What distinguishes these compounds is their ability to overcome the contradictory requirements for ferroelectricity and magnetism, albeit by different mechanisms and with various degrees of cross-coupling. One of the candidates, h-$LuFeO_3$, was originally typed as a room temperature multiferroic [80]. Just like the relative material ($LuFe_2O4$) this was dismantled.[584, 53] This system has hexagonal symmetry with space group $P6_3cm$ in epitaxially stabilized thin films. It is ferroelectric below 1020 K and a non-collinear antiferromagnet below 147 K [584]. This system is a derivative of $LuFe_2O_4$, which has a fascinating phase diagram series of relatively high temperature charge, spin, and structural transitions [82, 331] that emanates from the interplay between charge, structure, and magnetism.

Theorists investing their efforts into material initiatives have predicted many "high" temperature multiferroic materials but due to complications in synthesis techniques these materials have yet to be realized.[585] A number of new candidate multiferroic materials that have been successfully synthesized include CuO[581] and the hexagonal rare-earth manganites and ferrites such as $YMnO_3$ and $LuFe_2O_4$ respectively. Composites (heterostructures) that separate the component of ferroelectricity and ferromagnetism come in many flavors e.g. superlattice or rods and nanoparticles in a matrix.[3, 586, 587]

High quality epitaxial h-$LuFeO_3$ films, of depth 50 nm, were grown at 800°C on (111)-orientated yttria-stabilized zirconia substrates using molecular-beam epitaxy [584], and film quality was assessed by x-ray diffraction and susceptibility. Optical measurements were carried out using a Perkin-Elmer λ-900 spectrometer (0.41-6.53 eV) in both transmittance and reflectance mode, and the absorption [$\alpha(E)$] was determined via combined Glover-Tinkham and Kramers-Kronig techniques [399]. Magnetic circular dichroism (MCD) was performed at the National High Magnetic Field Laboratory, Tallahassee using the Split-Florida Helix magnet up to 30 T [588]. The beam path included a monochrometer, chopper, and photoelastic modulator connected to individual lock-in amplifiers, this is thoroughly discussed previously Subsubsec. 3.3.3. The MCD signal was determined from the ratio of the photoelastic modulator and beam chopper responses, respectively. These signals were separated by standard lock-in amplifier methodology.[562] Photoconductivity was performed on a custom-made setup that included a Xenon lamp, contact tips, picoammeter, and power meter, along with a series of narrow bandpass filters and a sputtering system for deposition of 250 μm Pt contacts. The narrow bandpass filters covered the range of 0.62–3.65 eV allowing for capturing slices of the optical spectrum. The contacts were First principles calculations were performed using the density functional theory + U method including spin-orbit coupling, as implemented in the full-electron WIEN2K package with U=4.5 eV and J=0.95 eV for Fe.

Thin film growth

Epitaxial h-$LuFeO_3$ thin films were grown by Darrell G. Schlom's team at Cornell University. Films were grown ≈800 °C with thickness ≈50 nm were deposited on

Yttria-stabalized Zirconia substrates by molecular-beam epitaxy.[222]

Transmittance and reflectance measurements

The near-infrared, visible, and near-ultraviolet spectra were measured with a modified Perkin-Elmer λ-900 spectrometer. Variable temperature spectroscopies were carried out between 4.2 and 600 K using an open-flow helium cryostat and temperature controller. Spectral resolution was 1 nm in the near-infrared, visible, and near-ultraviolet. The absorption spectrum was calculated from the transmittance and reflectance using Glover-Tinkham and Kramers-Kronig analysis.

Field dependent measurements - magnetic circular dichroism

The magneto-optical, MCD, properties were measured at the National High Magnetic Field Laboratory (NHMFL) in Tallahassee, FL, using the Split-Florida Magnet, a 300 W Xe lamp, a 1/4 meter monochromator, a optical chopper, optical lenses, a linear polarizer, and photoelastic modulator, the magnet produces magnetic fields up to 30 T. The signal-to-noise ratio was increased by chopping unmodulated light; dynamic separation of right and left circularly polarized light (RCP & LCP) in time, $\delta(t) = \lambda/4 \sin(\omega t)$, was achieved by passing linearly polarized light through a photoelastic modulator. These signals were separated by standard lock-in amplifier methods.[69, 517, 562]. The experiments were carried out between 4.2 and 300 K in the spectral range of 0.8 - 3 eV using InGaAs and Si diode detectors. Data were collected on both increasing and decreasing magnetic field. The MCD response was calculated as $I_{MCD} = \frac{C_x - C_y}{P_x - P_y}$, here C is the chopper lock-in signal and P is the PEM lock-in signal.

MCD was used to measure a spectrally resolved picture of the magnetization dependence on the underlying electronic structure and give understanding of their coupling. MCD is fundamentally a detection of the difference in transmission of right- and left-circularly polarized light (T_R and T_L, respectively), $(T_R - T_L)/(T_R + T_L)$. If a response is detected this can be first attributed to the existence of a time-reversal-symmetry-breaking (time non-invariant) phenomena e.g. magnetization. MCD response also arises due to spin-orbit interaction. These occur over specific wavelength regimes and thus can elucidate the coupling of a magnetic specimen, such as magnetic semiconductors, to optical constants of the investigated material. Our MCD measurements were carried out at the National High Magnetic Field Laboratory, samples were mounted in a 10 T superconducting magnet with direct optical access, in transmission mode at 1.6 K. The optical path consisted of a 300 W Xe lamp, and a 1/4 meter monochromator, followed by lenses and a glan-cube to obtain linear polarized light. The signal-to-noise ratio was increased by chopping the light, followed by dynamic separation of right and left circularly polarized light (RCP and LCP) in time, $\delta(t) = \lambda/4 \sin(\omega t)$, was achieved by passing linearly polarized light through a photoelastic modulator (PEM).[70, 64] The modulated light was detected by a combination of detectors, Si and InGaAs diodes. These signals were separated by standard lock-in amplifier methods, referenced to the chopper and PEM frequencies with values equivalent to $T_R + T_L$ and $T_R - T_L$, respectively.[562]

3.5.4 $LuFe_2O_4$

Thin film growth

Epitaxial $LuFe_2O_4$ thin films were grown by Darrell G. Schlom's team at Cornell University. Films were grown ≈800 degC with thickness ≈75 nm were deposited on $MgAl_2O_4$ substrates by molecular-beam epitaxy.[337]

Transmittance and reflectance measurements

The optical absorption coefficient was determined by measuring the transmittance and reflectance over 0.5–6.5 eV. In the range below 3.0 eV we used pure transmittance data to calculate the absorption coefficient. Above this regime, we implemented Glover-Tinkham analysis in the range where transmittance and reflectance data were both of vital importance to determine the optical properties of the film.[337] The data were merged in the range of 2.5–3.0 eV due to significant overlap and shape trends.

Chapter 4

Magnetic field tunability of spin-polarized excitations in a high-temperature magnet

Magnetic atoms, such as Iron, keep
Unpaired Electrons in their middle shell,
Each one a spinning Magnet that would leap
... In Units growing visible, the World we wield!

John Updike

Midpoint - THE DANCE OF THE SOLIDS

In order to comprehend the spin-charge interactions in $NiFe_2O_4$, we employed MCD, (magneto-)photoconductivity, and complementary first principle calculations along with prior optical absorption to unravel the intricacies of electronic structure

in this system. Analysis of the MCD elucidated a large number of spin down states that are well isolated; additionally, photoconductivity that depends on magnetic field, helps reveal a metamagnetic transition involving spin on the Ni center that switches the electronic structure of this system. These findings open the door for the creation and control of spin polarized excitations from minority channel charge transfer in spinel ferrites.[127, 302, 558, 307, 4]

4.1 Exploring the metamagnetic transition involving the Ni spin flip

Magnetic field drives a reorientation of the Ni spins at a critical field $B_{c(Ni)}$ of 0.3 T [Fig. 4.1 (b)].[286] The Fe spins presumably saturate at much higher fields ($B_{c(Fe)}$). Figure 4.1(c) displays the calculated density of states with well-known spin-split valence and conduction bands. The latter arises naturally from coupling of the two independent sublattices and suggests that $NiFe_2O_4$ may be able to support spin-polarized optical excitations.[284, 307, 589] Recent electronic structure calculations combined with linear optical spectroscopy revealed $NiFe_2O_4$ as an indirect gap material.[556] In fact, the 1.6 eV indirect gap along with the 2.4 and 2.8 eV direct gaps overlap the solar spectrum.[556] That said, questions have arisen [557] about the indirect nature of the 1.6 eV gap that require deeper investigation. Additionally, experimental evidence verifying (or refuting) key aspects of the predicted electronic structure[556, 284] is highly desirable. Strikingly, we find - via the combination of a carefully coordinated series of advanced experiments and calculations - that $NiFe_2O_4$ supports magnetic

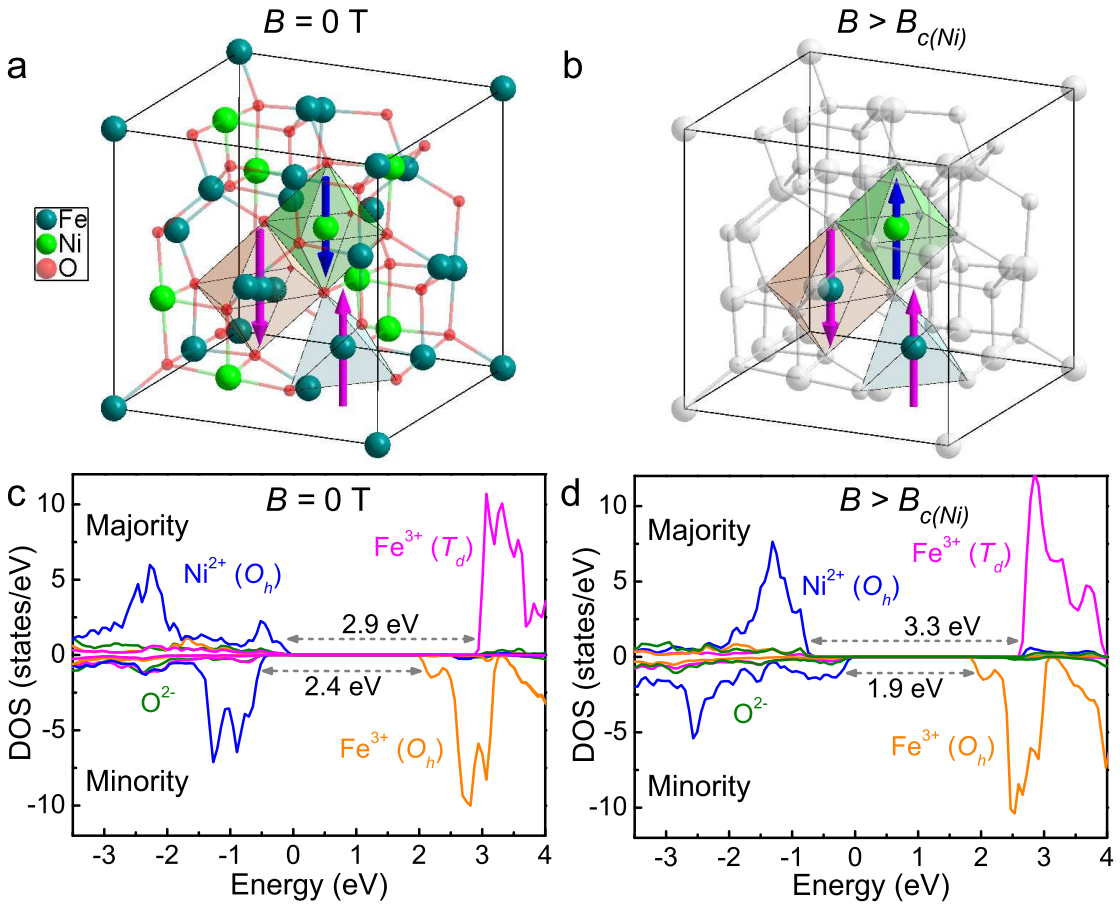

Figure 4.1: (a, b) Crystal structure of $NiFe_2O_4$ showing the spin configuration at zero field and above $B_{c(Ni)}$ where the Ni spin is flipped to align with the field. (c, d) Projected density of states (DOS) from hybrid functional calculations[556] depicting Ni (O_h) to Fe (T_d and O_h) charge transfer excitations in the minority and majority channels in the two spin configurations of interest.

field tunable spin-polarized excitations.

4.2 Experimental evidence for tunability and control of spin-polarized excitations

4.2.1 Optical signatures of spin-polarized excitations

Figure 4.2(a) displays the MCD spectrum of $NiFe_2O_4$ in an applied field of ± 10 T at 1.6 K. The linear absorption spectrum ($\alpha(E)$) is included for comparison, and the 1.6, 2.4, and 2.8 eV band gaps are indicated on the energy axis.[556] Examination of the spectra in Fig. 4.2(a) immediately reveals a large number of states below the majority channel gap. The local maxima in the dichroic response also coincide with inflection points in the absorption. This correspondence demonstrates an important derivative relationship that we discuss in detail below.

MCD is a powerful tool for unveiling spin-dependent electronic structure because it probes the field-induced difference in the absorption between right- and left-circularly polarized light (RCP and LCP, often denoted as + and -).[547, 590, 591] The magnitude of the dichroic response, I_{MCD}, can be expressed as: [590, 591]

$$I_{MCD} \approx \frac{(\alpha_+(E) - \alpha_-(E))d}{2} \approx \frac{\Delta E}{2} \frac{1}{\alpha(E)} \frac{d\alpha(E)}{dE}. \tag{4.1}$$

Here, $\alpha(E)$ is the linear absorption, $\alpha_+(E) - \alpha_-(E)$ represents the differential absorption between RCP and LCP light, $d\alpha(E)/dE$ is the derivative of absorption

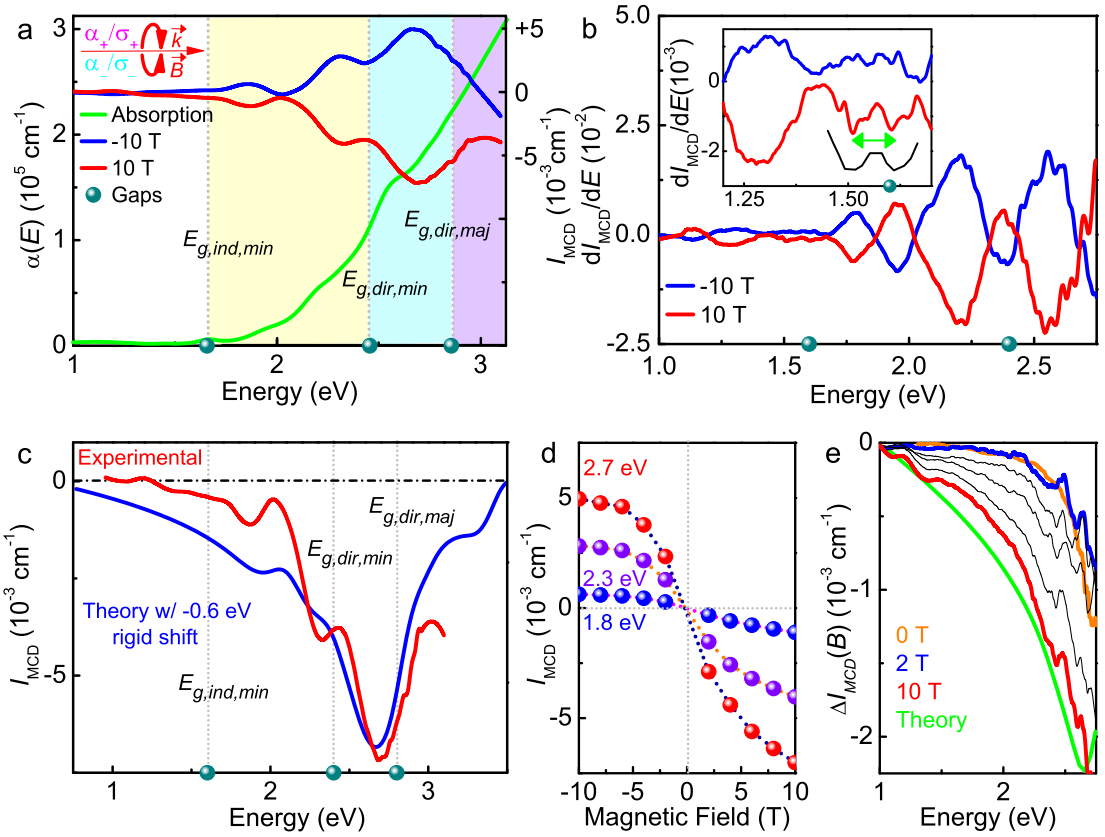

Figure 4.2: (a) MCD spectra of $NiFe_2O_4$ at ± 10 T along with the linear absorption. The points on the energy axis define the band gaps,[556] and the shaded regions emphasize the character of the excitations in each energy window. The schematic in upper left show correlation between geometry of the transitions and optical path in the Faraday geometry. Here, $\alpha_{\pm}$ and $\sigma_{\pm}$ are the absorption coefficient and helicity intensities, respectively. $\vec{k}$ and $\vec{B}$ are the propagation and magnetic field directions, respectively. (b) Derivative of I_{MCD}, along with inset emphasizing the spectral asymmetry near 1.57 eV and 100 meV splitting. (c) Comparison of experimental and theoretical MCD spectra (with a rigid shift of -0.6 eV). (d) MCD intensity at constant energies vs. field. The dashed lines guide the eye. (e) Residual MCD signal obtained from the difference of I_{MCD} in the positive and negative field directions along with the corresponding theoretical difference between the calculated MCD response when Ni spin is parallel to Fe (O_h) vs. Fe (T_d) moments.

with respect to energy, ΔE is the change in energy of the peak position, and d is the thickness of the film. Further, the resulting contrast in $\alpha_{\pm}(E)$ correlates with $\sigma_{\pm}$, the helicity.[590] This relationship shows a direct proportionality between I_{MCD} and $d\alpha(E)/dE$. Recalling that absorption is a joint density of states effect, the dichroic response will be related to critical points in the band structure, highlighting the link with the electronic structure. Complementary modeling of the dichroic response implemented the previously calculated matrix elements of the optical conductivity tensor [556] and the following expression for the MCD intensity:[592]

$$I_{MCD} \approx \frac{d\omega}{2c}\,\mathrm{Im}(n_{+} - n_{-}) \approx \frac{2\pi d}{c}\,\mathrm{Im}[\frac{\sigma_{xy}}{(1 + \imath\frac{4\pi}{\omega}\sigma_{xx})^{1/2}}]. \tag{4.2}$$

Here, $n_{\pm} = (\epsilon_{xx} \pm \epsilon_{xy})^{1/2}$ is the refractive index of RCP (or LCP) light arising from the dielectric function ϵ, d is film thickness, and c is the speed of light.

Returning to the spectra in Fig. 4.2(a), we see that the derivative-like features in the dichroic response of $NiFe_2O_4$ can be assigned based upon an understanding of the band structure and projected density of states.[556] Importantly, there are a large number of features in the 1.5 to 2.8 eV energy window - where only minority channel charge transfer excitations are active. This is strong evidence for spin-polarized excitations.[547, 551, 552] Spectral features emanating from on-site d-to-d excitations are also apparent.[593] In addition to being a sensitive technique for locating important features in the density of states, dispersions in the MCD spectra give reliable estimates of the spin splitting between majority and minority bands. We find exchange splittings in the range of 0.2 to 0.3 eV depending upon the excitation, in reasonable agreement with theoretical predictions.[284, 285]

Figure 4.2(b) displays the derivative of the MCD spectrum as a function of energy. This rendering shows how gap energies correspond to local extrema in dI_{MCD}/dE at 1.6, 2.4, and 2.8 eV. Another important energy scale, missed previously, appears at ≈1.8 eV. dI_{MCD}/dE in the region near the indirect gap is especially interesting.[594] A doublet structure centered at 1.57 eV, emphasized by the black line, is clearly observed in the data taken at +10 T, whereas in the opposite (-10 T) field direction, the doublet is absent. The total splitting of this doublet in the spin down channel is 100 meV. Dividing by two yields the mediating phonon energy of 50 meV - matching nicely with the O-Fe-O bending mode.[556] Furthermore, this doublet does not have a node. Since a single angular momentum of light is being absorbed in the relevant energy window, we conclude that the fundamental gap excitation is spin polarized. We attribute this finding to the spin-split band structure and the two distinct symmetry environments of the Fe centers.

Figure 4.2(c) compares the experimental MCD spectrum of $NiFe_2O_4$ with that calculated using Eqn. 4.2. In this panel, the theoretical curve has been rigidly shifted to account for over-estimation of the band gap within the hybrid functional method.[556] The excellent overall agreement between the measured and calculated spectra immediately verifies that the theoretical MCD response captures the essential aspects of the electronic structure. This is emphasized by critical points in the band structure.

Figure 4.2(d) displays constant energy cuts of the dichroic response vs. magnetic field. The resulting curves reveal a non-linear progression akin to magnetization,[286, 595] although saturation occurs much more slowly due to the local nature of this

probe [596] and with some asymmetry compared with $M(B)$ that is accounted for by the metamagnetic transition (discussed below). Optical tracking of $M(B)$ is extremely important for optical data storage and advanced sensing.[130] It is therefore striking that constant energy cuts of the dichroic response reveal such a correlation - even as new types of excitations are accessed under magnetic field. Figure 4.2(e) displays the difference in I_{MCD} for the two different field directions ($\pm B$). The contrast grows with increasing energy and applied field reaching values of -2.5$\times 10^{-3}$ cm^{-1} at 2.75 eV and 10 T.

The electronic structure of $NiFe_2O_4$, as probed by MCD spectroscopy, depends intimately on the spin state of the transition metal cations. Detailed analysis of the electronic structure under different spin configurations provides a striking account of ΔI_{MCD}. Recall that the excitation spectrum in ordinary ferromagnets, e.g. iron, does not depend on field direction: all states "flip" (invert) their spin under applied field, giving equal access to transitions. Introducing a second magnetic sublattice does not in itself change this picture. However, in $NiFe_2O_4$, and indeed in other inverted spinels, two transition metal centers comprise one sublattice, and the spins associated with the Ni ions change polarization (i.e. switch magnetic sublattices) across $B_{c(Ni)}$. Comparison of the predicted partial densities of states [Fig. 4.1 (c,d)] reveals precisely how the metamagnetic transition modifies the electronic structure. While the density of states associated with the Fe centers remains fairly rigid and relatively insensitive to changes in the microscopic spin arrangement, that associated with the Ni^{2+} ions is modified significantly. In fact, these bands move from the majority (minority) to minority (majority) channel as the Ni spin flips, providing carriers in the Ni states

access to a completely different set of spin-allowed charge transfer excitations.[4] As a result, the MCD spectrum of $NiFe_2O_4$ is altered dramatically across $B_{c(Ni)}$.

4.2.2 Exciting higher magnetic field investigations via first-principle electronic structure calculations

Naturally, we sought to predict how the metamagnetic transition affects the electronic structure. MCD spectra computed for the field-induced state ($B > \pm B_{c(Ni)}$) show two primary differences when compared to the ground state ($B = 0$). First, all features shift to higher energies (e.g. 70 meV for the 2.7 eV excitation); and second, the intensity is lost below ≈3.3 eV, at which point the spectra begin to develop qualitative differences, as shown by Fig. 4.2(e). Close inspection of the spectra in Fig. 4.2(a) reveals peak position offsets of about 50 meV, in excellent agreement with these predictions.

Figure 4.3 summarizes how the DOS evolves with the microscopic spin arrangement on the Ni and Fe sites. The left-hand side shows the ferrimagnetic ground state in the absence of an external magnetic field, with the spins on the octahedral Ni^{2+} sites aligned with those on the octahedral Fe^{3+} sites and opposed to those on the tetrahedral sites. Above the first critical field $B_{c(Ni)}$, the Ni spins flip into alignment with the tetrahedral Fe spins, giving an excited state that is 248 meV/f.u. above that of the ground state. This situation is shown in the middle panel and is discussed extensively in the main text. At a second much higher critical field $B_{c(Fe)}$, all spins are forced into alignment, giving the fully ferromagnetic state seen in the right-hand side of this figure. Here, ΔE/f.u. = 613 meV. The fully polarized state of $NiFe_2O_4$

has not been experimentally realized.

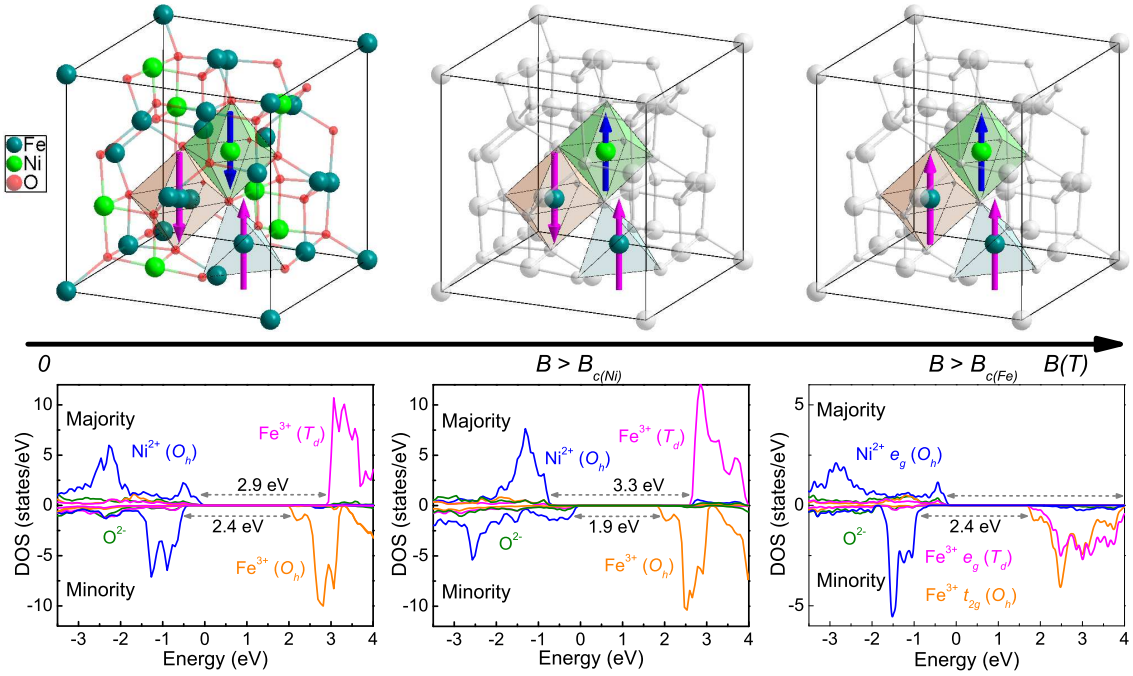

Figure 4.3: (top) Diagram showing typical spin orientations and (bottom) projected DOS at (left to right) $B = 0\,\mathrm{T}$, $B > B_{c(Ni)}$, and $B > B_{c(Fe)}$. In this work, we focus on $B_{c(Ni)}$.

Figure 4.4 summarizes the calculated MCD spectra of $NiFe_2O_4$ for the three different spin configurations. As discussed in the main text, flipping the Ni^{2+} spin across $B_{C(Ni)}$ alters the spectrum significantly (dark blue to light blue). Close inspection of Fig. 4.4 (a) reveals that increasing the field above $B > B_{c(Ni)}$ reduces the fine structure slightly and shifts the main peak (at $\approx$2.6 eV) to higher energies. As discussed in the main text, these predictions are in excellent agreement with our measurements. Even larger contrast is predicted to occur near 4 and 6.5 eV. This is beyond the range of our experiments.

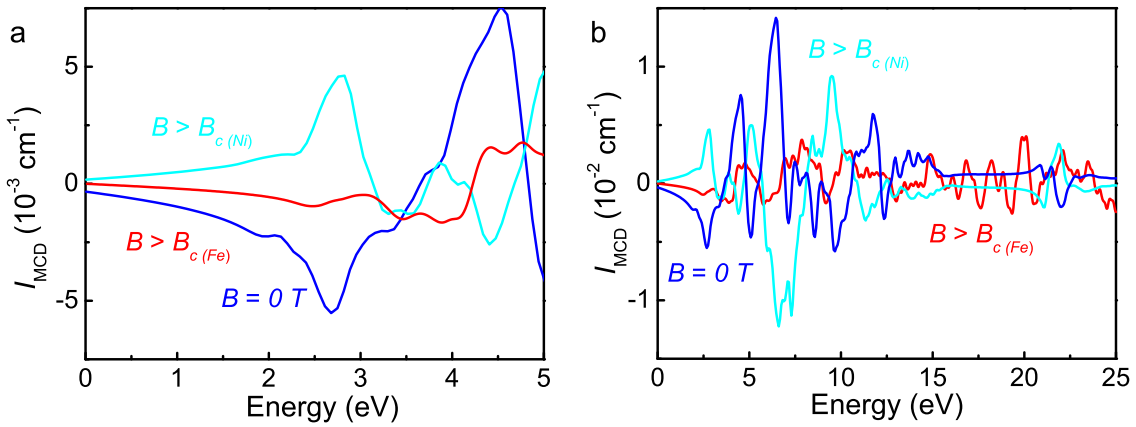

Figure 4.4: (a) Close-up view of the theoretical MCD spectra for the three magnetic states discussed above. (b) Calculated MCD spectra for the same three magnetic states over a wider energy range. In both panels, the energy scale has been shifted by -0.6 eV.

The calculated MCD response of the fully polarized state ($B > B_{c(Fe)}$) is indicated by the red lines in Fig. 4.4. This type of magnetic quantum phase transition occurs when the effective applied field overpowers the internal field to fully saturate the spin. Comparison reveals that the predicted MCD response level is overall lower. New features also emerge in previously flat portions of the spectrum - for instance, between 15 and 20 eV. We anticipate that these predictions will motivate measurements of $NiFe_2O_4$ and other spinel ferrites at even higher magnetic fields.

4.2.3 Probing the spin-charge interaction and establishing energy window

To provide additional information on the interplay between charge and spin, we measured the photoconductivity of $NiFe_2O_4$ [Fig. 4.5(a)]. This property derives

from the creation of electron-hole pairs with light: $\sigma_{PC} \propto \eta\ \alpha(E)\ \tau$. Here, σ_{PC} represents the photoconductance, η is the probability of creating a carrier, $\alpha(E)$ is the absorption coefficient, and τ is the carrier lifetime. Comparison with the absorption spectrum reveals that photoconductivity begins to develop near the fundamental gap - evidence that there are indeed important electronic states in the energy window below 2.8 eV deriving from the two discrete symmetry environments of the Fe centers. Figure 4.5(b) displays typical current vs. voltage (I-V) curves with white light on and off. The data in panel (a) were obtained from similar I-V curves collected at specific illumination energies. Application of a magnetic field provides an opportunity to further explore the photo-excited minority channel carriers. Figure 4.5(c) displays a typical set of I-V curves taken at 2.0 eV. As a reminder, light at this energy excites the Ni $O_h \rightarrow$ Fe O_h charge transfer in the minority channel. The illumination and magnetic field conditions are indicated as ($h\nu$, B). Using I-V curves like those in Fig. 4.5(c), we determined field-induced changes in photoconductivity. Figure 4.5(d) summarizes these findings by plotting them as magnetoresistances. It is immediately apparent that $NiFe_2O_4$ exhibits strong field effects (-6.5%) in the range where only minority carriers are active. Furthermore, this response is well above the standard magnetoresistance (on the order of -1%).[73] We conclude that light and field together are more effective than field alone - at least in the energy window between the minority channel indirect and direct gaps. Another key point that emerges from this work is that the negative tunnel magnetoresistance observed in spin-filter devices with ultra-thin $NiFe_2O_4$ barriers[285] extends beyond the static limit.

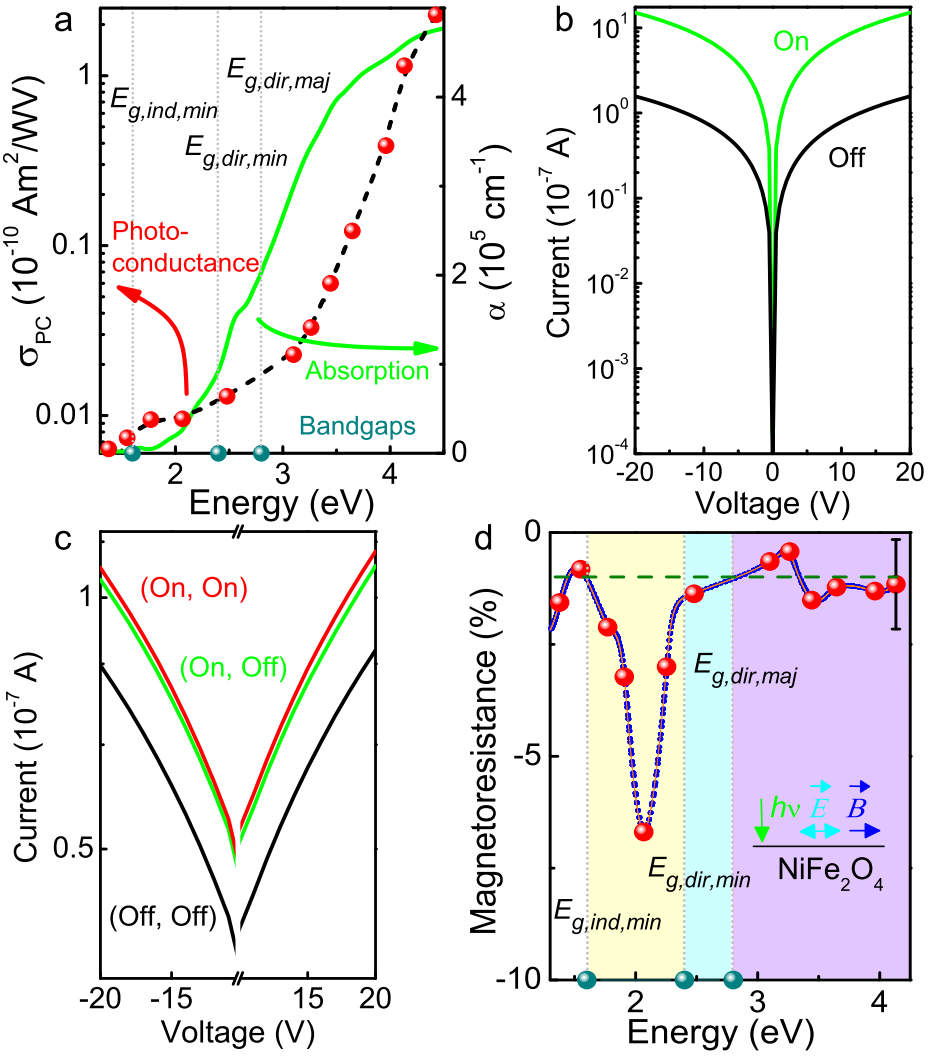

Figure 4.5: (a) Photoconductance of $NiFe_2O_4$ measured at a series of illumination energies compared with the absorption spectrum. (b) Example I-V curves taken using a broadband tungsten lamp. (c) Example I-V curves using a combination of light (2.0 eV) and magnetic field (≈1.5 T) as indicated. (d) Field-induced changes in photoconductivity are displayed as magnetoresistance. The blue line guides the eye. The teal dots on the energy axis indicate band gap positions, the shaded regions emphasize the character of the excitations in each energy window, and the dashed horizontal dark green line denotes the intrinsic magnetoresistance.[73] The schematic shows the measurement geometry.

4.3 Where does this put $NiFe_2O_4$?

The effects discussed here are quite different from those that arise in dilute magnetic semiconductors and many of the chalcogenides. The unusual electronic properties of the former are generally attributed to impurity band interactions,[595, 590] whereas the latter emanate from strong spin-orbit coupling and include spin-split bands, Rashba splitting, and topologically-protected surface states. [597, 598] The spin-polarized character of the excitations in $NiFe_2O_4$ instead emerges from the two independent magnetic sublattices - an aspect of the crystal, chemical, and electronic structure that will be replicated (in some form) in other spinel ferrites. These materials, already well known for their high Curie temperatures and robust moments, should be explored for enhanced effects, with additional advantages if the active energy window has a healthy overlap with the solar spectrum.

Chapter 5

Chemical tuning of the optical band gap in spinel ferrites: $NiFe_2O_4$ vs $CoFe_2O_4$

Since nothing probably is a greater drawback to the successful development of a new hypothesis than overstepping its boundaries, I have always stood for making as close a connection between the hypothesis of quanta and the classical dynamics as possible, and for not stepping outside of the boundaries of the latter until the experimental facts leave no other course open.

Max Planck

Theory of Heat Radiation 2nd ed.

We employed optical spectroscopy, high-quality epitaxial thin film growth, and first-principles calculations to investigate the electronic structure of $CoFe_2O_4$. The spectroscopic analysis was compared with $NiFe_2O_4$ to assemble a deeper understanding of the size and covalency effects of the second metal ion in spinel ferrites. Our work reveals $CoFe_2O_4$ to be fundamentally an indirect band gap material (1.2 eV, X $\rightarrow$ Γ in the spin-down channel) with a direct gap at 2.7 eV. We also used temperature dependence to investigate the robustness of the direct band gap, $\approx$2.8 eV at low temperature. This feature remains virtually constant up to the T_C, softening by $\approx$0.13 eV. These results, along with the magnetic properties, show that the stability of the electronic structure can be valuable for usage in the spintronics world.

5.1 Optical properties of $CoFe_2O_4$

Figure 5.1 displays the 300 K absorption spectrum of the $CoFe_2O_4$ film grown at 690 °C (red) along with similar data on the Ni-analog (blue, from Ref. [314]) for comparison. While there are many similarities in the response, there are important differences as well. One such difference is the absorption onset. α(E) for $CoFe_2O_4$ begins to rise much sooner than that of $NiFe_2O_4$, a response that can be anticipated by examining the relative appearance of the two films (insets, Fig. 5.1). $CoFe_2O_4$ is overall darker when photographed in both transmittance and reflectance. For traditional semiconductors like silicon,[559] it is well established that plots of $(\alpha E)^2$ and $(\alpha E)^{0.5}$ vs energy reveal direct and indirect band gaps as 5.1

$$\alpha(E) = \frac{A}{E}(E - E_{g,dir})^{0.5} + \frac{B}{E}(E - E_{g,ind} \mp E_{ph})^2. \tag{5.1}$$

Despite their more complicated band structures, this approach is commonly extended to allow analysis of oxides. [599, 600] In $CoFe_2O_4$, linear fits were obtained for both cases.

As shown in Fig. 5.1(b), a plot of $(\alpha E)^{0.5}$ vs. energy reveals an indirect band gap in $CoFe_2O_4$ at 1.17±0.08 eV. This gap value is significantly smaller than that of $NiFe_2O_4$ (1.64 eV),[314] as anticipated from the absorption spectrum and examination of the films themselves. We extract a coupling phonon energy[559] on the order of 50 meV that corresponds to a O-Fe-O bending mode, similar to $NiFe_2O_4$.[296, 314] The direct gap analysis (Fig. 5.1(b)) makes use of an $(\alpha E)^2$ vs. energy plot as well. It reveals a direct charge gap at 2.74±0.10 eV. Comparing the indirect and direct gap values clearly reveals that $CoFe_2O_4$ displays a fundamental indirect energy gap, similar to the situation in $NiFe_2O_4$. Prior optical work[300, 573] did not uncover the indirect gap excitation, so our findings are in sharp contrast with the reports that $CoFe_2O_4$ is a direct gap material. Notable also is the large difference between the indirect and direct gap in $CoFe_2O_4$ (see Table 5.1).

We can assign the excitations in Fig. 5.1(a) using the results from our first principles electronic structure calculations (Fig. 5.2). The strongly hybridized Co + O valence edge permits both Op $\rightarrow$ transition metal d charge transfer and intersite metal d $\rightarrow$ metal d, d-d, charge-transfer-like transitions. Interestingly, the localized Co states near the valence band edge could make intersite $d \rightarrow d$ excitations comparable in strength to those of $p \rightarrow d$ origin. Clearly, transitions in the minority channel (Co + O $\rightarrow$ Fe(O_h)) define the absorption edge and the fundamental indirect gap, similar to the situation in $NiFe_2O_4$. The strong band above 3 eV is due to a

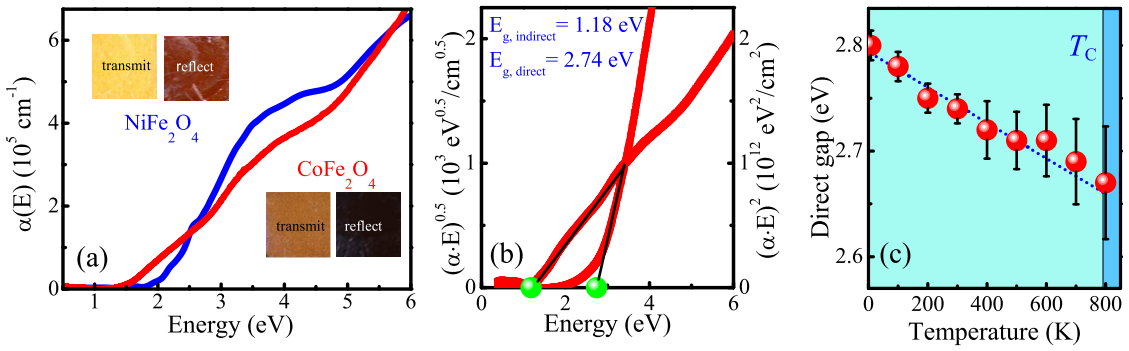

Figure 5.1: 300 K absorption spectrum of $CoFe_2O_4$ and $NiFe_2O_4$ grown at 690 °C. Insets: photos comparing transmittance and reflectance of $CoFe_2O_4$ and $NiFe_2O_4$ in a microscope with standard lamp. (b) Optical band gap analysis for the $CoFe_2O_4$ film. (c) dependence of the direct band gap on measurement temperature upon approach to T_C at 795 K.

combination of majority and minority channel excitations. In the majority channel, Co $d \rightarrow$ Fe(T_d) d and O $p \rightarrow$ Fe(T_d) d dominate, whereas in the minority channel, O $p \rightarrow$ Fe(O_h) + Co d and Co $d \rightarrow$ Fe(O_h) + Co d excitations are allowed in addition to the fundamental transitions. This band edge determines the character of the direct gap. The latter could be in either spin channel. The most likely candidates are listed in Table 5.1.

Interestingly, the optical absorption spectra of films grown at 520 and 365 °C are virtually identical to that of films grown at 690 °C (Fig. 5.1). This is different than what is found in $NiFe_2O_4$ thin films.[314] While surprising on first inspection, this finding can be understood by recalling the dissimilar evolution of the unit cell structure with growth temperature in the two materials.[286] X-ray diffraction measurements show that $NiFe_2O_4$ films become progressively strained due to an increase in the out-of-plane lattice parameter at lower growth temperatures. By contrast,

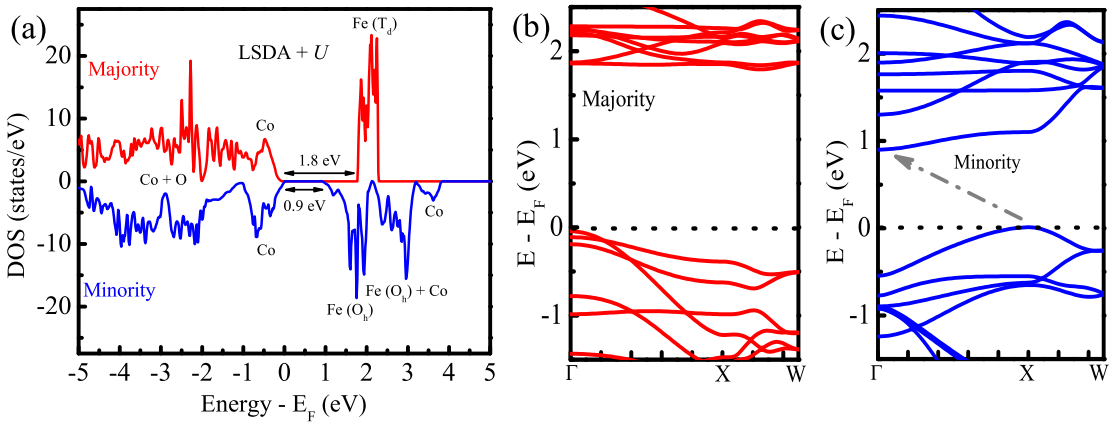

Figure 5.2: (a) Density of states of $CoFe_2O_4$ calculated using the LSDA+U method. Energy bands along Γ – X – W for (b) minority and (c) majority channels. The minority channel exhibits an indirect gap between X and Γ. In both channels, the lowest conduction band is nearly flat over a wide region, character that probably leads to many nearly-degenerate transitions.

Table 5.1: Experimental and theoretical optical band gap values of $CoFe_2O_4$ (in eV).

Gap form	Experimental gaps	Band gap	LSDA+U	GGA+U
Indirect	1.2 (from $(\alpha E)^{0.5}$ V E plot)	$E_{g,min}(X \rightarrow \Gamma)$	0.9	1.5
Direct	2.7 (from $(\alpha E)^2$ V E plot)	$E_{g,min}(X \rightarrow X)$	1.0	1.6
		$E_{g,min}(\Gamma \rightarrow \Gamma)$	1.4	2.0
		$E_{g,min}(W \rightarrow W)$	1.9	2.3
		$E_{g,maj}(\Gamma \rightarrow \Gamma)$	1.9	2.1

$CoFe_2O_4$ films grow almost strain-free between 300 and 700 °C.[286] We conclude that the optical properties of spinel ferrites are more sensitive to unit cell parameter changes than film epitaxy. The insensitivity of the band gap to growth temperature also supports this supposition.

We also carried out variable temperature optical measurements between 4 and 800 K. The latter is very close to T_C. The temperature dependence of the direct gap in $CoFe_2O_4$ is shown in Fig. 5.1(c). It displays a systematic quasi-linear decrease from 2.80 eV at 4.2 K 2.67 eV at 800 K. Overall, the direct gap softens by only 0.13 eV over the temperature range investigated and remains robust on approach to T_C = 795 K. This insensitivity to temperature and robustness on approach to T_C implies relatively weak charge-spin coupling in $CoFe_2O_4$ compared to other multifunctional oxides like $BiFeO_3$.[601, 602, 603] The modest temperature dependence can probably be understood in terms of thermal broadening effects, which creates virtual states between the valence band maximum and conduction band minimum, reducing the average gap value. That the semiconducting character of this spinel ferrite remains robust up to very high temperature certainly broadens the utility of this material.

Figure 5.2(a) displays the density of states as obtained with LSDA+U. Comparison with GGA+U is reported in Table 5.1. Due to the agreement between these methods (mainly a rigid shift that changes the gap values), we shall only discuss LSDA+U results here. Our calculations correctly capture the semiconducting nature of $CoFe_2O_4$. The majority and minority channels are spin-split both in the valence and conduction bands, and the gap is found to be much larger in the majority channel (1.8 eV) than in the minority channel (0.9 eV). We also verified that the octahedral sites strongly prefer antiferromagetic alignment with the tetrahedral sites, consistent with the super-exchange picture and irrespective of the inversion factor. In the fully inverted structure, the Fe^{3+} moments are completely compensated, and the net moment arises only from Co^{2+} ($3\mu_B$/f.u.), consistent with previous reports.[288]

Both Co^{2+} and Fe^{3+} are in the high-spin configuration. The density of states is qualitatively similar to that of the Ni-analogue [314] except for the difference in band gap values (Fig. 5.2(a)). Like $NiFe_2O_4$, we see narrow conduction band states belonging to minority octahedral Fe and Co d states and majority tetrahedral Fe d states. The valence band can be separated into strongly localized Fe states 7-8 eV below the Fermi level (not shown in figure) and a broad hybridized band of Co and O states near E_F. The most perceptible difference between $CoFe_2O_4$ and $NiFe_2O_4$ is the stronger presence of localized Co states at the valence band edge, whereas in $NiFe_2O_4$, the Ni states are more hybridized. The projected DOS is provided in Fig. 5.3. From these plots it is most evident that the Co d band dominates the valence band edge at the Fermi energy E_F with a finite level of exchange splitting, presenting the spin-down (minority) channel nearest the surface. Additionally, the Fe_{oct} d band is primarily responsible for creating the minimum energy conduction band edge.

To analyze the nature of the gap, we plot the LSDA+U bands along the lines Γ – X – W for the minority and majority channels (Fig. 5.2(b) and (c)). The majority channel conduction band is practically dispersionless, whereas the valence band maximum is clearly at the Γ point. This difference yields a direct gap at 1.9 eV. There are additional indirect gaps very close to this energy, notably from Γ to between X and W point (1.8 eV). We find more dispersive valence bands in the minority channel of $CoFe_2O_4$ compared to $NiFe_2O_4$, with a clear indirect gap candidate between X ($k = \frac{2\pi}{a}[100]$) and Γ, the difference in energy being 0.9 eV. This result agrees quite well with recent literature reports. [284] There are also direct gaps very close to this indirect gap. Notable ones are at X (1.0 eV), Γ (1.4 eV) and

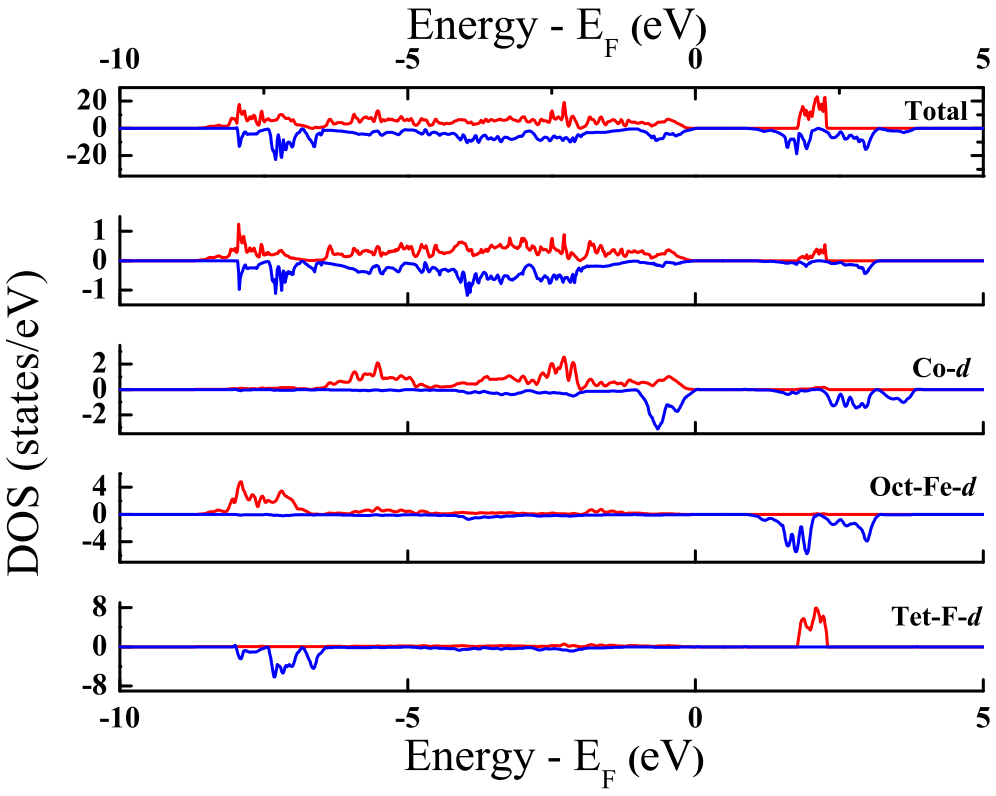

Figure 5.3: Total and partial density of states of $CoFe_2O_4$ calculated via local density approximation and incorporating the Hubbard U values for Fe and Co ($LDA + U$.)

W (1.9 eV) (Table 5.1). Overall there is reasonable agreement with the experimental result that the fundamental gap is indirect, which theory assigns to the minority channel.[604]

Motivated by experimental reports of 70-80% partial inversion in $CoFe_2O_4$ powder samples and nanoparticles,[308, 605] we performed additional relaxation and density-of-states calculations on a 75% inverted structure by swapping an octahedral Co with a tetrahedral Fe site while preserving the antiferromagnetic tetrahedral-octahedral spin alignment. Our main findings are as follows. Energetically, we find that this partially inverted configuration has higher energy compared to the fully inverted case ($\sim$70 meV/f.u) implying that these are metastable states. Secondly, the magnetic moment is higher (4.0 μB/f.u) as the extra moment from the uncompensated Fe lattice outweighs the loss in moment at the Co site. Enhanced magnetization values, sometimes observed in thin films,[286, 567] can thus be rationalized by invoking the presence of these metastable, partially inverted configurations. Electronically, we find that partial inversion introduces tetrahedral Co states at the majority channel valence band-edge which reduces the gap to 1.3 eV. The minority valence band-edge, however, remains largely unchanged, i.e. octahedral Co states occupy the band-edge, just like the fully inverted configuration, and the tetrahedral Co states are deeper. The conduction band-edge character in both channels is also similar to the fully inverted case, i.e. tetrahedral and octahedral Fe states define the majority and minority band-edges, respectively. As a result, the minority channel gap is largely unaffected and widens slightly to 1.0 eV; however, it is also clearly evident that by dispersing the Co amongst the O_h and T_d interstitial cites the majority channel gap

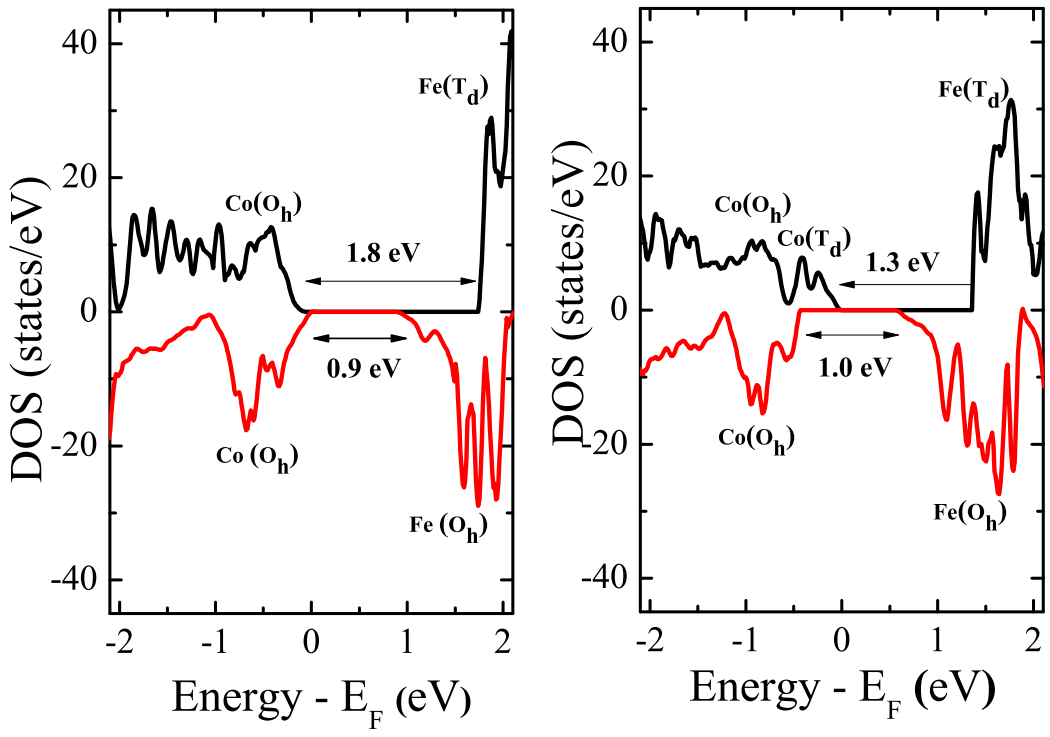

Figure 5.4: Near Fermi level DOS for the 28-atom fully inverted structure (space group *Imma*, left panel) and 75% partial inverted structure (right panel). The major difference is the appearance of tetrahedral Co states in the majority band which reduces the gap value from 1.8 eV to 1.3 eV. The minority gap is largely unaffected.

narrows significantly, on the order of 0.5 eV. Taken together, our calculations show that partial inversion has limited effect on the fundamental minority channel gap and mainly changes the band-edge character of the majority channel via appearance of tetrahedral Co states. The band edges in the two different configurations are shown in Fig. 5.4 (b).

The difference in the optical and electronic properties between $CoFe_2O_4$ and $NiFe_2O_4$ is quite analogous to the trend observed between CoO and NiO. It is well

known that NiO has a larger band gap than CoO (4.0 vs 2.4 eV)[606], increased hybridization[607], and a higher magnetic ordering temperature (530 vs 291 K). A similar mechanism is likely at work in the spinel ferrites since the occupied Fe states are deeper and well localized in both systems and do not affect the interaction between Ni(Co) and oxygen. The smaller $NiFe_2O_4$ unit cell compared to that of $CoFe_2O_4$ (8.34 vs 8.39 Å) results in a shorter Ni-O bond length which promotes covalency and, in turn, greater hybridization and super-exchange interaction, which manifest in a higher Curie temperature. The band gap trend can probably be traced to the fact that the Ni^{2+} ($3d^8$) ion is smaller than the Co^{2+} ion ($3d^7$)[608] which creates deeper Ni^{2+} states due to stronger electrostatic interaction. Therefore the energy gap between occupied and unoccupied levels widens going from $CoFe_2O_4$ to $NiFe_2O_4$, other factors being equal.

Finally, our work reveals that the band gap hierarchy of $CoFe_2O_4$ is quite similar to that of Si, the most investigated indirect band gap material.[609] It also has a strong overlap with the solar spectrum. $CoFe_2O_4$ and other spinel oxides have much lower band gaps than many other complex oxides, such as room temperature ferroelectric perovskites ($BaTiO_3$ or $PbTiO_3$ for example) where the charge gaps are typically over 3 eV.[610] Extension to other members of the spinel ferrite family will be a subject of further investigation.

5.2 Fancy a Spin on a High-Temperature Magnet?

5.2.1 Deeper spectroscopic investigation of novel electronic and magnetic material $CoFe_2O_4$

Multifunctional, high Curie temperature magnetic semiconductors are tailor-made for modern device applications. They naturally provide sizable magnetic moments, switchable spin states, and spin dependent band gaps for use in spintronics, spin-caloritronics, and straintronics.[611, 282, 612, 613] Moreover, the use of spin rather than charge is crucial for the development of ultra-low power devices because there is less heat to dissipate. Among the various candidate materials, iron oxides are well studied, sustainable, and earth-abundant. The spinel ferrites, with general formula AFe_2O_4, are particularly attractive with $CoFe_2O_4$ and $NiFe_2O_4$ as flagship examples.

$CoFe_2O_4$ is well-known as a magnetic semiconductor [Fig. 5.5]. The Curie temperature, T_C, is 795 K,[569] and the coercivity and saturation magnetization are 1.1 T and 450 emu/cm^3, respectively.[286] Saturation of the Co moments occurs at $B_{s,Co} \approx 3$ T.[286] Thus, a small applied field drives the system from a $\downarrow\uparrow\uparrow$ to $\downarrow\downarrow\uparrow$ configuration and *vice versa*, upon field reversal. Field therefore allows selection of one magnetic state over another. Presumably, the iron moments saturate at even higher magnetic fields (giving the $\uparrow\uparrow\uparrow$ configuration), although the exact value of $B_{s,Fe}$ has not yet been measured. Confinement and strain provide additional control of the magnetic state.[614] The magnetocrystalline anisotropy of $CoFe_2O_4$ is 2×10^6 ergs/cm^3,[615] and the magnetostrictive coefficient along the [100] direction is large: -5.90×10^{-4}.[616, 617, 618] Together, these properties have led to

contemporary usage in spin-filtering heterostructures, composite multiferroics, and embedded nano-structures. [286, 619, 620, 621, 622]

Recent work uncovers fascinating electronic properties as well.[569, 616, 116, 284] Analysis of the spectral functions and partial densities of states [Fig. 5.5(b, c)] reveals sizable exchange splittings, a fundamental indirect band gap, and the possibility of spin-polarized current emanating from low energy minority channel excitations. Importantly, $CoFe_2O_4$ has an overall low electronic energy scale compared to similar materials like $NiFe_2O_4$ and Co:ZnO.[116, 623, 624] Our recent spectroscopic work on epitaxial thin films of $CoFe_2O_4$ uncovers a 1.2 eV indirect gap, a hierarchy of higher energy direct gaps, and favorable overlap with the solar spectrum.[116] These findings raise questions about broader aspects of the electronic structure in $CoFe_2O_4$ and the Ni analog. For instance, what are the band polarizations that contribute to magnetism, and how does the I-V curve respond to light? These issues are central to advancing the microscopic understanding of high T_C magnetic oxides and their many applications. Spinel ferrites are also well-suited to the development of structure-property relations.[625, 566, 626] Just as in perovskites, transition metal centers bring in electron correlation, anisotropy, and control charge, spin, and local lattice environment. To first order, the charge, spin, orbital, and lattice channels operate independently, although their entanglement leads to compelling interactions along with opportunities for property control under external stimuli.[12, 627, 628, 629] At the same time, spinel ferrites sport degrees of freedom that reach beyond those in perovskites, e.g. the cation inversion parameter λ.[308, 630, 631] This provides a framework for the development of new and useful properties as well as novel physics.

In this work, we bring together magnetic circular dichroism (MCD) and photoconductivity to investigate entangled electronic and magnetic degrees of freedom in the spinel ferrite $CoFe_2O_4$. Our objective is to determine the spin polarization and the rotation (which is proportional to magnetization), and by so doing uncover the bands and charges that are responsible for the unique magnetic properties. Even though there has been other magneto-spectroscopy of spinels,[635, 636] to our knowledge, there has been no work on these issues - an important oversight considering the very real application potential of these compounds. Analysis reveals (i) a broad energy window of purely minority channel excitations that overlaps well with the solar spectrum, (ii) magnetic field tunability of these states that derives from field-induced switching of the spin state and the spin-charge coupling in this system, and (iii) enhanced photoconductivity under applied magnetic field. Comparison with the Ni analog [116, 301] also allows the development of several important structure-property relations particularly with regard to the role of the inversion fraction. Taken together, we uncover an energy window in the electronic structure where light generates spin-polarized carriers and where magnetic field influences the relevant charge excitations. We discuss how high temperature magnets like $CoFe_2O_4$ and $NiFe_2O_4$ offer new opportunities for light harvesting and oxide electronics.[4, 302]

5.2.2 Uncovering the spin-dependent excitations and coercivity as a function of energy in spinel ferrites

Figure 5.6(a) displays the MCD spectrum of $CoFe_2O_4$ in applied fields up to $\pm 10\,T$ at $1.6\,K$. The trends are overall systematic with increasing and decreasing field, as

expected. For comparison, we include the linear absorption spectrum ($\alpha(E)$), with the 1.2 and 2.7 eV band gaps indicated on the energy axis.[116] Examination of the spectra in Fig. 5.6(a) immediately reveals a large number of states below the majority channel direct gap (2.7 eV). Moreover, local maxima in the dichroic response coincide with inflection points in the absorption spectra. This demonstrates an important derivative relationship between I_{MCD} and $\alpha(E)$. The magnitude of the dichroic response is often expressed as: [590]

$$I_{MCD} \approx \frac{(\alpha_+(E) - \alpha_-(E))d}{2} \approx \frac{\Delta E}{2} \frac{1}{\alpha(E)} \frac{d\alpha(E)}{dE}. \tag{5.2}$$

Here, $\alpha_+(E) - \alpha_-(E)$ is the absorption difference between right and left circularly polarized light, $d\alpha(E)/dE$ is the energy-dependent derivative of absorption, ΔE is the change in energy of the peak position, and d is the film thickness. Further, the resulting contrast in $\alpha_\pm(E)$ correlates with $\sigma_\pm$, the helicity.[590] Note that there is a direct proportionality between I_{MCD} and $d\alpha(E)/dE$. Absorption is a joint density of states effect, so I_{MCD} highlights critical points in the band structure.

Direct assignment of the spectral features of $CoFe_2O_4$ comes from an understanding of the band structure and projected density of states [Fig. 5.5 (b) and (c)].[116] Minority-channel transitions involving hybridized Co + O $\rightarrow$ Fe(O_h) are responsible for the absorption edge and the fundamental indirect gap. These transitions are categorized as intersublattice charge transfer [Fig. 5.5(f)]. They also give a direct gap excitation in the spin-down channel due to the substantial oscillator strength and magnitude of the absorption (1×10^5 cm^{-1}). The direct gap arising from majority-channel transitions consists of Co(O_h) + O $\rightarrow$ Fe(T_d) excitations. Of course, when

$\lambda = 0.75$, this becomes Co(O_h) + Co(T_d) + O $\rightarrow$ Fe(T_d).

Returning to Fig. 5.6(a), there are several features in the 1.5 to 2.5 eV energy window - where only minority channel charge transfer excitations are expected - indicating that there are excitations that exist solely in the spin-down channel. The lowest energy excitation, centered at 1.8 eV, presents considerable asymmetry on the low energy tail, suggesting that the nearby indirect gap excitation may be affecting the lineshape. By comparison, the excitation centered at $\approx$2.2 eV has the expected Lorentzian lineshape. Beyond the exquisite sensitivity for locating important features in the density of states, dispersion in MCD spectra gives reliable estimates of the spin splitting between majority and minority bands. We find exchange splittings of 0.15 eV, in reasonable agreement with theoretical predictions.[284, 116]

Figure 5.6(b) displays the derivative of the MCD spectrum dI_{MCD}/dE as a function of energy at $\pm$10 T. There are several intriguing features that give rise to zero-crossings near 1.2, 1.8, 2.15, and 2.7 eV. As a reminder, the indirect gap in the minority channel is at 1.2 eV, and the direct gap in the majority channel is at 2.7 eV. The energy scale at $\approx$1.8 eV - indicated by the node in dI_{MCD}/dE - is also important, although it was overlooked in our prior analysis of the absorption spectrum. We assign this feature as a Co (e_g) $\rightarrow$ Fe (t_{2g}) excitation. By comparison, the zero crossing in dI_{MCD}/dE near 2.2 eV seems to be a density of states effect. The full band gap hierarchy in $CoFe_2O_4$ is thus 1.2 eV (indirect, minority channel), 1.8 eV (direct, minority channel), and 2.7 eV (direct, majority channel).

The MCD spectrum of $CoFe_2O_4$ is similar in magnitude to that of $NiFe_2O_4$,[301] although, in the Ni analog oscillator strength and the series of band gaps are pushed

to higher energies. The excitations in $CoFe_2O_4$ thus have a much better overlap with the solar spectrum from both a band gap and density of states perspective. The fact that $\lambda \approx 0.75$ in $CoFe_2O_4$ is not readily apparent from the MCD data, although as discussed above, it does affect the assignments. The complexity of the charge transfer excitations below 2.5 eV may be responsible for the additional oscillator strength.

From the preceding discussion and Eqn. 5.2, we see that the electronic aspects of the dichroic response of $CoFe_2O_4$ are fairly straightforward. But what about the magnetic response, and what effect will a change in spin state have on I_{MCD}? In other words, we know that applied field flips spin on the Co sites and drives a $\downarrow\uparrow\uparrow$ to $\downarrow\downarrow\uparrow$ transition at $B_{c,Co}$ [Fig. 5.5(b)]. We do not, however, yet know the electronic signatures of this entanglement.

The connection between magnetic circular dichroism and the spin state can be understood in a straightforward manner by recalling that time reversal symmetry is broken in magnetic materials. This means that separate wave vectors $\vec{k}_+$ and $\vec{k}_-$ must be used to define the propagation of right and left circularly polarized light [Fig. 5.5(e)], which results in the development of off-diagonal elements in the complex dielectric tensor $\overleftrightarrow{\epsilon}(E)$.[637] In addition to separate wave vectors being required to describe the propagation of right and left circularly polarized light, all of the optical constants are energy dependent and tensorial in nature. For example, the complex refractive index is $\overleftrightarrow{n}(E) = \overleftrightarrow{n}'(E) + \overleftrightarrow{n}''(E) = \sqrt{\overleftrightarrow{\epsilon}(E)\overleftrightarrow{\mu}(E)}$. Moreover, the extinction coefficient $\overleftrightarrow{n}''(E)$ is proportional to absorption $\overleftrightarrow{\alpha}(E)$. Therefore, off-diagonal components of the dielectric tensor (or the fact that the magnetic permeability of a magnetic material $\overleftrightarrow{\mu}$ is not 1.0) are directly connected to the absorption (and in

turn the absorption difference between right and left circularly polarized light). More precisely, the information derived from the dielectric tensor, and hence the refractive indices ($\overleftrightarrow{n}_{\pm} = n'_{\pm} + in''_{\pm}$) for right and left circularly polarized light, is expressed in the relationships in Eqns. 5.3 – 5.6.[547] Taking the z direction as being parallel to the magnetization $\vec{m}$, the dielectric tensor appears as the following:

$$\overleftrightarrow{\epsilon} = \begin{vmatrix} \epsilon_{xx} & i\epsilon_{xy} & 0 \\ -i\epsilon_{xy} & \epsilon_{yy} & 0 \\ 0 & 0 & \epsilon_{zz} \end{vmatrix}, \tag{5.3}$$

$$\approx \overleftrightarrow{n}^2 \begin{vmatrix} 1 & iQ\vec{m}_z & 0 \\ -iQ\vec{m}_z & 1 & 0 \\ 0 & 0 & 1 \end{vmatrix}, \tag{5.3a}$$

$$\overleftrightarrow{\epsilon}_{\pm} = \overleftrightarrow{\epsilon}_{xx} \pm \overleftrightarrow{\epsilon}_{xy}, \tag{5.4}$$

$$\overleftrightarrow{n}_{\pm} = \sqrt{\overleftrightarrow{\epsilon}_{\pm}} \approx \overleftrightarrow{n}_0 \pm \frac{\overleftrightarrow{\epsilon}_{xy}}{2\overleftrightarrow{n}_0}, \tag{5.5}$$

$$\overleftrightarrow{n}_0 = \sqrt{\overleftrightarrow{\epsilon}_{xx}\overleftrightarrow{\mu}_{xx}}. \tag{5.6}$$

These relationships demonstrate the attenuation of circularly polarized light as it evolves across a medium. Here, $\overleftrightarrow{n}_{\pm} = (\epsilon_{xx} \pm \epsilon_{xy})^{1/2}$ is the refractive index, as expressed by Eqns. 5.3 – 5.6, for right and left circularly polarized light arising from the dielectric function $\overleftrightarrow{\epsilon}$. It is also customary to define $\vec{m}$ as the magnetization and Q as a material-specific magneto-optic constant. The correlation between the imaginary component of the refractive index $n''_{\pm}$ and absorption provides a direct

correspondence between the magnetic polarization underlying the transition and the dichroic response. Therefore, an assignment of the magnetic nature of the electronic structure underpinning specific spectroscopic transitions follows logically. An important caveat to these relationships is that the nature of the excitation precludes $\overleftrightarrow{\mu} = 1$ and thus the refractive index includes this salient component as shown in Eqn. 5.6. This makes magnetic circular dichroism a sensitive tool for probing both electronic and magnetic properties.

Figure 5.6(c) shows the residual MCD signal. This quantity is defined as the difference in the MCD spectra taken in the positive and negative field directions: $\Delta I_{MCD} = I_{MCD}(E, B) - I_{MCD}(E, -B)$. Physically, ΔI_{MCD} represents the difference in the dichroic response between the $\downarrow\uparrow\uparrow$ and $\downarrow\downarrow\uparrow$ states. In other words, field selects the magnetic state, and ΔI_{MCD} represents the asymmetry in the number of spin-dependent states present in the excitation upon reversing the applied magnetic field. In $NiFe_2O_4$, electronic structure calculations reveal that the Ni states reside in either the minority or majority channel depending on whether spins are in the $\downarrow\uparrow\uparrow$ or $\downarrow\downarrow\uparrow$ state.[301] A similar swap of the Co density of states is anticipated here as magnetic field is swept across $B_{c,Co}$. [116] Just as I_{MCD} quantifies the number of states involved in Co $\rightarrow$ hybridized Fe(O_h)+Co excitations (with Co charge accessing a different set of states above the Fermi level depending on the field direction), ΔI_{MCD} reveals the small fraction of excitations that are spin independent and insensitive to field reversal. They probably involve ions other than Co, e.g. Fe and O. The overall size of the residual signal represented by ΔI_{MCD} is small. It is on the order of 10^{-5} near $B_{c,Co}$, increasing to 10^{-4} at full field. Overall, the MCD spectrum of $CoFe_2O_4$

is controlled by the underlying spin state ($\downarrow\uparrow\uparrow$ or $\downarrow\downarrow\uparrow$) and spin-charge interactions. Use of a small (rather than large) field to flip the Co spins obviously assures a modest residual signal.

To further explore the energy and magnetic field dependence of the dichroic response of $CoFe_2O_4$, we created contour plots of these spectra. The data in Fig. 5.6(a) are thus a set of constant field cuts through the contour plot of Fig. 5.6(d). Examination of I_{MCD} in the contour format reveals that the slope increases near 2.5 – 3 T depending upon the energy. This suggests that a more detailed analysis of this edge may provide useful information about how the electronic excitations depend upon the spin state (and how they change across the coercive field). Figure 5.6(e) displays the change in separation of the contour lines, dI_{MCD}/dB, as a function of energy and magnetic field. The largest changes are between 1.7 and 2.1 eV. This indicates that low energy charge transfer excitations are most strongly correlated with the spin state as well as with spin-polarized absorption. Figure 5.6(f) cuts the dI_{MCD}/dB data in the contour plot at selected energies. Again, we see that changes are most pronounced between 1.7 and 2.1 eV (where the mixed state transitions in the minority channel reside) and that the high energy regime ($E >$2.25 eV) is effectively flat. We conclude that applied field controls these states and excitations through the spin-charge interaction.

In order to provide additional information on how these light-generated spin-polarized carriers can be controlled, we carried out a series of magnetic field sweeps of the dichroic response and compared the results to the magnetization of $CoFe_2O_4$ [Fig. 5.5(d)] which we already know is hysteretic. The latter is expected because

spinel ferrites are well known ferrimagnets, although it is not entirely obvious that the hysteretic nature of the $\downarrow\uparrow\uparrow$ to $\downarrow\downarrow\uparrow$ transition in $CoFe_2O_4$ will be reflected in the magneto-optical properties. Examination of Fig. 5.7(a) reveals that there is little effect near the fundamental indirect gap - mainly because there are so few Co states with which to work. Higher energies are different. Here, a clear hysteresis develops in the MCD response [Fig. 5.7(b)]. This is important and interesting because optical tracking of a magnetic hysteresis loop has a number of applications. That the size of the loop depends upon energy is, however, an unexpected surprise. Figure 5.7(c) displays the coercive field as a function of energy. Interestingly, this data tracks a Brillouin-like function, which is akin to following the number of Co-related magnetic states. Overall, the field sweeps of the dichroic response in $CoFe_2O_4$ show that there is a large energy window with promise for ultra-low power devices because of the magnetically-switchable optical response.

5.2.2.1 Conservation of electromagnetic angular momentum

A well known concept in physical systems is that energy, mass, and linear momentum must be conserved; however, angular momentum should be included in this list. Electromagnetic waves have angular momentum, just the same as particles. The separation of this angular momentum into constituents, e.g. orbital and spin, has proven to be quite controversial but we will refrain from introducing this argument. This arises in photons from the right- and left-circular polarizations having a projection of their angular momentum along the direction of propagation, helicity, equal to ± 1, respectively. These raising and lowering operators taking values in units of $\hbar$.

Linearly polarized light is in a superposition of these two states. When decomposing information presented by MCD, it is important to consider that the conservation of angular momentum is the primary driving force behind the magnitude of response. Principally this provides information about the changing angular momentum projected along the magnetic field direction,

$$\vec{L} = m\vec{v}r, \tag{5.7}$$

becomes

$$\vec{L} = rp\sin\theta, \tag{5.8}$$

as shown by Fig. 3.19. In the above equations, $\vec{L}$ is the orbital angular momentum, m is the mass of the particle, $\vec{v}$ is the velocity, r is the radius or rotation and $\sin\theta$ represents the angle of $\vec{L}$ with respect to the magnetic field direction. A similar structure appears when considering the spin angular momentum $\vec{S}$. This suggests that as the planar radius gets larger (smaller) the effective number of magnetic moments invoked grows (shrinks) systematically. This results from torque $\vec{T}$ acting on the magnetic dipole moment $\vec{m}$ from the external magnetic field $\vec{B}_0$ through the angular momentum $\vec{P}$, via the gyromagnetic ratio γ

$$\gamma\vec{B}_0 \times \vec{P} = \vec{T}. \tag{5.9}$$

To clarify, the gyromagnetic ratio appears as $\gamma = \vec{m}/\vec{P}$. Additionally, when spin-orbit interaction is significant the outcome communicates direct information about the nature of the spin angular momentum component that is parallel to the magnetic

field. Interestingly, when considering a microscopic model of circularly polarized transitions occurring specifically between magnetically differentiated electronic bands the RCP and LCP give access to the dispersion.[530, 531]

Incident circularly polarized photons each impart one quantum of orbital angular momentum ($\Delta M_L = \pm 1$).[72, 525, 526, 375] Thus ΔM_L becomes the primary (or minimum) selection rule used in MCD. Additionally, the total angular ΔM_J momentum remains conserved in both magnitude and direction when a photon is absorbed, thus if spin-orbit interaction comes into play, the selection rule shifts to $\Delta M_J = \pm 1$ On an important note, the transition is spin dependent because the helicity, the projection of the angular momentum onto the linear momentum, couples to the parallel spin direction. A more visual explanation of helicity is the resulting vector executes a clockwise or counterclockwise helical precession motion about the propagation direction with respect to time.

Upon consideration of the tensors in the main text, the tensor can be broken into two regions, (i) symmetric and (ii) antisymmetric. The former can be diagonalized by a proper rotation of the coordinate system, this means that the symmetric components $i = j$ do not contribute to the magneto-optical effects, such as MCD. However, the antisymmetric (off-diagonal) components do contribute to the MCD response and can be considered to first order as having a direct dependence upon the magnetization and/or magnetic field. We can understand the connection between magnetization, coercive field, and energy by reexamining Eqns. 5.3 and 5.3a. In cubic materials such as $CoFe_2O_4$, the dielectric tensor $\overleftrightarrow{\epsilon}$ correlates directly with the magnetization $\vec{m}$ and the Q's which are material-specific magneto-optic constants.

We also know from the calculated density of states and experimental magnetization [Fig. 5.5(b,c,d)] that excitations in this range emanate mainly from valence band Co states and that the coercive field pertains only to the spin response of Co centers.

We can understand the connection between magnetization, coercive field, and energy by reexamining Eqns. 5.3 and 5.3a. In cubic materials such as $CoFe_2O_4$, the dielectric tensor $\overleftrightarrow{\epsilon}$ correlates directly with the magnetization $\vec{m}$ and the Q's which are material-specific magneto-optic constants. We also know from the calculated density of states and experimental magnetization [Fig. 5.5(b,c)] that excitations in this range emanate mainly from valence band Co states and that the coercive field pertains only to the spin response of Co centers.

5.2.2.2 Tools for probing electronic and magnetic properties

When considering the application of an optical probe, a critical component emerges by the description from the interaction of light and matter. The optical properties of a given medium are determined by the dielectric tensor which derives its constituents from the motion of the electrons within the material. In the presence of an external magnetic field $\vec{B}$, a charge q moving with velocity $\vec{v}$ will experience a Lorentz force $\vec{F}$, shown here by the vector cross product $\vec{F} = q(\vec{v} \times \vec{B})$. This can naturally be extended to oscillating dipoles, i.e. $\vec{F} = d\vec{p}/dt \times \vec{B}$. The applied magnetic field will exert torque on the dipole when the magnetic field is perpendicular to it; moreover, this suggests that materials experience a Lorentz force when exposed to light. The force points toward (away from) the center of the circle for RCP (LCP). Accordingly, we invoke these principles to investigate the response of the electronic and magnetic properties

spectroscopically, in the form of magnetic circular dichroism. MCD powerfully, yet delicately, unmasks spin-dependent electronic structure components via field-induced differences in the absorption of right and left circularly polarized light (RCP/+ and LCP/-), I_{MCD}.[547, 590, 591]

In the framework of magneto-optical experiments two processes are taking place, the phase and amplitude of the transmitted wave being recorded are altered and attenuated as $\exp\{(iEn'_{\pm}z/c)\}$ and $\exp\{(-En''_{\pm}z/c)\}$, respectively. Here E is the energy and z is the direction of propagation. The differing propagation velocities produce a rotation of the effective polarization via the phase shifts, this corresponds to the conventional Faraday rotation. When considering the polarization dependent absorption rate of the two circularly polarized modes, the ellipticity is affected.

5.2.2.3 Substrate response

The substrate used for epitaxial growth of $CoFe_2O_4$ was spinel $MgAl_2O_4$. It has been assumed that this spinel would be magneto-optically silent[638] but this assumption was made without conclusive evidence to rationalize the statement. Fig. 5.9(a) shows how the MCD response of the 100 µm substrate varies across the energy spectrum at ±10 T. The data are obtained by measuring the spectra at 10 T, 0 T going down, −10 T, and finally at 0 T going up. Once each spectrum is measured the average of the 0 T spectra is calculated and substrated from the ±10 T spectra. Importantly, the result averages near 0 response, so that the response of the substrate does not impinge upon the MCD response of $CoFe_2O_4$.

Fig. 5.9(b) displays a similar style of spectrum but with the average of the 0 T

spectra substracted from the individual 0 T spectra, red and blue lines. The green line shows the result of adding these values together. This shows that the disparity of these spectra averages to 0 response.

5.2.2.4 Data interpretation

In Fig. 3.21 (a) we show a process that is most easily aligned with atomic and molecular measurements but can be extrapolated to solids. The primary difference between individual particle and solid based measurements is the bandwidth of the excitation. For the atomic case, the bandwidth reduces to its narrowest with a lower limit based upon the natural linewidth, governed by the following relationships:

$$\Delta\nu = \frac{1}{2\pi\Delta t}, \tag{5.10}$$

$$\phi(\nu) = \frac{\frac{\Delta\nu}{2\pi}}{(\nu-\nu_0)^2 + (\frac{\Delta\nu}{2\pi})^2}, \tag{5.11}$$

$$\frac{1}{\Delta t} \approx A_{nn'}. \tag{5.12}$$

The natural linewidth for a classic example, $n = 2$–$n = 1$ hydrogen excitation, with a frequency of ν =2.5×10^{15} Hz and a lifetime Δt of $10^{-9}s$ is 10^8 Hz. When considering solids, the bandwidth can become many orders of magnitude large than the natural linewidth due to formation of bands. The work presented in this ESI and the accompanying paper corresponds to the latter, solid case. The model presented by Fig. 3.21 (a) suggests the aforementioned selection rule $\Delta M_J = \pm 1$ shown in Fig. 3.21 (b). The traditional model, derived from Kubo dielectric susceptibility formalism,[69] presented for MCD two structures appear in spectra, including: (i)

absorption and (ii) derivative shaped features. These are shown by Fig. 3.21 (c), top and bottom, respectively. The derivative-like is the predominant feature expressed in MCD spectra. However, the model does breakdown when the separation of the two extrema becomes comparable to the excitonic bandwidth of the parent excitation.[503, 639]

5.2.2.5 Dispersion expressing exchange driven spin splitting

In Fig. 5.10 (a) we show how the energetic separation of the helicity-dependent absorptions is presented as rigid shifts of the band edge. The total splitting ΔE is equivalent to two times the exchange splitting because each helicity-dependent absorption will shift accordingly based on the exchange splitting. Of course, what is being shown here is a schematic and exaggerates any changes over that which is experimentally observed. However, the important point is that the exchange splitting drives the helicity-dependent absorption and therefore presents spin-dependent excitations that are in line with the $\alpha(E)$ edge.

5.2.3 Photoconductivity reveals electronic structure of $CoFe_2O_4$

Motivated by recent work in which iron oxides like $BiFeO_3$ are used as active elements of a solar cell,[601] we decided to take a step toward evaluating $CoFe_2O_4$ for light harvesting applications. Photoconductivity is well-suited for this purpose, and it is naturally connected to the series of band gaps, the spin split electronic structure in spinel ferrites, and the entanglement of charge and spin. These measurements also provide another opportunity to compare the electronic properties of $CoFe_2O_4$ with

those of the Ni analog.[116]

Figure 5.8 summarizes the photoconductivity of $CoFe_2O_4$. This property derives from the creation of electron-hole pairs with light: $\sigma_{PC} \propto \eta\ \alpha(E)\ \tau$.[640] Here, σ_{PC} is the photoconductance, η is the probability of creating a carrier, $\alpha(E)$ is the absorption coefficient, and τ is the carrier lifetime. Figure 5.8(a) displays typical current vs. voltage (I-V) curves with white light on and off. The open-circuit voltage of $V_{OC} = 100\,\mathrm{mV}$ at an intensity of $\approx 50\,\mathrm{kW\,m^{-2}}$. The data in panel (b) were obtained from similar I-V curves collected at specific illumination energies. Comparison reveals that photoconductivity tracks the absorption spectrum (shown here on a log scale) reasonably well. Closer examination of Fig. 5.8(b) reveals three regions of particular interest. That centered near 1.0 eV is connected with charge transfer excitations across the fundamental indirect band gap. There is also a d-to-d excitation in the vicinity, but a localized excitation will not carry current. However, the d-to-d excitation does perturb the electronic distribution and therefore provide a route for increased current. This works to effectively decrease local electronic correlations, both spatially and temporally. σ_{PC} is largest near 2.0 eV - just above the direct gap in the minority channel. σ_{PC} continues to rise at energies above the direct gap in the majority channel, with a feature near 3.5 eV that is most likely related to additional structure in the joint density of states. The non-zero photoconductance below the majority channel direct gap is particularly important. It provides evidence that there are indeed important electronic states in the energy window below 2.8 eV arising from the two discrete symmetry environments of the Fe centers. We therefore see that the minority channel states can carry current and that this current can be

created with light. A similar situation occurs in $NiFe_2O_4$ - although the overall energy scale is higher. The Ni compound also has less structure in σ_{PC}.[301] Exchange splitting is the origin of spin-dependent excitations in the ferromagnetic insulator $Y_3Fe_5O_{12}$ as well.[301, 641]

Application of a magnetic field provides an opportunity to further explore the photo-excited minority channel carriers. This is because applied field drives a $\downarrow\uparrow\uparrow$ to $\downarrow\downarrow\uparrow$ transition on the Co sites.[286] Figure 5.8(a) displays a typical set of I-V curves taken at under white light. As a reminder, light at this energy excites the Co $O_h \rightarrow$ Fe O_h charge transfer in the minority channel. The illumination and magnetic field conditions are indicated as ($h\nu$, B). Using I-V curves like those in Fig. 5.8(a), we determined field-induced changes in photoconductivity at various energies. Figure 5.8(c) summarizes these findings by plotting them as magnetoresistances. It is immediately apparent that $CoFe_2O_4$ exhibits strong field effects (-8%) in the range where only minority carriers are active. The strongest effect is near 1.8 eV. This response is well above the standard magnetoresistance (on the order of -1%).[73, 467] We conclude that light and field together are more effective than field alone - at least in the energy window between the minority channel indirect and the majority channel direct gaps. Moreover, magnetoresistance in $CoFe_2O_4$ (-8%) is significantly larger than that in $NiFe_2O_4$ (-6.5%) - even though the 1.5 T field applied here is not enough to fully saturate the Co moments. Spin-dependent excitations can be manipulated with external electric and/or magnetic fields in $Y_3Fe_5O_{12}$ as well. [16]

5.2.3.1 Response of electrons in strongly correlated systems

The many-body interactions existing naturally within the ground state of a material can be categorized as Coulomb (charge) and/or Fermi (spin) correlations. Coulombic correlation develops from the electrostatic interactions of charge carriers; whereas, Fermionic correlation evolves from the spin interaction of the charge carriers, i.e. the Pauli exclusion principle. [642] These interactions offer a wealth of potential applications, e.g. nanoelectronics and spintronics. For an example of these correlations, the *d*-orbital electrons tend to dominate the electric and magnetic properties of transition metal oxides, e.g. spinel ferrites.

5.2.4 Conclusion

In summary, we measured the magneto-optical properties of $CoFe_2O_4$ and compared them with prior optical absorption and first principles electronic structure calculations. Careful analysis of the dichroic response reveals that the full band gap hierarchy is 1.2 eV (indirect, minority channel), 1.8 eV (direct, minority channel), and 2.7 eV (direct, majority channel). The energy scale is overall lower than that of the Ni analog, and this series of band gaps has a strong overlap with the solar spectrum. Photoconductivity shows that the minority channel states can carry current, that this current can be created with light, and that it depends upon magnetic field. Moreover, we show that applied magnetic field switches the spin state, and by so doing, modifies the electronic properties. Spin-charge coupling, while dramatic in $NiFe_2O_4$, seems to be even more important in the Co compound, probably because the inversion fraction makes a combination of charge transfer excitations more promi-

nent. This work opens the door to new applications of spinel ferrites that exploit magnetic field control of electronic properties.

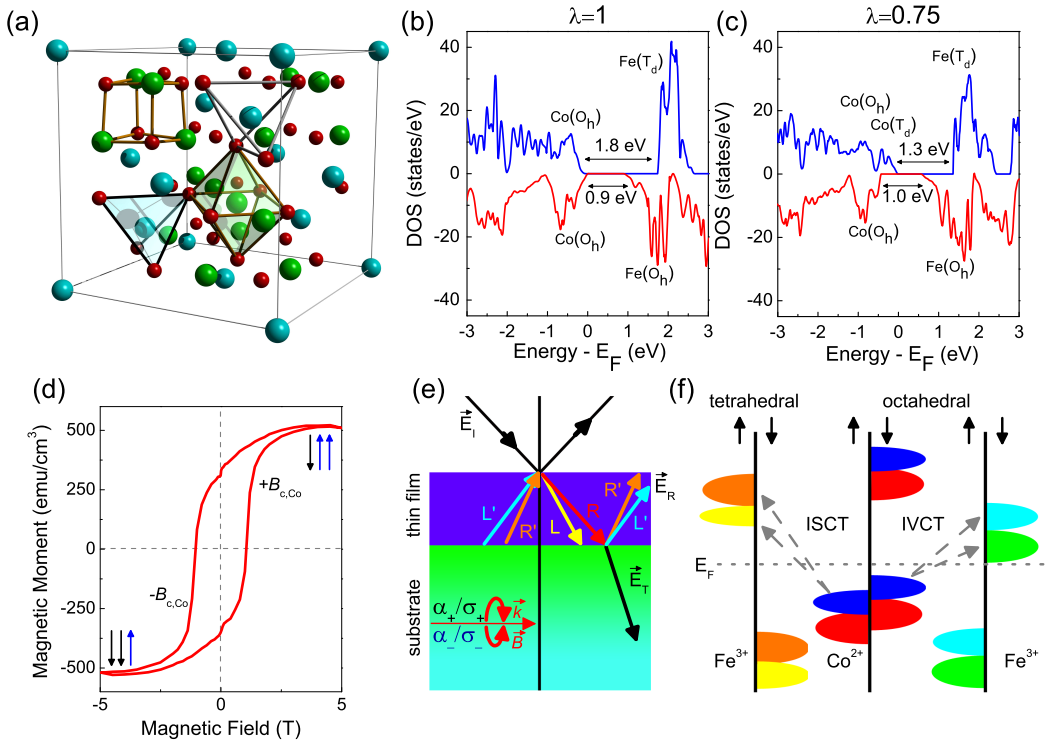

Figure 5.5: (Color online) (a) $CoFe_2O_4$ displays the typical AB_2O_4 spinel crystal structure (space group $Fd\bar{3}m$, No.: 227).[632] This system has an inversion fraction λ of $\approx$ 0.75, so an explicit rendering can be written as $\{Co_{0.25}Fe_{0.75}\}_{tet}[Co_{0.75}Fe_{1.25}]_{oct}O_4$.[633] Here, $\{\}_{tet}$ refers to the tetrahedral site, and $[]_{oct}$ refers to the octahedral site.[634] By comparison, $NiFe_2O_4$ is a fully inverse spinel.[60, 291] (b, c) Calculated electronic structures of $CoFe_2O_4$ from Ref. [116] carried out using $LDA + U$ with U_{eff} = 4.5 eV for Fe and 4.0 eV for Co for the fully inverse and $\lambda = 0.75$ cases, respectively. The band gaps in the minority and majority channel are labeled. (d) Magnetization data from Ref. [286] shows the hysteresis loop, the coercive field, and how the $\downarrow\uparrow\uparrow$ and $\downarrow\downarrow\uparrow$ states are switched at $B_{c,Co}$. (e) Four wave schematic of our magneto-optical experiments. In general, the wave vectors for right- and left-circularly polarized light will differ. (f) The excitations fall into two categories: (i) intersublattice charge transfer ISCT and (ii) intervalence charge transfer IVCT.

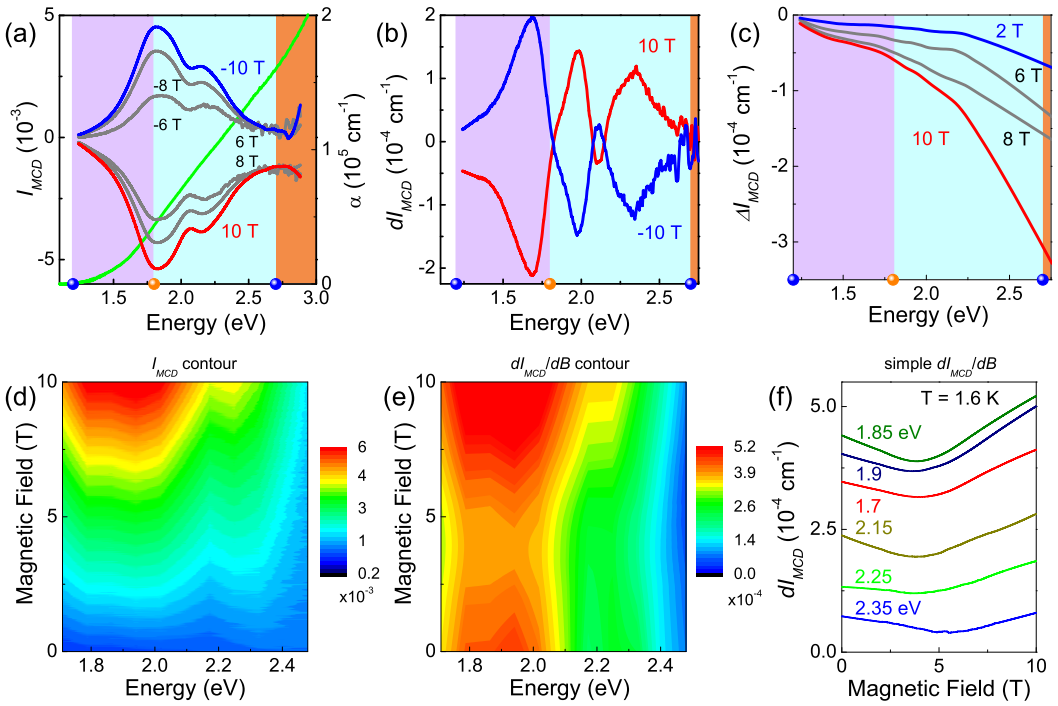

Figure 5.6: (Color online) (a) MCD spectra of $CoFe_2O_4$ at 1.6 K and $\pm$10 T along with the linear absorption (green line) for comparison. The points on the energy axis define the band gaps, with their corresponding assignment at the top.[116] The Faraday measurement geometry is indicated by the inset to the bottom right of panel (a). (b) Derivative of I_{MCD} with respect to energy, emphasizing the inflection points. (c) Residual MCD signal obtained from the difference of I_{MCD} in the positive and negative field directions: $\Delta I_{MCD} = I_{MCD}(E, B) - I_{MCD}(E, -B)$. This corresponds to the difference between the $\downarrow\downarrow\uparrow$ and $\downarrow\uparrow\uparrow$ states. (d) Contour plot of the MCD spectrum (I_{MCD}) in the energy-magnetic field plane. The data in panel (a) is a set of constant field cuts of this surface. (e) Contour plot of dI_{MCD}/dB as a function of energy and magnetic field. (f) Constant energy cuts of dI_{MCD}/dB vs. magnetic field plot.

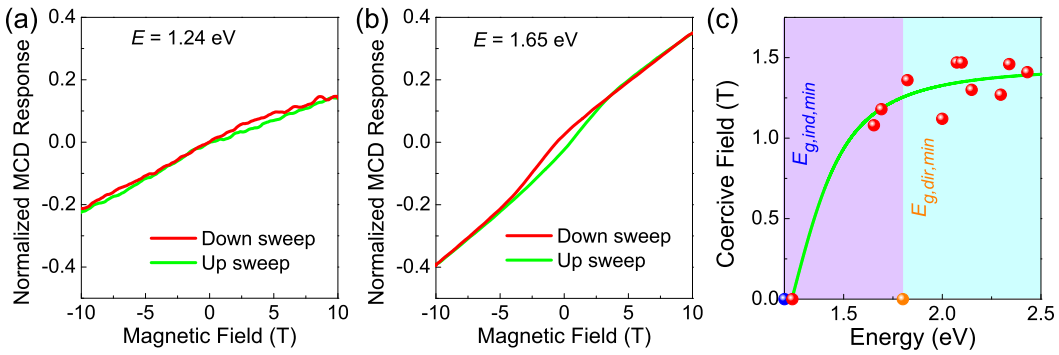

Figure 5.7: (Color online) (a, b) Representative field sweeps of $CoFe_2O_4$ showing the development of the optical hysteresis loop with energy. (c) Phase diagram displaying the energy dependence of the coercive field at 1.6 K. The minority channel indirect and direct gaps are labeled, and the coercive field data are fit with a Brillouin-like function, $B_c(E) = \frac{2B_c+1}{2B_c}\coth\left(\frac{2B_c+1}{2B_c}E\right) - \frac{1}{2B_c}\coth\left(\frac{1}{2B_c}E\right)$. Here, B_c is the coercive field and E is the energy.

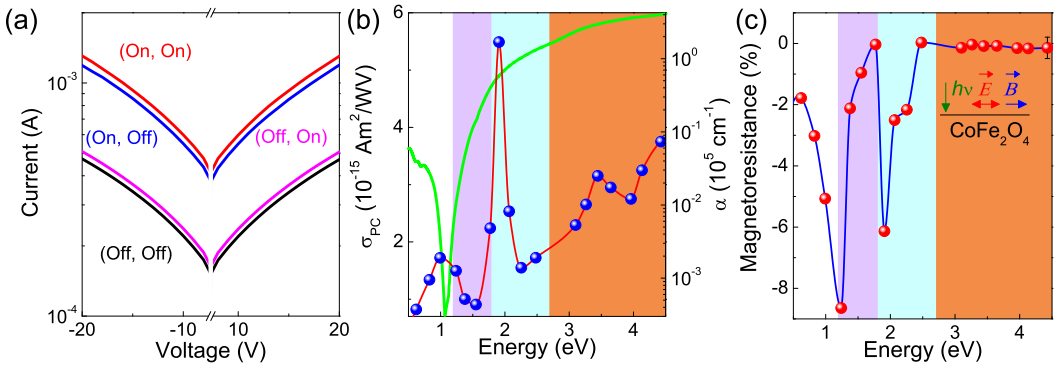

Figure 5.8: (Color online) (a) Representative I-V curves of $CoFe_2O_4$ taken under broad band (white) light at 300 K. Light and magnetic field are indicated to be on or off as $(h\nu, B)$. (b) Room temperature photoconductivity of $CoFe_2O_4$ vs. energy, at -20 V, along with the absorption spectrum for comparison. The log scale for absorption emphasizes features below 2 eV. (c) Optically enhanced magnetoresistance of $CoFe_2O_4$ vs. energy at 300 K. The band gaps are in (b) and (c) are 1.2 eV (minority, indirect), 1.8 eV (minority, direct), and 2.7 eV (majority, direct).

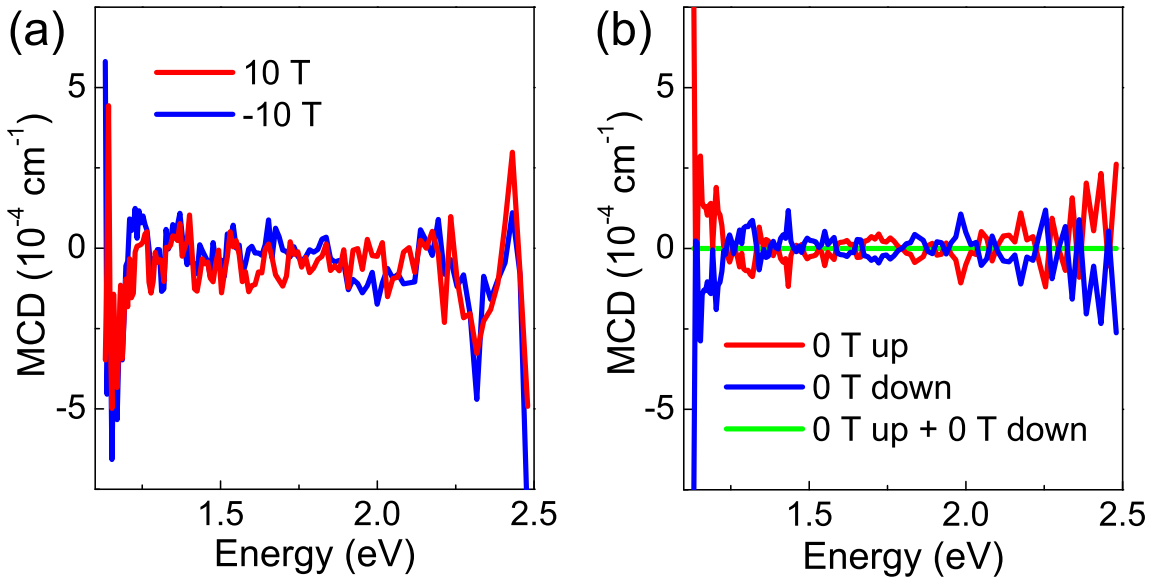

Figure 5.9: The MCD response of $MgAl_2O_4$ is shown to be magneto-optically silent. (a) $\pm 10\,T$ MCD response of the substrate is effectively flat across spectrum. (b) The MCD response of the substrate at $0\,T$, the distinction between the two is the direction that the field was before reaching $0\,T$.

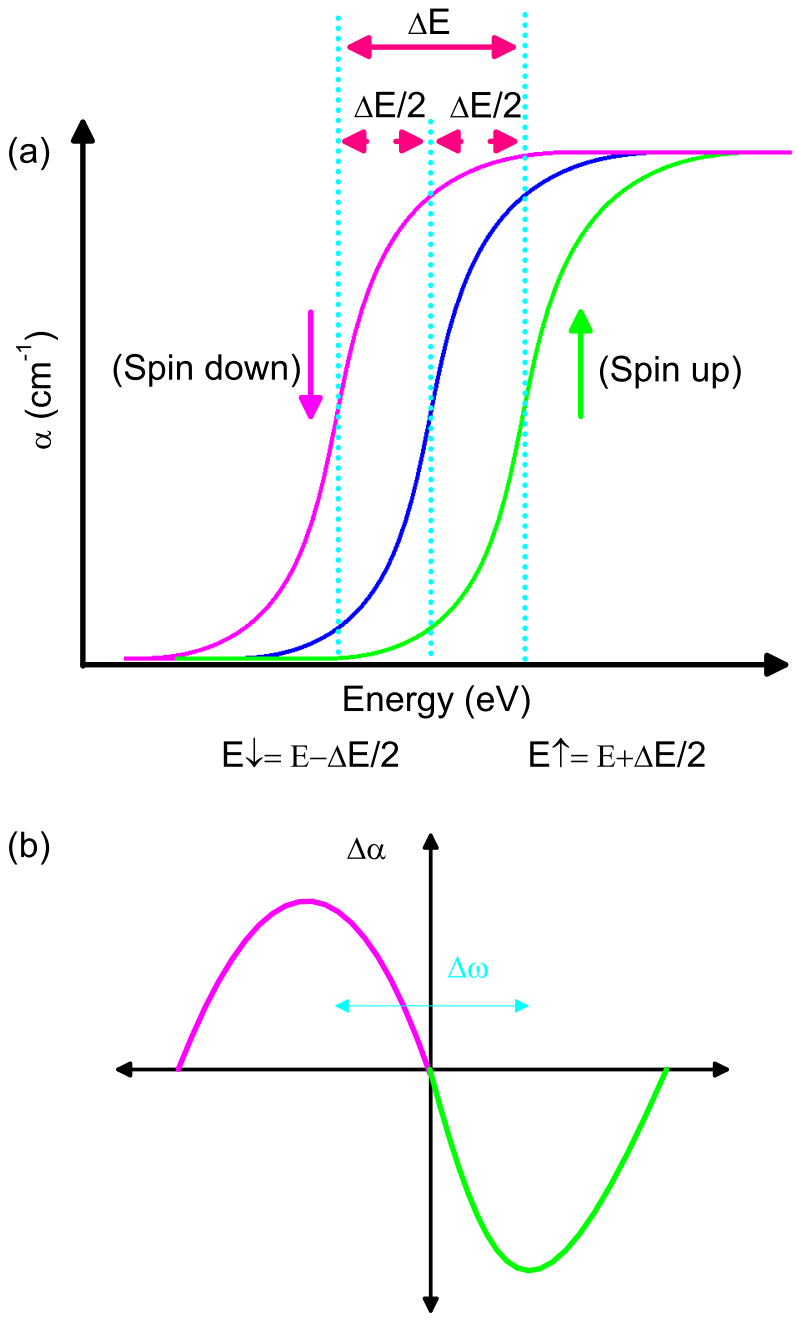

Figure 5.10: (a) Shown here is the rigid shift of the $\alpha(E)$ edge with respect to spin (helicity) dependence. The blue line corresponds to the 0 T spectrum. (b) This panel shows the derivative-like dispersion response expected from panel (a), centered at the crossover energy.

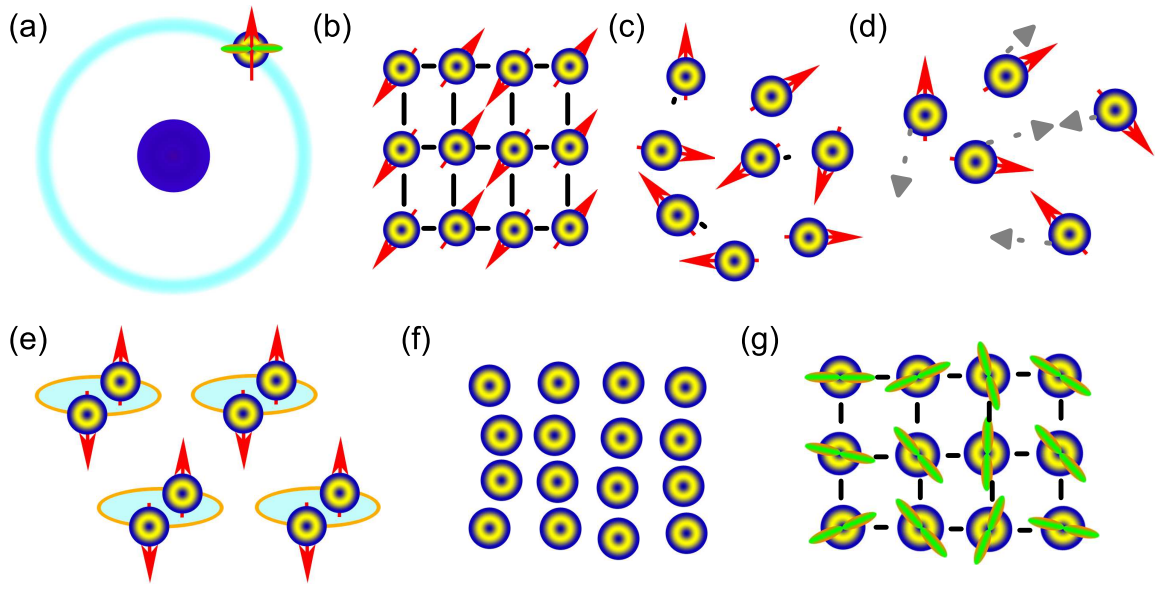

Figure 5.11: (a) The environment induced by correlated electrons motivates electronic phase emergence via entanglement, rather than mere co-existence, of spin, charge, orbital, and lattice degrees of freedom. The phases include (b) solid, (c) liquid, (d) gas, (e) superfluid, (f) liquid crystal, and (g) orbital liquid.

Chapter 6

Optical response of *h*-$LuFeO_3$ and $LuFe_2O_4$

> Always a fascination for the human mind, symmetry plays a fundamental role in modern physics.
>
> Surin Bangu
>
> The Oxford Handbook of Philosophy of Physics
>
> *Symmetry*

We brought together optical absorption spectroscopy, magnetic circular dichroism, photoconductivity, and first principles calculations to reveal intricacies in the electronic structure of *h*-$LuFeO_3$. Surprisingly, we uncover direct gaps at both 1.1 and 2.0 eV, different than previously supposed [643]. The 1.1 eV feature, which we assign as hybridized Fe $3d_{z^2}$ + O $2p_z \rightarrow$ Fe d excitations, is challenging to identify

due to its modest intensity which derives from the low density of states. The 2.0 eV direct gap is stronger and arises from $p-d$ charge-transfer excitations. It displays a 10 meV jump through the Néel temperature due to spin-charge coupling. That said, the overall absorption coefficient in h-$LuFeO_3$ is lower than that in many other complex oxides like $LuFe_2O_4$ and $BiFeO_3$. This difference emanates from the fact that the valence states are primarily in the spin-up channel whereas the conduction states are mostly in the spin-down channel. As a result of the gap hierarchies and relatively high magnetic ordering temperature, h-$LuFeO_3$ may find applications beyond light harvesting in sensing and flash memory devices.

6.1 Direct band gaps in multiferroic h-$LuFeO_3$

Figure 6.1(a) displays the absorption spectrum of h-$LuFeO_3$ at 4 and 300 K. The response is typical of a semiconductor. Plots of $(\alpha E)^2$ and $(\alpha E)^{0.5}$ vs. energy [559] reveal direct and indirect band gaps as

$$\alpha(E) = \frac{A}{E}(E - E_{g,dir})^{0.5} + \frac{B}{E}(E - E_{g,ind} \mp E_{ph})^2. \tag{6.1}$$

Here, $\alpha(E)$ is the absorption coefficient, $E_{g,dir}$ is the direct gap energy, $E_{g,indir}$ is the indirect gap energy, E_{ph} is the phonon energy mediating any indirect gap component, E is the photon energy, and A and B are coefficients. This approach was developed for traditional semiconductors with single strictly parabolic bands and has been extended

to analyze oxides, despite their more complicated band structures [599, 600, 314]. Our analysis reveals the presence of at least two direct gaps [Fig. 6.1(b, c)]. Consistent with prior work, we easily identify the 2.0 eV direct gap [643]. The spectrum also displays a lower energy structure on top of a long near infrared tail. These features were previously assigned as impurities and multiple reflections [643]. However, in our analysis, we find evidence for a direct gap at 1.1 eV [Fig. 6.1(c)], which we assign as the fundamental gap of $LuFeO_3$. This structure also has a minor contribution from indirect character. As discussed below, a 1.1 eV gap is strikingly consistent with predictions from first principles calculations [328]. Interestingly, the 1.1 eV direct gap in h-$LuFeO_3$ is smaller than that of several other iron-containing oxides including $CoFe_2O_4$ (1.2 eV), $NiFe_2O_4$ (1.6 eV), and $BiFeO_3$ (2.7 eV) [601, 314, 337, 116, 644]. $LuFe_2O_4$ is different in that it is an indirect gap material [82, 337].

The left panel of Fig. 6.2 shows h-$LuFeO_3$'s density of states, calculated in the GGA + U + SOC framework. The data is for the weakly ferromagnetic A_2 magnetic state which is the zero temperature ground state from theory [328]. Neutron diffraction data [80] have indicated a low temperature A' configuration which is nearly degenerate in energy to A_2 [328]. In this respect, the optical properties are expected to be similar. Our calculations show h-$LuFeO_3$ to be an insulator with a band gap of 1.0 eV, consistent with the aforementioned optical absorption analysis. The valence band edge is dominated by Fe $3d$ and O p states, mainly in the spin-up channel. There is a natural node in the density of states near -1.6 eV that will be important in later discussion. Strongly hybridized O + Fe states are deeper, around

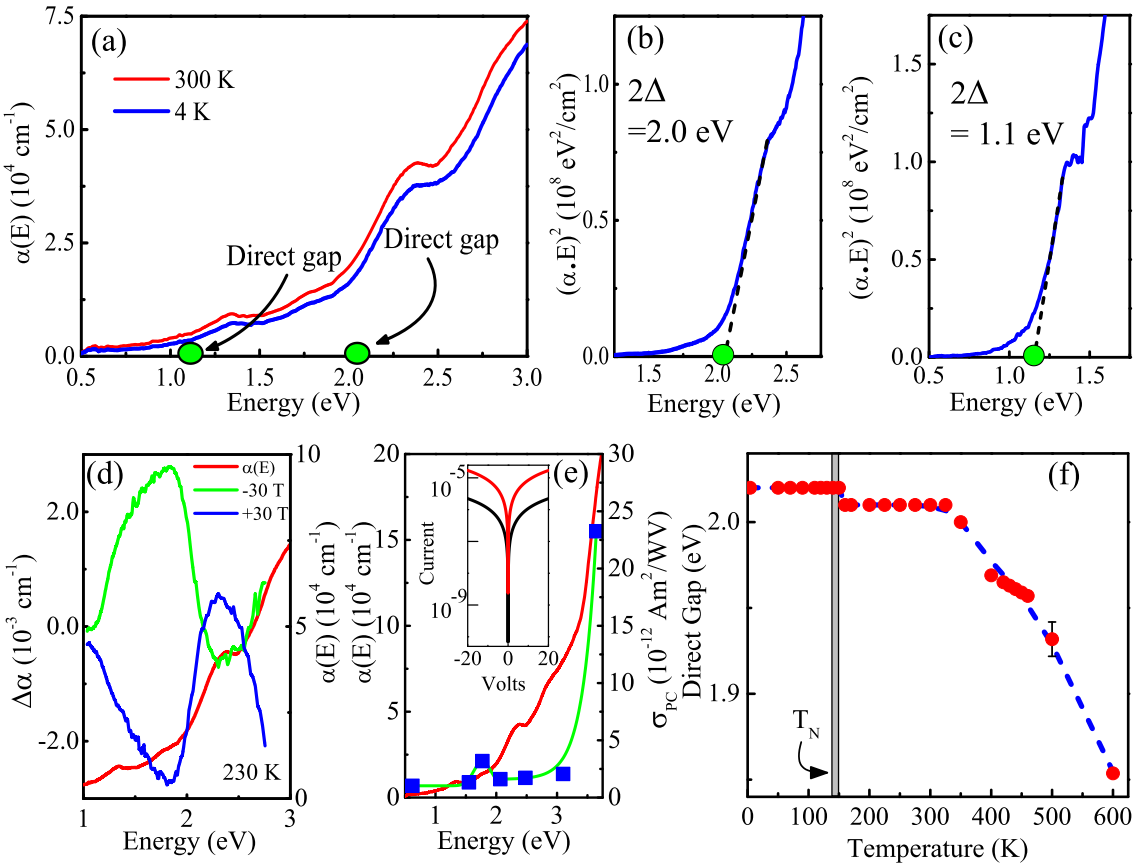

Figure 6.1: (a) Absorption spectra of h-$LuFeO_3$ at 300 and 4 K. (b, c) Direct gap analysis of the 4 K data. (d) Magnetic circular dichroism in the high temperature paramagnetic phase (230 K) compared to the room temperature optical absorption. (e) Photocurrent of h-$LuFeO_3$ (blue squares) compared with the 300 K absorption spectrum. The green line guides the eye. The inset shows I–V curves taken with a broadband xenon source with on:off given as red:black. (f) Temperature dependence of the 2.0 eV direct gap.

2.0 eV below the Fermi level, and they are equally populated in either channel. The conduction band edge consists of spin-down Fe $3d$ states (d_{xz}, d_{yz}, d_{xy}, and $d_{x^2-y^2}$ orbitals) with higher Fe $3d_{z^2}$ states about 2.0 eV above the Fermi level. Even though crystal field theory assigns Fe^{3+} to the high-spin d^5 state, our calculations indicate

substantial down-spin Fe DOS up to the valence band edge. This allows on-site Fe $d-d$ transitions and $p-d$ charge transfer excitations. We identity the latter of these excitations as candidates for the fundamental gap. The 2.0 eV direct gap is primarily due to charge-transfer $p-d$ excitations from deeper O p to empty Fe $3d$. The overall low oscillator strength of the experimental absorption spectrum emanates from the fact that the valence states are mostly in the spin-up channel whereas the conduction states are principally in the spin-down channel. Even above 2.0 eV, the absorption coefficient doesn't rise into the charge-transfer usual 10^5 cm^{-1} range. This is because there are very few unoccupied spin-up Fe states, which prohibits any substantial optical absorption in the spin-up channel. Due to the spin selection rule, spin-up to spin-down transitions are formally spin-forbidden, and although spin-orbit coupling relaxes this selection rule, the probability of carrier excitation by this mechanism is relatively low.

To analyze the nature of the fundamental and higher energy gaps, we plot the GGA + U bands along certain high symmetry points, as shown in the right panel of Fig. 6.2. Both the valence band maximum and the conduction band minimum are flat from Γ to the A point of the Brillouin zone. That both bands are nearly dispersionless means that h-$LuFeO_3$ is essentially a direct gap system with a primary band gap of ≈1.0 eV. The valence band- maximum is a combination of Fe $3d_{3z^2}$ and apical O-$2p_z$ states. Numerous nearly-degenerate indirect gaps are also close to the direct gap. This observation is consistent with the partial indirect character observed for the lower gap in our optical analysis. The 2.0 eV direct gap can be assigned to $p-d$ charge-transfer excitations as well. Again, the optical absorption coefficient

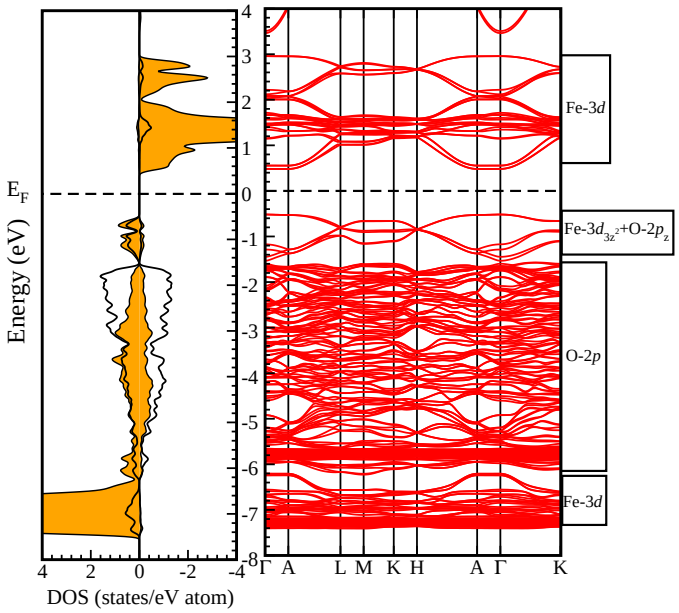

Figure 6.2: Left: density of states of h-$LuFeO_3$ calculated using the GGA + U + SOC method. Right: energy bands of h-$LuFeO_3$ at high symmetry points in the Brillouin zone. A direct gap at Γ, A, and points between is predicted.

is low, even above 2.0 eV, because the valence states are primarily in the spin-up channel whereas the conduction states are mainly in the spin-down channel.

Additional evidence for a lower energy band gap in h-$LuFeO_3$ comes from magnetic circular dichroism spectra. We focussed our efforts between 1.0 and 2.75 eV, searching for evidence of electronic excitations in this region, with the expectation that any dichroic response will provide insight into the nature of the important states, both in the paramagnetic and non-collinear antiferromagnetic phases. Figure 6.1(d) displays the dichroic response of h-$LuFeO_3$ in the paramagnetic phase at -30 to 30 T ($H \parallel \vec{k}$) along with the room temperature optical absorption for comparison. We find a strong dichroic response throughout the investigated spectral range. One lobe

peaks (dips) near 1.8 eV and is more than 1.0 eV wide. After a zero-crossing near 2.1 eV, a second lobe starts to take shape. Much of this structure is well below the larger (2.0 eV) direct gap of h-$LuFeO_3$. The presence of dichroically-active features down to almost 1.0 eV supports our proposal for important electronic states in this region. Density of states data reveals that the dichroically active excitations involve both Fe d and Fe $3d_{z^2}$ + O $2p_z$ hybridized states. As we discuss below, band structure effects are largely responsible for the shape of the dichroic response.

One prominent model for describing the dichroic characteristics of materials in their paramagnetic state [535] can be written as

$$\Delta\alpha_{r-l}(E) = \frac{-16\pi^3 EN}{3hc} H \left[\frac{\mathscr{A}}{h} \frac{\partial g(E)}{\partial E} + \left(\mathscr{B} + \frac{\mathscr{C}}{k_b T} \right) g(E) \right]. \tag{6.2}$$

Here, differential optical absorption $\Delta\alpha_{r-l}(E)$ depends upon $\mathscr{A}$, $\mathscr{B}$, and $\mathscr{C}$, parameters that represent excited state Zeeman effects, mixing of zero-field states, and the ground state population distribution, respectively [71, 535]. In addition, E is the energy of the photon, N is the number of unit cells/cm^3, and $g(E)$ is the band shape function (related to density of states), h is Planck's constant, k_B is Boltzmann's constant, c is the speed of light, and T is the temperature. But what accounts for the characteristic shape of the dichroic response in Fig. 6.1(d)? A careful look at the valence band density of states immediately reveals a mechanism. The natural node in the density of states near -1.6 eV will cause $g(E)$ to approach zero, effectively eliminating any contribution of the $\mathscr{B}$ and $\mathscr{C}$ terms to the dichroic response at 1.8 eV where the maxima and minima occur. At the same time, the shape of the response is driven by the derivative, $\partial g(E)/\partial E$. This amplifies the $\mathscr{A}$ term and is

most likely responsible for the large peak (dip) structure in the dichroic response. In fact, it drives all three of the features in the spectrum. Therefore, we find that band structure effects (both the density of states itself and the energy derivative of this quantity) are responsible for the shape of the dichroic spectrum [645].

Photoconductivity measurements provide some support for the presence of electronic states below 2.0 eV, although the evidence is not as conclusive as that from the magnetic circular dichrosim. Figure 6.1(e) displays the photocurrent of h-$LuFeO_3$ taken at different energies compared with the linear absorption spectrum. I–V curves in the dark and under illumination with a broadband xenon source are also included. The photocurrent shows a small peak near 1.65 eV, in line with expectations from the optical response. This makes sense because $\sigma_{PC} \simeq \eta \cdot \alpha(E) \cdot \tau$, where σ_{PC} is the photo-induced conductivity, η is the quantum efficiency or probability of making photocarriers, $\alpha(E)$ is the absorption coefficient, and τ is the photo-carrier lifetime [646]. The increased photocurrent between 1 and 2.0 eV correlates well with evidence for a lower band gap. It is also in line with the aforementioned magnetic circular dichroism work, which reveals important electronic states in this region. The photocurrent and absorption coefficient both track to significantly higher values with increasing photon energy, evidence that the most important band gap is at 2.0 eV.

Finally, we carried out variable-temperature spectroscopic measurements between 4 and 600 K, searching for optical signatures of the Neél transition. This also reveals information about the spin-charge coupling. There are two candidates for the magnetic phase transition: 140 and 440 K [80]. Figure 6.1(d) displays the temperature dependence of the 2.0 eV direct gap. We found that at low temperature the depen-

dance was rigid and drops by ≈10 meV through the 140 K Néel temperature. This drop is the same order of magnitude as theexchange constant (J) [584, 324]. Although the band gap in h-$LuFeO_3$ is only weakly sensitive to the magnetic transition, the small but distinct 10 meV contraction is a signature of spin-charge coupling. Similar interactions are present in other multifunctional oxides like $BiFeO_3$ and $Ni_3V_2O_8$. [601] The gap softens above 300 K, reaching a value of 1.85 eV at 600 K. We find no evidence for spin-charge interactions near 440 K,[80] consistent with recent neutron diffraction.[222] The sensitivity of the 2.0 eV gap in h-$LuFeO_3$ to T_N has interesting parallels. The gap in $BiFeO_3$ softens through the 640 K Néel transition,[601] that in $LuFe_2O_4$ decreases through the 330 K charge ordering transition,[82] and that in $Ni_3V_3O_8$ hardens through the magnetic quantum critical transition.[647] By contrast, the 2.7 eV direct gap in $CoFe_2O_4$ is rigid up to approximately 800 K.[116]

6.2 The adsorption-controlled growth of $LuFe_2O_4$ by molecular-beam epitaxy

Figure 6.3 displays the ab-plane optical response of $LuFe_2O_4$ in epitaxial thin film form on $MgAl_2O_4$ compared with bulk single crystal data.[82] Comparison with first-principles calculations allows us to assign the observed excitations.[648] The band centered at ≈4 eV and the rising higher energy absorption can be assigned as a combination of O $p \rightarrow$ Fe d and O $p \rightarrow$ Lu s charge transfer excitations. A plot of $(\alpha E)^2$ vs. energy places the direct band gap at ≈3.4 eV. While the film is not fully commensurate, the average in-plane lattice constant of the film on $MgAl_2O_4$

from XRD is 3.42±0.02Å, which is 0.6% smaller than the bulk value of 3.44Å. This compressive strain blue-shifts the direct charge gap and the band maximum compared to similar structures in the single crystal. BiFeO3 displays similar behavior.[649] Previous measurements on single crystalline $LuFe_2O_4$ also identified an indirect band gap at 0.35 eV, a feature that is defined by the leading edge of the $Fe^{2+} \rightarrow Fe^{3+}$ charge transfer excitations that occur in the W layer (the iron oxide double layer).[82] The film shows a similar, but somewhat leakier tendency in the $(\alpha E)^{0.5}$ vs. energy plot, although due to limited optical density, our uncertainties are larger. Similar measurements on a film on SiC are less interpretable due to the 3.05 eV band gap of the substrate. The photos shown in Fig. 6.4 were taken on the FTIR microscope under identical illumination. The scenario presented here is purely in a reflectance geometry, where the light only comes from above the surface being photographed.

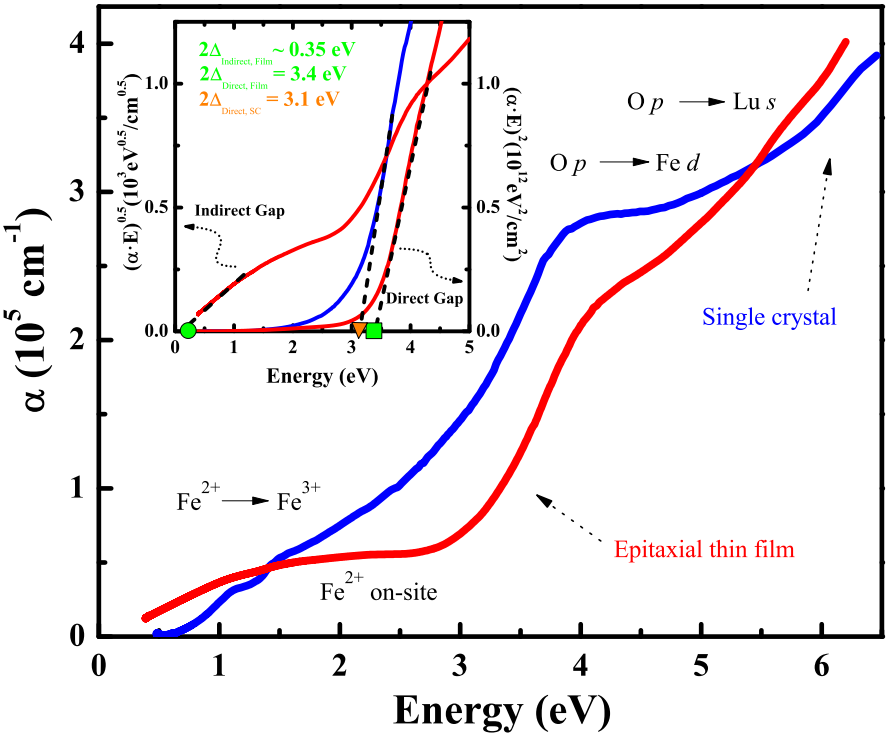

Figure 6.3: Optical response of a 75 nm thick (0001) $LuFe_2O_4$ film grown on (111) $MgAl_2O_4$ along with the ab-plane response of a $LuFe_2O_4$ single crystal [82] at 300 K. The film absorption was determined by a combination of direct calculation of absorption from transmittance (below ≈3 eV) and a Glover-Tinkham analysis of both transmittance and reflectance to obtain absorption above 3 eV. The data were merged between 2.5 and 3 eV, where there was substantial overlap. The inset shows the indirect and direct band gap analysis.

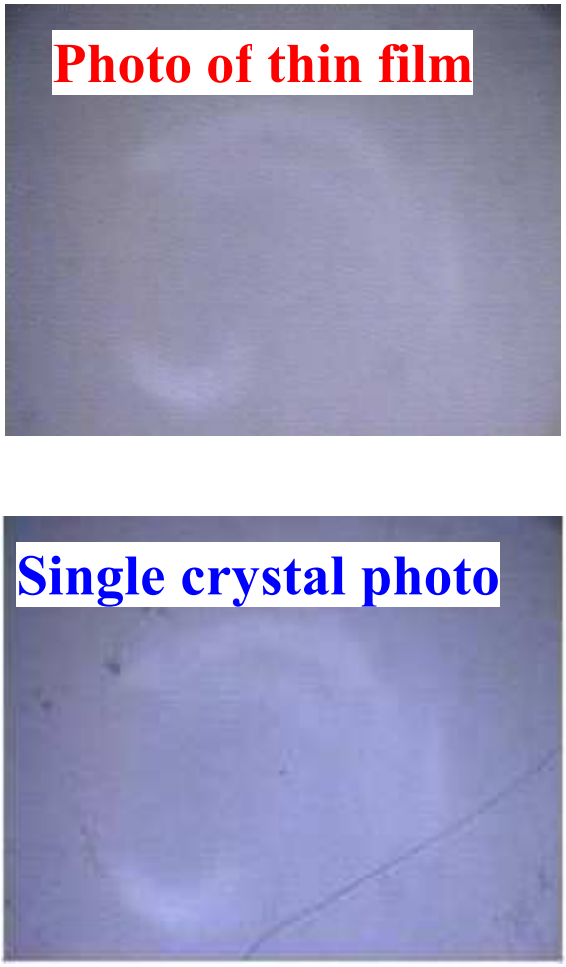

Figure 6.4: Pictures showing the visible difference between the thin film and single crystal. The most prevalent difference is the darker color of the thin film.

Chapter 7

Instrument and Experiment Design: Photoconductivity

"One of the deep secrets of life is that all that is really worth doing is what we do for others."

Lewis Carroll

7.1 Introduction

A significant portion of the work done for this dissertation was in the design and development of an instrument to measure photoconductivity. This brings together two techniques, spectroscopy and transport. Fundamentally photoconductivity is the photoelectric effect in insulators rather than metals. This result arises from altered lifetimes of the excitonic species that do not immediately recombine because of the applied electric field inducing perturbation from the particles equilibrium position,

thus producing an increase in the measured current through the sample. To begin we needed to decided what samples we would start with, because I was leading this endeavor we opted to start with samples that have a thin-film form factor. This form factor has impact onto how the sample interface is designed. One of the important factors taken into consideration is the theoretical measurement limit for signal detection of the current (I) magnitude. For transport measurements, the theoretical limit in a given measurement is determined by the noise generated by the resistance present in the circuit. As an example, voltage noise is proportional to the square root of the resistance, bandwidth, and absolute temperature, $N(V) \propto \sqrt{\rho \times \omega \pm \omega' \times T}$, falling into the regime of noise known as Johnson-Nyquist noise.[421]

7.2 Background

Functionally all materials are photoconductors, so why use this as a probing technique. The simple answer is that photoconductivity and spectroscopy are complimentary to each other. From a technical standpoint, photodetectors are divided into two classes: thermal and photon detectors.[650] The former detect a change in temperature upon absorption of light into its dark surface, whereas photon detectors implement the quantum photoelectric effect. In the latter, an absorbed photon excites an electron(s), these become the photocurrent or the photo-induced current. The lower bound of functionality for photodetectors is related to the energy of a

transition, such as the band gap or barrier height, this is described as

$$\lambda = \frac{hc}{\Delta E_g} = \frac{1.24}{\Delta E_g}. \tag{7.1}$$

Here, λ is the wavelength, c is the speed of light, and ΔE is the energy of the transition. Since the absorption of light is presented as the absorption coefficient (α), the magnitude of this value can help to indicate a few potentially useful attributes of the photodetector. One of these attributes is whether a wavelength regime would be an efficient producer of photoexcited electrons. Another is the depth of penetration, technically the absorption coefficient depicts the depth at which $1/e$ of the impinging photons will transmit, allowing one to measure specific portions of a system.[651] A schematicd circuit is shown in Fig. 7.2.

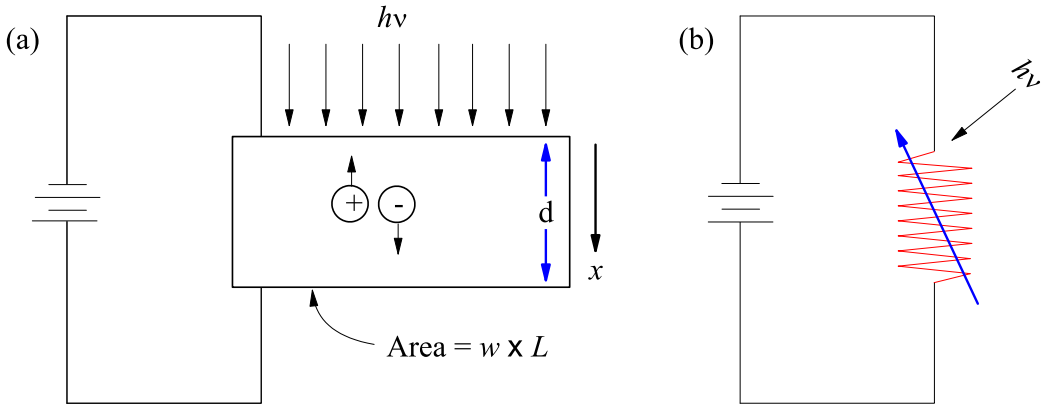

Figure 7.1: (a) Displays the circuit with the photoconductive element in place. (b) Shows an equivalent circuit with the photoconductive element replaced with an equivalent traditional circuit element, variable resistor.

This logically leads to the necessity of maximizing sensitivity. A potential metric for knowing how this is progressing is the quantum efficiency η, shown in the following

relationship

$$\eta = \frac{I_{ph}}{e\Phi} = \frac{I_{ph}}{den}\frac{h\nu}{P_{opt}}. \tag{7.2}$$

Here I_{ph} is the photocurrent, with Φ $(= \frac{P_{opt}}{h\nu})$ being the photon flux, and P_{opt} is the optical power, or irradiance. Deviance from ideal quantum efficiency (unity) occurs through mechanisms such as current loss, resulting from reflected or transmitted photons, and recombination. Similarly, the metric of responsivity $\mathscr{R}$ can be used, where the optical power is referenced

$$\mathscr{R} = \frac{I_{ph}}{P_{opt}} = \frac{\eta e}{h\nu} = \frac{\eta\lambda(\mu\text{m})}{1.24} * 0.25 A/W. \tag{7.3}$$

7.2.1 Performance - Steady State

Even in steady-state (quasi-equilibrium) conditions, this category of measurements stand outside of the Neumann principle.[652] This is because transport properties of crystals, e.g. thermal, electrical, thermoelectric power, and diffusivity, are fundamentally thermodynamically irreversible processes. The overall performance of a given photoconductor is measured in three parameters: quantum efficiency (η) and/or gain, response time, and sensitivity (detectivity). This is established by assuming a steady output of photons from the source reaching the surface of the conductor, uniformly of course. The area of the photoconductor (and of illumination in this assumption) is $A = W \times L$, with a total number of photons impinging upon the surface per unit time being $P_{opt}/h\nu$. A certain fraction of those are absorbed per unit time and per unit volume $R_\alpha = P_{opt}/h\nu/V_v$, the absorption rate. The ultimate result of this is

a steady-state, where the generation rate G and recombination rate of carriers are equal. In the case of the investigates material having a thickness being much greater than the penetration depth of the light ($D \gg 1/\alpha$), "all" light is absorbed. If this case is satisfied the steady-state generation (recombination) rate of carriers per unit volume appears as $G = \frac{\eta(P_{opt}/h\nu)}{WLD}$. Here, τ is the carrier lifetime, n is the density of excess carriers, and again η is the internal quantum efficiency. The concentration for the excess carriers can be expressed as $n = G\tau$. Eqn. 7.4, below, describes the internal quantum efficiency and how this value can be understood from measurement quantities,

$$\eta_i = \frac{G}{R_\alpha} = \frac{GV_v}{P_{abs}} = \frac{G}{P_{den}}. \tag{7.4}$$

Now that we have seen the internal quantum efficiency, detailing the ratio of generation rate to photon absorption rate, we should establish the external quantum efficiency:

$$\eta = \frac{I_{ph}/q}{P_{opt}/h\nu} = \frac{I_{ph}}{q} \cdot \frac{h\nu}{Popt}. \tag{7.5}$$

From this relationship we can see that the number of excitons collected per second, producing the photocurrent I_{ph}, is divided by the number of incident photons P_{opt}. This generally linear response relationship has a window of action for a given material, the upper bound in wavelength, of this window can be determined by the band gap of the material through the relationship shown in Eqn. 7.1.

Another important relationship emerges when the light is turned on (off)

$$n(t) = n(0)exp(\frac{-t}{\tau}). \tag{7.6}$$

In this it is seen that the increase in carrier concentration (density) changes exponentially. An example of this response is shown in Fig. 7.2.

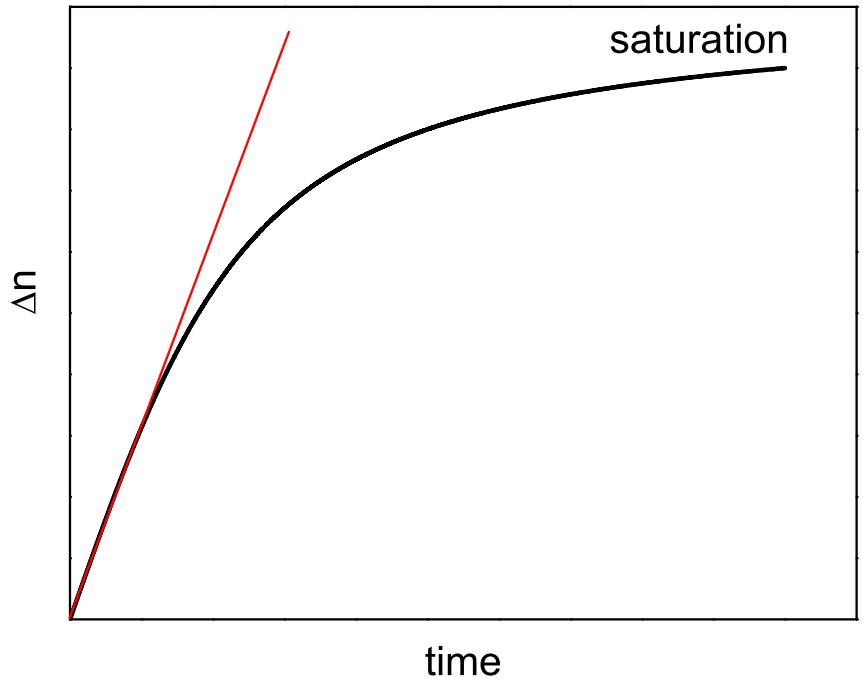

Figure 7.2: Shown here is how the carrier concentration changes versus time, it increases exponentially from the time of the light being turned on (off).

After exploring the operation in a pure sense, we need to bring to understand the limitations.

7.2.2 Noise

One of the most common limitations within a scientific endeavor is the noise level. The standard noises are white, shot, Johnson-Nyquist (thermal), $1/f$, random telegraph, and generation-recombination. Each of these could warrant a chapter to fully describe the result and signal processing effects. Taking the latter as an example, generation-recombination noise occurs due to the excitation and degeneration of electrons, only in semiconductors. It is caused by fluctuations in the number of carriers due to naturally occurring generation-recombination centers with proportionality to both temperature and biasing conditions.[653] Another functional route for noise is through the changing relays inside of the Keithley 6487. When the current level approaches a boundary for these changes, the quality of the data has a tendency to increase in noise. This is quite reminiscent to using the various detectors and/or lamps in the Equinox-55 microscope or the $\lambda - 900$. As the end of the range for the given detector is approached the data reliability wanes. This shows up as "random" oscillations in the data. Ultimately this is represented as a "small" fluctuation in the current.

7.3 Design and Building of the Instrument

7.3.1 Optical Path

In the building process of this instrument, we had to acquire many pieces of equipment, including optical and electronic components. We started with a blank canvas of an optical table. We have two light sources available to use at our discretion,

initially a broad band xenon lamp with an output of 300 W and finally a broad band 250 W xenon arc lamp. The power supply on the latter lamp allows for *in-situ* power regulation of the lamp, thus further measurements of intensity dependence can be taken into account. Currently the instrument is designed to measure the spectrum in a piecewise fashion using bandpass filters. A schematic of the design is shown in Fig. 3.25. The light source is a xenon lamp, this produces a macroscopic controlled quantity of photons, followed by an aperture to establish a Fourier plane for wavefronts, next the beam is reduced in size by using a focusing lens.[654, 655, 397] To send the light to the sample, the beam direction is changed by incorporation of a aluminum mirror, this is shortly followed by another lens to focus the beam onto the sample. We use geometric optical principles to create the path. The first principle statement of this approach is that a change in refractive index (either $n_{\pm}$) controls the direction of flow of the photons.[655, 656, 657, 382, 654, 658] This falls nicely under the description of Snell's law

$$n_1 sin\theta_1 = n_2 sin\theta_2. \tag{7.7}$$

Here, θ_n represent the angle between the surface normal and the incident and/or reflected light.

7.3.2 Sample Preparation

Now that we have photons impinging upon where the sample is to be placed we can prepare it to be measured. We must clean the surface to ensure that the leads adhere well. We will continue from this point as though we are intending to investi-

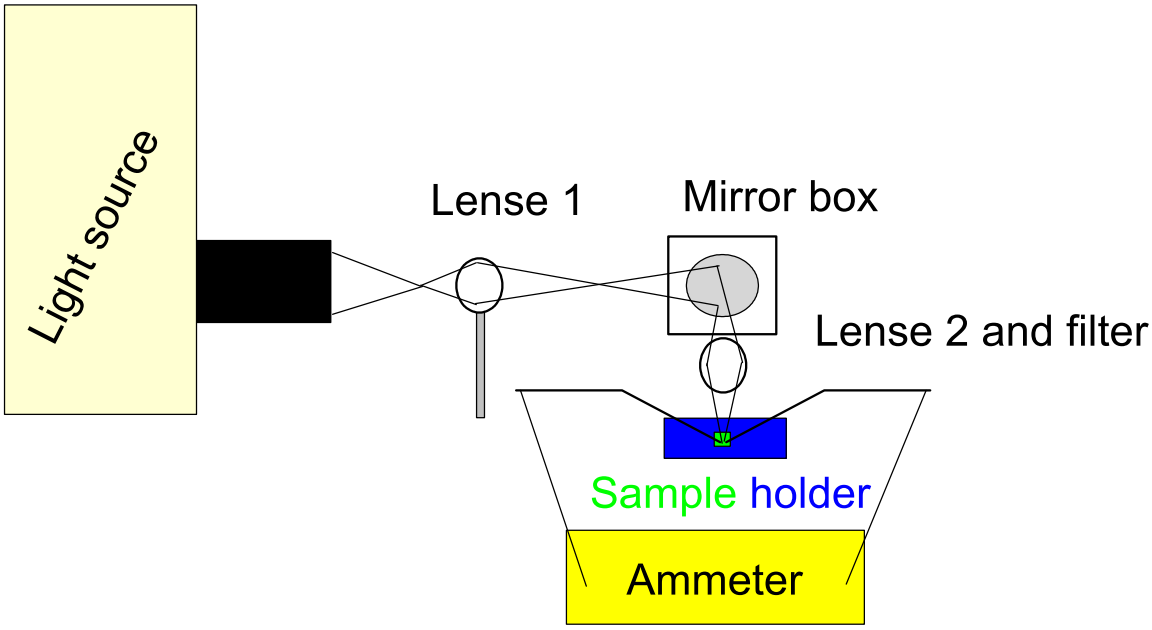

Figure 7.3: Schematic layout of the photoconductivity instrument, currently minimized to include as few components as necessary. These components include a light source, lenses (1 & 2), mirror box (with mirror inside), filter, sample space, and ammeter. This is designed to measure steady-state photoconductivity.

gate a thin-film ferrite; in principle the methodology can be adapted to any material or form. We place the sample in a pure solvent, such as optical/electronics grade acetone, and sonicate for upwards of 20 minutes. During this interim time we start cleaning and preparing the sputterer. This is done with a 50:50 mixture of acetone and ethanol along with just ethanol. We clean the bell jar of the sputterer with the mixture to remove any dust, previously deposited metal, and/or other loosely attached debris; the vacuum sealing o-ring is cleaned with the ethanol to keep the rubber moisturized, flexible, and remove oxidation. Periodic application of a small amount of low vapor pressure vacuum grease also improves the lifetime of the rubber seal. Now the sonication is complete and we inspect the sample under a high-power

microscope to look for remaining debris or residue, we also use the Bruker Equinox 55 with microscope attachment to examine the surface both using higher-power visualization and spectroscopically via reflectivity. After the sample is deemed clean, we glue it to a piece of silicon or glass slide, and build up the area around the sample with broken slip cover pieces to achieve a similar thickness. This prepares the area for the deposition mask, cleaned in a similar fashion as the sample. We place the mask over the sample and align to maximize the number of spots to be deposited on the surface. After aligning the mask, it is secured to the silicon with standard scotch tape.

7.3.2.1 Sputtering

From a traditional standpoint, it is best to measure in a parallel plate capacitor geometry. However, in situations where this not an accessible architecture one has the option to have contacts on the same plane of the material. This can take on a variety of configurations such as interdigitation, square array of dots, or triangular array of dots. With these same surface configurations, it is plausible to investigate just about any portion or direction of the material being sampled .[659] That being said, it is a logical extension to perceive doing anisotropic measurements in a multitude of environments, e.g. varied temperature and magnetic field.

Since everything is prepared to deposit spots onto the surface of the sample, we place the sample and mask assembly into the sputterer, close the top and start the vacuum pump. The procedure we have developed for sputtering is as follows. We allow the chamber to pump for at least 1 hour, establishing a pressure of at least

0.01 mBarr, on the front panel, in the worst case scenario. Following this we fill the bell with argon for 45 s seconds by pressing the leak button on the front panel. This is repeated 3-5 times with at least 15 min minutes between each "leak". These are done under dynamic pumping. The system automatically protects the turbo pump by slowing its velocity when the leak button is pressed. A primary goal of this is to help with pumping out unwanted gases from the chamber. Continuing on after the final "leak", one is to press the flush button on the front panel. A knob on the back allows for control of the flow rate (pressure) through a needle valve, this should be 0.01→0.03 mBarr. Do a final pre-check of the settings, such as density, thickness, and current. With the shutter still in place, press and hold pause/test button briefly to check if plasma plume is created. If plume appears, release the button and move the shutter out of the path, then press the start/stop to initiate deposition onto the sample. When thickness reaches preset value, the current will be shut off and deposition will stop. We allow the chamber to continue to pump for 15 minutes after the deposition stops, then turn the system off with the big red rocker switch. With the deposition finished, we can now prepare the sample to be exposed to an electric field.

7.3.2.2 Connecting Leads

For the majority of this instrument's lifetime, we have gone straight from the sputtering to putting the sample in place and attaching the leads. As of late we have switched the method of lead attachment, but that will be discussed a little later. The previous methodology to attaching the leads requires one to look at the surface while

moving the tungsten needle tips towards the dots via the position adjustment screws on the magnetic bases. A challenge of this method arises from the fact that you are moving in three dimensions but only see two, especially when looking through the microscope. Some adaptations have been implemented, such as an angled lamp to produce shadows. These shadows allow one to estimate the distance of the tip from the surface and have real-time information of progress concerning the connection of the leads. Another adaptation is running the time dependence program and listening for a relay to close. This occurs when the circuit is completed and current starts flowing.

Our more recent form of lead attachment includes using silver epoxy and wires that are $70 - 80\,\mu m$ in diameter. This combination allows for contacts that remain in place and can be attached/detached. Ultimately the approach takes a step towards eliminating the concern of longevity due to damaging the surface of the sample or scratching away the deposited metal pads. The use of more robust solid contacts allows for the opportunity to expand the capabilities of this instrument to include temperature dependence and greater sensitivity. The method of using silver epoxy is fairly standard within the realm of transport measurement groups.[660, 661]

Table 7.1 gives a list of suggested improvements that, given time and funding, would increase the sensitivity, variability, and applicability range of this instrument.

Table 7.1: Photoconductivity setup suggested upgrades

Improvement	**Sign of improvement [Expected]**
Soldering and/or wire-bonding leads onto sample	Decrease in overall noise level induced from environment
Use monochromator	Increase resolution of measurements and decrease wait time (drift) between spectral points
Use optical fiber for light directing	Improved power density and overall sensitivity & anisotropy measurements
Beam continuity (fewer hot spots)	Decrease thermal gradient and thus any concerns of thermoelectric current
Build a probe for use of superconducting magnet that implements the sample holder designed in the previous suggestion	Measure magneto-photoconductivity and Hall effect simultaneous with magneto-optical effects
Design sample stage	Increased sensitivity by maximizing 6 degrees of freedom (x, y, z) & (r, θ, ϕ) alignment
Design and implement a wavelength modulation setup	Improve clarity of features (direct visualization of derivative)

Continued on next page

Table 7.1 – *Continued.*

Improvement	**Sign of Improvement [Expected]**
Use a chopper and lock-in amplifiers	Increases signal to noise ratio, measure low frequency dependence, and gain more information about carriers involved
Incorporate multiple power meters	Measure transmittance & reflectance simultaneously along with photoconductivity
Use linearly polarized light	Garner deeper understanding of polarization dependence
Use right and left circularly polarized light	• Gives access to optical orientation and better understanding of magneto-optical properties/ potential for spintronics applications • Increases the overall range of experiments that can be achieved
Implement noise spectrum analysis	Increase sensitivity and reliability of results

Continued on next page

Table 7.1 – *Continued.*

Improvement	**Sign of Improvement [Expected]**
Start measuring ac	Introduces another degree of freedom to the measurement and another adjustable parameter

These suggestions would require that someone be highly interested in a wide variety of topics, such as optics, spectroscopy, transport, programming, engineering/design, and physics of low temperature measurements to incorporate by themselves. So, it is my suggestion to have a collaboration among a few people to achieve a high-quality result. In Fig. 7.4 I show a schematic representation of an end goal instrument design. Importantly, all of the elements between the monochromator and power meters Fig. 7.4 (b-g) will be on sliding rail systems to promote modulator in the measurement environment. The use of two power meters is to obtain information concerning modification to the attenuation or absorption of light through the sample. On a final note, one adaptation not shown in the schematic is the use of a fiber optical to bring the light into the sample space. The use of the optical fiber would be to maximize the power density.

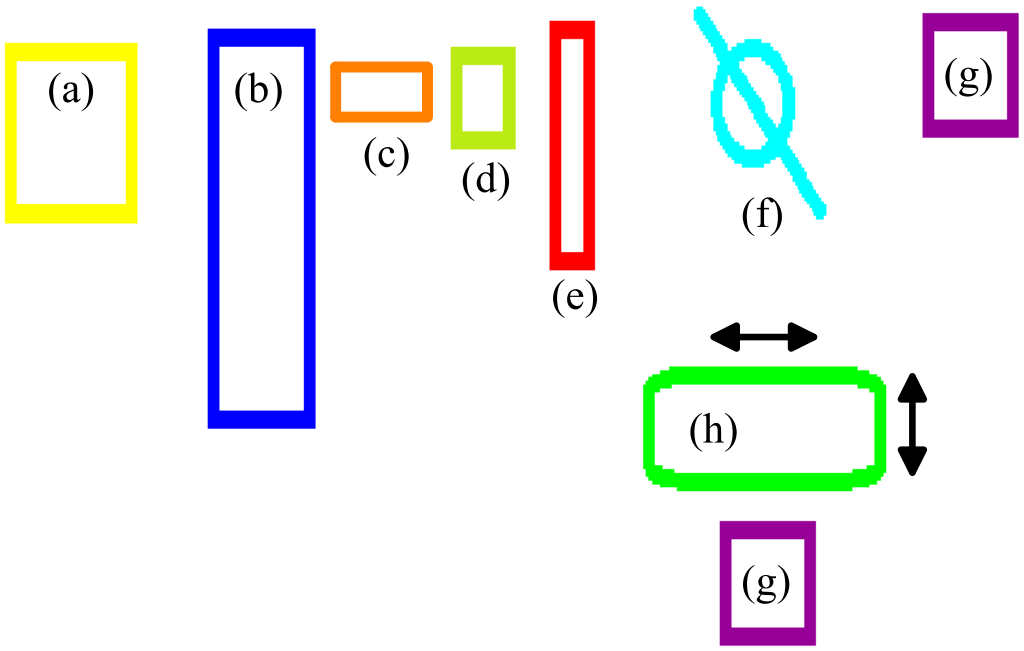

Figure 7.4: Schematic layout of a suggested setup end direction. The components of the instrument are labeled (a-h), where (a) is the light source, (b) is a monochromator, (c) is collimating optics, (d) is a position for a linear polarizer, (e) is a photo-elastic modulator (dynamic quarter waveplate), (f) is a beam splitter (or chopping mirror), (g) are power meter, and (h) is a sample stage.

7.4 User-interface and Data Collection

To collect data we wrote a program that gave us access to manipulating the state of the system and record any response given by the sample. We decided to use National Instruments LabVIEW, this language is based upon visual programming and allows one to create a virtual instrument (VI). Currently the program is separated into two approaches, time-dependence and I–V, at minimum these give access to information about the mobility and how many carriers are generated. Combined

they give access to much more information about the system such as carrier lifetime, predominant carrier charge sign, electronic structure, spin dependent excitations, and effective mass. The programs communicate to the Keithley 6487 through a GPIB cable (IEEE-488). Collection of the system state (data) is obtained by use of this connection. Initially the program clears the ammeter's memory and establishes the desired voltage. The available parameters that can be controlled directly through the VI include the time span of data acquisition, voltage, time resolution (dt), and the file name/location. One issue that arose during the usage of the time-dependence program for periods beyond 8 h is that the data points would start to become further and further apart.

After continued development, the two programs were integrated into one and after a multitude of iterations, many bugs were worked out and the program was tested to provided a result that the processor runs at 46% before adding a few extra pieces of information in to make the data more directly usable.

7.5 Magneto-photoconductivity

One of the most important upgrades that I implemented while building this instrument is inclusion of small magnets. The purpose for implementing magnets is to investigate production of spin-polarized current via optical conduction in spin-polarized excitations. For proof of principle, we opted to start with hard magnets. To do this we designed a carriage system so that we can slide the magnets towards and away from the sample position. Initially the carriage system and the sam-

ple mounting plate were on the same rails but after a bit of thought, spurred by significantly increased noise, we took the option to separate the three pieces. We designed the sample mounting plate to place the sample at mid-plane of the magnets. Thus to ensure that the applied field appears uniform to the sample. Magneto-photoconductivity experiments have certainly not been as widely applied as pure photoconductivity.[662, 663, 664]

One of the next primary upgrades is acquiring and implementing an electromagnet. This will grant access to investigating magnetic field dependence of the photoconductive response $\sigma_{pc}(H)$. Of course this is fundamentally limited by the heat produced in the resistive coil. Additionally, one could use the existing 14 T superconducting magnet by designing and building a probe.

7.6 Analysis

Photoconductivity is intimately connected to $\alpha(\omega)$ by the following relationship:

$$G = \eta(\frac{I_0}{E})(1-R)[1-exp(-\alpha(E)d)]/d. \tag{7.8}$$

Equation 7.8 shows how the generation rate of carriers G is related to the absorption coefficient $\alpha(E)$ and the quantum efficiency η which is the ratio of excited carriers created to the number of photons. This can be simplified to $\sigma_{PC} \sim\propto \eta \cdot \alpha(E) \cdot \tau$. Here, τ is the lifetime of the carriers being excited. [646] We can build a gedanken experiment that shows the displacement of the excitonic components (electrons and holes) and allows one to understand the increase in measured current. This thought

experiment goes as the following: Starting with the unperturbed system with the electrons in their equilibrium positions we excite the electron into the conduction band and thus create an exciton, of course with out the presence of an external field of 0 T the exciton recombines effectively instantaneously. Now we apply an external field and measure the conductivity. After some time we excite the electron, again creating the electron-hole pair, and the displacement before recombination is added to the measured conductivity, in the cases we have explored thus far, the sign of this value has always been positive but negatives signs have been reported.[665, 666, 667, 668, 669, 670] This displacement can be expressed as the

$$I_{total} = I_{off} + I_{ph}. \tag{7.9}$$

Where I_{total} represents the total current, I_{off} represents the current with the lights off, and I_{ph} represents the current with the circuit element (sample) having light shown on it. This leads us to expressing the difference between on and off

$$I_{ph} = I_{on} - I_{off}. \tag{7.10}$$

From this point we have a choice of either incorporating the power density into the analysis or taking a separate slice to see how the photocurrent increases with respect to increasing power density. To determine the conductance of the material at a given wavelength, we then divide by the voltage.

$$G = \frac{dI}{dV} \tag{7.11}$$

This should appear as approximately straight line, but will as expected have a discontinuity at 0 V, and anomalies at the gap voltage. This can be understood by relating the gap to a tunneling barrier, where the height is the E_g and its thickness is equivalent to $E_g/e|\vec{E}|$, where $|\vec{E}|$ is the magnitude of the electric field. Overall this looks like

$$t(\omega) = \frac{E_g - \hbar\omega}{e|\vec{E}|}.$$

The tensor described here starts out being completely diagonalized, assuming cubic symmetry as is the case for $NiFe_2O_4$ and $CoFe_2O_4$, and then after an induced magnetization by either lowering temperature or applying an external magnetic field results in the following (strictly for a cubic material)

$$\epsilon(\omega) = \begin{vmatrix} \epsilon_{xx} & \epsilon_{xy} & 0 \\ -\epsilon_{xy} & \epsilon_{yy} & 0 \\ 0 & 0 & \epsilon_{zz} \end{vmatrix}$$

.

From time-dependence data the opportunity to diagnose noise contribution arises. The first step in this is to establish the upper bound of the frequency regime, thereby filtering the data for high-frequency noise that is higher than scope of our measurement. This is based upon the Nyquist theorem, this will be 1/2 the frequency of data collection. With some extensive programmatic changes, an upper limit has been reached at 1000 Hz, while preserving a usable signal to noise ratio. Other accessible information include a combination of the generation rate (G) and the excited state

lifetime (τ).

$$\Delta\sigma = \sigma_{ph} = e(\mu_n \Delta n + \mu_p \Delta p) \tag{7.12}$$

$$\Delta n = G\tau_n \tag{7.13}$$

$$\sigma_{ph} = e\mu_n \Delta n \propto eG\tau_n\mu_n \tag{7.14}$$

$$G = \eta(I_0/h\nu)(1-R)[1-\exp(-\alpha d)]/d \tag{7.15}$$

The simplification from Eq. 7.12 to 7.14 arises because we can assume that one of the excitonic components will have a higher concentration and the free-carrier lifetimes will be adequately longer to validate exclusion of the other component (such as $\Delta n \gg \Delta p$.) As can be seen in the relationship of 7.14 and 7.15 by measuring the time it takes for the conductivity to saturate from the onset of the excitation source appears as an exponential function. As a result, it is possible to obtain the mobility within an order of magnitude. For example, we were able to measure the mobility of $NiFe_2O_4$ to be

7.7 Conclusion

To better clarify the deeper rational for implementing this methodology, we take a survey of the topics that were presented in this chapter. The Neumann theorem allows one to know that formally these measurements don't fall into the same category of thermodynamically reversible measurements as are the other methods included in

this dissertation.[193, 357] So, from this it is notable that the information gained will be unique amongst the techniques presented here within. In principle many environmental variables can be simulated including: high/low temperature, magnetic field, energy of photons, and high/low pressure.[671, 672] It was also mentioned that the physical process of probing has arisen in two styles, needle tip pressure contact and silver epoxy solid contact. By incorporating this flexibility of the measurement and the nature being of a functionally different format than the other methods currently in use in the lab, we see a result with incredible sensitivity to the materials band (electronic) structure, spin-dependence, and quasi-particle effective mass.[670, 673, 674, 87, 665, 667, 675, 676] Directly it is evident that the electronic excitations, e.g. charge transfer and band gap are going to be presented as major contributors to the changing conductivity. [87, 667]

Chapter 8

Summary

> [Of] three people walking together, at least one can be my teacher
>
> Confucius 517-478 B.C.E.

Strongly correlated electron materials have a multitude of emerging phenomena. These phenomenon can be tuned and manipulated via a large number of variables, e.g. epitaxial strain, size confinement, electric and magnetic field, temperature, and pressure (chemical and physical). We employed epitaxial strain, electric and magnetic field, temperature, and chemical pressure to investigate how electronic excitations such as the band gap respond in these varied environment. A second class of materials we investigated were multiferroics, typically these are strongly correlated materials. In $LuFe_2O_4$ we found that due to epitaxial strain the direct gap can be shifted to higher energy with a strain of just 0.6%. We also explored meta-stable structural phases stabilized via epitaxial strain, through this we established the magnetic phase

transition to be at 147 K.

Our lab had previously investigated the linear optical properties of $NiFe_2O_4$ at room temperature, establishing a hierarchy of gaps with the fundamental being an indirect minority channel gap at 1.6 eV.[314] The hierarchy continues with a 2.4 eV direct minority channel gap and a 2.8 eV direct majority channel gap. Ultimately, some concerns with the nature of the fundamental gap were presented.[557] We decided to continue the investigation with more advanced instrumentation and methodology. We measured magnetic circular dichroism, photoconductivity in and out of a magnetic field, and employed complimentary first principles calculations. The findings from this endeavor validate that the fundamental gap is indeed indirect, doublet structure around the fundamental gap energy. They also show that the excitations below ≈2.8 eV are spin polarized, due to the spin-split band structure and the two symmetries of the Fe^{3+} ions. What seems to be the most interesting finding occurs serendipitously, we show a metamagnetic transition that is responsible for variation from $M(B)$ experiments.[286] This metamagnetic transition is induced by the flipping of the Ni spin and modifies the electronic structure significantly. Overall, the effects discussed here are quite different from those that arise in dilute magnetic semiconductors and many of the chalcogenides. The unusual electronic properties of the former are attributable to impurity band interactions,[595, 590] whereas the latter are due to strong spin-orbit coupling and include spin-split bands, Rashba splitting, and topologically-protected surface states. [597, 598] The spin-polarized character of the excitations in $NiFe_2O_4$ instead emerges from the two independent magnetic sublattices - an aspect of the crystal, chemical, and electronic structure that will

be replicated (in some form) in other spinel ferrites. Another key point becomes apparent from this work is that the negative tunnel magnetoresistance observed in spin-filter devices with ultra-thin $NiFe_2O_4$ barriers[285] can be extended beyond the static limit and into the visible optics regime. Other spinel ferrites, already well known for their high Curie temperatures and robust moments, should be explored for enhanced effects, with additional advantages if the active energy window has a healthy overlap with the solar spectrum.

We measured the optical response of epitaxial $CoFe_2O_4$ thin films and compared our findings with complementary first principles calculations. This spinel oxide is an minority channel indirect band gap material. We extract a 1.2 eV indirect gap and a higher energy direct gap at 2.7 eV. The latter is robust on approach to the 795 K Curie temperature, a consequence of weak charge-spin coupling. A comparison with similar work on the Ni analog reveals that the band gaps are significantly lower in $CoFe_2O_4$, a trend that we attribute primarily to ionic size effects. This opens up the possibility of band gap tuning via chemical substitution and strain in the spinel ferrites, along with wider applications that many high T_C oxides enjoy.

We brought together optical absorption, magnetic circular dichroism, and photoconductivity to investigate the electronic structure of epitaxial thin films of h-$LuFeO_3$ and compared our findings with complementary first principles calculations. Surprisingly, we uncover a 1.1 eV direct gap emanating from hybridized Fe $3d_{z^2}$ + O $2p_z \rightarrow$ Fe d excitations in addition to the previously reported direct gap at 2.0 eV. The latter is sensitive to the magnetic ordering transition due to spin-charge coupling.[677] The overall absorption coefficient is lower than that in many other

complex oxides and emanates from the fact that the valence states are mostly in the spin-up channel whereas the conduction states are principally in the spin-down channel. The observation that the fundamental gap is lower than previously supposed can be advantageous for light harvesting. Moreover, even with a 147 K ordering temperature, multiferroicity in h-$LuFeO_3$ is achieved at relatively high temperature, a characteristic that may allow fabrication of low power, voltage-controlled magnetic devices operating at liquid nitrogen temperature.

The field of multiferroics is a treacherous terrain of high's and low's for material scientists. When a new material presents itself as a multiferroic the results might be inconclusive but because the field is so "hot" it is important to report the findings quickly. Such a result happened in the case of $LuFe_2O_4$; however, importance does not lie on the true or false nature of a claim, it lies in the details of the continued and inspired work. Previous work focused on bulk single crystal form factors, our work highlighted the significance of epitaxial single crystal thin films. We showed that the direct gap shifts in the higher energy direction by $\approx$0.4 eV (3.0–3.4 eV) in comparison to the bulk single crystal. The epitaxial strain resulted in a 0.6% (3.44–3.42Å) change in the in-plane lattice parameter. The fundamental indirect gap at (0.35 eV) in the single crystalline investigation shifted to a lower energy in the thin film form but the uncertainties of the measurements were significant enough to not allow for full assignment of the electronic excitation, due to limited optical density.

I suggest further work be done to thoroughly investigate underlying mechanistic causes for the optically enhanced magnetoresistance, a potentially interesting offshoot of this would be to investigate plasmons and how they can play a role in this

for nanostructures. The first step in this would be to develop several instrumental adaptation and upgrades to the existing photoconductivity setup, many are already listed in Table 7.1. One upgrade not listed is designing/building a probe for the superconducting magnet that the group has. Additionally, incorporating ultra-thin films and bulk samples into this investigation would give the opportunity to rule-in or -out size-dependency. This work spills over to continuing magnetic circular dichroism (MCD). This will help to establish understanding of the nature of MCD more broadly when applied to solid state materials, especially with regards to thin-film ferrites. This field has classically focused atomic and molecular systems but the more recent work has moved toward condensed matter science. I think it would be ever so valuable to investigate superlattices, low anisotropy nano-particulates, interface science, and multiphase interaction with this evolving tool. These are just a start of the possibilities of extended research that has been initiated by the endeavors I have undertaken. However, if someone is to take on any these challenges I believe that it will be required of them to develop a theory for explaining the deeper findings and to explain the physics of what is happening. If someone happens to read this and be inspired, I want them to know that they can find me and contact me if I am still alive. I believe part of my purpose on this Earth is to offer inspiration in times of drought and fear.

Bibliography

[1] M. Müller, M. Luysberg, and C. M. Schneider. Appl. Phys. Lett., **98**, 142503 (2011). 1

[2] G.-X. Miao, M. Müller, and J. S. Moodera. Phys. Rev. Lett., **102** (2009). 1

[3] R. E. Newnham, D. P. Skinner, and L. E. Cross. Mater. Res. Bull., **13**, 525 (1978). 2, 35, 172

[4] H. Y. Hwang, Y. Iwasa, M. Kawasaki, B. Keimer, N. Nagaosa, and Y. Tokura. Nat. Mater., **11**, 103 (2012). xv, 2, 3, 6, 22, 53, 62, 163, 178, 185, 204

[5] M. Hoppe, S. Döring, M. Gorgoi, S. Cramm, and M. Müller. Phys. Rev. B, **91** (2015). 2, 3

[6] M. Imada, A. Fujimori, and Y. Tokura. Rev. Mod. Phys., **70**, 1039 (1998). 2, 3

[7] J. Heber. Nature, **459**, 28 (2009). 2

[8] E. Dagotto. Science, **309**, 257 (2005). 3, 26

[9] P. Schlottmann. Physica B, **404**, 2699 (2009). 3

[10] E. Dagotto. *Nanoscale Phase Separation and Colossal Magnetoresistance*, vol. 136 of *Springer Series in Solid-State Sciences*. Springer Berlin Heidelberg, Berlin, Heidelberg (2003). 3

[11] A. Weiße and H. Fehske. The European Physical Journal B - Condensed Matter, **30**, 487 (2002). 3

[12] H. Takagi and H. Y. Hwang. Science, **327**, 1601 (2010). 3, 35, 203

[13] B. Cui, C. Song, F. Li, G. Y. Wang, H. J. Mao, J. J. Peng, F. Zeng, and F. Pan. Sci. Rep., **4**, 4206 (2015). 3

[14] N. C. Bristowe, J. Varignon, D. Fontaine, E. Bousquet, and P. Ghosez. Nat. Commun., **6**, 6677 (2015). 3, 42

[15] A. M. Oleś. J. Phys.: Condens. Matter, **24**, 313201 (2012). 3

[16] E. Morosan, D. Natelson, A. H. Nevidomskyy, and Q. Si. Adv. Mater., **24**, 4896 (2012). 3, 219

[17] Y. Suzuki. APL Mater., **3**, 062402 (2015). 3

[18] L. I. Vergara, J. Cao, N. Rogado, Y. Q. Wang, R. P. Chaudhury, R. J. Cava, B. Lorenz, and J. L. Musfeldt. Phys. Rev. B, **80** (2009). xv, 4

[19] J. P. Velev, S. S. Jaswal, and E. Y. Tsymbal. Philosophical Transactions of the Royal Society A: Mathematical, Physical and Engineering Sciences, **369**, 3069 (2011). xv, 6

[20] P. Zubko, S. Gariglio, M. Gabay, P. Ghosez, and J.-M. Triscone. Annu. Rev. Condens. Matter Phys., **2**, 141 (2011). 7, 22

[21] C. Krey, S. Legl, S. R. Dunsiger, M. Meven, J. S. Gardner, J. M. Roper, and C. Pfleiderer. Phys. Rev. Lett., **108** (2012). 7

[22] T. Goto, T. Kimura, G. Lawes, A. P. Ramirez, and Y. Tokura. Phys. Rev. Lett., **92** (2004). 7, 22, 38

[23] M. H. Phan, N. A. Frey, M. Angst, J. de Groot, B. C. Sales, D. G. Mandrus, and H. Srikanth. Solid State Commun., **150**, 341 (2010). 7

[24] M. L. Foo, Y. Wang, S. Watauchi, H. W. Zandbergen, T. He, R. J. Cava, and N. P. Ong. Phys. Rev. Lett., **92** (2004). 7

[25] X. S. Xu, T. V. Brinzari, S. McGill, H. D. Zhou, C. R. Wiebe, and J. L. Musfeldt. Phys. Rev. Lett., **103** (2009). 8

[26] P. Chen, N. Lee, S. McGill, S.-W. Cheong, and J. L. Musfeldt. Phys. Rev. B, **85** (2012). 8

[27] P. Naumov, S. C. Lee, N. Ishizawa, Y. G. Jeong, I. H. Chung, and S. Fukuzumi. J. Phys. Chem. A, **113**, 11354 (2009). 8

[28] A. G. Gavriliuk, I. S. Lyubutin, and V. V. Struzhkin. JETP Lett., **86**, 532 (2007). 8

[29] A. E. Smith, H. Mizoguchi, K. Delaney, N. A. Spaldin, A. W. Sleight, and M. A. Subramanian. J. Am. Chem. Soc., **131**, 17084 (2009). 8

[30] J. Li, Z. Shan, and E. Ma. MRS Bull., **39**, 108 (2014). 8

[31] V. Kempe. *Inertial MEMS: Principles and Practice*. Cambridge University Press, Cambridge (2011). 8

[32] W. S. Choi, J.-H. Kwon, H. Jeen, J. E. Hamann-Borrero, A. Radi, S. Macke, R. Sutarto, F. He, G. A. Sawatzky, V. Hinkov, M. Kim, and H. N. Lee. Nano Lett., **12**, 4966 (2012). 8, 9

[33] J. A. Mundy, C. M. Brooks, M. E. Holtz, J. A. Moyer, H. Das, A. F. Rébola, J. T. Heron, J. D. Clarkson, S. M. Disseler, Z. Liu, A. Farhan, R. Held, R. Hovden, E. Padgett, Q. Mao, H. Paik, R. Misra, L. F. Kourkoutis, E. Arenholz, A. Scholl, J. A. Borchers, W. D. Ratcliff, R. Ramesh, C. J. Fennie, P. Schiffer, D. A. Muller, and D. G. Schlom. Nature, **537**, 523 (2016). 8

[34] Y. Zhou and K. M. Rabe. Phys. Rev. B, **88**, 094416 (2013). 8

[35] D. G. Schlom, L.-Q. Chen, C.-B. Eom, K. M. Rabe, S. K. Streiffer, and J.-M. Triscone. Annu. Rev. Mater. Res., **37**, 589 (2007). 9

[36] D. G. Schlom, L.-Q. Chen, C. J. Fennie, V. Gopalan, D. A. Muller, X. Pan, R. Ramesh, and R. Uecker. MRS Bull., **39**, 118 (2014). 9

[37] D. Zhang, S. Zhuo, H. Zhang, P. Wang, and J. Jiang. Dalton Trans., **44**, 4655 (2015). 9

[38] J. Chakhalian, J. M. Rondinelli, J. Liu, B. A. Gray, M. Kareev, E. J. Moon, N. Prasai, J. L. Cohn, M. Varela, I. C. Tung, M. J. Bedzyk, S. G. Altendorf,

F. Strigari, B. Dabrowski, L. H. Tjeng, P. J. Ryan, and J. W. Freeland. Phys. Rev. Lett., **107** (2011). 9

[39] J. A. Moyer, R. Gao, P. Schiffer, and L. W. Martin. Sci. Rep., **5**, 10363 (2015). 9, 171

[40] H. Zheng. Science, **303**, 661 (2004). 9, 42, 171

[41] F. Zavaliche, H. Zheng, L. Mohaddes-Ardabili, S. Y. Yang, Q. Zhan, P. Shafer, E. Reilly, R. Chopdekar, Y. Jia, P. Wright, D. G. Schlom, Y. Suzuki, and R. Ramesh. Nano Lett., **5**, 1793 (2005). 9

[42] W. Eerenstein, N. D. Mathur, and J. F. Scott. Nature, **442**, 759 (2006). 9, 38, 171

[43] D. L. Li, Q. L. Ma, S. G. Wang, R. C. C. Ward, T. Hesjedal, X.-G. Zhang, A. Kohn, E. Amsellem, G. Yang, J. L. Liu, J. Jiang, H. X. Wei, and X. F. Han. Sci. Rep., **4**, 7277 (2014). 9

[44] W. H. Butler, X.-G. Zhang, T. C. Schulthess, and J. M. MacLaren. Phys. Rev. B, **63** (2001). 9

[45] S. J. Pearton, C. R. Abernathy, M. E. Overberg, G. T. Thaler, D. P. Norton, N. Theodoropoulou, A. F. Hebard, Y. D. Park, F. Ren, J. Kim, and L. A. Boatner. J. Appl. Phys., **93**, 1 (2003). 9

[46] Ü. Özgür, Y. I. Alivov, C. Liu, A. Teke, M. A. Reshchikov, S. Doğan, V. Avrutin, S.-J. Cho, and H. Morkoç. J. Appl. Phys., **98**, 041301 (2005). 9

[47] N. F. Mott. Proceedings of the Royal Society A: Mathematical, Physical and Engineering Sciences, **153**, 699 (1936). 9, 54, 108

[48] N. F. Mott. Proc. Phys. Soc. London, Sect. A, **62**, 416 (1949). 9, 28, 108

[49] N. Mott. Adv. Phys., **13**, 325 (1964). 9

[50] W. S. Choi and H. N. Lee. Phys. Rev. B, **91** (2015). 9

[51] K. Uchida, N. Miura, J. Kitamura, and H. Kukimoto. Phys. Rev. B, **53**, 4809 (1996). 9

[52] S. H. Jhang, M. Margańska, Y. Skourski, D. Preusche, M. Grifoni, J. Wosnitza, and C. Strunk. Phys. Rev. Lett., **106** (2011). 9

[53] B. S. Holinsworth, D. Mazumdar, C. M. Brooks, J. A. Mundy, H. Das, J. G. Cherian, S. A. McGill, C. J. Fennie, D. G. Schlom, and J. L. Musfeldt. Appl. Phys. Lett., **106**, 082902 (2015). 9, 41, 172

[54] L. Sponza, J. Goniakowski, and C. Noguera. Phys. Rev. B, **93** (2016). 9

[55] M. Arrigoni, E. A. Kotomin, and J. Maier. Isr. J. Chem. (2016). 9

[56] G. Zhang, M. B. Yu, C. H. Tung, and G. Q. Lo. Electron Device Letters, **29**, 1302 (2008). 9

[57] X. Liu, S. Middey, Y. Cao, M. Kareev, and J. Chakhalian. MRS Commun., **6**, 133 (2016). 9

[58] C. Noguera and J. Goniakowski. J. Phys.: Condens. Matter, **20**, 264003 (2008). 9

[59] Y. Suzuki. Annu. Rev. Mater. Res., **31**, 265 (2001). 10, 57

[60] J. A. Moyer, C. A. F. Vaz, E. Negusse, D. A. Arena, and V. E. Henrich. Phys. Rev. B, **83**, 035121 (2011). xvii, 10, 222

[61] D. Venkateshvaran, M. Althammer, A. Nielsen, S. Geprägs, M. S. Ramachandra Rao, S. T. B. Goennenwein, M. Opel, and R. Gross. Phys. Rev. B, **79** (2009). 10

[62] J. Takaobushi, H. Tanaka, T. Kawai, S. Ueda, J.-J. Kim, M. Kobata, E. Ikenaga, M. Yabashi, K. Kobayashi, Y. Nishino, D. Miwa, K. Tamasaku, and T. Ishikawa. Appl. Phys. Lett., **89**, 242507 (2006). 10

[63] G. Kotliar and D. Vollhardt. Phys. Today, **57**, 53 (2004). 11, 26

[64] H. Wu, H. Gan, H. Zheng, J. Lu, H. Zhu, Y. Ji, G. Li, and J. Zhao. Solid State Commun., **151**, 456 (2011). 11, 126, 175, 373

[65] N. Kobayashi and K. Nakai. Chem. Commun., 4077 (2007). 11

[66] In N. Kobayashi and A. Muranaka (editors), *Circular Dichroism and Magnetic Circular Dichroism Spectroscopy for Organic Chemists*, 1–41. Royal Society of Chemistry, Cambridge (2011). 11

[67] C. D. Stanciu, F. Hansteen, A. V. Kimel, A. Kirilyuk, A. Tsukamoto, A. Itoh, and T. Rasing. Phys. Rev. Lett., **99**, 047601 (2007). 11

[68] A. R. Khorsand, M. Savoini, A. Kirilyuk, A. V. Kimel, A. Tsukamoto, A. Itoh, and T. Rasing. Phys. Rev. Lett., **108** (2012). 11

[69] S. Sugano, N. Kojima, M. Cardona, P. Fulde, K. von Klitzing, H.-J. Queisser, R. Merlin, and H. Störmer (editors). *Magneto-Optics*, vol. 128 of *Springer Series in Solid-State Sciences*. Springer Berlin Heidelberg, Berlin, Heidelberg (2000). xix, 11, 165, 169, 174, 216, 380, 382

[70] N. Rawat, Z. Pan, C. J. Lamarche, A. Wetherby, R. Waterman, T. Tokumoto, J. G. Cherian, R. L. Headrick, S. A. McGill, and M. I. Furis. Sci. Rep., **5**, 16536 (2015). 11, 130, 175, 371

[71] W. R. Mason. *A practical guide to magnetic circular dichroism spectroscopy*. Wiley-Interscience, Hoboken, N.J (2007). 11, 90, 138, 141, 234, 370, 372

[72] J. Mack, M. J. Stillman, and N. Kobayashi. Coord. Chem. Rev., **251**, 429 (2007). 11, 141, 213

[73] C. Jin, Q. Zhang, W. B. Mi, E. Y. Jiang, and H. L. Bai. J. Phys. D: Appl. Phys., **43**, 385001 (2010). xvii, 14, 53, 188, 189, 219

[74] M. Bibes and A. Barthelemy. **54**, 1003 (2007). 15

[75] R. M. Bozorth, E. F. Tilden, and A. J. Williams. Phys. Rev., **99**, 1788 (1955). 15

[76] Y. Suzuki, G. Hu, R. van Dover, and R. Cava. J. Magn. Magn. Mater., **191**, 1 (1999). 15

[77] T. Dhakal, D. Mukherjee, R. Hyde, P. Mukherjee, M. H. Phan, H. Srikanth, and S. Witanachchi. J. Appl. Phys., **107**, 053914 (2010). 15

[78] W. Wang. *Electronic structure and magnetism of transition metal oxides : the case of Fe3O4*. Theses, Université de Cergy Pontoise (2012). 15

[79] U. Chowdhury, S. Goswami, D. Bhattacharya, J. Ghosh, S. Basu, and S. Neogi. Appl. Phys. Lett., **105**, 052911 (2014). 16

[80] Z. Wang, X. Zhong, R. Yu, Z. Cheng, and J. Zhu. Nat. Commun., **4**, 1395 (2013). 16, 57, 172, 230, 235, 236

[81] M. A. Subramanian, T. He, J. Chen, N. S. Rogado, T. G. Calvarese, and A. W. Sleight. Adv. Mater., **18**, 1737 (2006). 17

[82] X. S. Xu, M. Angst, T. V. Brinzari, R. P. Hermann, J. L. Musfeldt, A. D. Christianson, D. Mandrus, B. C. Sales, S. McGill, J.-W. Kim, and Z. Islam. Phys. Rev. Lett., **101** (2008). xviii, 17, 61, 172, 230, 236, 237, 238

[83] S. Matityahu, A. Aharony, O. Entin-Wohlman, and S. Katsumoto. Phys. Rev. B, **87** (2013). 18

[84] Sangjun Lee and Sangin Kim. IEEE Photonics Journal, **5**, 4800610 (2013). 18

[85] C. S. Helrich. *The Classical Theory of Fields*. Graduate Texts in Physics. Springer Berlin Heidelberg, Berlin, Heidelberg (2012). DOI: 10.1007/978-3-642-23205-3. 18, 80, 107

[86] M. I. Dyakonov (editor). *Spin physics in semiconductors*. No. 157 in Springer series in solid-state sciences. Springer, Berlin (2008). xviii, 18, 30, 357, 358, 359

[87] N. V. Joshi. *Photoconductivity: Art: Science & Technology*. CRC Press/Taylor & Francis, Boca Raton (1990). 19, 261

[88] W. H. Butler. Sci. Technol. Adv. Mater., **9**, 014106 (2008). 19

[89] H.-U. Habermeier. Mater. Today, **10**, 34 (2007). 22

[90] Y. Tokura and H. Y. Hwang. Nat. Mater., **7**, 694 (2008). 22

[91] S. Sachdev. Rev. Mod. Phys., **75**, 913 (2003). 22

[92] N. P. Armitage, P. Fournier, and R. L. Greene. Rev. Mod. Phys., **82**, 2421 (2010). 22

[93] M. B. Salamon and M. Jaime. Rev. Mod. Phys., **73**, 583 (2001). 22

[94] M. L. Medarde. J. Phys.: Condens. Matter, **9**, 1679 (1997). 22

[95] G. Catalan. Phase Transitions, **81**, 729 (2008). 22

[96] D. Meyers, J. Liu, J. W. Freeland, S. Middey, M. Kareev, J. Kwon, J. M. Zuo, Y.-D. Chuang, J. W. Kim, P. J. Ryan, and J. Chakhalian. Sci. Rep., **6**, 27934 (2016). 22

[97] R. Batterman (editor). *The Oxford Handbook of Philosophy of Physics*. Oxford University Press, 1 ed. (2013). DOI: 10.1093/oxfordhb/9780195392043.001.0001. 22

[98] J. Wang. Science, **299**, 1719 (2003). 22, 40, 43, 172

[99] S.-W. Cheong and M. Mostovoy. Nat. Mater., **6**, 13 (2007). 22, 35, 38, 172

[100] M. Angst, R. P. Hermann, A. D. Christianson, M. D. Lumsden, C. Lee, M.-H. Whangbo, J.-W. Kim, P. J. Ryan, S. E. Nagler, W. Tian, R. Jin, B. C. Sales, and D. Mandrus. Phys. Rev. Lett., **101** (2008). 22, 38

[101] G. Lawes, M. Kenzelmann, N. Rogado, K. H. Kim, G. A. Jorge, R. J. Cava, A. Aharony, O. Entin-Wohlman, A. B. Harris, T. Yildirim, Q. Z. Huang, S. Park, C. Broholm, and A. P. Ramirez. Phys. Rev. Lett., **93** (2004). 22, 38

[102] C.-G. Stefanita. *Magnetism*. Springer Berlin Heidelberg, Berlin, Heidelberg (2012). xv, 63

[103] J. Chakhalian, A. J. Millis, and J. Rondinelli. Nat. Mater., **11**, 92 (2012). 26

[104] J. Quintanilla and C. Hooley. Phys. World, **22**, 32 (2009). 26

[105] Y. Tokura. Phys. Today, **56**, 50 (2003). 26, 29

[106] A. Frano. *Spin Spirals and Charge Textures in Transition-Metal-Oxide Heterostructures*. Springer Theses. Springer International Publishing, Cham (2014). 26

[107] T.-h. Arima. Nat. Mater., **7**, 12 (2008). 26

[108] Y. Zhou and S. Ramanathan. Crit. Rev. Solid State Mater. Sci., **38**, 286 (2013). 26

[109] M. Lorenz, M. S. Ramachandra Rao, T. Venkatesan, E. Fortunato, P. Barquinha, R. Branquinho, D. Salgueiro, R. Martins, E. Carlos, A. Liu, F. K. Shan, M. Grundmann, H. Boschker, J. Mukherjee, M. Priyadarshini, N. DasGupta, D. J. Rogers, F. H. Teherani, E. V. Sandana, P. Bove, K. Rietwyk, A. Zaban, A. Veziridis, A. Weidenkaff, M. Muralidhar, M. Murakami, S. Abel, J. Fompeyrine, J. Zuniga-Perez, R. Ramesh, N. A. Spaldin, S. Ostanin, V. Borisov, I. Mertig, V. Lazenka, G. Srinivasan, W. Prellier, M. Uchida, M. Kawasaki, R. Pentcheva, P. Gegenwart, F. Miletto Granozio, J. Fontcuberta, and N. Pryds. J. Phys. D: Appl. Phys., **49**, 433001 (2016). 26

[110] E. Dagotto and Y. Tokura. MRS Bull., **33**, 1037 (2008). 26

[111] Y. Tokura and N. Nagaosa. Science, **288**, 462 (2000). 26

[112] E. Y. Tsymbal, E. R. A. Dagotto, C.-B. Eom, and R. Ramesh (editors). *Multifunctional Oxide Heterostructures*. Oxford University Press (2012). 26

[113] V. I. Anisimov, J. Zaanen, and O. K. Andersen. Phys. Rev. B, **44**, 943 (1991). 26, 27

[114] V. I. Anisimov, I. S. Elfimov, N. Hamada, and K. Terakura. Phys. Rev. B, **54**, 4387 (1996). 26, 27

[115] V. N. Antonov, B. N. Harmon, and A. N. Yaresko. Phys. Rev. B, **67** (2003). 26, 171

[116] B. S. Holinsworth, D. Mazumdar, H. Sims, Q.-C. Sun, M. K. Yurtisigi, S. K. Sarker, A. Gupta, W. H. Butler, and J. L. Musfeldt. Appl. Phys. Lett., **103**,

082406 (2013). xv, xvii, 26, 53, 72, 203, 204, 205, 206, 209, 218, 222, 223, 230, 236, 330

[117] C. Cheng. J. Magn. Magn. Mater., **325**, 144 (2013). 27

[118] A. Rohrbach, J. Hafner, and G. Kresse. Phys. Rev. B, **69** (2004). 27

[119] N. F. Mott. *Metal-Insulator Transition*. Taylor & Francis, Bristol ; Philadelphia, 2 ed. (1990). 27

[120] H. Fritzsche and D. Adler (editors). *Localization and Metal-Insulator Transitions*. Springer US, Boston, MA (1985). 27

[121] F. Gebhard. *The Mott Metal-Insulator Transition*, vol. 137 of *Springer Tracts in Modern Physics*. Springer Berlin Heidelberg, Berlin, Heidelberg (2000). 27

[122] A. C. Hewson and V. Zlatić (editors). *Concepts in Electron Correlation*. Springer Netherlands, Dordrecht (2003). 27

[123] A. I. Liechtenstein, V. I. Anisimov, and J. Zaanen. Phys. Rev. B, **52**, R5467 (1995). 27

[124] Y. M. Ksendzov. Phys. Status Solidi B, **93**, 415 (1979). 27

[125] J. Hubbard. Proceedings of the Royal Society A: Mathematical, Physical and Engineering Sciences, **276**, 238 (1963). 28

[126] R. Rauer. *Optical spectroscopy of strongly correlated transition-metal oxides*. Cuvillier, Göttingen, 1. aufl ed. (2005). OCLC: 181546020. 29, 121, 129

[127] S. A. Wolf, D. D. Awschalom, R. A. Buhrman, J. M. Daughton, S. Von Molnar, M. L. Roukes, A. Y. Chtchelkanova, and D. M. Treger. Science, **294**, 1488 (2001). 29, 54, 178, 348

[128] F. Pulizzi. Nat. Mater., **11**, 367 (2012). 29

[129] S. D. Sarma. Amer. Sci., **89**, 516 (2001). xviii, 30, 344, 345, 346, 348, 359

[130] I. Žutić, J. Fabian, and S. D. Sarma. Rev. Mod. Phys., **76**, 323 (2004). 30, 32, 33, 184, 345

[131] S. A. Tarasenko. Phys. Usp., **53**, 739 (2010). 30, 105, 360

[132] Y. G. Kusrayev. Semicond. Sci. Technol., **23**, 114013 (2008). 30

[133] Y. G. Kusrayev. Phys. Usp., **53**, 725 (2010). 30

[134] M. Ziese and M. J. Thornton (editors). *Spin Electronics*, vol. 569 of *Lecture Notes in Physics*. Springer Berlin Heidelberg, Berlin, Heidelberg (2001). 30, 348, 391

[135] D. D. Awschalom, R. A. Buhrman, J. M. Daughton, S. von Molnár, and M. L. Roukes (editors). *Spin Electronics*. Springer Netherlands, Dordrecht (2004). 30

[136] C. Chen, Z. Tao, C. Hernandez-Garcia, P. Matyba, A. Carr, R. Knut, O. Kfir, D. Zusin, C. Gentry, P. Grychtol, O. Cohen, L. Plaja, A. Becker, A. Jaron-Becker, H. Kapteyn, and M. Murnane. Sci. Adv., **2**, e1501333 (2016). 30

[137] R. Völkl. *Spin dynamics and spatially resolved spin transport phenomena in GaAs based structures*. phd (2014). 30

[138] J. Fabian, A. Matos-Abiague, C. Ertler, P. Stano, and I. Zutic. Acta Phys. Slov., **57**, 566 (2007). xv, 30, 31, 32, 33, 66

[139] M. Cygorek, P. I. Tamborenea, and V. M. Axt. Phys. Rev. B, **92** (2015). 30

[140] M. A. Noyan and J. M. Kikkawa. Appl. Phys. Lett., **107**, 032406 (2015). 30

[141] E. L. Ivchenko, L. E. Golub, A. A. Levchenko, S. A. Babin, V. G. Kurt, and V. N. Lukash. Phys. Usp., **55**, 808 (2012). 30

[142] V. A. Ivanov, T. G. Aminov, V. M. Novotortsev, and V. T. Kalinnikov. Russ. Chem. Bull., **53**, 2357 (2004). 30

[143] I. Appelbaum, B. Huang, and D. J. Monsma. Nature, **447**, 295 (2007). 30

[144] G. Schmidt, D. Ferrand, L. W. Molenkamp, A. T. Filip, and B. J. van Wees. Phys. Rev. B, **62**, R4790 (2000). 30

[145] E. J. L. McInnes, E. Pidcock, V. S. Oganesyan, M. R. Cheesman, A. K. Powell, and A. J. Thomson. J. Am. Chem. Soc., **124**, 9219 (2002). 31

[146] T. Manago. In *MEMS, NANO and Smart Systems, 2003. Proceedings. International Conference on*, 142–147. IEEE (2003). 31, 360

[147] In R. Fornari, H. Kamimura, and P. Bhattacharya (editors), *Comprehensive Semiconductor Science and Technology*, vol. 6, 615–647. Elsevier, Amsterdam (2011). 31

[148] M. Johnson and R. H. Silsbee. Phys. Rev. Lett., **55**, 1790 (1985). 32

[149] M. Johnson and R. H. Silsbee. Phys. Rev. B, **37**, 5312 (1988). 32

[150] M. Johnson and R. H. Silsbee. Phys. Rev. B, **35**, 4959 (1987). 32, 359

[151] R. H. Silsbee. Bull. Magn. Reson., **2**, 284 (1980). 32

[152] M. Trassin. J. Phys.: Condens. Matter, **28**, 033001 (2016). 33

[153] V. K. Joshi. Engineering Science and Technology, an International Journal, **19**, 1503 (2016). 33, 359

[154] M. Sharad and K. Roy. J. Appl. Phys., **115**, 17C737 (2014). 33

[155] A. Hirohata, H. Sukegawa, H. Yanagihara, I. Žutić, T. Seki, S. Mizukami, and R. Swaminathan. Transactions on Magnetics, **51**, 1 (2015). 33

[156] V. Kantser. Moldavian Journal of the Physical Sciences, **4**, 5 (2005). 33

[157] M. O. Luen. *Spintronics: Towards Room Temperature Ferromagnetic Devices via Mn and Rare Earth Doped GaN.* Ph.D. thesis, North Carolina State University (2010). 33

[158] M. N. Hoda and Bharati Vidyapeeth's Institute of Computers Applications and Management (editors). *Proceedings of the 5th National Conference on Computing for Nation Development (10th - 11th March, 2011) INDIACom-2011: [held in New Delhi].* Bharati Vidyapeeth's Institute of Computer Applications and Management (BVICAM), New Delhi (2011). OCLC: 931721883. 33

[159] I. Žutić and A. Petukhov. Nat. Nanotechnol., **4**, 623 (2009). 33

[160] C. Felser and G. H. Fecher (editors). *Spintronics*. Springer Netherlands, Dordrecht (2013). 33

[161] C. Felser, G. H. Fecher, and B. Balke. Angew. Chem. Int. Ed., **46**, 668 (2007). 33

[162] E. R. Hedin and Joe (editors). *Spintronics in Nanoscale Devices*. Pan Stanford Publishing (2013). 33

[163] Q.-f. Sun and X. C. Xie. Phys. Rev. B, **75**, 155306 (2007). 33

[164] J. Valasek. Phys. Rev., **17**, 475 (1921). 34

[165] V. Wadhawan. *Introduction to Ferroic Materials*. Gordon and Breach Science Publishers (2000). 34, 36, 364

[166] V. K. Wadhawan. Resonance, **7**, 15 (2002). 34, 364

[167] P. Curie. Journal de Physique Théorique et Appliquée, **3**, 393 (1894). 34

[168] A. F. Chalmers. Brit. J. Phil. Sci., **21**, 133 (1970). 34

[169] B. W. Roberts. Philosophy of Science, **80**, 579 (2013). 34

[170] J. Rosen. *Symmetry Rules*. The Frontiers Collection. Springer Berlin Heidelberg, Berlin, Heidelberg (2008). 34

[171] J. Earman. International Studies in the Philosophy of Science, **18**, 173 (2004). 34

[172] K. Brading and E. Castellani (editors). *Symmetries in Physics: Philosophical Reflections*. Cambridge University Press, Cambridge (2003). 34

[173] J. Ismael. Synthese, **110**, 167 (1997). 34

[174] G. A. Smolenskii and V. A. Bokov. J. Appl. Phys., **35**, 915 (1964). 34

[175] E. Ascher. J. Appl. Phys., **37**, 1404 (1966). 35

[176] H. Schmid. Ferroelectrics, **427**, 1 (2012). 35

[177] H. Schmid. Ferroelectrics, **162**, 317 (1994). 35, 43, 171

[178] R. Ramesh and N. A. Spaldin. Nat. Mater., **6**, 21 (2007). 35

[179] M. Fiebig, T. Lottermoser, D. Meier, and M. Trassin. Nature Reviews Materials, **1**, 16046 (2016). xv, 35, 36, 40, 41, 42, 67

[180] M. Bibes. Nat. Mater., **11**, 354 (2012). 35

[181] N. A. Hill. The Journal of Physical Chemistry B, **104**, 6694 (2000). 35, 38, 42, 171

[182] H. Schmid. J. Phys.: Condens. Matter, **20**, 434201 (2008). 35

[183] K. Aizu. J. Phys. Soc. Jpn., **27**, 387 (1969). 35, 36

[184] K. Aizu. Phys. Rev. B, **2**, 754 (1970). 36

[185] D. B. Litvin. Acta Crystallographica Section A: Foundations of Crystallography, **64**, 316 (2008). 36

[186] Ferroelasticity : Materials that possess stable spontaneous deformation. This deformation can be hysterectically switched by an applied stress. 36

[187] E. K. Salje. Annu. Rev. Mater. Res., **42**, 265 (2012). 36

[188] Ferroelectricity : Materials that possess stable spontaneous polarization. This polarization can be hysterectically switched by electric field vector. 36

[189] Ferromagnetic : Materials that possess stable spontaneous magnetization. This magnetization can be hysterectically switched by magnetic field vector. 36

[190] Ferrotorodicity : Materials that possess a stable and spontaneous curl of magnetization or polarization. Hysterectically switched via (H x E) vector. 36

[191] T. Castán, A. Planes, and A. Saxena. Phys. Rev. B, **85**, 144429 (2012). 36

[192] J. Nye. *Physical Properties of Crystals : Their Representation by Tensors and Matrices*. Oxford University Press (1985). 37

[193] R. R. Birss. Rep. Prog. Phys., **26**, 307 (1963). 37, 261

[194] L. Landau and E. M. Lifshitz. *Electrodynamics of Continuous Media*. Pergamon, Oxford ; New York, 1 ed. (1960). 37, 42, 90, 122, 123

[195] M. Fiebig, T. Lottermoser, D. Fröhlich, A. V. Goltsev, and R. V. Pisarev. Nature, **419**, 818 (2002). 38

[196] T. Kimura, T. Goto, H. Shintani, K. Ishizaka, T. Arima, and Y. Tokura. Nature, **426**, 55 (2003). 38, 171

[197] N. Hur, S. Park, P. A. Sharma, J. S. Ahn, S. Guha, and S.-W. Cheong. Nature, **429**, 392 (2004). 38

[198] A. Malashevich, S. Coh, I. Souza, and D. Vanderbilt. Phys. Rev. B, **86** (2012). 39

[199] A. Saxena and A. Planes (editors). *Mesoscopic Phenomena in Multifunctional Materials*, vol. 198 of *Springer Series in Materials Science*. Springer Berlin Heidelberg, Berlin, Heidelberg (2014). 39

[200] A. Saxena. Integr. Ferroelectr., **131**, 3 (2011). 39

[201] A. S. Nowick. *Crystal Properties via Group Theory*. Cambridge University Press, Cambridge (1995). 39, 364

[202] M. Fiebig. J. Phys. D: Appl. Phys., **38**, R123 (2005). 39, 43

[203] J.-P. Rivera. Ferroelectrics, **161**, 147 (1994). 39

[204] B. B. Krichevtsov, V. V. Pavlov, and R. V. Pisarev. Soviet Journal of Experimental and Theoretical Physics Letters, **49**, 535 (1989). 39

[205] G. T. Rado, J. M. Ferrari, and W. G. Maisch. Phys. Rev. B, **29**, 4041 (1984). 39

[206] I. Dzyaloshinskii. Soviet Journal of Experimental and Theoretical Physics Letters, **10**, 328 (1959). 39

[207] D. N. Astrov. Soviet Journal of Experimental and Theoretical Physics Letters, **11**, 708 (1960). 39

[208] A. Sekine and K. Nomura. J. Phys. Conf. Ser., **592**, 012128 (2015). 39

[209] M. Naka and S. Ishihara. Sci. Rep., **6**, 20781 (2016). 39

[210] J.-Q. Dai, H. Zhang, and Y.-M. Song. J. Magn. Magn. Mater., **324**, 3937 (2012). 39

[211] J.-Q. Dai, Y.-M. Song, and H. Zhang. J. Appl. Phys., **111**, 114301 (2012). 39

[212] D. Khomskii. Physics, **2** (2009). 40, 171, 172

[213] J. Lee, S. A. Trugman, C. L. Zhang, D. Talbayev, X. S. Xu, S.-W. Cheong, D. A. Yarotski, A. J. Taylor, and R. P. Prasankumar. Appl. Phys. Lett., **107**, 042906 (2015). 40

[214] E. Bousquet and A. Cano. J. Phys.: Condens. Matter, **28**, 123001 (2016). 40

[215] P. Barone and S. Picozzi. C. R. Phys., **16**, 143 (2015). 40

[216] J. B. Neaton, C. Ederer, U. V. Waghmare, N. A. Spaldin, and K. M. Rabe. Phys. Rev. B, **71** (2005). 40

[217] G. Catalan and J. F. Scott. Adv. Mater., **21**, 2463 (2009). 40

[218] M. Lilienblum, T. Lottermoser, S. Manz, S. M. Selbach, A. Cano, and M. Fiebig. Nat. Phys., **11**, 1070 (2015). 41

[219] C. J. Fennie and K. M. Rabe. Phys. Rev. B, **72** (2005). 41

[220] B. B. Van Aken, T. T. Palstra, A. Filippetti, and N. A. Spaldin. Nat. Mater., **3**, 164 (2004). 41

[221] M. Fiebig, D. Fröhlich, K. Kohn, S. Leute, T. Lottermoser, V. V. Pavlov, and R. V. Pisarev. Phys. Rev. Lett., **84**, 5620 (2000). 41

[222] S. M. Disseler, J. A. Borchers, C. M. Brooks, J. A. Mundy, J. A. Moyer, D. A. Hillsberry, E. L. Thies, D. A. Tenne, J. Heron, M. E. Holtz, J. D. Clarkson, G. M. Stiehl, P. Schiffer, D. A. Muller, D. G. Schlom, and W. D. Ratcliff. Phys. Rev. Lett., **114** (2015). 41, 42, 174, 236

[223] W. Wang, J. Zhao, W. Wang, Z. Gai, N. Balke, M. Chi, H. N. Lee, W. Tian, L. Zhu, X. Cheng, D. J. Keavney, J. Yi, T. Z. Ward, P. C. Snijders, H. M. Christen, W. Wu, J. Shen, and X. Xu. Phys. Rev. Lett., **110**, 237601 (2013). xvi, 41, 43, 59, 76

[224] N. Ikeda, H. Ohsumi, K. Ohwada, K. Ishii, T. Inami, K. Kakurai, Y. Murakami, K. Yoshii, S. Mori, Y. Horibe, and H. Kitô. Nature, **436**, 1136 (2005). 41, 60, 61, 171

[225] E. Bousquet, M. Dawber, N. Stucki, C. Lichtensteiger, P. Hermet, S. Gariglio, J.-M. Triscone, and P. Ghosez. Nature, **452**, 732 (2008). 41

[226] J. M. Rondinelli and C. J. Fennie. Adv. Mater., **24**, 1961 (2012). 41

[227] H. Katsura, N. Nagaosa, and A. V. Balatsky. Phys. Rev. Lett., **95** (2005). 42

[228] M. Mostovoy. Phys. Rev. Lett., **96** (2006). 42

[229] I. A. Sergienko and E. Dagotto. Phys. Rev. B, **73** (2006). 42

[230] T.-h. Arima. J. Phys. Soc. Jpn., **76**, 073702 (2007). 42

[231] T. Walther, N. Quandt, R. Köferstein, R. Roth, M. Steimecke, and S. G. Ebbinghaus. J. Eur. Ceram. Soc., **36**, 559 (2016). 42

[232] B. Fu, R. Lu, K. Gao, Y. Yang, and Y. Wang. EPL (Europhysics Letters), **111**, 17007 (2015). 42

[233] V. V. Shvartsman, F. Alawneh, P. Borisov, D. Kozodaev, and D. C. Lupascu. Smart Mater. Struct., **20**, 075006 (2011). 42

[234] N. A. Spaldin, S.-W. Cheong, and R. Ramesh. Phys. Today, **63**, 38 (2010). 42

[235] A. A. Belik, S. Iikubo, K. Kodama, N. Igawa, S.-i. Shamoto, S. Niitaka, M. Azuma, Y. Shimakawa, M. Takano, F. Izumi, and E. Takayama-Muromachi. Chem. Mater., **18**, 798 (2006). 43

[236] Li. Condens. Matter Phys., **15**, 13701 (2012). 43

[237] L. and founder of Everyday Interview Tips. 3 Types of Problem Solvers: Which One Are You? | Everyday Interview Tips. 43

[238] L. W. Martin, S. P. Crane, Y.-H. Chu, M. B. Holcomb, M. Gajek, M. Huijben, C.-H. Yang, N. Balke, and R. Ramesh. J. Phys.: Condens. Matter, **20**, 434220 (2008). 43

[239] L. Martin and R. Ramesh. Acta Mater., **60**, 2449 (2012). 43

[240] M. Bibes, J. E. Villegas, and A. Barthélémy. Adv. Phys., **60**, 5 (2011). 44

[241] L. D. Landau and E. Lifshitz. On the theory of the dispersion of magnetic permeability in ferromagnetic bodies (1935). 45

[242] C. Kittel. Phys. Rev., **73**, 155 (1948). 45

[243] G. G. Robbrecht and J. L. Verhaeghe. Nature, **182**, 1080 (1958). 45

[244] E. Spencer, L. Ault, and R. LeCraw. Proc. IRE, **44**, 1311 (1956). 45

[245] M. S. Sodha and N. C. Srivastava. *Microwave Propagation in Ferrimagnetics*. Springer US, Boston, MA (1981). DOI: 10.1007/978-1-4757-5839-9. 45, 53

[246] R. Gerber, C. D. Wright, and G. Asti (editors). *Applied Magnetism*. Springer Netherlands, Dordrecht (1994). DOI: 10.1007/978-94-015-8263-6. 45

[247] Ü. Özgür, Y. Alivov, and H. Morkoç. J. Mater. Sci.: Mater. Electron., **20**, 789 (2009). 45, 53

[248] Ü. Özgür, Y. Alivov, and H. Morkoç. J. Mater. Sci.: Mater. Electron., **20**, 911 (2009). 45

[249] R. F. Soohoo. *Microwave magnetics*. Harper and Row, New York (1985). 45, 53

[250] B. Lax and K. J. Button. *Microwave Ferrites and Ferrimagnetics*. McGraw Hill, New York (1962). 45, 53

[251] B. Schneider. Phys. Status Solidi B, **51**, 325 (1972). 45

[252] M. Haidar. *Role of surfaces in magnetization dynamics and spin polarized transport : a spin wave study*. phdthesis, Université de Strasbourg (2012). 45, 49

[253] Y. Zhang, X. S. Wang, H. Y. Yuan, S. S. Kang, H. W. Zhang, and X. R. Wang. J. Phys.: Condens. Matter, **29**, 095806 (2017). 45

[254] D. Dalvit, P. Milonni, D. Roberts, and F. da Rosa (editors). *Casimir Physics*, vol. 834 of *Lecture Notes in Physics*. Springer Berlin Heidelberg, Berlin, Heidelberg (2011). DOI: 10.1007/978-3-642-20288-9. 45

[255] A. Jander, J. Moreland, and P. Kabos. Appl. Phys. Lett., **78**, 2348 (2001). 45

[256] G. Rupp, W. Wettling, R. Smith, and W. Jantz. J. Magn. Magn. Mater., **45**, 404 (1984). 45

[257] R. van den Doel, M. F. H. Schuurmans, and K. Weiss. Phillips J. Res., **34**, 91 (1979). 45

[258] T. Wolfram. J. Appl. Phys., **41**, 4748 (1970). 45

[259] Z. I. Al-Sahhar, M. M. Shabat, and H. J. El-Khozondar. SpringerPlus, **2**, 584 (2013). 45

[260] B. Zamir and R. Ali. JNSMAC, **47**, 11 (2007). 45

[261] O. Yaln (editor). *Ferromagnetic Resonance - Theory and Applications*. InTech (2013). DOI: 10.5772/50583. 45

[262] R. Marqus, F. Martn, and M. Sorolla. *Metamaterials with Negative Parameters*. John Wiley & Sons, Inc., Hoboken, NJ, USA (2007). DOI: 10.1002/9780470191736. 45

[263] A. G. Gurevich and G. A. Melkov. *Magnetization Oscillations and Waves*. CRC Press, Boca Raton, FL (1996). 45

[264] J. Weiner. *Light-matter interaction- physics and engineering and nanoscale*. Oxford University Press, New York, NY, 2nd edition ed. (2017). 46, 80, 85, 90

[265] M. B. Jungfleisch. *Spin pumping and inverse spin Hall effect in yttrium iron garnet/platinum heterostructures*. Ph.D. thesis, Ph. D. thesis, Department of Physics, TU Kaiserslautern, Germany (2013). 49, 53

[266] M. P. Ross. *Ross,Marc_Dissertation_2013.pdf*. Ph.D. thesis, University of München (2013). 49

[267] D. D. Stancil and A. Prabhakar. *Spin Waves*. Springer US, Boston, MA (2009). DOI: 10.1007/978-0-387-77865-5. 49, 50, 53, 90

[268] N. Mecking. *A comprehensive study of the AMR-induced microwave photovoltage, photocurrent and photoresistance in Permalloy microstrips*. Ph.D. thesis, Universität Hamburg (2008). 49

[269] V. Flovik. *Magnetization dynamics in nanostructures*. Ph.D. thesis, NTNU (2016). 49

[270] D. J. Adams. *Ferromagnetic Resonance Studies of Coupled Magnetic Systems*. Ph.D. thesis, University of New Orleans (2016). 49

[271] M. d'Aquino. *Nonlinear magnetization dynamics in thin-films and nanoparticles*. Ph.D. thesis, Università degli Studi di Napoli Federico II (2005). 49

[272] H. Seidel and H. Boyet. J. Appl. Phys., **28**, 452 (1957). 49

[273] D. Polder. Physica, **15**, 253 (1949). 49

[274] T. Gilbert. **40**, 3443 (2004). 49, 50

[275] R. A. Lukashev. *Handbook of Nanomagnetism: Applications and Tools* (2015). 49

[276] *Magnetism*. Springer Berlin Heidelberg, Berlin, Heidelberg (2006). DOI: 10.1007/978-3-540-30283-4. 50

[277] J. B. Goodenough. *Magnetism and chemical bond*, vol. 1. Interscience Publ. (1963). 51, 162

[278] J. Kanamori. J. Phys. Chem. Solids, **10**, 87 (1959). 51

[279] P. W. Anderson. Phys. Rev., **115**, 2 (1959). 51

[280] D. D. Awschalom and M. E. Flatté. Nat. Phys., **3**, 153 (2007). 53, 348

[281] R. Jansen. Nat. Mater., **11**, 400 (2012). 53

[282] J. C. Slonczewski. Phys. Rev. B, **82**, 0544403 (2010). 53, 166, 202

[283] J. S. Moodera, G.-X. Miao, and T. S. Santos. Phys. Today, **63**, 46 (2010). xviii, 53, 110, 166, 352, 356

[284] N. M. Caffrey, D. Fritsch, T. Archer, S. Sanvito, and C. Ederer. Phys. Rev. B, **87**, 024419 (2013). 53, 162, 178, 182, 197, 203, 206

[285] U. Lüders, M. Bibes, K. Bouzehouane, E. Jacquet, J.-P. Contour, S. Fusil, J.-F. Bobo, J. Fontcuberta, A. Barthélémy, and A. Fert. Appl. Phys. Lett., **88**, 082505 (2006). 53, 162, 182, 188, 264

[286] J. X. Ma, D. Mazumdar, G. Kim, H. Sato, N. Z. Bao, and A. Gupta. J. Appl. Phys., **108**, 063917 (2010). xvi, xvii, 53, 57, 74, 162, 163, 167, 178, 183, 194, 195, 199, 202, 203, 219, 222, 263

[287] Z. Szotek, W. M. Temmerman, A. Svane, L. Petit, P. Strange, G. M. Stocks, D. Ködderitzsch, W. Hergert, and H. Winter. J. Phys.: Condens. Matter, **16**, S5587 (2004). 54, 56

[288] Z. Szotek, W. M. Temmerman, D. Ködderitzsch, A. Svane, L. Petit, and H. Winter. Phys. Rev. B, **74** (2006). 54, 56, 167, 196

[289] D. Fritsch and C. Ederer. Appl. Phys. Lett., **99**, 081916 (2011). 54, 56, 166, 167

[290] D. Fritsch and C. Ederer. Phys. Rev. B, **82** (2010). 54, 56, 166, 167

[291] D. Fritsch and C. Ederer. Phys. Rev. B, **86**, 014406 (2012). xvii, 54, 56, 167, 222

[292] G. Kresse and J. Furthmüller. Computational Materials Science, **6**, 15 (1996). 54, 56, 171

[293] G. Kresse and D. Joubert. Phys. Rev. B, **59**, 1758 (1999). 54, 56, 171

[294] V. Antonov, B. Harmon, and A. Yaresko. *Electronic structure and magneto-optical properties of solids*. Kluwer Academic Publishers, Dordrecht; Boston (2004). 54, 56, 126

[295] P. E. Blöchl. Phys. Rev. B, **50**, 17953 (1994). 54, 56, 171

[296] R. Waldron. Phys. Rev., **99**, 1727 (1955). 54, 167, 193

[297] S. Balaji, R. Kalai Selvan, L. John Berchmans, S. Angappan, K. Subramanian, and C. Augustin. Materials Science and Engineering: B, **119**, 119 (2005). 54

[298] S. N. Dolia, R. Sharma, M. P. Sharma, and N. S. Saxena. Indian Journal of Pure & Applied Physics, **44**, 774 (2006). 54

[299] J. Haetge, C. Suchomski, and T. Brezesinski. Inorg. Chem., **49**, 11619 (2010). 54

[300] R. C. Rai, S. Wilser, M. Guminiak, B. Cai, and M. L. Nakarmi. Appl. Phys. A, **106**, 207 (2012). 54, 193

[301] B. S. Holinsworth, H. Sims, J. G. Cherian, D. Mazumdar, N. C. Harms, B. C. L. Chapman, A. Gupta, S. A. McGill, and J. L. Musfeldt. Phys. Rev. B, **96**, 094427 (2017). xv, 72, 204, 206, 209, 219

[302] S. Bader and S. Parkin. Annu. Rev. Condens. Matter Phys., **1**, 71 (2010). 54, 163, 178, 204, 348

[303] J. S. Moodera, X. Hao, G. A. Gibson, and R. Meservey. Phys. Rev. Lett., **61**, 637 (1988). 54

[304] J. S. Moodera, R. Meservey, and X. Hao. Phys. Rev. Lett., **70**, 853 (1993). 54

[305] T. S. Santos and J. S. Moodera. Phys. Rev. B, **69** (2004). 54

[306] R. Meservey and P. M. Tedrow. Phys. Rep., **238**, 173 (1994). xviii, 54, 350, 356

[307] P. V. Lukashev, J. D. Burton, A. Smogunov, J. P. Velev, and E. Y. Tsymbal. Phys. Rev. B, **88** (2013). 55, 162, 163, 178

[308] D. Carta, M. F. Casula, A. Falqui, D. Loche, G. Mountjoy, C. Sangregorio, and A. Corrias. J. Phys. Chem. C, **113**, 8606 (2009). 57, 199, 203

[309] U. Lüders, M. Bibes, J.-F. Bobo, M. Cantoni, R. Bertacco, and J. Fontcuberta. Phys. Rev. B, **71**, 134419 (2005). 57

[310] N. Nakagawa, H. Y. Hwang, and D. A. Muller. Nat. Mater., **5**, 204 (2006). 57

[311] L. F. Kourkoutis, H. L. Xin, T. Higuchi, Y. Hotta, J. H. Lee, Y. Hikita, D. G. Schlom, H. Y. Hwang, and D. A. Muller. Philos. Mag., **90**, 4731 (2010). 57

[312] M. Varela, T. J. Pennycook, W. Tian, D. Mandrus, S. J. Pennycook, V. Peña, Z. Sefrioui, and J. Santamaria. J. Mater. Sci., **41**, 4389 (2006). 57

[313] P. Palmero. Nanomaterials, **5**, 656 (2015). 57

[314] Q. C. Sun, C. S. Birkel, J. Cao, W. Tremel, and J. L. Musfeldt. ACS Nano, **6**, 4876 (2012). 57, 58, 167, 192, 193, 194, 197, 230, 263, 325, 330

[315] V. Kumbhar, A. Jagadale, N. Shinde, and C. Lokhande. Appl. Surf. Sci., **259**, 39 (2012). 57

[316] C. P. Bean and J. D. Livingston. J. Appl. Phys., **30**, S120 (1959). 58

[317] C. Tannous and J. Gieraltowski. Eur. J. Phys., **29**, 475 (2008). 58

[318] R. Kurchania, D. Rathore, and R. K. Pandey. J. Mater. Sci.: Mater. Electron., **26**, 9355 (2015). 58

[319] V. Blanco-Gutiérrez, E. Climent-Pascual, R. Sáez-Puche, and M. J. Torralvo-Fernández. Phys. Chem. Chem. Phys., **18**, 9186 (2016). 58

[320] M. Fukuhara. Phys. Lett. A, **313**, 427 (2003). 58

[321] V. Blanco-Gutierrez, R. Saez-Puche, and M. J. Torralvo-Fernandez. J. Mater. Chem., **22**, 2992 (2012). 58

[322] S. Cao, X. Zhang, K. Sinha, W. Wang, J. Wang, P. A. Dowben, and X. Xu. Appl. Phys. Lett., **108**, 202903 (2016). 59, 60

[323] Y. K. Jeong, J.-H. Lee, S.-J. Ahn, and H. M. Jang. Chem. Mater., **24**, 2426 (2012). 59

[324] H. Wang, I. V. Solovyev, W. Wang, X. Wang, P. J. Ryan, D. J. Keavney, J.-W. Kim, T. Z. Ward, L. Zhu, J. Shen, X. M. Cheng, L. He, X. Xu, and X. Wu. Phys. Rev. B, **90** (2014). 59, 236

[325] E. Magome, C. Moriyoshi, Y. Kuroiwa, A. Masuno, and H. Inoue. Japanese Journal of Applied Physics, **49**, 09ME06 (2010). 59

[326] A. A. Bossak, I. E. Graboy, O. Y. Gorbenko, A. R. Kaul, M. S. Kartavtseva, V. L. Svetchnikov, and H. W. Zandbergen. Chem. Mater., **16**, 1751 (2004). 59

[327] H. R. Eisenberg and D. Kandel. Phys. Rev. Lett., **85**, 1286 (2000). 59

[328] H. Das, A. L. Wysocki, Y. Geng, W. Wu, and C. J. Fennie. Nat. Commun., **5** (2014). xvi, 75, 230

[329] W. Wang. *Growth and Characterization of Hexagonal Lu-Fe-O Multiferroic Thin Films*. Ph.D. thesis, University of Tennessee - Knoxville (2012). xvi, 75

[330] M. Isobe, N. Kimizuka, J. Iida, and S. Takekawa. Acta Crystallogr., Sect. C: Cryst. Struct. Commun., **46**, 1917 (1990). 60

[331] N. Kimizuka, A. Takenaka, Y. Sasada, and T. Katsura. Solid State Commun., **15**, 1321 (1974). 60, 172

[332] N. Kimizuka and T. Katsura. J. Solid State Chem., **13**, 176 (1975). 60

[333] S. M. Gaw, H. J. Lewtas, D. F. McMorrow, J. Kulda, R. A. Ewings, T. G. Perring, R. A. McKinnon, G. Balakrishnan, D. Prabhakaran, and A. T. Boothroyd. Phys. Rev. B, **91** (2015). 60

[334] N. Ikeda. J. Phys.: Condens. Matter, **20**, 434218 (2008). 60, 61

[335] Y. Yamada, K. Kitsuda, S. Nohdo, and N. Ikeda. Phys. Rev. B, **62**, 12167 (2000). 60

[336] X. S. Xu, J. de Groot, Q.-C. Sun, B. C. Sales, D. Mandrus, M. Angst, A. P. Litvinchuk, and J. L. Musfeldt. Phys. Rev. B, **82** (2010). 60

[337] C. M. Brooks, R. Misra, J. A. Mundy, L. A. Zhang, B. S. Holinsworth, K. R. O'Neal, T. Heeg, W. Zander, J. Schubert, J. L. Musfeldt, Z.-K. Liu, D. A. Muller, P. Schiffer, and D. G. Schlom. Appl. Phys. Lett., **101**, 132907 (2012). 61, 176, 230

[338] J. Liu, Y. Wang, and J. Dai. Thin Solid Films, **518**, 6909 (2010). 61

[339] M. Zeng, J. Liu, Y. Qin, H. Yang, J. Li, and J. Dai. Thin Solid Films, **520**, 6446 (2012). 61

[340] V. Barone. *Computational Strategies for Spectroscopy: from Small Molecules to Nano Systems*. Wiley (2011). 78, 79

[341] H. Solheim. *Theoretical studies of natural and magnetic circular dichroism*. Ph.D. thesis, Artic University of Norway (2011). 79, 90, 119

[342] S. Gasiorowicz. *Wiley: Quantum Physics, 3rd Edition - Stephen Gasiorowicz*. Wiley, New York, 3 ed. (2003). 79, 371

[343] D. Andrews. *Molecular Photophysics and Spectroscopy*. Morgan & Claypool Publishers (2014). 79

[344] D. Bhattacharya, N. Vaval, and S. Pal. J. Chem. Phys., **138**, 094108 (2013). 79

[345] G. Benno and K. Joachim. October, 31st (2003). 79

[346] F. Wooten. *Optical Properties of Solids*. Academic Press, New York, NY (1972). 80, 81, 99, 100, 168

[347] M. Tinkham. *Far infrared properties of solids*. Plenum Publishing, Plenum, NY (1970). 80, 97, 148, 164, 168

[348] D. Fleisch. *A Student's Guide to Maxwell's Equations*. Cambridge University Press, Cambridge ; New York (2008). 80

[349] R. Becker and F. Sauter. *Electromagnetic fields and interactions*. Dover Publications, New York (1982). 80

[350] R. Fitzpatrick. *Electromagnestism and Optics*. University of Texas (1981). 80

[351] A. R. Harish and M. Sachidananda. *Antennas and wave propagation*. Oxford University Press, USA (2007). 80

[352] E. C. Jordan and K. G. Balmain. *Electromagnetic waves and radiating systems*. Englewood Cliffs, N.J. : Prentice-Hall, 2nd ed ed. (1968). 80

[353] J. D. Kraus and D. A. Fleisch. *Electromagnetics : with applications*. Boston : WCB/McGraw-Hill, 5th ed ed. (1999). 80

[354] D. K. Cheng. *Fundamentals of engineering electromagnetics*. Reading, Mass Addison-Wesley Pub. Co (1993). 80

[355] O. S. Heavens. *Optical properties of thin solid films*. Courier Corporation (1991). 81, 95, 99

[356] H. A. Macleod. *Thin-film optical filters*. Series in optics and optoelectronics. CRC Press/Taylor & Francis, Boca Raton, FL, 4th ed ed. (2010). OCLC: ocn176924832. 81, 99

[357] L. D. Barron. *Molecular Light Scattering and Optical Activity*. Cambridge University Press, New York, NY, 2 ed. (2009). xiii, 84, 128, 131, 145, 261, 379

[358] M. Born and E. Wolf. *Principles of optics: electromagnetic theory of propagation, interference and diffraction of light*. Cambridge University Press, Cambridge ; New York, 7th expanded ed ed. (1999). xvi, 85, 86, 90, 95

[359] A. M. Stewart *. J. Mod. Opt., **52**, 1145 (2005). 87

[360] A. M. Stewart. International Journal of Optics, **2011**, e728350 (2011). 87

[361] K. Y. Bliokh, A. Y. Bekshaev, and F. Nori. New J. Phys., **15**, 033026 (2013). 87

[362] K. T. Mcdonald. *Orbital and Spin Angular Momentum of Electromagnetic Fields*. 87

[363] L. Marrucci. Mol. Cryst. Liq. Cryst., **488**, 148 (2008). 87

[364] S. M. Barnett. J. Mod. Opt., **57**, 1339 (2010). 87

[365] J. Sjoholm. *Angular Momentum of Electromagnetic Radiation. Fundamental physics applied to the radio domain for innovative studies of space and development of new concepts in wireless communications*. Ph.D. thesis, Uppsala University (2009). 87

[366] M. Mansuripur. Phys. Rev. A, **84**, 033838 (2011). 87

[367] K. Y. Bliokh, J. Dressel, and F. Nori. New J. Phys., **16**, 093037 (2014). 87

[368] S. M. Barnett, L. Allen, R. P. Cameron, C. R. Gilson, M. J. Padgett, F. C. Speirits, and A. M. Yao. J. Opt., **18**, 064004 (2016). 87

[369] I. Bialynicki-Birula and Z. Bialynicka-Birula. Opt. Commun., **264**, 342 (2006). 87

[370] K. Y. Bliokh, A. Y. Bekshaev, and F. Nori. Nat. Commun., **5**, 3300 (2014). 87

[371] M. Levy and D. Karki. Sci. Rep., **7**, 39972 (2017). 87, 123

[372] D. Singleton. Am. J. Phys, **66**, 697 (1998). 87

[373] L. Allen, M. W. Beijersbergen, R. J. C. Spreeuw, and J. P. Woerdman. Phys. Rev. A, **45**, 8185 (1992). 87, 108

[374] H. Luo, Z. Ren, W. Shu, and S. Wen. Phys. Rev. A, **77** (2008). xvi, 89

[375] G. A. Landrum, C. A. Ekberg, and J. W. Whittaker. Biophys. J., **69**, 674 (1995). 90, 141, 213, 366

[376] J. Pade. In *Quantum Mechanics for Pedestrians 1: Fundamentals*, 41–54. Springer International Publishing, Cham (2014). 90

[377] F. W. Hehl and Y. N. Obukhov. *Foundations of Classical Electrodynamics*. Birkh?user Boston, Boston, MA (2003). DOI: 10.1007/978-1-4612-0051-2. 90

[378] M. Dressel and G. Grüner. *Electrodynamics of solids: optical properties of electrons in matter*. Cambridge University Press, Cambridge ; New York (2002). 90, 99, 120

[379] A. M. Smith. *From Sight to Light: The Passage from Ancient to Modern Optics*. University of Chicago Press (2014). DOI: 10.7208/chicago/9780226174938.001.0001. 90

[380] A. Glindemann. *Principles of Stellar Interferometry*. Astronomy and Astrophysics Library. Springer Berlin Heidelberg, Berlin, Heidelberg (2011). DOI: 10.1007/978-3-642-15028-9. 90

[381] D. J. Griffiths. *Introduction to electrodynamics*. Prentice Hall, Upper Saddle River, N.J, 3rd ed ed. (1999). 90, 138

[382] J. D. Schmidt. *Numerical simulation of optical wave propagation with examples in MATLAB*. SPIE, Bellingham, Wash (2010). OCLC: ocn606405811. 90, 247

[383] L. Novotny and B. Hecht. *Principles of nano-optics*. Cambridge university press (2012). 90

[384] R. W. Ditchburn and U. Liddel. Phys. Today, **7**, 17 (1954). 90

[385] R. W. Ditchburn. *Light*. Blackie and Sons, Glasgow. 90

[386] L. Linner. **37**, 410 (1989). 92

[387] A. R. von Hippel. *Dielectric and Waves*. Wiley, New York (1954). 92

[388] A. R. von Hippel. *Dielectric Materials and Applications*. Wiley, New York (1954). 92

[389] D. D. Stancil. J. Appl. Phys., **59**, 218 (1986). 92

[390] K. Maaz (editor). *Magnetic Materials*. InTech (2016). DOI: 10.5772/61497. 92

[391] I. D. Vagner, B. I. Lembrikov, and P. Wyder. *Electrodynamics of Magnetoactive Media*, vol. 135 of *Springer Series in Solid-State Sciences*. Springer Berlin Heidelberg, Berlin, Heidelberg (2004). DOI: 10.1007/978-3-662-06941-7. 92

[392] S. McLeod. Self Concept | Simply Psychology (2008). 95

[393] P. H. Berning and A. F. Turner. JOSA, **47**, 230 (1957). 95

[394] P. Jepsen, D. Cooke, and M. Koch. Laser & Photonics Reviews, **5**, 124 (2011). 95

[395] R. Sato and H. Shirai. 703–704. IEEE (2014). 95

[396] J. L. Martínez, I. Moreno, M. del Mar Sánchez-López, A. Vargas, and P. García-Martínez. Opt. Express, **22**, 25866 (2014). 95

[397] G. R. Fowles. *Introduction to Modern Optics*. Dover Publications, New York, 2 ed. (1989). 95, 247

[398] J. E. Davis. *Multilayer reflectivity* (2014). 95

[399] R. E. Glover and M. Tinkham. Phys. Rev., **108**, 243 (1957). 97, 148, 173

[400] R. E. Glover III and M. Tinkham. Phys. Rev., **104**, 844 (1956). 97

[401] F. Gao, G. L. Carr, C. D. Porter, D. B. Tanner, S. Etemad, T. Venkatesan, A. Inam, B. Dutta, X. D. Wu, G. P. Williams, and others. Phys. Rev. B, **43**, 10383 (1991). 97, 148

[402] F. Gao. *Temperature Dependence of Infrared and Optical Properties of High-Temperature Superconductors*. Ph.D. thesis, University of Florida (1992). 97, 148

[403] H. W. Verleur. JOSA, **58**, 1356 (1968). 97

[404] D. M. Roessler. Br. J. Appl. Phys., **16**, 1119 (1965). 99, 129

[405] C. F. Bohren. Eur. J. Phys., **31**, 573 (2010). 99, 129

[406] J. Bechhoefer. Am. J. Phys, **79**, 1053 (2011). 99

[407] K. Jezierski. J. Phys. C: Solid State Phys., **19**, 2103 (1986). 99

[408] J. S. Toll. Phys. Rev., **104**, 1760 (1956). 99

[409] J. D. Jackson. *Classical Electrodynamics, 3rd Edition - John David Jackson*. John Wiley & Sons, Ltd, New York, NY, 3 ed. (1975). 99, 115, 138

[410] A. K. Garg. *Classical electromagnetism in a nutshell*. Princeton University Press, Princeton [N.J.] (2012). OCLC: ocn751250687. 99, 115, 138

[411] F. E. M. Silveira and S. M. Kurcbart. EPL (Europhysics Letters), **90**, 44004 (2010). 100

[412] D. B. Tanner. Department of Physics, University of Florida, USA (2013). 100

[413] D. B. Tanner. Phys. Rev. B, **91**, 035123 (2015). 100

[414] O. Stenzel. *The physics of thin film optical spectra: an introduction*. No. 44 in Springer series in surface sciences. Springer, Berlin ; New York (2005). 100, 129

[415] O. Stenzel. *The Physics of Thin Film Optical Spectra*, vol. 44 of *Springer Series in Surface Sciences*. Springer International Publishing, Cham (2016). 100

[416] P. C. Martin. Phys. Rev., **161**, 143 (1967). 100, 145

[417] V. Lucarini (editor). *Kramers-Kronig relations in optical materials research*. No. v. 110 in Springer series in optical sciences. Springer, Berlin ; New York (2005). OCLC: ocm57355550. 100, 129

[418] P. B. Allen. In S. G. L. a. M. L. Cohen (editor), *Contemporary Concepts of Condensed Matter Science*, vol. 2 of *Conceptual Foundations of MaterialsA Standard Model for Ground- and Excited-State Properties*, 165–218. Elsevier (2006). DOI: 10.1016/S1572-0934(06)02006-3. 102

[419] K. Rajeshwar, R. Nottenburg, V. R. P. Verneker, and J. Dubow. Phys. Status Solidi A, **58**, 245 (1980). 103

[420] A. K. Jonscher. Nature, **267**, 673 (1977). 103

[421] L. L. M. Handbook. Chapter, **7**, 54 (2004). xvi, 104, 241

[422] N. V. Volkov, A. S. Tarasov, M. V. Rautskii, A. V. Lukyanenko, F. A. Baron, I. A. Bondarev, S. N. Varnakov, and S. G. Ovchinnikov. Journal of Surface Investigation. X-ray, Synchrotron and Neutron Techniques, **9**, 984 (2015). 105, 110, 360

[423] N. V. Volkov, A. S. Tarasov, E. V. Eremin, F. A. Baron, S. N. Varnakov, and S. G. Ovchinnikov. J. Appl. Phys., **114**, 093903 (2013). 105

[424] C. L. Yang, H. T. He, L. Ding, L. J. Cui, Y. P. Zeng, J. N. Wang, and W. K. Ge. Phys. Rev. Lett., **96** (2006). 105, 360, 361

[425] K. E. Ballantine, J. F. Donegan, and P. R. Eastham. Sci. Adv., **2**, e1501748 (2016). 107

[426] N. B. Simpson, K. Dholakia, L. Allen, and M. J. Padgett. Opt. Lett., **22**, 52 (1997). 107

[427] A. T. O'Neil, I. MacVicar, L. Allen, and M. J. Padgett. Phys. Rev. Lett., **88** (2002). 107

[428] K. Y. Bliokh, F. J. Rodríguez-Fortuño, F. Nori, and A. V. Zayats. Nat. Photonics, **9**, 796 (2015). 108

[429] K. Y. Bliokh and F. Nori. Phys. Rep., **592**, 1 (2015). 108, 140

[430] J. H. Poynting. Proceedings of the Royal Society A: Mathematical, Physical and Engineering Sciences, **82**, 560 (1909). 108

[431] R. A. Beth. Phys. Rev., **50**, 115 (1936). 108

[432] M. Padgett and L. Allen. Contemp. Phys., **41**, 275 (2000). 108

[433] M. Padgett, J. Courtial, and L. Allen. Phys. Today, **57**, 35 (2004). 108

[434] J. Cugnon. Open Journal of Microphysics, **01**, 41 (2011). 108

[435] B. J. Smith and M. G. Raymer. New J. Phys., **9**, 414 (2007). 108

[436] I. Bialynicki-Birula. In *Progress in Optics*, vol. 36, 245–294. Elsevier (1996). 108

[437] N. Chandrasekar. Adv. Studies Theor. Phys, **6**, 391 (2012). 108

[438] C. Roychoudhuri. Am. J. Phys, **83**, 286 (2015). 108

[439] B. J. Pearson and D. P. Jackson. Am. J. Phys, **78**, 471 (2010). 108

[440] M. V. Berry. 6–11 (1998). 108

[441] S. M. Barnett and L. Allen. Opt. Commun., **110**, 670 (1994). 108

[442] C.-F. Li. Phys. Rev. A, **80** (2009). 108

[443] D. L. Andrews and M. Babiker (editors). *The Angular Momentum of Light*. Cambridge University Press, Cambridge (2012). 108

[444] L. Allen, M. Padgett, and M. Babiker. In *Progress in Optics*, vol. 39, 291–372. Elsevier (1999). 108

[445] A. M. Yao and M. J. Padgett. Adv. Opt. Photonics, **3**, 161 (2011). 108

[446] Z.-Y. Zhou, Y. Li, D.-S. Ding, W. Zhang, S. Shi, B.-S. Shi, and G.-C. Guo. Light: Science & Applications, **5**, e16019 (2016). 108

[447] U. Mizutani. *Introduction to the electron theory of metals*. Cambridge University Press, Cambridge ; New York (2001). 108

[448] A. Fert. Thin Solid Films, **517**, 2 (2008). 108

[449] S. Shen, P. R. Ohodnicki, S. J. Kernion, and M. E. McHenry. J. Appl. Phys., **112**, 103705 (2012). 108

[450] S. Bandyopadhyay and M. Cahay. *Introduction to Spintronics*. CRC Press, 2nd ed. (2015). 108

[451] S. Maekawa, S. O. Valenzuela, E. Saitoh, and T. Kimura (editors). *Spin Current*. Oxford University Press (2012). DOI: 10.1093/acprof:oso/9780199600380.001.0001. 108

[452] F. Duan and J. Guojun. *Introduction to Condensed Matter Physics: Volume 1*. WORLD SCIENTIFIC (2005). 108

[453] M. L. Plumer, J. van Ek, D. Weller, G. Ertl, R. Gomer, H. Lüth, and D. L. Mills (editors). *The Physics of Ultra-High-Density Magnetic Recording*, vol. 41 of *Springer Series in Surface Sciences*. Springer Berlin Heidelberg, Berlin, Heidelberg (2001). xvi, 109, 110

[454] N. Volkov, G. Petrakovskii, P. Böni, E. Clementyev, K. Patrin, K. Sablina, D. Velikanov, and A. Vasiliev. J. Magn. Magn. Mater., **309**, 1 (2007). 110

[455] Y. Tokura. Rep. Prog. Phys., **69**, 797 (2006). 110

[456] B. Dieny. In *Magnetoelectronics*, 67–377. Academic Press, San Diego (2004). 110

[457] J. E. Hirsch. Phys. Rev. Lett., **83**, 1834 (1999). 110

[458] C. Schindler. *Quantum spin transport in semiconductor nanostructures*. Ph.D. thesis, TECHNISCHE UNIVERSITÄT MÜNCHEN, MÜNCHEN, Germany (2012). 110

[459] Y. A. Bychkov and E. I. Rashba. Soviet Journal of Experimental and Theoretical Physics Letters, **39**, 78 (1984). 110

[460] G. Dresselhaus. Phys. Rev., **100**, 580 (1955). 110

[461] M. Cardona, N. E. Christensen, and G. Fasol. Phys. Rev. B, **38**, 1806 (1988). 110

[462] X. Gao, J. A. Woollam, R. D. Kirby, D. J. Sellmyer, C. T. Tanaka, J. Nowak, and J. S. Moodera. Phys. Rev. B, **59**, 9965 (1999). 117

[463] P. S. Pershan. J. Appl. Phys., **38**, 1482 (1967). 119

[464] M. Mansuripur. Optics and Photonics News, **10**, 32 (1999). 119

[465] H. Bennett. Phys. Rev., **137**, 448 (1965). 120

[466] J. L. Erskine and E. A. Stern. Phys. Rev. B, **12**, 5016 (1975). 120

[467] Z. Quan, W. Liu, X. Li, X. Xu, K. Addison, D. Score, and G. Gehring. Mater. Lett., **65**, 2982 (2011). 120, 121, 219

[468] H. R. Hulme. Proceedings of the Royal Society A: Mathematical, Physical and Engineering Sciences, **135**, 237 (1932). 120, 139

[469] L. Onsager. Phys. Rev., **37**, 405 (1931). 120

[470] L. Onsager. Phys. Rev., **38**, 2265 (1931). 120

[471] S.-Y. Huang, D. Qu, and C.-L. Chien. In *Solid State Physics*, vol. 64, 53–82. Elsevier (2013). 120

[472] X. Huang, L. Wang, L. Chen, J. Zhao, and H. Zheng. The European Physical Journal B, **85** (2012). 121

[473] R. Kubo. J. Phys. Soc. Jpn., **12**, 570 (1957). 121

[474] L. C. Lew Yan Voon and M. Willatzen. In *The k p Method*, 55–77. Springer Berlin Heidelberg, Berlin, Heidelberg (2009). DOI: 10.1007/978-3-540-92872-0_4. 121

[475] A. Lomax. Geophys. J. Int., **138**, 702 (1999). 122

[476] M. Mansuripur and D. P. Tsai. Opt. Commun., **284**, 707 (2011). 122

[477] P. M. Morse and H. Feshbach. *Methods of theoretical physics*. McGraw-Hill, New York (1953). OCLC: 530876. 122

[478] A. M. Mahmoud, A. R. Davoyan, and N. Engheta. Nat. Commun., **6**, 8359 (2015). 122

[479] L. Bi, J. Hu, P. Jiang, H. S. Kim, D. H. Kim, M. C. Onbasli, G. F. Dionne, and C. A. Ross. Materials, **6**, 5094 (2013). 122

[480] R. J. Potton. Rep. Prog. Phys., **67**, 717 (2004). 122, 123, 126

[481] A. L. Shelankov and G. E. Pikus. Phys. Rev. B, **46**, 3326 (1992). 123, 126

[482] M. Iwanaga, A. S. Vengurlekar, T. Hatano, and T. Ishihara. Am. J. Phys, **75**, 899 (2007). 123

[483] P. Kumar. *Nonlinear effects in magnetic garnet films and nonreciprocal optical Bloch oscillations in waveguide arrays*. Ph.D., Michigan Technological University, United States – Michigan (2013). 123

[484] M. Saito, K. Taniguchi, and T.-h. Arima. J. Phys. Soc. Jpn., **77**, 013705 (2008). 123

[485] B. B. Krichevtsov, V. V. Pavlov, and R. V. Pisarev. Zh. Eksp. Teor. Fiz, **94**, 284 (1988). 123

[486] T. Kodera, D. L. Sounas, and C. Caloz. In *2013 International Symposium on Electromagnetic Theory*, 397–400 (2013). 123

[487] G. F. Dionne, G. A. Allen, P. R. Haddad, C. A. Ross, and B. Lax. Lincoln Laboratory Journal, **15**, 323 (2005). 123

[488] G. N. Afanasiev. J. Phys. D: Appl. Phys., **34**, 539 (2001). 123

[489] G. van der Laan. Journal of Synchrotron Radiation, **8**, 1059 (2001). xiii, 123, 126, 128

[490] G. van der Laan. In E. Beaurepaire, H. Bulou, L. Joly, and F. Scheurer (editors), *Magnetism and Synchrotron Radiation: Towards the Fourth Generation Light Sources*, vol. 151, 257–287. Springer International Publishing, Cham (2013). 123

[491] I. Crassee, J. Levallois, A. L. Walter, M. Ostler, A. Bostwick, E. Rotenberg, T. Seyller, D. van der Marel, and A. B. Kuzmenko. Nat. Phys., **7**, 48 (2011). xvi, 124, 150

[492] V. Heine. *Group Theory in Quantum Mechanics*. Pergamon (1960). 123

[493] M. Tinkham. *Group theory and quantum mechanics*. Dover Publications, Mineola, N.Y (2003). 123

[494] B. L. van der Waerden. *Group Theory and Quantum Mechanics*, vol. 214 of *Grundlehren der mathematischen Wissenschaften*. Springer Berlin Heidelberg, Berlin, Heidelberg (1974). 123

[495] E. Beaurepaire, H. Bulou, F. Scheurer, and J.-P. Kappler (editors). *Magnetism: A Synchrotron Radiation Approach*, vol. 697 of *Lecture Notes in Physics*. Springer Berlin Heidelberg (2006). 126

[496] E. Beaurepaire, H. Bulou, F. Scheurer, and K. Jean-Paul (editors). *Magnetism and Synchrotron Radiation*, vol. 133 of *Springer Proceedings in Physics*. Springer Berlin Heidelberg, Berlin, Heidelberg (2010). xiii, 126, 128

[497] V. N. Muthukumar, R. Valentí, and C. Gros. Phys. Rev. B, **54**, 433 (1996). 126

[498] š. Višňovský. Czech. J. Phys., **34**, 969 (1984). 126

[499] F. Stern. In *Solid State Physics*, vol. 15, 299–408. Elsevier (1963). 129

[500] Y. Kyung Lim and H. J Lee. The Open Plasma Physics Journal, **5** (2012). 129

[501] J. C. Idrobo, J. Rusz, J. Spiegelberg, M. A. McGuire, C. T. Symons, R. R. Vatsavai, C. Cantoni, and A. R. Lupini. Advanced Structural and Chemical Imaging, **2** (2017). 130

[502] J. Mack and M. J. Stillman. In R. A. Scott (editor), *Encyclopedia of Inorganic and Bioinorganic Chemistry*. John Wiley & Sons, Ltd, Chichester, UK (2011). 131, 135, 376

[503] C. J. Barrows, V. A. Vlaskin, and D. R. Gamelin. The Journal of Physical Chemistry Letters, **6**, 3076 (2015). 131, 217

[504] S. Ye, G. Xue, I. Krivokapic, T. Petrenko, E. Bill, L. Que Jr, and F. Neese. Chem. Sci., **6**, 2909 (2015). 131

[505] W. Kuch, A. Dittschar, K. Meinel, M. Zharnikov, C. M. Schneider, J. Kirschner, J. Henk, and R. Feder. Phys. Rev. B, **53**, 11621 (1996). 131

[506] B. R. Hollebone and M. J. Stillman. J. Chem. Soc., Faraday Trans. 2, **74**, 2107 (1978). 131

[507] H. Isago. *Optical Spectra of Phthalocyanines and Related Compounds*. NIMS Monographs. Springer Japan, Tokyo (2015). 131

[508] F. Pineider, G. Campo, V. Bonanni, C. de Julián Fernández, G. Mattei, A. Caneschi, D. Gatteschi, and C. Sangregorio. Nano Lett., **13**, 4785 (2013). 131

[509] G. Weick and D. Weinmann. Phys. Rev. B, **83** (2011). 131

[510] Y. Gu and K. G. Kornev. Journal of the Optical Society of America B, **27**, 2165 (2010). 131

[511] R. W. Schwartz, A. K. Banerjee, A. C. Sen, and M. Chowdhury. Journal of the Chemical Society, Faraday Transactions 2, **76**, 620 (1980). 131

[512] S. Marcet, D. Ferrand, D. Halley, S. Kuroda, H. Mariette, E. Gheeraert, F. J. Teran, M. L. Sadowski, R. M. Galera, and J. Cibert. Phys. Rev. B, **74** (2006). 131

[513] F. C. Brown and G. Laramore. Appl. Opt., **6**, 669 (1967). 131

[514] K. Binnemans. Coord. Chem. Rev., **295**, 1 (2015). 131

[515] B. Henderson and G. F. Imbusch. *Optical spectroscopy of inorganic solids*. Monographs on the physics and chemistry of materials ;. Clarendon Press, (1989). 131, 135

[516] H. Tanaka, W. M. Jadwisienczak, H. Saito, V. Zayets, S. Yuasa, and K. Ando. J. Phys. D: Appl. Phys., **47**, 355001 (2014). 131

[517] A. E. Sokolov, S. G. Ovchinnikov, V. N. Zabluda, A. M. Kal'sin, and Y. V. Zubavichus. JETP Lett., **97**, 98 (2013). 135, 165, 169, 174

[518] M. Ying, W. Dizayee, Z. X. Mei, X. L. Du, A. M. Fox, and G. A. Gehring. J. Phys. D: Appl. Phys., **48**, 255502 (2015). 135, 138, 139

[519] H. Tanaka. *Zeeman Splitting Caused by Localized sp-d Exchange Interaction in Ferromagnetic GaMnAs Observed by Magneto-Optical Characterization*. Ph.D. thesis, Ohio University (2015). 135

[520] G. B. Scott, D. E. Lacklison, H. I. Ralph, and J. L. Page. Phys. Rev. B, **12**, 2562 (1975). 135, 138

[521] G. B. Scott, D. E. Lacklison, and J. L. Page. J. Phys. C: Solid State Phys., **8**, 519 (1975). 135

[522] D. Rudolf. *Femtosecond Spin Dynamics in Magnetic Multilayers Employing High Harmonics of Laser Radiation*, vol. 70. Forschungszentrum Jülich (2013). xvi, 137, 138

[523] R. Serber. Phys. Rev., **41**, 489 (1932). 139

[524] T. Higuchi and M. Kuwata-Gonokami. Nat. Commun., **7**, 10720 (2016). 139

[525] G. Molina-Terriza, J. P. Torres, and L. Torner. Nat. Phys., **3**, 305 (2007). xvi, 140, 141, 143, 213

[526] J. P. Torres and L. Torner (editors). *Wiley: Twisted Photons: Applications of Light with Orbital Angular Momentum - Juan P. Torres, Lluis Torner*. Wiley, Verlag (2011). 140, 141, 213

[527] I. V. Lerner, B. L. Althsuler, V. I. Fal'ko, and T. Giamarchi (editors). *Strongly Correlated Fermions and Bosons in Low-Dimensional Disordered Systems*. Springer Netherlands, Dordrecht (2002). 140, 371

[528] C. A. Balanis. *Advanced engineering electromagnetics*. John Wiley & Sons, Hoboken, N.J, 2nd ed ed. (2012). 140

[529] R. E. Collin. *Foundations for microwave engineering*. IEEE Press series on electromagnetic wave theory. IEEE Press, New York, 2nd ed ed. (2001). 140

[530] J. T. Wang, S. Hall, Y. Zhen, and D. S. Guo. J. Supercond. Novel Magn., **23**, 1155 (2010). 141, 213

[531] Y. Xu and S. Thompson (editors). *Spintronic Materials and Technology*. Taylor & Francis, New York (2006). 141, 213

[532] M. E. McCarville. *The magnetic circular dichroism of biologically interesting molecules*. Ph.D. thesis, Princeton (1967). 141

[533] A. D. Buckingham and P. J. Stephens. Annu. Rev. Phys. Chem., **17**, 399 (1966). 141, 366

[534] P. J. Stephens. J. Chem. Phys., **52**, 3489 (1970). 141

[535] P. J. Stephens. Adv. Chem. Phys., **35**, 197 (1976). 141, 234, 366

[536] Nat. Mater., **9**, 955 (2010). 141

[537] N. Kondo. Chem. Vap. Deposition, **2**, 24 (1996). 141

[538] J. K. Furdyna. J. Appl. Phys., **64**, R29 (1988). 141

[539] W. Pötz, J. Fabian, and U. Hohenester (editors). *Modern aspects of spin physics*. No. 712 in Lecture notes in physics. Springer, Berlin ; New York (2007). 141

[540] J. A. Gaj, J. Ginter, and R. R. Ga\lązka. Phys. Status Solidi B, **89**, 655 (1978). 141

[541] J. A. Gaj and J. Kossut (editors). *Introduction to the Physics of Diluted Magnetic Semiconductors*, vol. 144 of *Springer Series in Materials Science*. Springer Berlin Heidelberg, Berlin, Heidelberg (2010). 141, 379

[542] A. D. Poularikas. *The handbook of formulas and tables for signal processing*. The electrical engineering handbook series. CRC Press ; Springer : IEEE Press, Boca Raton, Fla. : [New York, NY] (1999). 145

[543] A. Moscowitz. In I. Prigogine (editor), *Advances in Chemical Physics*, vol. 4, 67–112. John Wiley & Sons, Inc., Hoboken, NJ, USA (1962). 145

[544] W. Moffitt and A. Moscowitz. J. Chem. Phys., **30**, 648 (1959). 145

[545] R. A. Harris. J. Chem. Phys., **43**, 959 (1965). 145

[546] P. N. Schatz, A. J. McCaffery, W. Suëtaka, G. N. Henning, A. B. Ritchie, and P. J. Stephens. J. Chem. Phys., **45**, 722 (1966). 145

[547] G. A. Gehring, M. S. Alshammari, D. S. Score, J. R. Neal, A. Mokhtari, and A. M. Fox. J. Magn. Magn. Mater., **324**, 3422 (2012). 148, 180, 182, 208, 215

[548] M. Tinkham and R. E. Glover III. Phys. Rev., **110**, 778 (1958). 148

[549] R. Swanepoel. J. Phys. E: Sci. Instrum., **16**, 1214 (1983). 150

[550] J. C. Manifacier, J. Gasiot, and J. P. Fillard. J. Phys. E: Sci. Instrum., **9**, 1002 (1976). 150

[551] W. R. Branford, J. R. Neal, C. L. Spencer, G. A. Gehring, A. M. Fox, N. Popovici, R. C. da Silva, O. Conde, and L. F. Cohen. vol. 893, 1199–1200. AIP (2007). 150, 182

[552] J. R. Neal, A. J. Behan, R. M. Ibrahim, H. J. Blythe, M. Ziese, A. M. Fox, and G. A. Gehring. Phys. Rev. Lett., **96** (2006). 150, 182

[553] K. Chiu, T. Lee, and J. Quinn. Surf. Sci., **58**, 182 (1976). 150

[554] P. Y. Yu and M. Cardona. *Fundamentals of Semiconductors*. Graduate Texts in Physics. Springer Berlin Heidelberg, Berlin, Heidelberg (2010). 161

[555] N. D. Spencer and J. H. Moore (editors). *Encyclopedia of chemical physics and physical chemistry*. Institute of Physics Pub, Bristol ; Philadelphia (2001). 161

[556] Q. C. Sun, H. Sims, D. Mazumdar, J. X. Ma, B. S. Holinsworth, K. R. O'Neal, G. Kim, W. H. Butler, A. Gupta, and J. L. Musfeldt. Phys. Rev. B, **86**, 205106 (2012). xvii, 162, 163, 178, 179, 180, 181, 182, 183

[557] C. Klewe, M. Meinert, A. Boehnke, K. Kuepper, E. Arenholz, A. Gupta, J.-M. Schmalhorst, T. Kuschel, and G. Reiss. J. Appl. Phys., **115**, 123903 (2014). 162, 178, 263

[558] A. P. Ramirez. Science, **315**, 1377 (2007). 163, 178

[559] J. I. Pankove. *Optical Processes in Semiconductors*. Dover Publications, New York (1971). 164, 168, 192, 193, 229

[560] D. J. Singh, R. C. Rai, J. L. Musfeldt, S. Auluck, N. Singh, P. Khalifah, S. McClure, and D. G. Mandrus. Chem. Mater., **18**, 2696 (2006). 164

[561] J. A. Larrabee, G. Schenk, N. Mitić, and M. J. Riley. Eur. Biophys. J., **44**, 393 (2015). 165, 371

[562] K. W. Hipps and G. A. Crosby. J. Phys. Chem., **83**, 555 (1979). 165, 169, 173, 174, 175

[563] G. E. W. Bauer, E. Saitoh, and B. J. van Wees. Nat. Mater., **11**, 391 (2012). 166

[564] D. C. Worledge and T. H. Geballe. J. Appl. Phys., **88**, 5277 (2000). 166

[565] T. R. Paudel, A. Zakutayev, S. Lany, M. d'Avezac, and A. Zunger. Adv. Funct. Mater., **21**, 4493 (2011). 166

[566] M. N. Iliev, D. Mazumdar, J. X. Ma, A. Gupta, F. Rigato, and J. Fontcuberta. Phys. Rev. B, **83**, 014108 (2011). 166, 203

[567] U. Lüders, A. Barthélémy, M. Bibes, K. Bouzehouane, S. Fusil, E. Jacquet, J.-P. Contour, J.-F. Bobo, J. Fontcuberta, and A. Fert. Adv. Mater., **18**, 1733 (2006). 166, 199

[568] A. V. Ramos, M.-J. Guittet, J.-B. Moussy, R. Mattana, C. Deranlot, F. Petroff, and C. Gatel. Appl. Phys. Lett., **91**, 122107 (2007). 166, 352

[569] A. V. Ramos, T. S. Santos, G. X. Miao, M.-J. Guittet, J.-B. Moussy, and J. S. Moodera. Phys. Rev. B, **78**, 180402 (2008). 166, 202, 203, 354

[570] F. Rigato, S. Piano, M. Foerster, F. Giubileo, A. M. Cucolo, and J. Fontcuberta. Phys. Rev. B, **81** (2010). 166

[571] B. B. Nelson-Cheeseman, F. J. Wong, R. V. Chopdekar, E. Arenholz, and Y. Suzuki. Phys. Rev. B, **81**, 214421 (2010). 166

[572] In the context of this work the band gap hierarchy refers to the presence of multiple charge gaps in the optical absorption spectrum. 167

[573] A. V. Ravindra, P. Padhan, and W. Prellier. Appl. Phys. Lett., **101**, 161902 (2012). 167, 193

[574] J. Coey. *Magnetism and Magnetic Materials*. Cambridge University Press (2010). 171

[575] X. L. Lu, J. W. Zhang, C. F. Zhang, J. C. Zhang, and Y. Hao. RSC Adv., **5**, 58640 (2015). 171

[576] T. Amrillah, S. K. Vandrangi, Y. Bitla, T. H. Do, S.-C. Liao, C.-Y. Tsai, Y.-Y. Chin, Y.-T. Liu, M.-L. Lin, Q. He, H.-J. Lin, H.-Y. Lee, C.-H. Lai, E. Arenholz, J.-Y. Juang, and Y.-H. Chu. Nanoscale, **8**, 8847 (2016). 171

[577] M. Artus, L. Ben Tahar, F. Herbst, L. Smiri, F. Villain, N. Yaacoub, J.-M. Grenèche, S. Ammar, and F. Fiévet. J. Phys.: Condens. Matter, **23**, 506001 (2011). 171

[578] C. M. Folkman, S. H. Baek, H. W. Jang, C. B. Eom, C. T. Nelson, X. Q. Pan, Y. L. Li, L. Q. Chen, A. Kumar, V. Gopalan, and S. K. Streiffer. Appl. Phys. Lett., **94**, 251911 (2009). 171

[579] C. Beekman, W. Siemons, T. Z. Ward, J. D. Budai, J. Z. Tischler, R. Xu, W. Liu, N. Balke, J. H. Nam, and H. M. Christen. Appl. Phys. Lett., **102**, 221910 (2013). 171

[580] C. Ederer and N. A. Spaldin. Phys. Rev. B, **71** (2005). 171, 172

[581] T. Kimura, Y. Sekio, H. Nakamura, T. Siegrist, and A. P. Ramirez. Nat. Mater., **7**, 291 (2008). 172

[582] V. V. Pavlov, A. R. Akbashev, A. M. Kalashnikova, V. A. Rusakov, A. R. Kaul, M. Bayer, and R. V. Pisarev. J. Appl. Phys., **111**, 056105 (2012). 172

[583] T. Zhao, A. Scholl, F. Zavaliche, K. Lee, M. Barry, A. Doran, M. P. Cruz, Y. H. Chu, C. Ederer, N. A. Spaldin, R. R. Das, D. M. Kim, S. H. Baek, C. B. Eom, and R. Ramesh. Nat. Mater., **5**, 823 (2006). 172

[584] J. A. Moyer, R. Misra, J. A. Mundy, C. M. Brooks, J. T. Heron, D. A. Muller, D. G. Schlom, and P. Schiffer. APL Mater., **2**, 012106 (2014). 172, 173, 236

[585] X. Z. Lu and H. J. Xiang. Phys. Rev. B, **90** (2014). 172

[586] M. S. Ivanov, N. E. Sherstyuk, E. D. Mishina, A. S. Sigov, V. M. Mukhortov, and V. T. Moshnyaga. Ferroelectrics, **433**, 158 (2012). 172

[587] S. Dussan, A. Kumar, J. F. Scott, S. Priya, and R. S. Katiyar. Appl. Phys. Lett., **97**, 252902 (2010). 172

[588] 25 T in the Split-Florida Helix at the National High Magnetic Field Laboratory refers to the magnetic field strength within the sample volume at the magnet's

mid-plane location. For MCD, which requires magneto-optical Faraday geometry, we have displaced the sample slightly above the mid-plane and thereby achieve field strengths as high as 30 T. 173

[589] D. Xiao, G.-B. Liu, W. Feng, X. Xu, and W. Yao. Phys. Rev. Lett., **108** (2012). 178

[590] M. Dobrowolska, K. Tivakornsasithorn, X. Liu, J. K. Furdyna, M. Berciu, K. M. Yu, and W. Walukiewicz. Nat. Mater., **11**, 444 (2012). 180, 182, 190, 205, 215, 263

[591] W. D. Rice, P. Ambwani, M. Bombeck, J. D. Thompson, G. Haugstad, C. Leighton, and S. A. Crooker. Nat. Mater., **13**, 481 (2014). 180, 215

[592] M. Amft, T. Burkert, B. Sanyal, and P. Oppeneer. Physica B, **404**, 3782 (2009). 182

[593] K. Ohgushi, Y. Okimoto, T. Ogasawara, S. Miyasaka, and Y. Tokura. J. Phys. Soc. Jpn., **77**, 034713 (2008). 182

[594] J. Donecker and J. Kluge. Phys. Status Solidi B, **77**, 243 (1976). 183

[595] M. A. Meeker, B. A. Magill, G. A. Khodaparast, D. Saha, C. J. Stanton, S. McGill, and B. W. Wessels. Phys. Rev. B, **92**, 125203 (2015). 183, 190, 263

[596] S. Manz, M. Matsubara, T. Lottermoser, J. Büchi, A. Iyama, T. Kimura, D. Meier, and M. Fiebig. Nat. Photonics, **10**, 653 (2016). 184

[597] C. L. Kane and E. J. Mele. Phys. Rev. Lett., **95** (2005). 190, 263

[598] G. Aivazian, Z. Gong, A. M. Jones, R.-L. Chu, J. Yan, D. G. Mandrus, C. Zhang, D. Cobden, W. Yao, and X. Xu. Nat. Phys., **11**, 148 (2015). 190, 263

[599] K. H. Kim, K. C. Park, and D. Y. Ma. J. Appl. Phys., **81**, 7764 (1997). 193, 230

[600] X. S. Xu, J. F. Ihlefeld, J. H. Lee, O. K. Ezekoye, E. Vlahos, R. Ramesh, V. Gopalan, X. Q. Pan, D. G. Schlom, and J. L. Musfeldt. Appl. Phys. Lett., **96**, 192901 (2010). 193, 230

[601] S. R. Basu, L. W. Martin, Y. H. Chu, M. Gajek, R. Ramesh, R. C. Rai, X. Xu, and J. L. Musfeldt. Appl. Phys. Lett., **92**, 091905 (2008). 196, 217, 230, 236

[602] M. O. Ramirez, A. Kumar, S. A. Denev, Y. H. Chu, J. Seidel, L. W. Martin, S.-Y. Yang, R. C. Rai, X. S. Xue, J. F. Ihlefeld, N. J. Podraza, E. Saiz, S. Lee, J. Klug, S. W. Cheong, M. J. Bedzyk, O. Auciello, D. G. Schlom, J. Orenstein, R. Ramesh, J. L. Musfeldt, A. P. Litvinchuk, and V. Gopalan. Appl. Phys. Lett., **94**, 161905 (2009). 196

[603] By contrast, $CoFe_2O_4$ displays strong spin-lattice interactions.[314]. 196

[604] The LSD+U and GGA+U methods underestimate the higher gaps considerably compared to our experimental data. Underestimation of gap values is a well-known shortcoming of the method which can be improved, in principle, by using computationally expensive techniques (such as hybrid functionals and/or the

many-body GW method). An alternate possibility is the presence of optically forbidden transitions between valence and conduction bands. 199

[605] T. Inoue. Electrochemical Society of Japan, **23**, 24 (1955). 199

[606] R. J. Powell and W. E. Spicer. Phys. Rev. B, **2**, 2182 (1970). 201

[607] R. Zimmermann, P. Steiner, R. Claessen, F. Reinert, S. Hüfner, P. Blaha, and P. Dufek. J. Phys.: Condens. Matter, **11**, 1657 (1999). 201

[608] R. D. Shannon. Acta Crystallographica Section A, **32**, 751 (1976). 201

[609] M. S. Hybertsen and S. G. Louie. Phys. Rev. Lett., **55**, 1418 (1985). 201

[610] S. H. Wemple. Phys. Rev. B, **2**, 2679 (1970). 201

[611] J. Philip, A. Punnoose, B. I. Kim, K. M. Reddy, S. Layne, J. O. Holmes, B. Satpati, P. R. LeClair, T. S. Santos, and J. S. Moodera. Nat. Mater., **5**, 1613 (2006). 202

[612] K. Uchida, J. Xiao, H. Adachi, J. Ohe, S. Takahashi, J. Ieda, T. Ota, Y. Kajiwara, H. Umezawa, H. Kawai, G. E. W. Bauer, S. Maekawa, and E. Saitoh. Nat. Mater., **9**, 894 (2010). 202

[613] Y. P. Sukhorukov, A. V. Telegin, A. P. Nosov, V. D. Bessonov, and A. A. Buchkevich. JETP Lett., **104**, 384 (2016). 202

[614] S. Matzen, J.-B. Moussy, P. Wei, C. Gatel, J. C. Cezar, M. A. Arrio, P. Sainctavit, and J. S. Moodera. Appl. Phys. Lett., **104**, 182404 (2014). 202

[615] M. Tachiki. Progress of Theoretical Physics, **23**, 1055 (1960). 202

[616] J. A. Moyer, C. A. F. Vaz, D. P. Kumah, D. A. Arena, and V. E. Henrich. Phys. Rev. B, **86**, 174404 (2012). 202, 203

[617] M. D. Sturge, E. M. Gyorgy, R. C. LeCraw, and J. P. Remeika. Phys. Rev., **180**, 413 (1969). 202

[618] D. Hunter, W. Osborn, K. Wang, N. Kazantseva, J. Hattrick-Simpers, R. Suchoski, R. Takahashi, M. L. Young, A. Mehta, L. A. Bendersky, S. E. Lofland, M. Wuttig, and I. Takeuchi. Nat. Commun., **2**, 518 (2011). 202

[619] R. V. Chopdekar and Y. Suzuki. Appl. Phys. Lett., **89**, 182506 (2006). 203

[620] H. Ryu, P. Murugavel, J. H. Lee, S. C. Chae, T. W. Noh, Y. S. Oh, H. J. Kim, K. H. Kim, J. H. Jang, M. Kim, C. Bae, and J.-G. Park. Appl. Phys. Lett., **89**, 102907 (2006). 203

[621] C. Schmitz-Antoniak, D. Schmitz, P. Borisov, F. M. F. de Groot, S. Stienen, A. Warland, B. Krumme, R. Feyerherm, E. Dudzik, W. Kleemann, and H. Wende. Nat. Commun., **4**, 3051 (2013). 203

[622] H. Zheng, J. Wang, S. E. Lofland, Z. Ma, L. Mohaddes-Ardabili, T. Zhao, L. Salamanca-Riba, S. R. Shinde, S. B. Ogale, F. Bai, D. Viehland, Y. Jia, D. G. Schlom, M. Wuttig, A. Roytburd, and R. Ramesh. Science, **303**, 661 (2004). 203

[623] Q. C. Sun, C. S. Birkel, J. Cao, W. Tremel, and J. L. Musfeldt. ACS Nano, **6**, 4876 (2012). 203

[624] C. Song, X. J. Liu, K. W. Geng, F. Zeng, and F. Pan. J. Appl. Phys., **101**, 103903 (2007). 203

[625] A. Pulido, L. Chen, T. Kaczorowski, D. Holden, M. A. Little, S. Y. Chong, B. J. Slater, D. P. McMahon, B. Bonillo, C. J. Stackhouse, A. Stephenson, C. M. Kane, R. Clowes, T. Hasell, A. I. Cooper, and G. M. Day. Nature, **543**, 657 (2017). 203

[626] F. M. Michel, V. Barron, J. Torrent, M. P. Morales, C. J. Serna, J.-F. Boily, Q. Liu, A. Ambrosini, A. C. Cismasu, and G. E. Brown. Proceedings of the National Academy of Sciences, **107**, 2787 (2010). 203

[627] E. M. Wheeler, B. Lake, A. T. M. N. Islam, M. Reehuis, P. Steffens, T. Guidi, and A. H. Hill. Phys. Rev. B, **82**, 140406 (2010). 203

[628] A. Uehara, H. Shinaoka, and Y. Motome. Phys. Rev. B, **92**, 195150 (2015). 203

[629] S. Pal and S. Lal. Phys. Rev. B, **96**, 075139 (2017). 203

[630] Z. Yan, D. A. Keller, K. J. Rietwyk, H.-N. Barad, K. Majhi, A. Ginsburg, A. Y. Anderson, and A. Zaban. Energy Technology, **4**, 809 (2016). 203

[631] Here λ quantifies the fraction of divalent cations occupying octahedral rather than (normal) tetrahedral sites. 203

[632] W. G. Fateley, N. T. McDevitt, and F. F. Bentley. Appl. Spectrosc., **25**, 155 (1971). xvii, 222

[633] Y. H. Hou, Y. J. Zhao, Z. W. Liu, H. Y. Yu, X. C. Zhong, W. Q. Qiu, D. C. Zeng, and L. S. Wen. J. Phys. D: Appl. Phys., **43**, 445003 (2010). xvii, 222

[634] Excursions of λ away from 1(0) are in part due to the different ionic radii of Fe^{3+} (0.79 Å) and Co^{3+} (0.75 Å). This structure can be broken up into octants, alternating between tetrahedron and cubes with the 4 O ions in each octant occupying the same orientations. xvii, 222

[635] V. Kocsis, S. Bordács, J. Deisenhofer, K. Ohgushi, Y. Kaneko, Y. Tokura, and I. Kézsmárki. Submitted (2017). 204

[636] Y. Iwasaki, T. Fukumura, H. Kimura, A. Ohkubo, T. Hasegawa, Y. Hirose, T. Makino, K. Ueno, and M. Kawasaki. Appl. Phys Express, **3**, 103001 (2010). 204

[637] The Onsager relation suggests that a symmetric dielectric tensor will have symmetry to off-diagonal components under time reversal upon reversal of the magnetic field, or magnetization, $\epsilon_{ij}(B) = \epsilon_{ji}(-B)$. Therefore, for each pair of symmetrical $i \neq j$ components they will be proportaional to $\pm$ components of B. Thus, the off-diagonal components correspond to MCD response and should be considered to first order as having a direct dependence upon the magnetization and/or magnetic field. 207

[638] V. Zviagin, P. Richter, T. Böntgen, M. Lorenz, M. Ziese, D. R. T. Zahn, G. Salvan, M. Grundmann, and R. Schmidt-Grund. Phys. Status Solidi B, **253**, 429 (2016). 215

[639] Y. Ishikawa and H. Yao. Chem. Phys. Lett., **609**, 93 (2014). 217

[640] P. K. Bandyopadhyay and G. P. Summers. Phys. Rev. B, **31**, 2422 (1985). 218

[641] Y.-N. Xu, Z.-Q. Gu, and W. Y. Ching. J. Appl. Phys., **87**, 4867 (2000). 219

[642] E. J. Tyrrell and S. Tomić. J. Phys. Chem. C, **119**, 12720 (2015). 220

[643] W. Wang, Z. Gai, M. Chi, J. D. Fowlkes, J. Yi, L. Zhu, X. Cheng, D. J. Keavney, P. C. Snijders, T. Z. Ward, J. Shen, and X. Xu. Phys. Rev. B, **85** (2012). 228, 230

[644] The calculated conduction bands are also more dispersive than those in the spinel ferrites.[314, 116]. 230

[645] First, there is a feature in the DOS around −0.9 eV and from here it is ≈1.5 eV to the conduction band edge plus a rigid shift that is noted by the difference between theory and experiment (0.9 vs 1.1 eV band gap). Second, we see a feature in the DOS around −1.6 eV and from here it is ≈2.1 eV to the conduction band edge, which again via the rigid shift correlates to the smaller intensity feature in the MCD. Finally, we see a sharp rise in the DOS just after the ≈1.6 eV node. This results in a feature in the MCD that is not fully resolved but present none-the-less. If we take a qualitative look at the slopes for these three regions, we see that the first is a fairly strong slope which gives a strong intensity in the MCD response. The second is far less dispersed and thus has a significantly weaker contribution to the response. The final region has a steep

slope and this is represented in the data as a significant increase in response. 235

[646] S. Kasap and P. Capper (editors). *Springer Handbook of Electronic and Photonic Materials*. Springer Handbooks. Springer, Verlag (2007). 235, 257

[647] P. Chen, B. S. Holinsworth, K. R. O'Neal, T. V. Brinzari, D. Mazumdar, Y. Q. Wang, S. McGill, R. J. Cava, B. Lorenz, and J. L. Musfeldt. Phys. Rev. B, **89** (2014). 236

[648] H. J. Xiang and M.-H. Whangbo. Phys. Rev. Lett., **98** (2007). 236

[649] P. Chen, N. J. Podraza, X. S. Xu, A. Melville, E. Vlahos, V. Gopalan, R. Ramesh, D. G. Schlom, and J. L. Musfeldt. Appl. Phys. Lett., **96**, 131907 (2010). 237

[650] S. Kogan. *Electronic Noise and Fluctuations in Solids:*. Cambridge University Press, Cambridge (1996). xix, 241, 384, 389, 393

[651] S. M. Sze and K. K. Ng. *Physics of semiconductor devices*. Wiley-Interscience, Hoboken, N.J, 3rd ed ed. (2007). 242

[652] J. F. Nye. *Physical properties of crystals: their representation by tensors and matrices*. Clarendon Press ; Oxford University Press, Oxford [Oxfordshire] : New York, 1st published in pbk. with corrections, 1984 ed. (1984). 243

[653] V. Mitin, L. Reggiani, and L. Varani. Noise and Fluctuations Control in Electronic Devices, 11–30 (2002). 246

[654] J. W. Goodman. *Introduction to Fourier Optics*. series in electrical and computer engineering. McGraw Hill, New York, NY, 2 ed. (1996). 247

[655] E. Hecht. *Optics*. Pearson education. Addison-Wesley, San Francisco, 4. ed., intern. ed., [nachdr.] ed. (2010). OCLC: 846202400. 247

[656] A. G. Marshall and F. R. Verdun. *Fourier transforms in NMR, optical, and mass spectrometry: a user's handbook*. Elsevier, Amsterdam (1990). OCLC: 246688092. 247

[657] S. R. Seshadri. *Complex space source theory of spatially localized electromagnetic waves*. Mario Boella series on electromagnetism in information & communication. SciTech Publishing, an imprint of the IET, Edison, NJ (2014). 247

[658] J.-M. Mariotti. In D. M. Alloin and J.-M. Mariotti (editors), *Diffraction-Limited Imaging with Very Large Telescopes*, 3–32. Springer Netherlands, Dordrecht (1989). 247

[659] C. Shekhar, C. E. ViolBarbosa, B. Yan, S. Ouardi, W. Schnelle, G. H. Fecher, and C. Felser. Phys. Rev. B, **90** (2014). 249

[660] P. Mele, T. Endo, S. Arisawa, C. Li, and T. Tsuchiya (editors). *Oxide Thin Films, Multilayers, and Nanocomposites*. Springer International Publishing, Cham (2015). 251

[661] K. A. Borup, J. de Boor, H. Wang, F. Drymiotis, F. Gascoin, X. Shi, L. Chen, M. I. Fedorov, E. Müller, B. B. Iversen, and G. J. Snyder. Energy Environ. Sci., **8**, 423 (2015). 251

[662] L. Xie and X. Cui. Proceedings of the National Academy of Sciences, **113**, 3746 (2016). 257

[663] S. D. Ganichev, V. V. Bel'kov, S. A. Tarasenko, S. N. Danilov, S. Giglberger, C. Hoffmann, E. L. Ivchenko, D. Weiss, W. Wegscheider, C. Gerl, D. Schuh, J. Stahl, J. De Boeck, G. Borghs, and W. Prettl. Nat. Phys., **2**, 609 (2006). 257

[664] Q. Wu, Y. Liu, H. Wang, Y. Li, W. Huang, J. Zhao, and Y. Chen. Sci. Rep., **7**, 40558 (2017). 257

[665] V. Malinovsky, V. Novikov, and B. Sturman. Phys. Lett. A, **112**, 237 (1985). 258, 261

[666] S. B. Syamala and C. Sudha Kartha. *Photoconductivity studies on some semiconducting thin films for photovoltaic applications*. Ph.D. thesis, Cochin University of Science & Technology (2004). 258

[667] R. H. Bube. *Photoelectronic properties of semiconductors*. Cambridge University Press, Cambridge ; New York (1992). 258, 261

[668] N. A. Davidenko, I. I. Davidenko, N. A. Derevyanko, A. A. Ishchenko, L. I. Kostenko, E. V. Mokrinskaya, S. L. Studzinskii, L. S. Tonkopieva, and N. G. Chuprina. High Energy Chem., **45**, 240 (2011). 258

[669] A. Serpi. Phys. Status Solidi A, **133** (1992). 258

[670] C. H. Lui, A. J. Frenzel, D. V. Pilon, Y.-H. Lee, X. Ling, G. M. Akselrod, J. Kong, and N. Gedik. Phys. Rev. Lett., **113** (2014). 258, 261

[671] A. F. Th. Hoekstra, T. F. Rosenbaum, and A. S. Roy. Rev. Sci. Instrum., **73**, 119 (2002). 261

[672] P. Savić and V. Urošević. Chem. Phys. Lett., **135**, 393 (1987). 261

[673] F. Capasso, K. Mohammed, and A. Y. Cho. Physica B+C, **134**, 487 (1985). 261

[674] F. Capasso, K. Mohammed, and A. Cho. Surf. Sci., **174**, 501 (1986). 261

[675] R. A. Street, K. W. Song, J. E. Northrup, and S. Cowan. Phys. Rev. B, **83** (2011). 261

[676] C. Longeaud, J. A. Schmidt, and R. R. Koropecki. Phys. Rev. B, **73** (2006). 261

[677] W. S. Choi, S. J. Moon, S. S. A. Seo, D. Lee, J. H. Lee, P. Murugavel, T. W. Noh, and Y. S. Lee. Phys. Rev. B, **78**, 054440 (2008). 264

[678] W. Schokley, J. Bardeen, and W. H. Brattain. Science, **108**, 678 (1948). 344

[679] W. Brattain and C. Garrett. Physica, **20**, 885 (1954). 344

[680] W. H. Brattain. Science, **126**, 151 (1957). 344

[681] J. Bardeen. Nobel Lecture (1956). 344

[682] W. Schokley. Nobel Lecture (1956). 344

[683] G. E. Moore. Electronics, **38**, 114 (1965). 344

[684] R. C. Jaeger (editor). *Introduction to Microelectronic Fabrication*, vol. 5 of *Solid State Devices*. Pearson, 2 ed. (2001). 344

[685] S. Datta and B. Das. Appl. Phys. Lett., **56**, 665 (1990). 345

[686] I. Žutić, J. Fabian, and S. Das Sarma. Phys. Rev. B, **64** (2001). 345

[687] F. Meier and B. P. Zakharchenya (editors). *Optical Orientation*, vol. 8 of *Modern Problems in Condensed Matter Sciences*. North-Holland, New York (1984). 345, 371

[688] I. Žutić, J. Fabian, and S. Das Sarma. Appl. Phys. Lett., **79**, 1558 (2001). 345, 348

[689] B. Wolf, Y. Tsui, D. Jaiswal-Nagar, U. Tutsch, A. Honecker, K. Remović-Langer, G. Hofmann, A. Prokofiev, W. Assmus, G. Donath, and others. Proceedings of the National Academy of Sciences, **108**, 6862 (2011). 349

[690] J. Bardeen. Phys. Rev. Lett., **6**, 57 (1961). 349

[691] J. G. Simmons. J. Appl. Phys., **34**, 1793 (1963). xviii, 350, 353

[692] P. M. Tedrow, R. Meservey, and B. B. Schwartz. Phys. Rev. Lett., **24**, 1004 (1970). 350

[693] I. I. Mazin. Phys. Rev. Lett., **83**, 1427 (1999). 351

[694] M. Julliere. Phys. Lett. A, **54**, 225 (1975). 351

[695] S. Duhot and R. Mélin. Phys. Rev. B, **76** (2007). xviii, 352

[696] J.-G. J. Zhu and C. Park. Mater. Today, **9**, 36 (2006). xviii, 353

[697] H. Swagten. In *Handbook of Magnetic Materials*, vol. 17, 1–121. Elsevier (2007). xviii, 353

[698] J. S. Moodera, T. S. Santos, and T. Nagahama. J. Phys.: Condens. Matter, **19**, 165202 (2007). xviii, 352, 356

[699] A. Saffarzadeh. J. Magn. Magn. Mater., **269**, 327 (2004). 355

[700] R. H. Fowler and L. Nordheim. Proceedings of the Royal Society A: Mathematical, Physical and Engineering Sciences, **119**, 173 (1928). 355

[701] E. Y. Tsymbal, O. N. Mryasov, and P. R. LeClair. J. Phys.: Condens. Matter, **15**, R109 (2003). xviii, 356

[702] P. LeClair, J. Moodera, and H. Swagten. In J. A. C. Bland and B. Heinrich (editors), *Ultrathin Magnetic Structures III*, 51–97. Springer-Verlag, Berlin/Heidelberg (2005). xviii, 356

[703] B. Prasad and M. G. Blamire. Appl. Phys. Lett., **109**, 132407 (2016). xviii, 356

[704] Q. Yang, P. Holody, S.-F. Lee, L. L. Henry, R. Loloee, P. A. Schroeder, W. P. Pratt, and J. Bass. Phys. Rev. Lett., **72**, 3274 (1994). 359

[705] M. Johnson and R. H. Silsbee. Phys. Rev. Lett., **60**, 377 (1988). 359

[706] S. A. Chambers. Mater. Today, **5**, 34 (2002). 359

[707] S. Das Sarma, J. Fabian, X. Hu, and I. Žutić. Superlattices Microstruct., **27**, 289 (2000). 359

[708] E. I. Rashba. Phys. Rev. B, **62**, R16267 (2000). 359

[709] V. M. Karpan. *Towards perfect spin-filtering: a first-principles study*. University of Twente (2008). 359

[710] A. T. Hanbicki, B. T. Jonker, G. Itskos, G. Kioseoglou, and A. Petrou. Appl. Phys. Lett., **80**, 1240 (2002). 359

[711] B. T. Jonker, G. Kioseoglou, A. T. Hanbicki, C. H. Li, and P. E. Thompson. Nat. Phys., **3**, 542 (2007). 359

[712] I. Appelbaum. Philosophical Transactions of the Royal Society A: Mathematical, Physical and Engineering Sciences, **369**, 3554 (2011). 359

[713] A. A. Sukhanov and V. A. Sablikov. Semiconductors, **47**, 1456 (2013). 359

[714] K.-R. Jeon, H. Saito, S. Yuasa, and R. Jansen. Phys. Rev. B, **91** (2015). 359

[715] V. Edelstein. Solid State Commun., **73**, 233 (1990). 360

[716] J.-i. Inoue, G. E. W. Bauer, and L. W. Molenkamp. Phys. Rev. B, **67**, 033104 (2003). 360

[717] Y. K. Kato, R. C. Myers, A. C. Gossard, and D. D. Awschalom. Phys. Rev. Lett., **93** (2004). 360

[718] S. D. Ganichev, M. Trushin, and J. Schliemann. arXiv preprint arXiv:1606.02043 (2016). 360

[719] I. Zutic and E. Y. Tsymbal (editors). *Handbook of spin transport and magnetism*. Chapman and Hall/CRC (2011). 360, 361

[720] C. J. Ballhausen. *Molecular Electronic Structures of Transition Metal Complexes*. McGraw-Hill, New York (1979). 366

[721] T. Carroll. Phys. Rev., **52**, 822 (1937). 366

[722] H. Eyring, J. Walter, and G. E. Kimball. *Quantum Chemistry*. John Wiley And Sons Inc. (1944). 366

[723] G. C. Schatz and M. A. Ratner. *Quantum Mechanics in Chemistry*. Dover Publications, New York (2002). 366

[724] I. N. Levine. *Quantum Chemistry*. Pearson, New York, NY, 6 ed. (2014). 366

[725] J. S. Kolb. *MCD-Spektroskopie eines LD-LISC-Komplexes*. Ph.D. thesis, Universitätsbibliothek (2007). 370

[726] R. G. Graham. Chem. Phys. Lett., **133**, 193 (1987). 371

[727] P. T. Fonseca, A. R. B. d. Castro, G. Tosin, J. F. Citadini, and R. Basílio. Braz. J. Phys., **37** (2007). 371

[728] J.-M. Tang and M. E. Flatté. Phys. Rev. Lett., **101** (2008). 371

[729] E. I. Solomon, E. G. Pavel, K. E. Loeb, and C. Campochiaro. Coord. Chem. Rev., **144**, 369 (1995). 372

[730] F. Neese and E. I. Solomon. Inorg. Chem., **38**, 1847 (1999). 372

[731] J. Mack, Y. Morita, S. Higashibayashi, H. Sakurai, and N. Kobayashi. Chem. Phys. Lett., **556**, 188 (2013). 376

[732] R. S. Knox. Photochem. Photobiol., **77**, 492 (2003). 378

[733] R. S. Knox and B. Q. Spring. Photochem. Photobiol., **77**, 497 (2003). 378

[734] G. A. Osborne. J. Chem. Phys., **56**, 609 (1972). 379

[735] W. Mac, A. Twardowski, and M. Demianiuk. Phys. Rev. B, **54**, 5528 (1996). 379

[736] G. A. Prinz. Science, **282**, 1660 (1998). 379

[737] K. Ando. Science, **312**, 1883 (2006). xix, 379, 381

[738] N. Kobayashi and A. Muranaka. *Circular Dichroism and Magnetic Circular Dichroism Spectroscopy for Organic Chemists*. The Royal Society of Chemistry (2012). 379

[739] B. J. Hales. In M. W. Ribbe (editor), *Nitrogen Fixation*, vol. 766, 207–219. Humana Press, Totowa, NJ (2011). 379

[740] J. Szczytko, W. Mac, A. Stachow, A. Twardowski, P. Becla, and J. Tworzydklo. Solid State Commun., **99**, 927 (1996). 379

[741] J. Szczytko, W. Bardyszewski, and A. Twardowski. Phys. Rev. B, **64** (2001). 379

[742] M. Arciszewska and M. Nawrocki. J. Phys. Chem. Solids, **47**, 309 (1986). 379

[743] S.-H. Wei and A. Zunger. Phys. Rev. B, **35**, 2340 (1987). xix, 382

[744] K. Ando, K. Takahashi, T. Okuda, and M. Umehara. Phys. Rev. B, **46**, 12289 (1992). xix, 382

[745] C. Beenakker and C. Schönenberger. Phys. Today, **56**, 37 (2003). 383

[746] J. Müller. ChemPhysChem, **12**, 1222 (2011). xix, 383, 393, 397

[747] M. Zhu. *Electrical Transport Studies of Molecular Beam Epitaxy Grown Gallium Manganese Arsenide Epilayers and Heterostructures*. ProQuest (2008). xix, 383, 385, 397

[748] E. Nelson, E. Nelson, E. Nelson, and E. Nelson. *Dynamical theories of Brownian motion*, vol. 2. Princeton university press Princeton (1967). 384

[749] J. Dunkel. *Relativistic Brownian motion and diffusion processes*. Ph.D. thesis, Ph. D. Thesis, Universität Augsburg (2008). 384

[750] G. E. Uhlenbeck and L. S. Orenstein. Phys. Rev., **36**, 823 (1930). 384

[751] R. Mauri. *Non-Equilibrium Thermodynamics in Multiphase Flows*. Soft and Biological Matter. Springer Netherlands, Dordrecht (2013). 384

[752] P. D. W. Brenig. In *Statistical Theory of Heat*, 69–72. Springer Berlin Heidelberg (1989). DOI: 10.1007/978-3-642-74685-7_14. 384

[753] M. von Smoluchowski. Ann. Phys., **326**, 756 (1906). 384

[754] W. Sutherland. Philosophical Magazine Series 6, **9**, 781 (1905). 384

[755] J. B. Perrin and F. Soddy. *Brownian Movement and Molecular Reality*. Taylor & Francis, London (1910). 384

[756] H. D. Xiong. *Low frequency noise and charge trapping in MOSFETs*. Ph.D. thesis, Vanderbilt University (2004). 385

[757] B. Raquet. In M. Ziese and M. J. Thornton (editors), *Spin Electronics*, vol. 569, 232–273. Springer Berlin Heidelberg, Berlin, Heidelberg (2001). 385

[758] Y. Li. Optimization of Hall Magnetometry and Single Magnetic Nanoparticle Measurements (2003). xix, 385, 393

[759] M. Zhu, X. Li, G. Xiang, and N. Samarth. Phys. Rev. B, **76**, 201201 (2007). 385

[760] J. B. Johnson. Nature, **119**, 50 (1927). 389

[761] J. B. Johnson. Phys. Rev., **32**, 97 (1928). 389

[762] H. Nyquist. Phys. Rev., **32**, 110 (1928). 389

[763] W. Schottky. Ann. Phys., **362**, 541 (1918). 390

[764] F. Hooge. Phys. Lett. A, **29**, 139 (1969). 391

[765] J. Bernamont. Proceedings of the Physical Society, **49**, 138 (1937). 394

[766] A. Van Der Ziel. Physica, **16**, 359 (1950). 394

Appendices

Appendix A

Spintronics

A.1 History

First a brief history, electronic technology has evolved tremendously since the introduction of the first realistically practical transistor, in 1947.[678, 679, 680, 681, 682] This ushered in the silicon technology, or microelectronics, era. Ever since then conventional microelectronics have been improved to obtain better performance, faster speeds, greater energy efficiency, progressively smaller architectures, and ultimately cheaper fabrication. This has followed the prediction by Moore's Law;[683] however, this law can not continue to be followed indefinitely. As the size of the transistor continues decreasing, severe problems emerge; thermal noise, leakage current, dielectric breakdown, and *etc.*[684] The final limit of this function ends when the dimension of an atom is the size of a single transistor.[129]

A.2 Devices

Spintronics being strongly driven towards improving the functionality of devices, suggests the necessity to conceive device architectures. The original schematic for a spintronic derived device instituted the conventional microelectronic architecture for a transistor, as shown in Fig. A.2.1 (a).[685] One electrode represents the emitter (E_e), whereas the other is the collector (E_c) (operating with the same principles as the source and drain in a traditional field effect transistor.) Functionally, the E_e sends electrons towards E_c that initially have a spin orientation that is parallel to E_e. E_c, having the same direction of magnetization as E_e, acts as a spin filter; E_c accepts electrons having the same spin only. Assuming no scattering of the spins all emitted electrons pass through and enter E_c, as seen in Fig. A.2.1 (b). In the scenario when the gate electrode E_g acts upon the system Fig. A.2.1 (c). The electron spins are forced to precess, akin to how a spinning top responds under the force of gravity. This modulates the electron current and changes the current flowing through the external circuit by the degree of precession.[685, 129]

A spintronic photovoltaic device is shown in Fig. A.2.2 (a).[686] This invokes the application of a spin-polarized p-n junction. As with traditional photovoltaic cells, a source of light shining on the depletion layer generates excitons. With internal electric field (on the order of 10^4 $\mathrm{V\,cm^{-1}}$), the electrons are promptly swept to the n-type regime of the semiconductor. When a circuit is connected to the junction edges, a current flows. Moreover, if the light is circularly polarized, then the current is spin polarized. This presents one mechanism for converting photons into oriented spins and advantageously even a spin current.[130, 687, 688]

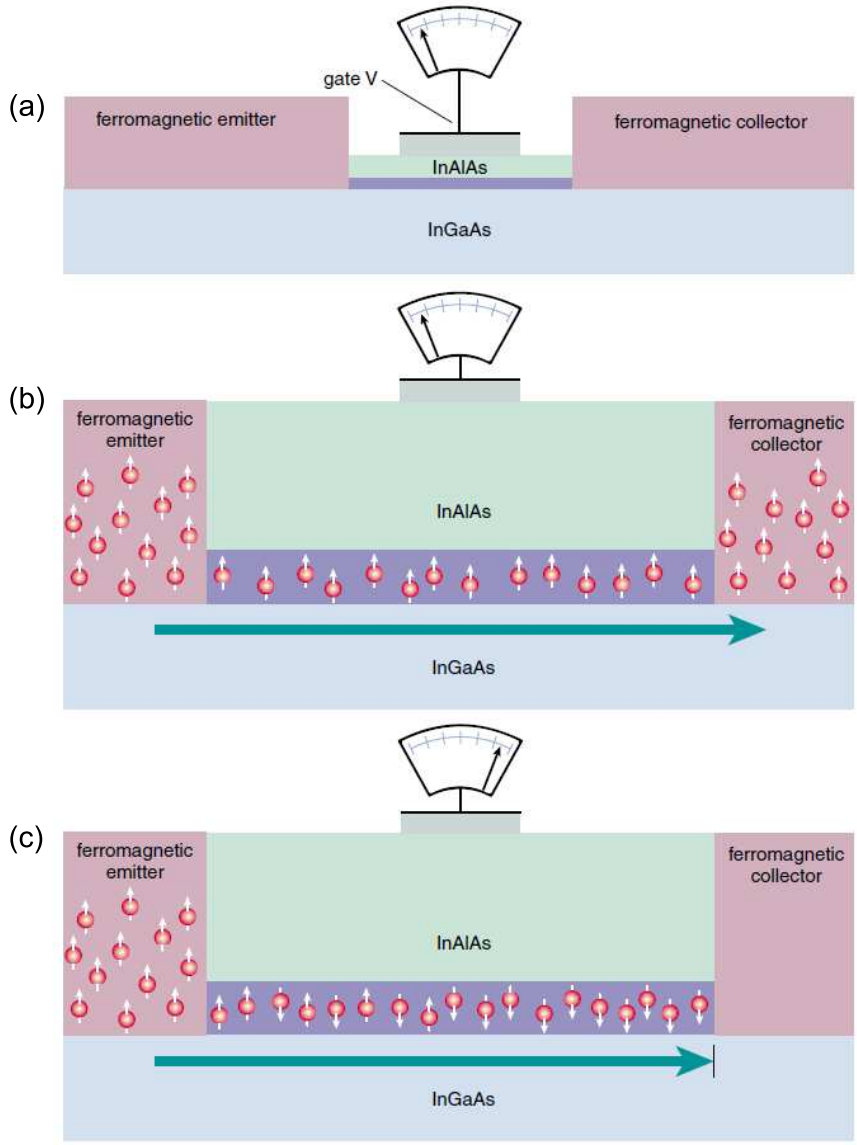

Figure A.2.1: Datta and Das proposed a spin-transistor design that is based upon the conventional microelectronic architecture. (after Ref. [129])

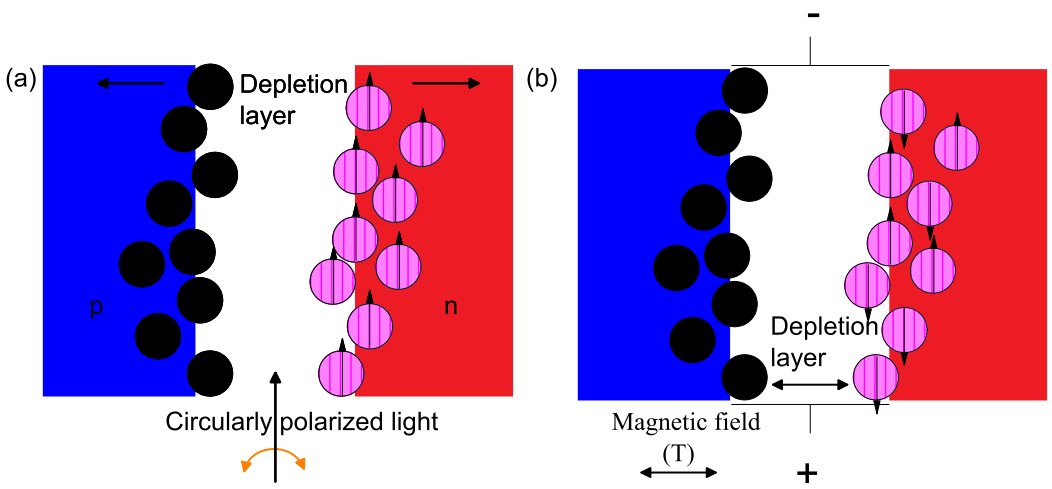

Figure A.2.2: (a) Displays a spintronic solar cell, the circular polarized light creates spin-polarized electron-hole pairs (excitons) in the depletion zone. The electric field will sweep the holes to the p-type region, where as the electrons will be swept to the n-type region. (b) In traditional semiconductors dopants (impurity atoms) produce the p- or n-type materials. However, if these impurities are magnetic then the width of the depletion layer is alter by the strength of the magnetic field. Resulting in a change in the amount of current flowing in the external current.

For a final device example, a continued look at the p-n junction based environment is implemented to explore a spintronic based magnetic field effect transistor, as shown Fig. A.2.2 (b). Here, the width of the depletion layer is modified by the strength of the applied magnetic field, perpendicular to the electric field direction. The limits are if the depletion layer is wider than the electrodes (no current flows) and if the depletion layer becomes finitely thin then the current reaches its maximum. A spin-polarized current would result from this environment.[129, 688]

A.2.1 Spin-polarized current production

Insulating magnetic materials show promise for the production of spin-polarized currents.[127, 134, 302, 280] One great benefit to using insulating materials for spin-polarized current production is the limited eddy currents. The architecture that directly allows for implementation of the spin-filtering effect integrates a very thin insulating barrier between the electrodes. The barriers magnetic properties spin split the lowest energy, above the Fermi energy, conduction band. This occurs naturally in the case of $NiFe_2O_4$. The spin-splitting of the conduction band produces a spin-dependent tunneling barrier height $\Phi_{\uparrow\downarrow}$. This shows up on the probability of transmission for an electron current passing through the barrier. Importantly, the architecture defined derives its spin selectivity from the magnetic properties of just one layer. Whereas in the traditional ferromagnet/insulator/ferromagnet tunnel junctions the spin selectivity depends upon the available states of the second electrode. A simple mathematical description of the transmission probability for a non-magnetic tunnel barrier is as follows

$$T(E) \propto \exp\left(-\frac{2d}{\hbar}\sqrt{\frac{2m}{\hbar^2}(\Phi - E_{kin})}\right). \tag{A.2.1}$$

Here, d is the thickness, m is the effective mass of the tunneling particle (electron), E_{kin} is its kinetic energy, and Φ represents the barrier height. The barrier height is also the offset from the lowest conduction band and the Fermi energy. This expression reveals a critical component that controls the electron transmission, the probability for tunneling has an exponential dependence on the barrier thickness and a square root dependence on the potential barrier height. This conditional nature will play a central role in spin filtering, as discussed later in this subsection.

To more completely mathematically express the tunneling current one must consider the Fermi golden rule and there by regard the density of states (DOS) of the two magnetic electrodes, $N_{1,2}(E)$, the probability of transmission through the barrier, square of a matrix element $|M|^2$, and the probability of states being occupied in the first electrode and the second electrode being empty, corresponding to the Fermi-Dirac distribution $f(E)$ [689, 690] This results in a tunneling current from electrode 1 to electrode 2 under an applied bias voltage eV being expressed by:

$$I_{1,2}(V) = \int_{-\infty}^{+\infty} N_1(E) \cdot N_2(E + eV)|M|^2 f(E)[1 - f(E + eV)]dE \tag{A.2.2}$$

With the assumption that the tunneling current is comprised mostly of electrons near the Fermi energy (E_F), $f(E) \propto eV\delta(E - E_F)$, transmission matrix element $|M|^2$ is independent of E.[690] Subsequent to the integration, it is found that the

total current, $I = I_{1\to2} - I_{2\to1}$, is given by:

$$\frac{I}{V} \propto |M|^2 N_1(E_F) N_2(E_F) \tag{A.2.3}$$

To generalize the formalism (dissimilar electrodes), Simmons approximated an average barrier height, $\bar{\phi}$, and through the Wentzel-Kramers-Brillouin (WKB) approximation derived appropriate matrix elements $|M|^2$.[691] This led to the following expression for the tunneling current density (J):

$$J(V) = \frac{J_0}{d^2}(\bar{\phi} - \frac{eV}{2}) \exp\left[-Ad\sqrt{\bar{\phi} - \frac{eV}{2}}\right] - \frac{J_0}{d^2}(\bar{\phi} + \frac{eV}{2}) \exp\left[-Ad\sqrt{\bar{\phi} + \frac{eV}{2}}\right] \tag{A.2.4}$$

This allows one to show that in the tunneling regime, $eV \leq \bar{\psi}$, Eq. A.2.4 behaves as

$$J \sim \alpha V + \beta V^3. \tag{A.2.5}$$

This explains the parabolic shape commonly seen in conductance curves ($G = dI/dV$) experimentally. After these early efforts into understanding spin-polarized tunneling from a theoretical perspective, the first experimental evidence was presented by Meservey and Tedrow in 1970.[306, 692] This and this subsequent findings lead to many questions, e.g. how to define the polarization of the tunneling spin? The theoretical expectation for the value of the polarization P in a series of FM $3d$ transition metals investigations was negative but the experimentally realized value

was positive. From this a more precise mathematical definition of P arose for tunneling currents:

$$P = \frac{N_{\uparrow}(E_F)|M_{\uparrow}|^2 - N_{\downarrow}(E_F)|M\downarrow|^2}{N_{\uparrow}(E_F)|M_{\uparrow}|^2 + N_{\downarrow}(E_F)|M\downarrow|^2} \tag{A.2.6}$$

Mazin defined this equation very nicely, the square of the Fermi velocity, v^2, becomes the most important element to consider in $|M_{\uparrow,\downarrow}|^2$.[693] This result occurs because the electrons with an effective mass, m_e^*, closest to mass of a free electron will have the highest mobility i.e. highest v^2 will be the strongest components in the tunneling current. With that cleared up we can now look into the tunneling magnetoresistance, from this topic the highlight is the Julliére model.[694] His model centers on conservation of spin (i.e. spins do not flip), or conservation of angular momentum (Gauge symmetry), with the major implication being: tunneling can only occur between bands of the same spin orientation, as projected in the flow of Figs. A.2.3 and A.2.4. In the magnetic tunnel junction environment where the spin angular momentum is conserved, the conductance G is governed by the whether the magnetization (M_1&M_2) are parallel or antiparallel, as seen in Fig. A.2.4 (c). Moreover, if they are not purely parallel or antiparallel, then the conductance develops a proportionality $\cos\theta$ based upon the angle θ:

$$G(\theta) = \frac{1}{2}(G_P + G_{AP}) + \frac{1}{2}(G_P - G_{AP})\cos\theta. \tag{A.2.7}$$

The generation of a highly spin-polarized current of electrons has become a primary level focus in the field of spintronics. The applications need a maximum of

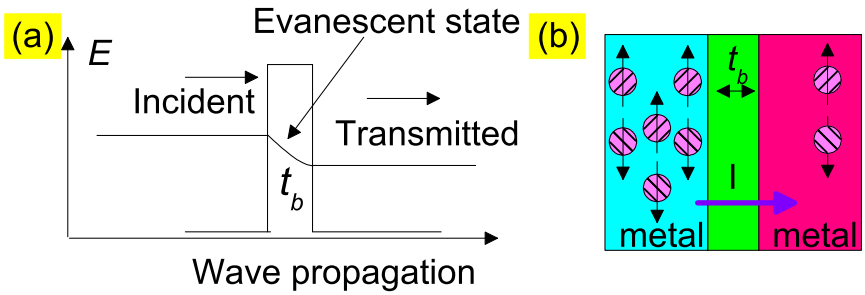

Figure A.2.3: (a) Wave nature of tunneling electrons, the wave is approaching from the left of the barrier t_b. The potential energy height of the barrier is higher than the energy E of the electron. Upon entering the barrier the oscillation becomes a evanescent wave quasi-particle,[695] with intensity falling off exponentially as expressed in Eq. A.2.1. If some amplitude still exists at the opposite of the barrier then a propagating wave reemerges and continues along its path. (b) Displays a tunneling current that corresponds to the particles with spin angular momentum. The probability of transmission is also governed by the amplitude ratio of the incident and transmitted waves.

spin-polarized current to acquire their highest efficiencies. Therefore, spin filtering stands out as a promising phenomenon in the field of spintronics both fundamentally and technologically, for the scenarios that require spin selectivity in the electrons transported across a magnetic tunnel barrier.

A.2.1.1 Phenomenological Origin

Spin filtering arises from exchange splitting of the energy levels showing up in the conduction band(s) of a magnetic insulator. Therefore, the tunneling barrier heights for spin-up and spin-down electrons, $\Phi_{\uparrow(\downarrow)}$, are not equal but result in a higher probability for a single form of the spin orientations.[568, 283, 698] The difference between $\Phi_{\uparrow}$ and $\Phi_{\downarrow}$ magnitudes is $2\Delta E_{ex}$, here ΔE_{ex} represents the exchange splitting for

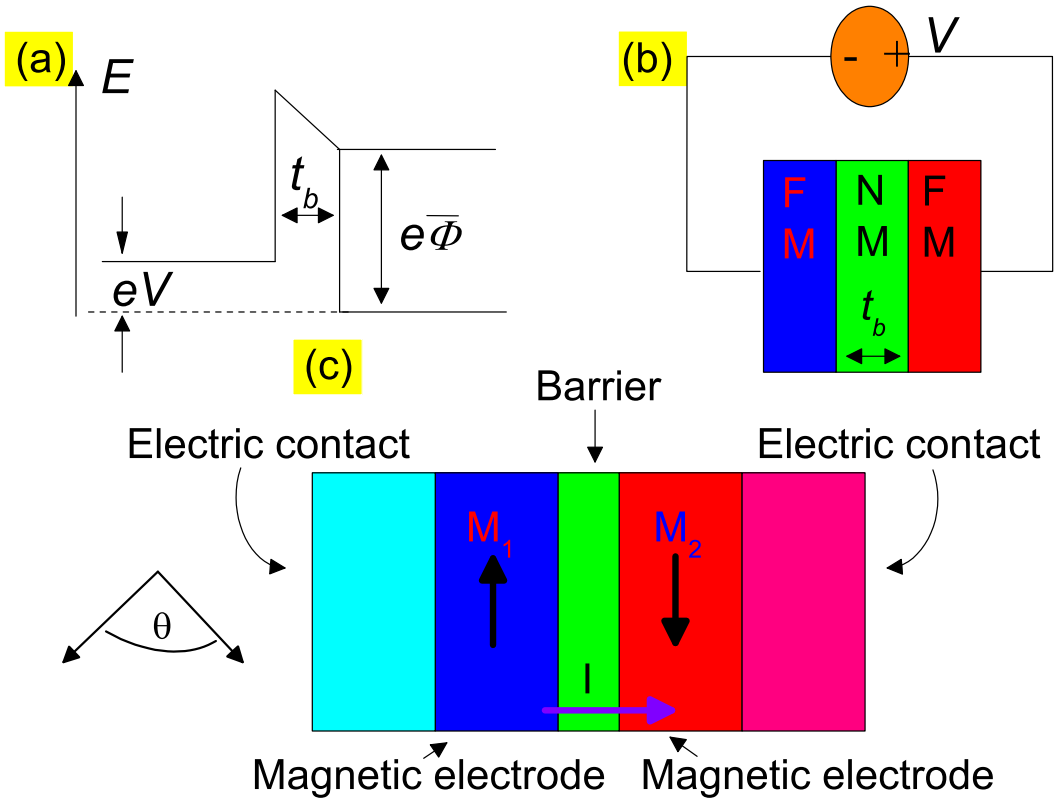

Figure A.2.4: (a) Schematic of the bias driving a tunnel junction. (b) A view of Simmon's I-V relation.[691] (c) A schematic displaying that the magnetization of magnetic electrode 1 M_1 and magnetic electrode 2 M_2 in a magnetic tunnel junction. The magnetization for both electrodes are in plane and the conductance is proportional to the angle θ between them, as shown by Eq. A.2.7.[696, 697]

the first level of the conduction bands. The value of $2\Delta E_{ex}$ is symmetric about the average barrier height $\bar{\Phi}$ The Φ-dependence is exponential, this meaning that even a small ΔE_{ex} can potentially produce high efficiency in spin filtering of the tunneling current density:

$$J_{\uparrow(\downarrow)} \propto exp(-\Phi_{\uparrow(\downarrow)}^{1/2} d). \tag{A.2.8}$$

An alternative understanding can be projected from the following:

$$\Phi_{\uparrow(\downarrow)} = \Phi_0 \pm \Delta E_{ex}. \tag{A.2.9}$$

The definition of the spin-filtering efficiency (polarization) of the tunnel barrier, P_{SF}, appears as:

$$P_{SF} = \frac{J_\uparrow - J_\downarrow}{J_\uparrow + J_\downarrow}. \tag{A.2.10}$$

Spin filtering marks its efficiency dependence on only a few parameters, $\bar{\Phi}$, ΔE_{ex}, and d, as described previously. Spin-polarized tunneling has strong dependence on the density of states at the Fermi level to determine P. This to say that when a non-magnetic electrode is combined with a magnetic insulator (semiconductor) as a spin filter barrier this architecture has the potential to produce current with $P \rightarrow 100\%$,[569] as shown in Fig. A.2.5. It is important to re-iterate that the difference between MTJ and spin filtering is where the magnetic component(s) are in the system. Intriguingly, the TMR of a spin-filtered current increases with increasing bias voltage up to a certain value, then upon continued increasing of bias voltage

the value decreases. This is exactly opposite of the MTJ result. This effect has been accepted as the signature of spin filtering in MTJs with a magnetic barrier.[699] Phenomonologically, the increasing TMR(V) in spin filter tunnel junctions can be explained by the spin-split nature of the conduction band in the spin filter, this overshadows the impact of magnon excitations for an extended operative range of applied V. This suggests that the spin-oriented electrons having a lower Φ acquire enough energy to tunnel across to their corresponding conduction band, because of their encroachement to the Fermi energy. This is commonly referred to as Fowler-Nordheim (F-N) tunneling.[700] Upon subsequently increasing the bias voltage the tunneling probability of the opposite spin-oriented electrons increase, increasing TMR(V). After the maximum is reached the value begins to decrease, eventually the magnon excitations start to assist the process.

Shortcoming of spin-polarized current production

As of thus far, we have discussed the amazing implications of spin transport with the purpose of separating the spin components and producing a spin-polarized current. However, the production of such current is not exactly trivial. When considering the transport of a spin population across an interface between a magnetic and a non-magnetic material, we must first see that the current density $\vec{J}$, to be discussed in further detail later (Sec. 3.2), becomes:

$$\vec{j}_M = -\sigma(\frac{p_n \mu_B}{e})\nabla V = 0, \tag{A.2.11}$$

$$\vec{j}_M = -(\frac{\sigma \mu_B^2}{e^2})\nabla(-H^*). \tag{A.2.12}$$

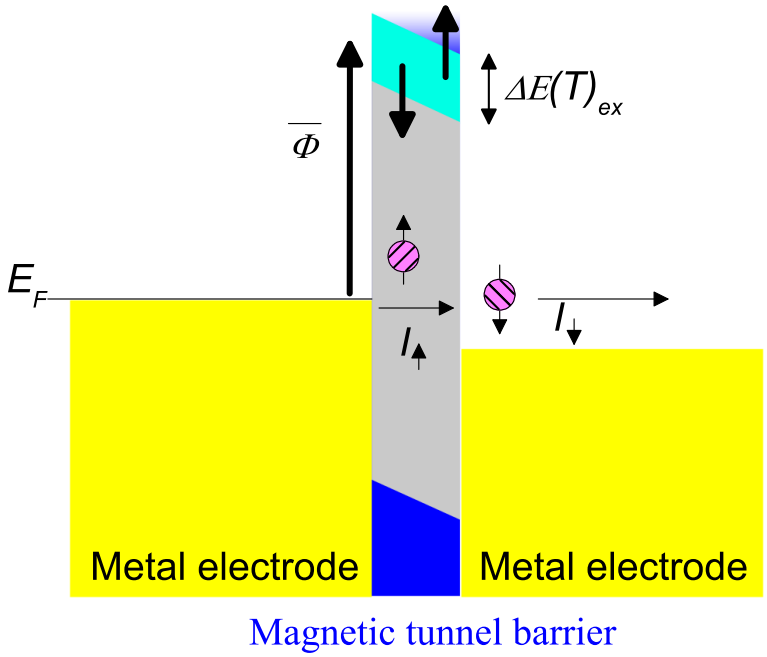

Figure A.2.5: When a material that has a non-zero magnetic moment is cooled below its T_C the barrier height for tunneling quasiparticles (electrons) depends upon the relative spin orientation. In the schematic shown here, the spin down electrons will tunnel with a more significant current than the spin up electrons. Therefore, a spin-polarized current will be produced.[306, 698, 283, 701, 702, 703]

In Eq. A.2.11, $\vec{j}_M$ is the magnetization current (or spin-polarized current) σ is the conductivity, p_n is the intrinsic spin polarization ($p_n = 0$ in non-magnetic materials), μ_B is the Bohr magneton, and ∇V is the voltage gradient across the circuit element. So, it is evident that the natural spin-polarized current density from a non-magnetic material will be 0. In Eq. A.2.12, $\nabla(-H^*)$ produces a dependency upon the gradient of the effective magnetic field resulting from the non-equilibrium spin accumulation in a non-magnetic material. The spin polarized electron current is driven by self-diffusion.[86] Now that we have the essentials for building an interface where a spin-polarized current flows between a non-magnetic and magnetic material, we will see what can hamper this. Some visualization of the changes as approaching the interface can be seen in Fig. A.2.6.

As per the normal form, I will keep with as much brevity as possible during this derivation to avoid the extremes of obscurity and prolixity.

The polarization of the spin-polarized current in the magnetic portion that reaches and crosses the interface is reduced with respect to the bulk, $\vec{J}_M < \vec{J}_{M,f}$. A generalized formula for the interfacial spin-polarized current is as the following:

$$\vec{J}_M = \frac{\eta\mu_B}{e}\vec{J}_q \left[\frac{\frac{1+G(\frac{p_f}{\eta})r_f(1-\eta^2)}{(1-p_f^2)}}{1+G(1-\eta^2)[\frac{r_n+r_f}{(1-p_f^2)}]} \right], \tag{A.2.13}$$

where $r_f = \delta_{s,f}/\sigma_f$ $r_n = \delta_{s,n}/\sigma_n$, $G = 1/R_i$. An important note, spin transport is governed by the relative values of intrinsic interface resistance, $R_i = 1/G$, resistance of the non-magnetic material equal to a spin depth r_n, and resistance of the magnetic material equal to a spin depth r_f.

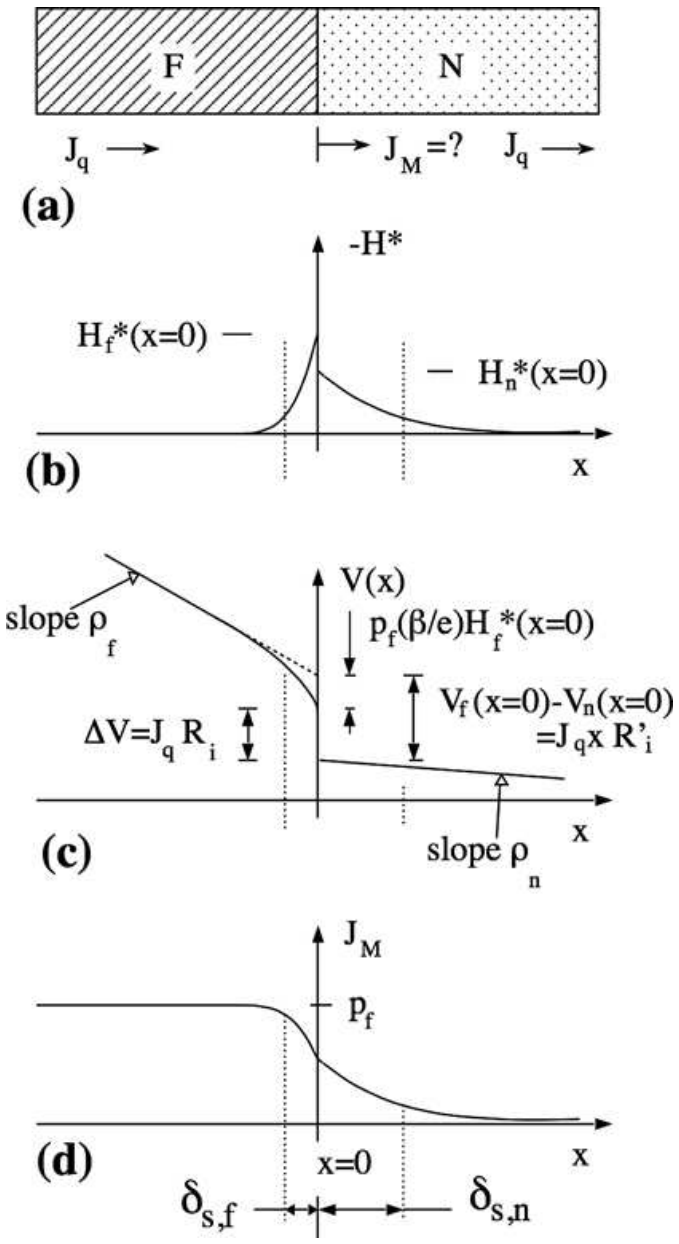

Figure A.2.6: (a) Shows a model interface for flowing charge and spin currents, $\vec{J}_q$ and $\vec{J}_M$, with $x = 0$ being at the interface. (b) Displays the magnetization potential with respect to x. The nonequilibrium spin population in F and N decays at the characteristic lengths of $\delta_{s,f}$ and $\delta_{s,n}$, respectively. (c) Shows how the position in the system effects the voltage. (d) Shows how the spin-polarized current $\vec{J}_M$ varies as approaching and moving away from the interface, after [86].

Now to consider the limiting cases for the interface spin-polarized current, first when the interfacial resistance is low, $R_i \to 0$. An example of such a case is a multilayer, current-perpendicular-to-the-plane giant magnetoresistance sample grown under ultrahigh vacuum.[704] In this scenario Eq. A.2.13 is reduced to the following:[150, 705]

$$\vec{J}_M = p_f \frac{\eta \mu_B}{e} \vec{J}_q \frac{1}{1 + (\frac{r_n}{r_f})(1 - p_f^2)}. \tag{A.2.14}$$

In the other extreme, when $R_i \to \infty$ the accumulated spin in N has the potential to be large, but the barrier prevents the necessary back diffusion. Therefore, the spin population of F remains relatively small and R_i dominates the voltage drop across the interface. In this scenario Eq. A.2.13 becomes:[150, 705]

$$\vec{J}_M = \eta \frac{\eta \mu_B}{e} \vec{J}_q, \tag{A.2.15}$$

where the interface parameter η defines the polarization fraction of carriers that are driven across the interface.[86] So, the end result of this is that the mismatch between resistances at the interface have the tendency to act like the cladding on optical fibers, keeping the bulk of the spin-polarized current on one side and thereby reducing the coherency length.[129, 153, 706, 707] Positively, some theoretical work has shown that by introducing a tunnel junction between F and N can significantly increase the spin coherency.[708, 709] The experimental result investigating this prediction are still coming to a head.[710, 711, 712, 713, 714]

Our work takes the phenomena of spin-polarized current production to a previously un-established regime, by imparting frequency dependency. Traditionally

speaking, magnetoresistance measures

$$MR(\%) = 100 \times \frac{R_{ph}(H) - R_{ph}(0)}{R_{ph}(0)}. \tag{A.2.16}$$

when incorporating magnetoresistance into our photoconductivity measurements we contemplated how to describe the resulting data. By looking at the traditional MR equation (Eq. A.2.16), it is readily determined that a linear relationship exists between the strength of the field (H) and the resulting $MR\%$.

I feel it is important to draw the distinction between spin photocurrent and current induced spin polarization. The effects are converse to each other in the sense that the spin photocurrent is induced by shining circularly polarized light on the material and the spin splitting of the electronic structure will show up as as a spin photocurrent or as an MCD effect (if the relative absorptivity is measured),[146] whereas, the current induced spin polarization occurs if an effective magnetic field is induced by the momentum carried by a current, or if the effective momentum is induced by the spin.[424]

Now we will more thoroughly define the independent effects. The spin photocurrent emerges from the differential absorption of circularly polarized light and in a $\vec{k}$-dependent spin-splitting electronic structure an applied electric field $\vec{E}$ would induce a current of both charge and spin.[715, 716, 717, 718] For example, in quantum well structures with a symmetry of C_{2v} when the incident radiation is in the (y, z) plane the induced photocurrent is along the x-axis. Establishing a net spin current relies upon breaking the equilibrium of the excited spin fluxes created in excitation, achieved spectroscopically via helicity and energy dependence.[422, 424, 131, 719]

The current-induced spin polarization arises from the Rashba coupling term, in the Hamiltonian this can be expressed as

$$H_{SO} = \alpha\vec{\sigma} \cdot \left(\vec{z} \times \vec{k}_{||}\right) = \alpha\vec{k}_{||} \cdot (\vec{\sigma} \times \vec{z}) \,. \tag{A.2.17}$$

Furthermore, the diffusive conductance tensor of a two-dimensional electron gas system with spin-orbit interaction shows that with an applied bias $\vec{E}_x$ produces a spin accumulation as the following:

$$\langle S_y \rangle = 4\pi e\tau D\lambda\vec{E}_x. \tag{A.2.18}$$

Here, $D = m_e/(2\pi\hbar^2)$ is the density of states per spin, τ is the lifetime or momentum relaxation time, and $\lambda = \alpha\langle\vec{E}_x\rangle/\hbar$ represents the Rashba interaction.[424, 719]

The mechanism we are proposing here is somewhat of a hyrbid of spin photocurrent and current induced spin polarization. The mechanism is shown in Fig. A.2.7 (c). I call it a hybrid because we are relying on the finite magnetism inherent to the magnetic insulator (semiconductor) and thereby obtain Figs. A.2.7 (a) and (b), without and with an applied magnetic field, respectively. The spin photocurrent emerges from the spin-polarized excitation present in the electronic structure, as exemplified by Fig. 2.12.

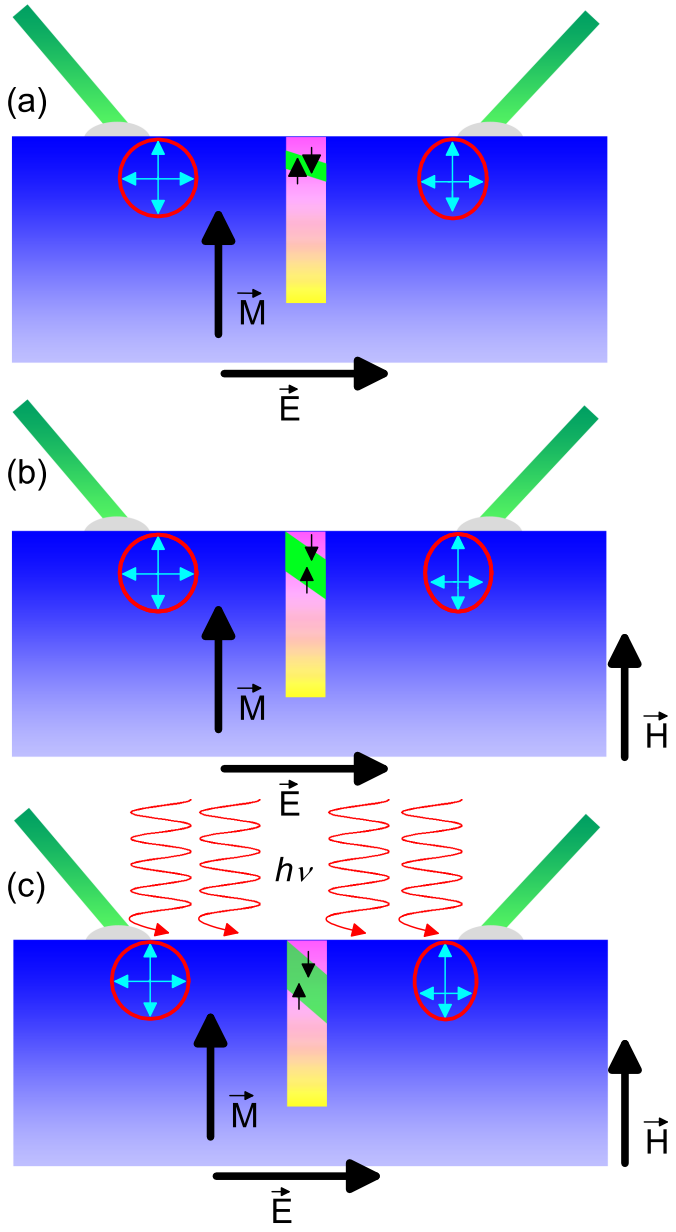

Figure A.2.7: Shown in panel (a) is the MR (spin filtering) effect as produced via tunneling through a thin film of a magnetic insulator in ambient conditions. (b) Display of how applying a magnetic field alters the spin-polarized current. Panel (c) shows the method by which we are producing an enhanced spin-polarized current. The resulting magnetoresistance can be projected along the frequency plane and thereby obtain information about high-frequency components of MR.

Appendix B

Multiferroics

B.1 Tensorial response

To better explain what a *special magnetic property* is, we need to look at equilibrium properties, more specifically equilibrium matter tensors, or properties that vary by direction. Generically a tensor property, say $\mathbf{T}$, relates a force, say $\mathbf{X}$, to a response, say $\mathbf{Y}$, through a linear constitutive relationship:

$$\mathbf{Y} = \mathbf{TX}. \tag{B.1.1}$$

An important note is that $\mathbf{X}$ does not have a restriction to the rate of application to the crystal. This results in changing from one equilibrium state to the next, until an ultimately final equilibrium state is attained and that this attainment is thermodynamically reversible. It is important to note that transport properties e.g. thermal conductivity, electrical conductivity, thermoelectric effect, and diffusivity are fun-

damentally thermodynamically irreversible processes. Thus the above constitutive tensor relationship does not apply to them because the nature of a thermodynamically irreversible process (increasing entropy) indicates a process that can not contain time-reversal symmetry, such as magnetic properties. Properties emerging in this nature do such if the constitutive relationship connecting the force and the response are not the same category of tensor, invariant vs. variant.[165, 166, 201] Now for a couple materials examples, first the magnetic permeability tensor μ is *not* a *special magnetic property*:

$$B_i = \mu_{ij} H_j. \tag{B.1.2}$$

μ is not a special magnetic property because both $\mathbf{B}$and$\mathbb{H}$ don't contain time-reversal symmetry. For the second example, the magnetoelectric tensor α_{ij} is a special magnetic property:

$$B_i = \alpha_{ij} E_j. \tag{B.1.3}$$

A powerful generalization to the constitutive relationship such as Eqn. B.1.3 is that if a tensor(s) without time-reversal symmetry appears in the relationship an odd number of times then the matter tensor will represent a special magnetic property.

Appendix C

Magnetic Circular Dichroism

C.1 Fundamental understanding

Quantum mechanical roots

The representative fundamental Hamiltonian that includes the Hamiltonian of the absorbing center plus impinging photon radiation looks like the following:

$$\mathcal{H} = \mathcal{H}_0 + \mathcal{H}_1. \tag{C.1.1}$$

Here, $\mathcal{H}_0$ is the un-evolved Hamiltonian, whereas $\mathcal{H}_1$ is then the response Hamiltonian from light-matter interaction. To deconvolute the scenario, this response only constitutes the electric dipole absorption; therefore, we can approximate $\mathcal{H}_1$ by:

$$\mathcal{H}_1 = -\vec{m} \cdot \vec{e}. \tag{C.1.2}$$

To clarify, here $\vec{m} = \Sigma_i e_i \vec{r}_i$ is the electric dipole operator and $\vec{e}$ is the electric field

due to the light. As an aside, this approximation has a significant degree of accuracy because $\vec{m}$ contributions are inherently $\approxeq 10^5$ (fives orders of magnitude) greater than the next and nearest operator.[375, 720] Therefore, if even a small component of $\vec{m}$ is present in the transition it will tend to dominate all other effects. Return to the discussion at hand, the microscopic electric field is related to the macroscopic field $\vec{E}$ by a proportionality constant $\vec{e} = \alpha E$.[533, 535, 721] Moreover, this results in the following Hamiltonian:

$$\mathcal{H}_1^{\pm}(z) = -\sqrt{2}\alpha|\vec{E}_{\pm}(z)|\,\mathrm{Re}(\vec{m}_{\pm}\exp\left[\frac{iEt}{\hbar}\right]). \tag{C.1.3}$$

Here, $\vec{m}_{\pm} = (1/\sqrt{2})(\vec{m}_x \pm i\vec{m}_y)$. From the above equation we can see that the natural consequence of light interacting with matter is an exponential relationship of the energy E, with the response scaled by the magnitude of the electric field.

The probability of a transition, namely an excitation from state a to state j, in a time-perturbed environment, as shown in Fig. C.1.1:

$$P_{a\to j} = \frac{1}{t}\left|\frac{1}{\hbar}\int_0^{\infty}\exp\left[\frac{iE_{ja}t}{\hbar}\right]\langle j|\mathcal{H}_1|a\rangle\,dt\right|^2 \tag{C.1.4}$$

Further derivation can be found in a large number of quantum chemistry texts.[722, 723, 724] Now that we have established what the light-matter interaction does to the Hamiltonian we can take a look at the outcome form applying a static magnetic field.

$$\mathcal{H} = \mathcal{H}_0^{\circ} + \mathcal{H}_0^{'}(H). \tag{C.1.5}$$

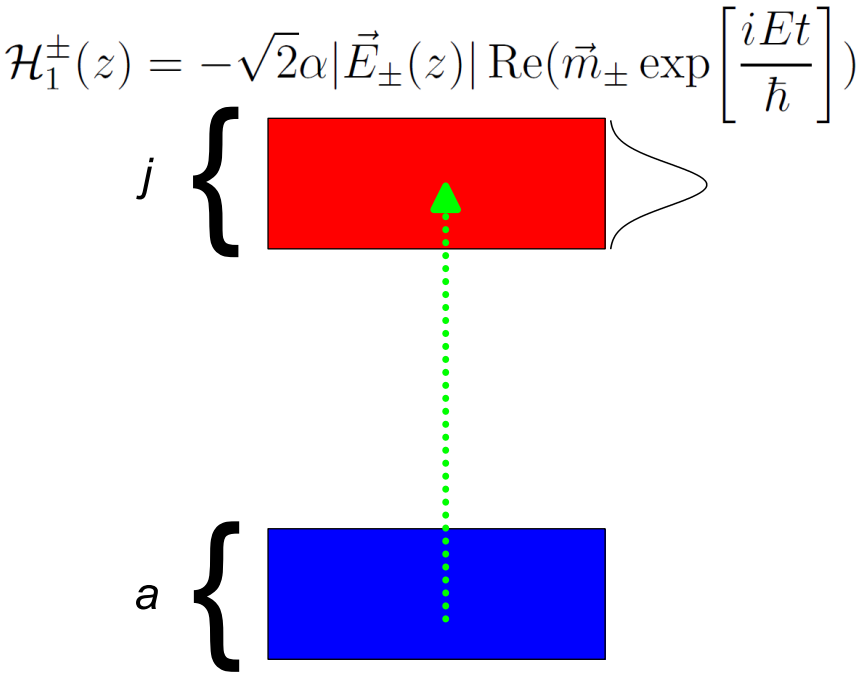

Figure C.1.1: Displaying the ground and excited eigenstates, a (blue) and j (red) of a given absorbing center. The Gaussian distribution on the right suggests the probability of absorption with respect to photon energy. The equation at the top is the governing equation as described by Eq. C.1.3.

Here, $\mathcal{H}_0^{\circ}$ is the zero-field (un-evolved) Hamiltonian and $\mathcal{H}_0^{'}$ is the magnetic field H perturbation. Since Maxwell's equations and the Beer-Lambert law have already been discussed in Secs. 3.1.1 and 3.1.4, respectively, we can assume the logical jump to the helicity dependent absorption being represented by:

$$\begin{aligned}\frac{\alpha_{\pm}}{E} &= \frac{\epsilon_{\pm}}{E}cz \\ &= \gamma_{\pm}\sum_{aj}\frac{N_a}{N}|\,\langle a|m_{\pm}|j\rangle\,|^2\delta(E_{ja}-E)cz. \end{aligned} \tag{C.1.6}$$

Here, left-hand-side of the above equation $\alpha_{\pm}$ is the absorption coefficient with helicity $\pm$ dependence at energy E, for the middle portion, $\epsilon_{\pm}$ is the helicity dependent dielectricity, on the right-side $|\langle a|m_{\pm}|j\rangle|^2$ is the square (magnitude) of the circularly polarized transition moment, $\delta(E_{ja} - E)$ is a Dirac delta function dispersion, c is the speed of light, and z is the frameworks z-direction, representing the direction of propagation for the light beam. Natural circular dichroism (CD) emerges out of this incorporation of helicity, $\Delta\alpha = \alpha_+ - \alpha_-$. Correlating this to the state transitions

$$\begin{aligned}\frac{\Delta\alpha_{\pm}}{E} &= \frac{\Delta\epsilon_{\pm}}{E}cz \\ &= \gamma_{\pm}\sum_{aj}\frac{N_a}{N}|\langle a|m_-|j\rangle|^2 - |\langle a|m_+|j\rangle|^2\delta(E_{ja} - E)cz. \end{aligned} \tag{C.1.7}$$

However, a side-effect of the assumption that only the electric dipole operator be taken into consideration is that truly the CD is zero

$$\alpha_+^{\circ} = \alpha_-^{\circ} \tag{C.1.8}$$

$$\Delta\alpha^{\circ} = 0 \tag{C.1.9}$$

because

$$|\langle a|m_+|j\rangle|^2 = |\langle a|m_-|j\rangle|^2 \tag{C.1.10}$$

In the consideration of further contributions (magnetic dipole and electric quadrupole), one will find the following absorption probability relationship, for fixed atomic

(molecular) coordinates:

$$
\begin{aligned}
P_{a\to j} &= \frac{\pi^2}{h^2}\left|\langle j|\sum(\frac{e_k}{m_k c})\vec{\pi}^*\vec{A}^0\cdot\vec{p}_k\exp\left(\frac{i2\pi\omega z_k}{c}\right)|a\rangle\right|^2 \\
&= \left[\frac{\pi^2(\vec{A}^0)^2}{(c^2h^2)}\right]\left|\langle j|\sum(\frac{e_k}{m_k})\vec{\pi}^*\frac{i2\pi m_k(E_j-E_a)}{h\vec{r}_k}(\frac{1+i2\pi\omega z_k}{c})|a\rangle\right|^2\rho_{aj}(\omega) \\
&= \left[\frac{\pi^2(\vec{A}^0)^2\nu^2|i|^2}{(c^2h^2)}\right]|\,\langle j|\vec{m}\cdot\vec{\pi}^*|a\rangle + \langle j|\vec{e}_z\times\vec{\pi}^*\vec{\mu}|a\rangle \\
&\quad + (\frac{i\pi\omega}{c})\,\langle j|\vec{\pi}_1^*\,Q_{xz}+\vec{\pi}_2^*\,Q_{yz}|a\rangle\,|^2\rho_{aj}(\omega). \qquad \text{(C.1.11)}
\end{aligned}
$$

Here, $\omega = \omega aj = (E_j - E_a)/h$ and $\vec{\pi} = (\vec{e}_x\pi_1 + \vec{e}_y\pi_2)$ is the unit vector describing how the polarization properties evolve while propagating in the z direction, ρ_{aj} is the absorption lineshape function as defined by $\int\rho_{aj}(\omega)d\omega = 1$. The first term invokes the electronic dipole transition operator $\vec{m}$, as previously described; the other terms include the magnetic dipole transition operator $\vec{\mu} = -e/(2m_e c)\sum(\vec{l}_k + 2\vec{s}_k) = -\mu_B\sum(\vec{l}_k + 2\vec{s}_k)$, where μ_B is the Bohr magneton (the fundamental unit for expressing the magnitude of magnetic moment); the orbital and spin angular momentum operators are shown by $\vec{l}_k$ and $\vec{s}_k$, respectively, in units of $h/2\pi = \hbar$; the last term incorporates the electric quadurpole operators $Q_{\alpha\beta} = \sum q_k(\vec{r}_{k\alpha}\vec{r}_{k\beta} - (\vec{r}_k\cdot\vec{r}_k/3)\delta_{\alpha\beta}$.

Now that we have the fundamental requirements of the MCD response, perturbation by an oscillating field (light) and perturbation by the static magnetic field, we need to take a look at the approximations that are invoked in the understanding of data structure.

As described in Secs. 3.1.1 and 3.1.4 in Eqns. 3.15 and 3.41 along with the definition of κ, we can see that by combining these with Eq. C.1.11 the absorption coefficient for circularly polarized light $\alpha_{\pm}(\omega)$ evolves as

$$\alpha_{\pm}(\omega) = \frac{(8\pi^3\omega)}{hc}(N_a - N_j)\Big|(\frac{\alpha}{\sqrt{n}})\,\langle j|m_{\mp}|a\rangle \pm \sqrt{n}[\,\langle j|\mu_{\mp}|a\rangle \pm (\frac{i\pi\omega}{c})\,\langle j|Q_{\mp}|a\rangle]\Big|^2 \rho_{aj}(\omega). \tag{C.1.12}$$

Now that we have included the electric and magnetic dipole operators along with the electric quadrupole the feasibility to derive an equation that incorporates both CD and MCD comes to life.[71, 725] We will now return to the simplified version that only includes the electric dipole operator and a summing over all eigenstates that are part of the $a \rightarrow j$ band transition. The differential absorption coefficient is

$$\Delta\alpha(\omega) = \frac{(8\pi^3\omega)}{hc}\sum_{aj}(N_a - N_j)[|\,\langle a|m_-|j\rangle\,|^2 - |\,\langle a|m_-|j\rangle\,|^2]\rho_{aj}(\nu) \tag{C.1.13}$$

A useful extension of this is to express the values in units of energy E:

$$\frac{\alpha}{E} = \frac{\gamma}{2}\sum\frac{(N_a - N_j)}{N}[|\,\langle a|m_-|j\rangle\,|^2 + |\,\langle a|m_-|j\rangle\,|^2]\rho_{aj}(E), \tag{C.1.14}$$

$$\frac{\Delta\alpha}{E} = \gamma\sum\frac{(N_a - N_j)}{N}[|\,\langle a|m_-|j\rangle\,|^2 - |\,\langle a|m_-|j\rangle\,|^2]\rho_{aj}(E), \tag{C.1.15}$$

where

$$E = h\nu \tag{C.1.16}$$
$$\gamma = 2N_0\pi^3\beta^2 cl \log\left(\frac{e}{250hcn}\right)$$

in Gaussian units.

From Table C.1.1 we can see that the energy and momentum of photons and electrons are measured by similar values; however, when considering angular momentum the total angular momentum must be conserved,[70, 726, 561, 687, 527, 727] with the caveat that in dilute magnetic semiconductor systems (DMS) this does not hold true.[728] In a circularly polarized light beam the photons exist in pure angular momentum states $\left|\vec{k}_+\right\rangle$ or $\left|\vec{k}_-\right\rangle$.[342] Whereas, a linearly polarized light beam is constructed of photons in a superposition of states $2^{-1/2}(\left|\vec{k}_+\right\rangle + \left|\vec{k}_-\right\rangle)$. This combination can additionally be expressed by the following relationship:

$$\vec{p} = \frac{1}{\sqrt{2}}[\sigma_+ \pm \sigma_-] \tag{C.1.17}$$

Approximations

To develop a theoretical construct and ultimately be able model the MCD response only two approximations need to be considered. The derivations included in this survey follow the notation in *Magnetic Circular Dichroism Spectroscopy.*

1. Franck-Condon/Born-Oppenheimer

2. Rigid-shift

Table C.1.1: Angular momentum

Photons		Electrons	
Energy	$E = hc/\nu$	Energy	$E = hc/\nu$
Momentum	$\vec{p} = h/2\pi\vec{k}$	Momentum	$\vec{p} = h/2\pi\vec{k}$
Angular momentum	$\pm h/2\pi$	Angular momentum	$\pm\frac{1}{2}h/2\pi$ (spin) $\pm nh/2\pi$ (orbit)

The Franck-Condon/Born-Oppenheimer (linear limit) approximation, in this environment the electronic excitation(s) is considered to be occurring on a time-scale short compared to the motion of the nuclear envelope, therefore, the transition probability is calculated for a "fixed" nuclear position. The primary assumption for the Franck-Condon approximation is that the Zeeman shifting $a_{\alpha\lambda}B$ is small compared to line(band)width Γ of the composite $A \rightarrow J$ band (this invokes the linear limit).[71, 729, 730] Fig. C.1.2 shows how this falls out of a experimental data set and fits to Langevin and Brillouin function.

A mathematical description for the Franck-Condon approximation requires inclusion of vibrational functions $|g\rangle$ and $|j\rangle$ within the respective ground A and excited J states, such as the following:

$$|A_{\alpha g}\rangle \;=\; \phi_{A\alpha}(q,Q)\chi_g(Q) \;=\; |A\alpha\rangle\,|g\rangle \tag{C.1.18}$$

$$|J_{\lambda j}\rangle \;=\; \phi_{J\alpha}(q,Q)\chi_j(Q) \;=\; |J\lambda\rangle\,|j\rangle \tag{C.1.19}$$

Now the summations from Eqs. C.1.14 and C.1.15 of α and $\Delta\alpha$ are to include $\alpha\lambda gj$, as can be deduced from Eqs. C.1.18 and C.1.19, therefore we obtain

$$\frac{\alpha}{E} = \frac{\gamma}{2}\sum(\frac{N_{A\alpha g} - N_{J\lambda j}}{N})(|\langle A_{\alpha g}|m_-|J_{\lambda j}\rangle|^2 - |\langle A_{\alpha g}|m_-|J_{\lambda j}\rangle|^2)\rho_{AJ}(E) \quad \text{(C.1.20)}$$

$$\frac{\Delta\alpha}{E} = \gamma\sum(\frac{N_{A\alpha g} - N_{J\lambda j}}{N})(|\langle A_{\alpha g}|m_-|J_{\lambda j}\rangle|^2 + |\langle A_{\alpha g}|m_-|J_{\lambda j}\rangle|^2)\rho_{AJ}(E) \quad \text{(C.1.21)}$$

With the application of a magnetic field, either external or internal (exchange coupling),[64] along the propagation direction of the light beam z, we can then assume the Zeeman perturbation $-\mu_z B$. Here, $\mu_z = \mu_B(L_z + 2S_z)B$, where μ_B is the Bohr magneton, and L_z and S_z are the orbital and spin angular momentum operators, respectively. It is assumed, as stated previously, that $-\mu_z B$ will be small compared to $k_B T$ and the bandwidth Γ.

Now for the rigid-shift approximation, this approximation makes the assumption that excitation(s) shift in energy similar to the Zeeman effect. However, an important caveat of this is that the response functions shape does not change. This is represented by:

$$\rho_{AJ}(E) = \rho_{AJ}(E - a_{\alpha\lambda}B) \quad \text{(C.1.22)}$$

where

$$\begin{aligned} a_{\alpha\lambda}B &= (E'_{J\lambda j} - E'_{A\alpha g}) - (E_{J\lambda j} - E_{A\alpha g})Aag) \\ &= -(\langle J_\lambda|\mu_z|J_\lambda\rangle^\circ - \langle A_\alpha|\mu_z|A_\alpha\rangle^\circ)B. \end{aligned} \quad \text{(C.1.23)}$$

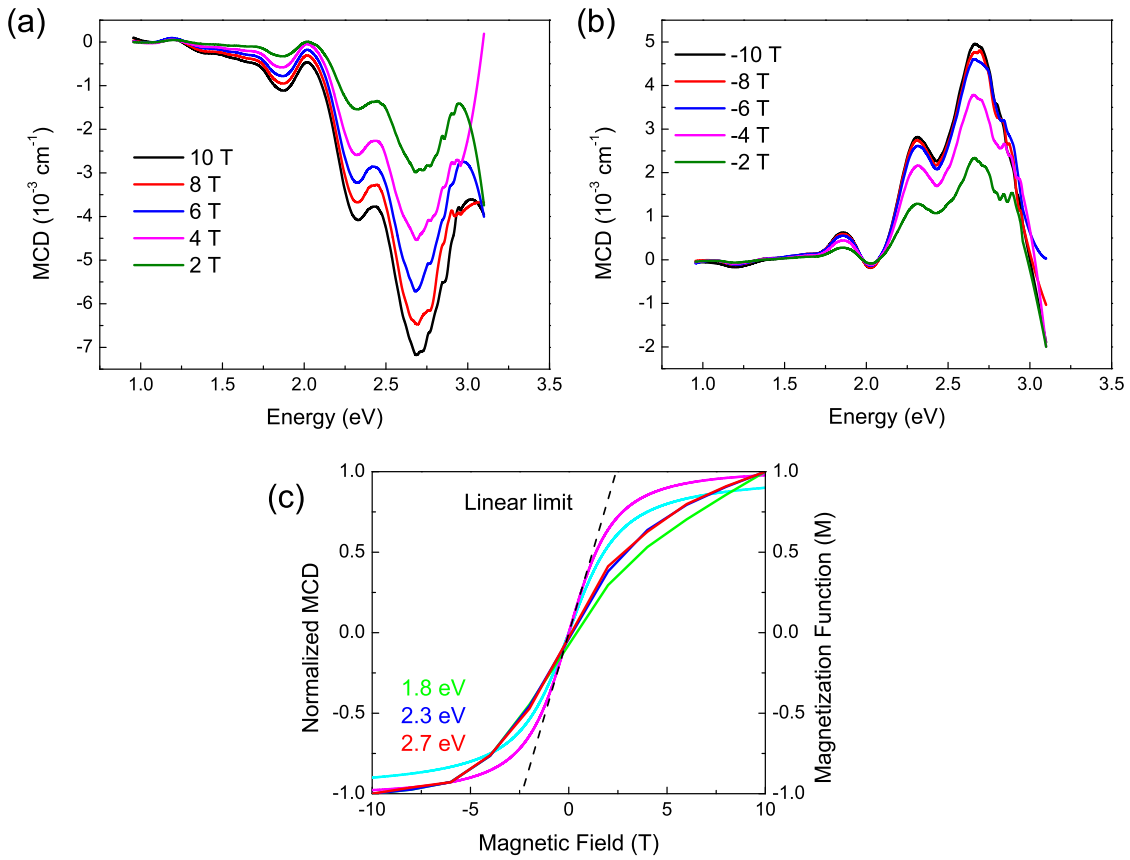

Figure C.1.2: (a-b) Displays the positive and negative field, respectively, MCD response for $NiFe_2O_4$. (c) Shows how the response varies with respect to field at a constant energy (eV). Franck-Condon (Linear-limit) approximation: As the magnetic field increases the MCD will follow a a linear response function, such as the Brillouin (magenta) or the Langevin (cyan). Then when the MCD response is on the order of, or large than, Γ the linearity will start to breakdown. This breakdown creates a deviation from the linear limit, expressed by the black dashed line.

A representative result is shown in Fig. C.1.3.

Now that we have all of the approximations and background information in place, we can take a look at the functional that can be used to model the MCD response

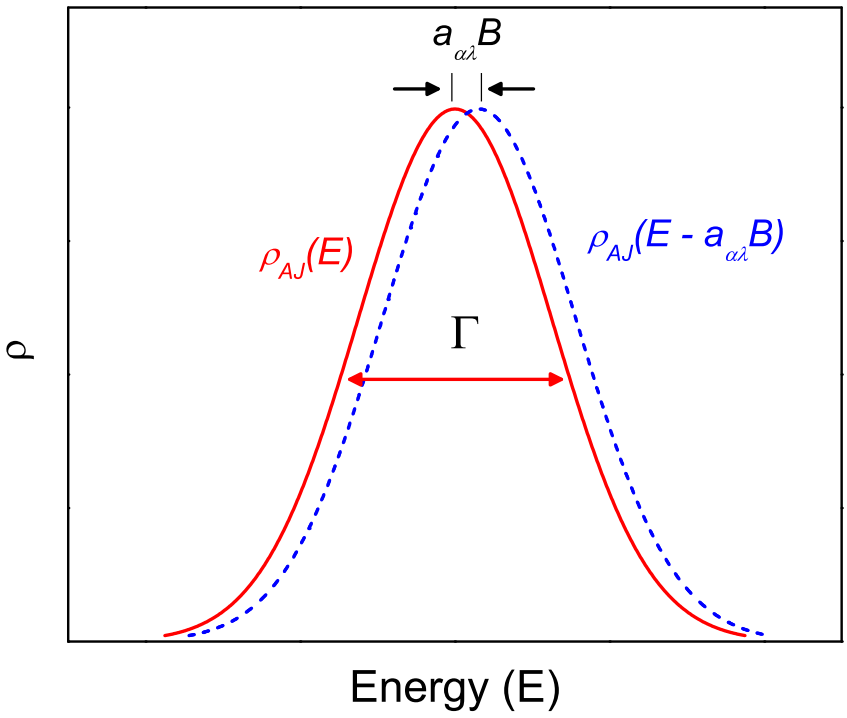

Figure C.1.3: Rigid-shift approximation: a shifting of the absorption band with only the Zeeman like perturbation as a driving mechanism and the shape ρ_{AJ} of the response does not change.

function. The subsequent expression falling out of the considered approximations takes the form of the following:

$$
\begin{aligned}
\Delta\alpha/E &= \gamma \sum (\frac{N_{A\alpha g} - N_{J\lambda j}}{N})(|\left\langle A_{\alpha g}|m_-|J_{\lambda j}\right\rangle|^2 - |\left\langle A_{\alpha g}|m_-|J_{\lambda j}\right\rangle|^2)\rho_{AJ}(E) \\
&= \gamma(\frac{N_g}{|A|\sum N_g})(1 + \left\langle A_\alpha|\mu_z|A_\alpha\right\rangle^\circ B/(k_B T))\left\langle g|j\right\rangle^2 \\
&\quad \times \left\{ \left[\left\langle A_\alpha|m_-|J_\lambda\right\rangle^\circ + \left[\sum_{K\neq A,\kappa} 1/(W_k^\circ - W_A^\circ)\left\langle A_\alpha|\mu_z|K_\kappa\right\rangle^\circ \left\langle K_\kappa|m_-|J_\lambda\right\rangle^\circ \right.\right.\right. \\
&\quad \left.\left.\left. + \sum_{K\neq J,\kappa} 1/(W_k^\circ - W_J^\circ)\left\langle A_\alpha|\mu_z|K_\kappa\right\rangle^\circ \left\langle K_\kappa|m_-|J_\lambda\right\rangle^\circ \right] B^2 \right] \right\} \\
&\quad - \left\{ \left[\left\langle A_\alpha|m_-|J_\lambda\right\rangle^\circ + \left[\sum_{K\neq A,\kappa} 1/(W_k^\circ - W_A^\circ)\left\langle A_\alpha|\mu_z|K_\kappa\right\rangle^\circ \left\langle K_\kappa|m_-|J_\lambda\right\rangle^\circ \right.\right.\right. \\
&\quad \left.\left.\left. + \sum_{K\neq J,\kappa} 1/(W_k^\circ - W_J^\circ)\left\langle A_\alpha|\mu_z|K_\kappa\right\rangle^\circ \left\langle K_\kappa|m_-|J_\lambda\right\rangle^\circ \right] B^2 \right] \right\} \\
&\quad \times [\rho_{AJ}(E) + (\left\langle J_\lambda|\mu_z|J_\lambda\right\rangle^\circ - \left\langle A_\alpha|\mu_z|A_\alpha\right\rangle^\circ) B\partial\rho_{AJ}(E)/\partial E]. \qquad \text{(C.1.24)}
\end{aligned}
$$

The intricate and burdensome nature of the preceding equation, expressing $\Delta\alpha$, can be simplified by organizing by the magnetic interaction form factors. After a bit of mathematical work, and discarding the B^2, the expression for the approximations becomes

$$
\Delta\alpha(E) = \gamma\mu_B B[\frac{A_1}{h}\frac{\partial g(E)}{\partial E} + \left(B + \frac{C}{k_b T}\right) g(E)]. \qquad \text{(C.1.25)}
$$

The resulting data in MCD is comprised of several attributes, i.e. Zeeman splitting, the effective derivative of $\alpha(E)$, and qualitative analysis of the Faraday A_1, B_0, and C_0.[502, 731]

In short order we can now define the Faraday A_1,B, and B terms, or A_1, B_0, and C_0. The subscripts represent the order of the spectral moments and therefore describe a respective series of band shapes.

$$
\begin{aligned}
A_1 \; &= \frac{1}{|A|} \sum_{\alpha\lambda} (\, \langle J_\lambda | L_z + 2S_z | J_\lambda \rangle - \, \langle A_\alpha | L_z + 2S_z | A_\alpha \rangle) \\
&\quad \times (| \, \langle A_\alpha | m_{-1} | J_\lambda \rangle \, |^2 - | \, \langle A_\alpha | m_{+1} | J_\lambda \rangle \, |^2) \qquad \text{(C.1.26)} \\
B_0 = \frac{2}{|A|} \, \mathrm{Re} \sum_{\alpha\lambda} \Bigg[& \sum_{K \neq J, \kappa} \frac{1}{W_K - W_J} \, \langle J_\lambda | L_z + 2S_z | K_\kappa \rangle \\
&\quad \times (\, \langle A_\alpha | m_{-1} | J_\lambda \rangle \, \langle K_\kappa | m_{+1} | A_\alpha \rangle - \, \langle A_\alpha | m_{+1} | J_\lambda \rangle \, \langle K_\kappa | m_{-1} | A_\alpha \rangle) \\
&\quad \sum_{K \neq A, \kappa} \frac{1}{W_K - W_A} \, \langle K_\kappa | L_z + 2S_z | A_\alpha \rangle \\
&\quad \times (\, \langle A_\alpha | m_{-1} | J_\lambda \rangle \, \langle J_\lambda | m_{+1} | K_\kappa \rangle - \, \langle A_\alpha | m_{+1} | J_\lambda \rangle \, \langle J_\lambda | m_{-1} | K_\kappa \rangle) \\
&\quad \times (| \, \langle A_\alpha | m_{-1} | J_\lambda \rangle \, |^2 - | \, \langle A_\alpha | m_{+1} | J_\lambda \rangle \, |^2) \Bigg] \qquad \text{(C.1.27)} \\
C_0 = \; & - \frac{1}{|A|} \sum_{\alpha\lambda} \, \langle A_\alpha | L_z + 2S_z | A_\alpha \rangle \\
&\quad \times (| \, \langle A_\alpha | m_{-1} | J_\lambda \rangle \, |^2 - | \, \langle A_\alpha | m_{+1} | J_\lambda \rangle \, |^2) \qquad \text{(C.1.28)}
\end{aligned}
$$

For a final definition, dipole strength parameter D_0, such that

$$
\frac{A}{E} = \gamma D_0 g(E), \qquad \text{(C.1.29)}
$$

hence

$$D_0 = \frac{1}{2|A|}\sum_{\alpha\lambda}(|\langle A_\alpha|m_{-1}|J_\lambda\rangle|^2 + |\langle A_\alpha|m_{+1}|J_\lambda\rangle|^2). \tag{C.1.30}$$

The dipole strength is a representation of the oscillator strength because the oscillator strength is proportional to the absolute square of the dipole moment operator,

$$f \propto |\vec{m}_\pm|^2 = \sum(e\vec{r})^2 \propto D_0. \tag{C.1.31}$$

Whereas it can be seen in Eq. C.1.30 that D_0 is a sum of both helicities absolute dipole transition moment operator value squared.[732, 733]

In atomic/molecular systems, the excitations energies are very narrow and tend to be well isolated. So, from a fundamental standpoint the spectrum should be "easily" interpreted.

On a final note, by taking the ratio of a Faraday term and the dipole strength, one can obtain results that are effectively independent from the medium effects and produce an otherwise inaccessible precision to the band-shape functions. Fo example, take the following ratio:

$$\frac{C_0}{D_0} = \frac{k_B T}{\beta B}\frac{\int \frac{\Delta\alpha_{MCD}(E)}{E}dE}{\int \frac{\alpha_{ABS}(E)}{E}dE}. \tag{C.1.32}$$

The numerator is the area "under" the MCD band and the denominator is the area under the absorption band. The can be used a metric to decide if an excitation is a d–d or charge-transfter CT excitation, such that if $C/D > 0.01$ then the transition is

a d–d and by logical deduction one can see that if $C/D < 0.01$ then the transition is a CT. Of course, one can also examine the absorption spectrum and/or the projected partial density of states. Taking the absorption spectrum as an example, if the value of $\alpha(E)$ rises sharply to a level that exceeds 10^{+5}cm^{-1}, then once could expect that the transition is a CT.

Solids and DMS

Over the span of approximately 3-4 decades the bulk of MCD work has focused on solid materials, specifically dilute magnetic semiconductors (DMS).[734, 735, 541] The most logical difference between atomic/molecular solutions vs solids is that the spectral features will be broadened.

Briefly about the drive behind DMS materials, a nonvolatile circuit would retain its logic state value even through powering on and off.[736] This type of circuit would allow for batteries in mobile computing platforms to last dramatically longer, ca. 1 week vs 1 day hours. High-density integrated circuits would be effectively free from heat production and thereby showing one route to increased efficiency. However, unfortunately this technology, i.e. nonvolatile transistors, does not currently exist. Enter DMS materials, they have the potential to be intrinsically nonvolatile because of the physical phenomena known as magnetic hysteresis.[737] Figure C.1.4 shows how the introduction of magnetic ions alters the density of states.

So, of course this beckons the questions, "How does the MCD response differ from that of atomic or molecular systems?" Since MCD offers a response in every material and material form, assuming transmittance (reflectance) is adequate to track said response.[357, 738, 739, 740, 741, 742] The first result of MCD in dilute magnetic

semiconductors is that the parent semiconductor will have an intrinsic response function that will then be amplified via the interstitial magnetic ions. This amplification arises through the exchange mechanism that is responsible for the magnetic ions to "see" each other, or exchange magnetic information through the lattice.[69] This can be seen in Fig. C.1.5.

C.1.1 Optical Activity

A materials response to external perturbating fields has culminated in a research field known as optical activity.

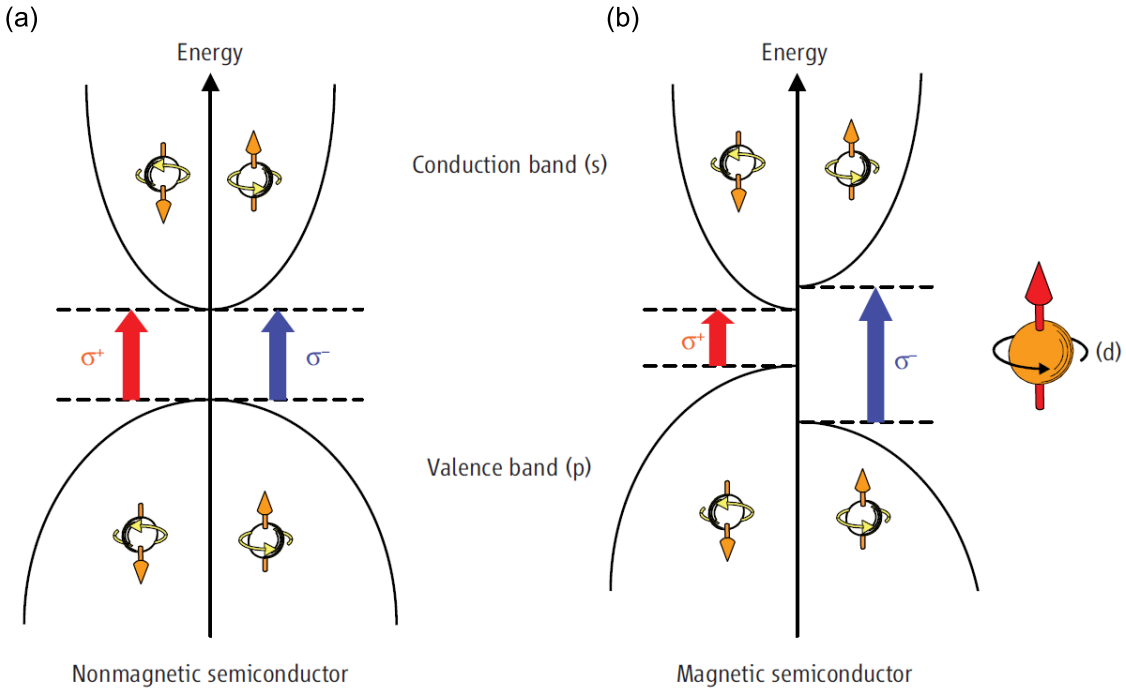

Figure C.1.4: (a) Shows a schematic density of states for a nonmagnetic semiconductor. By close examination it is evident that an excitation from the valence band to the conduction band has no spin dependence, therefore, spin-up and spin-down electrons have no distinguishing features. (b) Shows a schematic density of states for a magnetic semiconductor, in this scenario the d electrons from the magnetic ion interact with the s and p electrons from the semiconductor lattice. This interaction induces exchange splitting in the valence and conduction bands that depends upon the spin direction (Zeeman splitting). Therefore, the semiconductor has a spin-polarized band structure that results in a differential absorption (MCD effect) when comparing RCP and LCP (σ_+ and σ_-). Ultimately the MCD spectrum will display an amplified form of the parent semiconductors spectrum, after [737].

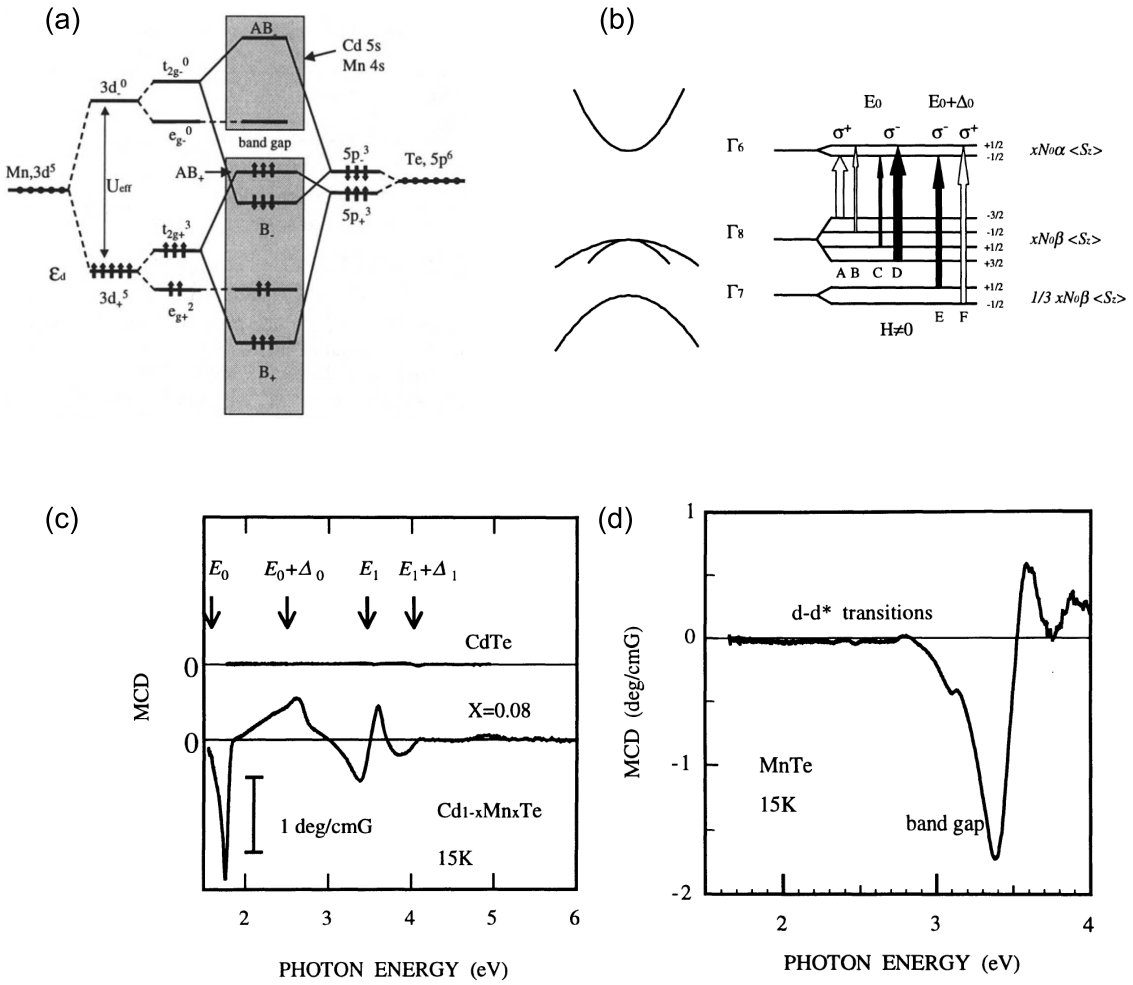

Figure C.1.5: (a) Schematic diagram of $p-d$ hybridization for $Cd_{1-x}Mn_xTe$. (b) Ordering of sublevels due to Zeeman splitting and the resulting helicity dependence (σ_+ and σ_-) of the optical transitions at Γ critical points in $Cd_{1-x}Mn_xTe$. (c) Transmission MCD spectra for CdTe (top) and $Cd_{0.92}Mn_{0.08}Te$ (bottom). Measurement was done at 15 K. The arrows indicate the excitation energies for $E_0, E_0+\Delta_0, E_1$, and $E_1+\Delta_1$. (d) Transmission MCD spectrum of zinc-blende MnTe film at 15 K. All figures are adapted from [69] but some also originate in [743, 744].

Appendix D

Photoconductivity

D.1 Noise

D.1.1 Introduction to noise

Whether noise is a nuisance or a signal may depend on whom you ask.[745, 746] Generally, noise (or fluctuations) is the spontaneous stochastic (random) variations of a physical quantity with respect to time.[747] More precisely, these fluctuations are random deviations of the quantities mean value either at a constant value or vary non-randomly in time. The variance manifests from the thermal motion of matter and its structure, existing in the full spectrum of transport material systems e.g. insulators, semiconductors, metals, and superconductors. The reason this deserves to be mentioned is that with the development of new instrumentation, or devices, the measurement accuracy of a physical quantity is intrinsically limited by the fluctuations magnitude. Positively, noise communicates the kinetic processes taking place in the matter

system, such as the molecular-kinetic conception of heat. For example, the theory of Brownian motion and then latter the experimental proof put a final check mark on the molecular-kinetic conception of heat.[748, 650, 749, 750, 751, 752, 753, 754, 755] Therefore, the physics of fluctuations is a highly valuable field for conceptual investigation.

Some semiconductors have internal mechanism(s) that allow the previously defined values to be greater than unity, gain up to 10^6. Ultimately the higher this value the higher the intrinsic noise. Low (no) noise is inherently the desire of all experimental methodologies. A little later a relationship will be defined that describes this desire. For now the path will continue on towards the sources of the noise that one must create a signal greater than, $S : N > 1$. The dark current is the intrinsic leakage current that occurs when the photodetector is under bias without being exposed to a photon source. The first limitation is that the temperature must be at a lower energy than the photon energy to be absorbed ($kT < h\nu$). Background radiation is another source of noise, this can be created by emission of "warm" bodies that are arbitrarily near the detector. Thermal noise (Johnson-Nyquist noise) results from the random thermally induced motion of carriers in the given resistive device or material. Shot noise arises due to single events of the photoelectric effect along with the fluctuations in statistics that correspond, appears more strongly as the source intensity falls off. This can be seen as the origin of Generation-Recombination noise, the fluctuation of the number of carriers being transported because some portion randomly recombines with traps. Flicker noise is another appears as $1/f$ and is due to random effects associated with surface traps. Since the appearance is characteristically $1/f$, the lower

the frequency the higher the noise.

In magnetic materials, the electric transport and magnetic properties are inherently linked, the magnetoresistance measurements provide information concerning magnetic instabilities. Additionally, spin-dependent scattering can be investigated to garner an understanding of the charge-spin coupling.

D.1.2 Mathematical description

Since noise refers to the physical quantity under investigation $V(t)$ fluctuating around a mean value, the quantity shows stochastic behavior in the time domain. Hence, the instantaneous value is impossible to predict discretely. To build a fundamental mathematical understanding of noise we must look at several concepts regarding time domain fluctuations, such as:[756, 757, 758, 759, 747]

- **The average value:**

$$\overline{V} = \lim_{T\to\infty} \frac{1}{T} \int_{-T/2}^{T/2} V(t)dt \tag{D.1.1}$$

  where T is the observation time.

- **The variance:**

$$\sigma^2 = \overline{(V(t) - \overline{V}^2)} = \overline{\delta V^2} = \overline{V^2} = \overline{V}^2 \tag{D.1.2}$$

- **The probability density function (PDF):**

$$P(V) = \frac{1}{\sqrt{2\pi\sigma^2}}\exp[-\frac{(V-\overline{V})^2}{2\sigma^2}] \tag{D.1.3}$$

- **The auto-correlation function:**

$$\psi_V(\tau) = \overline{V(\tau)V(t+\tau)} = \lim_{T\to\infty}\frac{1}{T}\int_{-T/2}^{T/2} V(t)V(t+\tau)dt \tag{D.1.4}$$

More precisely, Eqn. D.1.3 is used in the calculation of the probability of a continuous variable falling into a specific range of values. Therefore, if $V(t)$ has a PDF of $P(V)$, then the probability for $V(t)$ to be a value in an interval $[V, V + dV]$ is $P(V)dV$. In the scenario that a "large" number of independent effects and random events contribute to the overall fluctuations, the PDF becomes a Gaussian distribution function as seen in Eqn. D.1.3.

The auto-correlation function, Eqn. D.1.4, of a random process describes how different points in time are correlated in the process. Moreover, this function presents a measure for the memory of the process. In this function, τ represents the interval of two times points as the continuous variable changes with evolving time. To define, the auto-correlation function gives the mean square value of the fluctuations, at $\tau = 0$: $\psi_V(0) = \overline{V(t)^2}$

Of course, all of this discussion about the time domain information is gainful but a further informative and alternative way to characterize the fluctuations is to project and study them in the frequency domain. Importantly, the value in the frequency domain $V_T(\omega)$ is related to the time domain value $V(t)$ through the application of a Fourier transform and an inverse Fourier transform:

$$V_T(\omega) = \frac{1}{\sqrt{2\pi}} \int_{-T/2}^{T/2} V(t) \exp^{i\omega t}\, dt \tag{D.1.5}$$

$$V(t) = \frac{1}{\sqrt{2\pi}} \int_{-T/2}^{T/2} V(\omega) \exp^{-i\omega t}\, d\omega. \tag{D.1.6}$$

For completeness, the total energy of the signal, E, can be projected into the frequency domain to display the distribution of the signals energy with respect to frequency:

$$E = \lim_{T\to\infty} \int_{-T/2}^{T/2} V(t)^2 dt = \frac{1}{2\pi} \int_{-\infty}^{\infty} |V_T(\omega)| t^2 d\omega. \tag{D.1.7}$$

Now to obtain the average power for the fluctuations one can invoke the Parseval Theorem, as follows:

$$P = \lim_{T\to\infty} \frac{1}{T} \int_{-T/2}^{T/2} V(t)^2 dt = \lim_{T\to\infty} \frac{1}{2\pi} \int_{0}^{\infty} \frac{2|V_T(\omega)|t^2}{T} d\omega = S_V(\omega) d\omega. \tag{D.1.8}$$

In the above, Eqn. D.1.8, $S_V(\omega)$ represents the power spectral density (PSD) of the fluctuating quantity $V(t)$. This value is characterized by the following:

$$S_V(\omega) = \lim_{T\to\infty} \frac{2|V_T(\omega)|^2}{T}. \tag{D.1.9}$$

The PSD presents the magnitude of energy in the normalized frequency bands, this is used to define the noise level. Say we are looking at the fluctuation of voltage for example, the unit of $S_V(\omega)$ is V^2/Hz. When invoking the Parseval Theorem, the integration of the PSD (over all frequencies) produces the signal variance, with the caveat that the mean signal value is zero,

$$\overline{\delta V^2} = \int_0^\infty S_V(\omega) d\omega. \tag{D.1.10}$$

With all of the preceding in mind, it is important not to get overwhelmed by the number of equations; but, realize that the information gained from this formalism is to establish a lower bound on reliability, or a minimum to the level that is required to make the desired conjecture. We also need to define the forms of noise that are expected and how to work with them to further understand the information being presented.

D.1.3 Noise forms

Noise shows up in many shapes and sizes, specifically in solids, several types of noise can exist and independently establish the overall magnitude of fluctuations. Moreover, the noise foundation may be diverse (may be even specific to the sample

in question); however, a concise evaluation of the noise still may be made from the frequency dependence derived from the PSD. Four of the most common forms of electrical noise are: thermal, shot, flicker ($1/f$), and generation-recombination noise. The origins of the noise may emerge from a variety of sources e.g. defect motion, structural excitations, magnetic domains, spin fluctuations, charge carriers crossing an energy barrier, electronic traps, percolation effects, or current redistribution in an inhomogeneous material.[650]

In the spirit of this, I will write a brief paragraph about each of the four forms of electrical noise listed above.

First for thermal noise, which exists in virtually all electronic devices as a form of background noise. This form was first observed and described by Johnson in 1927.[760, 761] The theoretical perspective was established by Nyquist in 1928.[762] The various forms of noise can be correlated to colors, Johnson-Nyquist (thermal) noise is "white noise." This is the case because the PSD contains all frequencies and the energy is equally dispersed amongst them. Now to work out a small example, consider a device with a given resistance R at temperature T. The PSD of thermal noise will be given as $S_V(\omega) = 4k_BTR$, with the mean square voltage fluctuation being $\overline{V_n^2} = 4k_BTR\Delta\omega$. The $\Delta\omega$ represents the frequency bandwidth used to measure the voltage. Hence, by decreasing and matching the bandwidth with the frequency of desired signal one can improve the signal-to-noise ratio. One such measurement methodology is the application of phase sensitive detection with a lock-in amplifier. From a logical perspective, this form of noise is ubiquitous amongst all forms of measurements and appears in our photoconductivity experiments with $S_V(\omega) = 1 \times$

10^{-9}V.

Second we will look at another "white noise" know as shot noise. This was was observed by Schottky in 1918 in a thermionic tube.[763] This noise form is the result of random and discrete motion of charge carriers. When electrons are moving in an applied field that is running across an energy barrier, the potential energy of the electrons continues to build until their energy is high enough to bypass the barrier. After surpassing the energy barrier, the charge carriers brusquely transform the potential energy into kinetic energy. Therefore, fluctuations in the current are induced by this spontaneous transformation. For example, the PSD for shot noise produces a flat spectrum akin to that for thermal noise but in the current, the representation follows: $S_I(\omega) = 2qI$. The resulting fluctuations in current are: $I_{sh} = \sqrt{2qI\Delta\omega}$ with units of $A/\sqrt{Hz}$. In the above example, q is the charge for the carrier(s), I is the average current, and again $\Delta\omega$ is the bandwidth. Interestingly, shot noise does not have a dependence on temperature but is ever present when current flows and of course depends upon the charge of the carriers. Signal-to-noise of shot noise shows up as $I/\sqrt{2qI} \propto \sqrt{I}$. This relationship suggests that by applying a current that is larger, the noise will increase by factor of $sqrtI$. For example, if the current is increased by a factor of 400, then the noise will increase by only a factor of $\sqrt{400} = 20$. From an photoconductivity standpoint, this noise emerges from the dynamic fluctuation in the intensity of light (the number of impinging photons per second.) This is the case because the photons are independent of each other. Therefore, their occurrence and emission from the source is independent.

Next on the agenda is to cover a different color noise, "pink noise" or $1/f$ or flicker.

It is called pink noise because if one was to mix the light as a $1/f$ relationship, then the resulting PSD would favor the red hues of the spectrum, pink is very light red and would dominate the spectrum in magnitude. This form has been displayed in homogeneous semiconductors, metallic thin films, magnetic tunnel junctions, carbon nanotubes, and superconducting quantum interference devices (SQUID).[134] Since, $1/f$ noise scales inversely with the frequency it will also scale inversely with the size of the investigated system. Therefore, it becomes an ever increasing obstacle with the miniaturization of application based devices in the fields of information and sensing technology. Logically, $1/f$ noise has a PSD that becomes prominent at low frequencies and disappears into the background of white noise as $\omega \to \infty$. Moreover, this goes to say that the PSD diverges on both ends of the spectrum e.g. as $\omega \to 0$ or $\omega \to \infty$. The ubiquity of $1/f$ noise has been investigated very heavily, but no satisfactory mechanistic definition has been reached. So, the general suggestion is to view and investigate $1/f$ noise in specific systems. As mentioned the PSD diverges at both extremes of the spectrum, this looks like $S_V \propto 1/f^{\alpha}$. Empirically, the PSD established by F. N. Hooge in 1969[764] takes the form of $S_V(\omega) = \frac{\gamma_H V^2}{N f^{\alpha}}$, where $N = n\Omega$ is the number of charge carriers in the noise volume Ω of a sample with carrier concentration n_c, γ_H is the Hooge's constant that characterizes the noise level of the system. The exponent α remains near unity, $0.8 \leq \alpha \leq 1.4$. γ_H is dimensionless when $\alpha = 1$. Within the measurements that are to be obtained from the photoconductivity system, this will come into play when considering in the frequency dependence of voltage changes. Some thoughts to consider would be fluctuations in the mobility and/or the magnitude of n, the number of carriers, due

to defects and impurities.

Finally, we come to generation-recombination noise. This form of noise is of great importance in condensed matter systems. Using a semiconductor as an example, when electrons are excited into the conduction band an exciton (electron-hole pair) is created, at a later time they will recombine. If only one electron is excited, then the resistance would change in discrete steps resulting in the so-called "random telegraph signal" (RTS). Unfortunately, the noise associated with this is of a non-Gaussian type. When the noise lacks Gaussianity, the auto-correlation function, Eqn. D.1.4, to describe said distribution requires high-orders being introduced. The causality of this is (i) very few independent events i.e. only a few fluctuators couple more strongly to the resistivity than the others, or (ii) if the fluctuations are correlated i.e. the events are not independent. The 1st order Eqn. D.1.4 of a two-level system is shown in Fig. D.1.1. The PSD caused by RTS in the switching between two states with voltage amplitude ΔV and their characteristic lifetimes τ_1 and τ_2 is represented by the Lorentzian equation:

$$S_V(\omega) = \frac{4(\Delta V)^2}{\tau_1 + \tau_2} \cdot \frac{1}{(1/\tau_c)^2 + (2\pi f)^2} \tag{D.1.11}$$

where $1/\tau_c = 1/\tau_1 + 1/\tau_2$. Since we are referencing Eqn. D.1.4, the auto-correlation function, additional information shown in Fig. D.1.1 (c) is that at frequencies lower than f_c no "memory" is kept. Another mathematical representation of the Lorentzian spectrum is as follows:

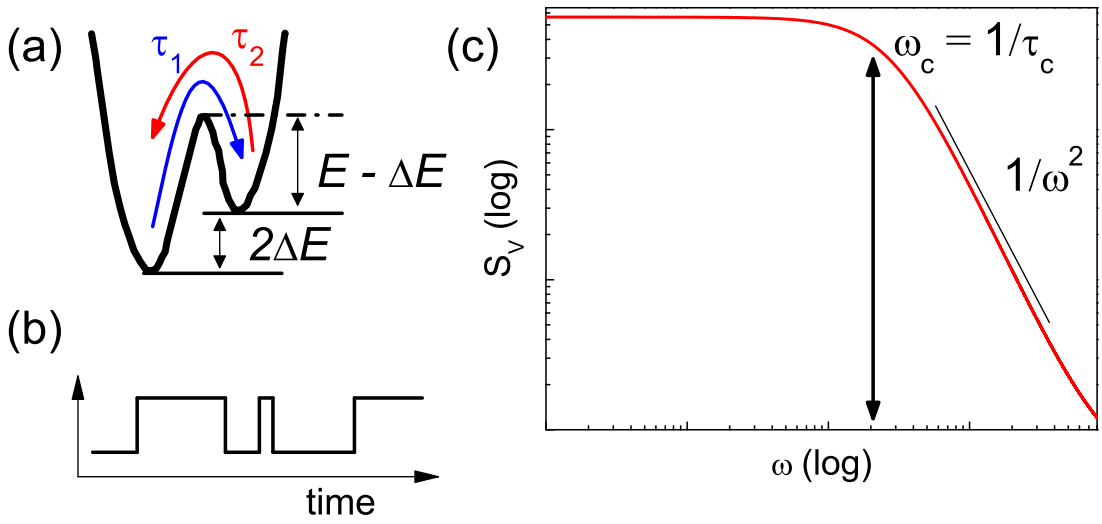

Figure D.1.1: A fluctuating two-level system, shown in (a) as a double-well potential with distinctive energies and time constants. (b) The random telegraph noise is displayed in the time domain; with (c) showing the resulting Lorentzian spectrum in the frequency domain. After [650, 758, 746]

$$S_V(\omega) = \frac{S_V^0(0)}{\cosh\left(\frac{\Delta E}{k_B T}\right)[\cosh^2(\frac{\Delta E}{k_B T}) + \omega^2 + \tau_c^2]}. \tag{D.1.12}$$

Here, $S_V^0(0)$ is the zero-frequency PSD at $\Delta E = 0$. In the limit where $\Delta E = 0$, this value is aboveboard to obtain:

$$S_V(\omega) \propto \frac{\tau_c}{1 + 4\pi^2\omega^2\tau_c^2} \tag{D.1.13}$$

As shown in Fig. D.1.1 (c) two main regions show up in the Lorentzian spectrum: (i) $S_V \propto 1/f^2$ and (ii) an almost flat region at $f \ll f_c$. In the former scaling changes to the latter when $f \gg f_c \sim \tau_c$ is no longer true. To draw a better understanding, the corner frequency is equivalent to the inverse of $2\pi\tau$, $f_c = 1/2\pi\tau$.

Now that we have seen the limiting case, two-level system, it is plausible to envision the result when generation-recombination comes into play. First to get the general information, GR noise is a directly result of fluctuations in the number of excited free carriers inside of a two terminal sample system. If we consider the generation rate to be $g(N)$ and the recombination rate to be $r(N)$. Then the fluctuation is well described by the differential equation:

$$\frac{dN}{dt} = g(N) - r(N) + \Delta g(t) - \Delta r(t). \tag{D.1.14}$$

Next, we need to broaden the response spectrum associated with the random transitions because the ground state and excitation state are no longer discrete because in principle we will not be shining singular photons onto the samples. As well, the samples that are investigated are solids, specifically macroscopic crystalline materials. So, one should expect that the valence and conduction states form bands. Additionally GR noise can occur from transition between the conduction band and localized states in the energy gap.

Interestingly, one potential mechanism for $1/f$ noise is the superposition of a statistically "large" number of independent Lorentzian spectra. Importantly for this is the characteristic lifetimes will have a proper distribution following:[765, 766]

$$S(\omega) \propto \int D(\tau) \frac{\tau}{1 + 4\pi^2\tau^2\omega^2} d\tau. \tag{D.1.15}$$

Here, τ is a characteristic time constant for the Lorentzian spectrum and $D(\tau)$ is the distribution function for τ. The understanding of noise involved in the transport

process allots for a deeper understanding of potential functionality.

Analysis

Closing out our overview on noise and noise forms, we will take a look at some analysis methods. The noise involved may be easily diagnosed, $n\times 60\,\mathrm{Hz}$, where n is an integer. It can always be extremely complex, with many overlapping frequency and phase components, such as building vibrations, temperature variations, other changes in environmental conditions, and fluctuations in the number of free carriers. To understand the forms and sources of noise involved, it is pertinent to do some math and learn some of the language of digital signal processing. The first step in this process is to measure time-dependence and then run the result, assuming the data points are of a consistent spreading, through a Fourier transform to obtain a spectrum of the frequency components.

To decipher the noise components, we can process the time-dependent data through a Fourier transform. To improve accuracy for the resulting spectrum of noise components, we first establish our boundaries. These boundaries include the high frequency limit, invoking the Nyquist theorem to determine this value, as follows

$$f_s = 2 \times f_{Nyquist}. \tag{D.1.16}$$

Here, f_s is the sampling frequency and $f_{Nyquist}$ represents the Nyquist frequency. Essentially this produces the upper bound in frequency that is minimally reliable to establishing the existence of an underlying component. The value of this limit is set by the average time between data points multiplied by two, of course since the data points are not equally spaced some consideration has to be taken there as well. To

set the lower limit in the frequency domain, we again invoke the Nyquist theorem and say that the minimum frequency is 1/2 of the total time for data collection. For example, if we measure for 30 minutes then the total number seconds is 1800 and the frequency will be 5.5×10^{-4} Hz.

When considering the Neumann theorem, the symmetry of a physical property of a material must be included in the symmetry of the Hamiltonian for the given material. However, this theorem breaks down when considering transport properties, the measurements are inherently not thermodynamically reversible processes. The entropy change within the system results in the theorem not holding up in transport environments.

Measurements of the noise components are done in the simplest manner by implementing a 4-terminal DC technique shown in Fig. D.1.2 (a). This resembles the same circuit layout for a 4-probe resistance measurement, with the addition of a capacitor C operating as a high pass filter to block the DC offset. A few limitations of this design are: the frequency range is limited to $f > f_{min} \sim 1/R_i C$, fluctuations in voltage source, and temperature instabilities.

If the noise is lower than f_{min} or the other limitations dominate the spectrum, then switch to a 5-terminal scheme as shown in Fig. D.1.2 (b). The two connected branches on the Hall bar, along with the two balancing resistors R_1 and R_2, create a bridge-type circuit thus eliminating the DC offset. Importantly, the external factors will now have a minimal impact due to the bridge balancing; therefore, the sample fluctuations will be less sensitive to the external sources and the frequency range will not have to be limited.

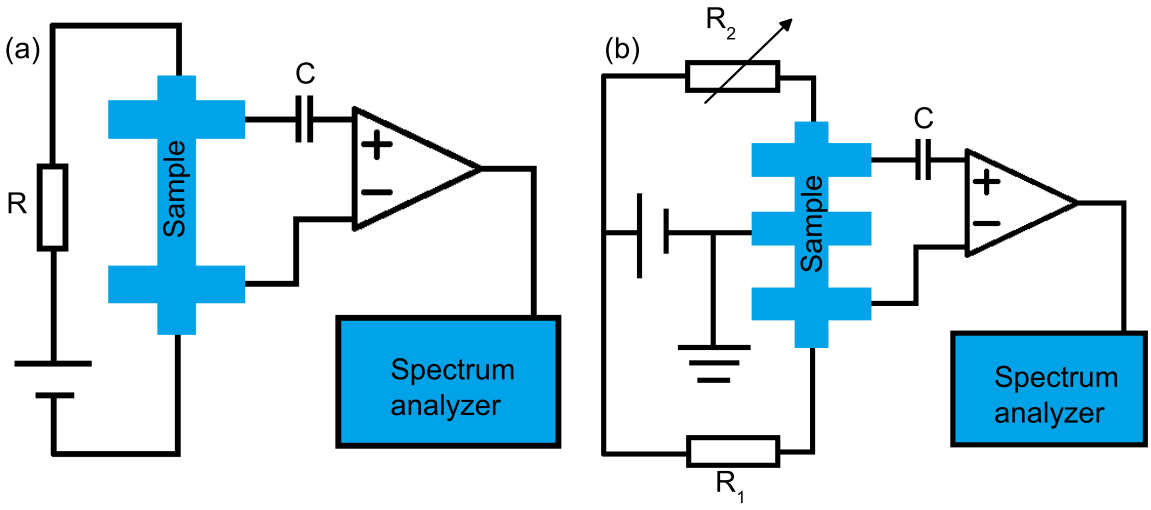

Figure D.1.2: Shown in (a) is a 4-terminal DC noise measurement setup and in (b) a 5-terminal DC setup invoking the use of a bridge-type circuit. After [747, 746]

At this point we have a fairly good picture of the noise sources and functions. It is my opinion that one should consider this a highly important part of the process when measuring transport properties, because by comparing the result from different portions of the measurement sequence it would be feasible to obtain a deeper understanding of the physical mechanisms of transport. If the development continues forward into measuring in AC environments. The resistance will fluctuate at the modulation frequency of the sinusoidally excited carriers, thus producing noise sidebands. To isolate the signal more effectively, an experimental circuit and system could follow Fig. D.1.3.

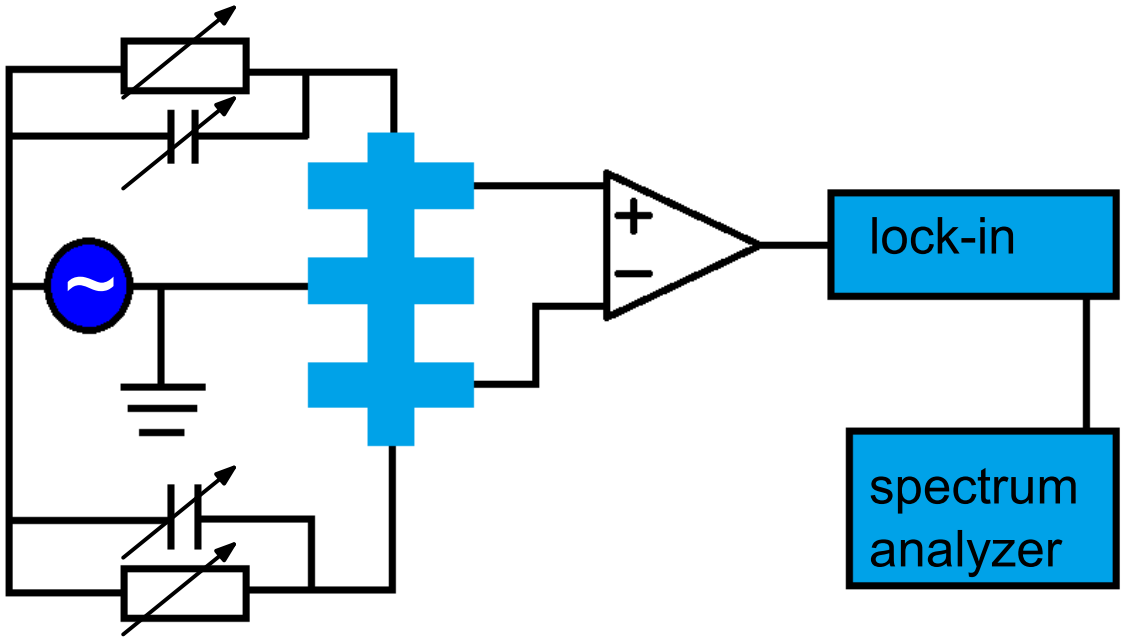

Figure D.1.3: Shown here is the circuit necessary to capture the noise spectrum from an AC circuit, with the AC current being $I = I_0 \sin(\omega_0 t)$

Vita

Brian Holinsworth was born in Fort Worth, Texas, USA. He attended Northeastern State University in Tahlequah, Oklahoma, USA between 2003 and 2008, where he received a B.S. degree majoring in Chemistry. After having starting a small business and having many real-world experiences, Holinsworth joined the research group of Dr. Janice L. Musfeldt in the spring 2011 pursuing his Ph.D. degree at the University of Tennessee. His research focuses on the spectroscopic investigations of thin-film complex ferrites. Brian Holinsworth received a Doctor of Philosophy Degree in Chemistry from the University of Tennessee in Spring 2018.